

Long-term imaging, automated high-content phenotyping and sorting of *C. elegans* larvae and embryos using microfluidic platforms

Thèse N° 7509

Présentée le 1^{er} novembre 2019

à la Faculté des sciences et techniques de l'ingénieur

Laboratoire de microsystemes 2

Programme doctoral en microsystemes et microélectronique

pour l'obtention du grade de Docteur ès Sciences

par

Hüseyin Baris ATAKAN

Acceptée sur proposition du jury

Prof. L. G. Villanueva Torrijo, président du jury

Prof. M. Gijs, directeur de thèse

Dr W. Keil, rapporteur

Prof. C. Ewald, rapporteur

Dr S. Carrara, rapporteur

2019

Science is the most real guide for civilization,
for life, for success in the world.
To search for a guide other
than science is absurdity,
ignorance and heresy.

— Mustafa Kemal Atatürk

Acknowledgements

To begin with, I would like to thank my scientific advisor **Prof. Martin Gijs** for giving me the opportunity to conduct my doctoral studies in his group. Martin has always believed in me and showed me a path to follow throughout this journey. Under his leadership, I can easily say that he made my doctoral studies go very smooth. He was also a great mentor, whenever I needed some career guidance, he was always there. Martin allows you to have some freedom during your projects but if he notices that you are losing your path, he brings his help into play. Martin also liked to challenge me to improve myself. Thanks to him, I acquired whole new image and video processing skills. Therefore, thank you Martin with my deepest gratitude for everything.

A special thanks goes to **Melis** and **Lucie**. I always enjoyed our short Turkish chats with Melis together and she has always been there for me when I needed administrative help. Lucie has always been so great at helping me out with my course registration/failure issues and I will definitely miss our lab hikes together. I am tremendously thankful to **Thomas** for his valuable ideas on our projects and **Jalil** for always backing us up in our teaching work and helping me out with the devices in our laboratory.

I would like to express my gratitude to **Matteo**. I believe we always clicked instantly on many of my projects in this thesis. Especially in the beginning of my studies, whenever I was quite lost, he was excellent at supervising me. He has always been great at showing a direction under his conceptualization. I would like to thank our collaborators from Laboratory of Integrative Systems Physiology, under scientific advisory of **Prof. Johan Awerx**, **Laurent** and **Kevin** for their valuable efforts in our collaborative projects. I am grateful to them for showing me a path to learn from nothing to a professional level on *C. elegans*. I believe we accomplished some great work together.

I thank **Prof. Guillermo Villanueva**, **Prof. Collin Ewald**, **Dr. Sandro Carrara** and **Dr. Wolfgang Keil** for accepting to be the jury members of this thesis and for their valuable scientific input. I would like to acknowledge the financial support of EU Ideas program (ERC-2012-AdG-320404). Many thanks also to all the CMI staff members for their support and help on micro-fabrication processes.

I am deeply thankful to our small Turkish community in Lausanne. **Alp**, **Baran**, **Fazil**, **Murat**, **Eda**, **Kadir** and **Okan**, I really enjoyed our chats and it felt quite good to speak Turkish every now and then. All former LMIS2 members, **Raphael**, **Cristina**, **Tuan**, **Li**, **Gergely**, **Fabien**, **Diego** and **Tuna**, thank you for sharing this journey with me and having some nice moments together. I truly thank our current group members, more specifically, **Vittorio** for a great

Acknowledgements

conference and a follow-up trip in Taiwan, **Yang** for our late night chat/research together, **Muaz** for our interesting talks on Middle East, **Farzad** for adding color to our group, **Roger** for always being there with his positive attitude, **Daniel** for being a loyal member of my chill breaks and **Xiaopeng** for being an awesome officemate. I am truly thankful to all my students whom I worked with during this journey, **Furkan, Rongrong, Farzaneh, Dilsher** and **Rami**. Working with them was a great experience, I learned a lot and I hope that I managed to teach them a thing or two.

I am sincerely grateful to my friends from my bachelor studies with whom I still keep in touch every day. **Denizhan, Ekrem, Tugberk, Duygu, Tunc, Yunus, Bora** and **Kivanc** have always been just one text message away whenever I wanted to talk about anything or had a problem to consult. My brothers from Zurich – **Tanju, Stanic, Rajko, Djole, Berkin** – for generating a wonderful Serb-Turk combo. I know I got friends for life, and our weekend get-togethers and getaway trips helped me a lot to endure the tough parts of this journey. I would like to express my gratitude to **Jenny** and once again to **Roger** for always being there for everything. There is so much, I have no idea where to start. Our dinners, weekend activities, chill breaks, a great car trip in the USA, their logistic help in Lausanne...Thank you both very much and I am sure we will maintain this bond wherever life takes us after. I am tremendously thankful to my flatmate **Vaibhav** for being the person he is, candid, chill and fun. Sharing a flat with someone for 4 years straight is no joke, I could not have imagined this if it was not for him. Congrats on your thesis too!

I am deeply thankful to my aunt, cousins and uncle for always being there for me, just a phone call or a text message away. My deepest gratitude goes to my mother and grandma. They say behind every great man there is a woman. While I am not a great man, I have been extremely lucky to have two great women behind me, supporting me at every step of my life, listening to all my complaints, calming me down when needed and entertaining me. Well...actually I was luckier than that, I met another great woman during this journey, having in total three great women behind me. **Raffa**, there is no way that I can thank enough in this thesis to you, it can go several pages and I might need to write another PhD thesis to adequately express my gratitude. You are the kindest person I have ever known and without you this work would not have been possible. Thank you a lot for your constant support, being there for me no matter what and being the person you are. A special thanks goes to exquisite **Raffa food** which deserves a separate sentence of acknowledgment here. Lastly, I would like to thank these three wonderful women once again and dedicate this thesis to them and to the memory of my father.

Lausanne, October 15, 2019

Baris

Abstract

The model organism *C. elegans* is frequently studied to address fundamental biological questions motivated by its short life cycle, small size, hermaphrodite behavior and well-annotated genome. In this work, we present novel microfluidic platforms that support long-term culture, automated high-content phenotyping, high-resolution imaging and multiplexing, as well as a hand-held device for sorting of larvae and embryos of *C. elegans*.

In the microfluidics-enabled studies of *C. elegans*, *in vivo* nematode culturing platforms that allow high-content phenotyping during worms' life cycle in an automated fashion have been rare so far. In our first study, we present a multiplexed polydimethylsiloxane (PDMS)-based microfluidic platform for the rapid high-content phenotyping of populations of *C. elegans* down to single animal resolution. We reversibly and frequently (every 35 minutes) confined nematodes during their life cycle inside tapered channels for stable fluorescence imaging and extraction of growth parameters, in combination with a determination of motility phenotypes obtained from video-recording (every 7 hours) of freely moving nematodes. We extracted 19 phenotypic parameters and proved that dietary restriction (DR) plays a crucial role in the disease regression of a worm model of Huntington's disease.

In a second work, we demonstrate a multiplexed, high-throughput and automated embryo phenotyping microfluidic platform to analyze embryogenesis of *C. elegans* under application of different chemical compounds. We performed up to 800-embryo experiments within a preparation time of only 35 minutes and executed 12 hours of imaging (with 5 and 10 minute intervals), which was followed by an automated phenotyping using machine learning and image processing approaches. Our validation study of osmosensation on the embryos indicated a developmental lag and an induction of mitochondrial stress in embryos exposed to high doses (200 mM) of glucose and NaCl, while small doses of sucrose and glucose accelerated development.

We also realized that microfluidic technologies could further be exploited for nematode studies at single organism resolution, providing more of a 'personalized' phenotyping while also collecting population-averaged information like in conventional bio-assays. In particular, we have realized a multiplexed, potentially high-throughput and high-resolution microfluidic platform to culture *C. elegans* from embryo to the adult stage at single-animal resolution. We first placed single embryos in growth chambers, observing the main embryonic stages (image-captured every 5 minutes) and continued with *C. elegans* larvae developmental studies (video-recorded every 4 hours). As a proof-of-concept, we exposed the nematodes to 8 different concentrations, from 1 nM to 1 mM, to the anthelmintic drug tetramisole diluted in

Abstract

an *E. coli* feeding solution, and we observed from our automated phenotyping results that towards the late stages of the nematodes' life, tetramisole influence on the development and motility became more prominent. We thereby showed that our device offers high-precision phenotyping of the impact of chemicals on *C. elegans*.

C. elegans is also an exceptionally valuable model organism to target epigenetic studies but most of these have focused so far on phenotypic variations over multiple generations, omitting the evaluation of epigenetic inheritance in the early stages of the nematodes' life. We have also realized an epigenetics-oriented microfluidic platform to observe mother-to-progeny heritable transmission in the nematode *C. elegans* at high-resolution, under significant automation and enabling a high degree of parallelization. After a 24 hours culture of nematodes starting from L4 larvae under application of various concentrations and durations of the drug doxycycline, we quantified the mitochondrial unfolded protein response (UPR^{mt}) of the first released *hsp-6::gfp* embryos by computing the average green fluorescent protein (GFP) intensity as an indicator to mitochondrial stress inheritance. After analyzing the different phenotypes with our automated and customized phenotyping algorithms, we noticed that a minimum doxycycline concentration of 30 µg/mL and a drug exposure time of 15 hours applied to the mothers could induce mitochondrial stress in embryos.

C. elegans-based assays require age-synchronized populations prior to experimentation to avoid any kind of outliers in the resulting data. There has been many proposed approaches to synchronize populations of *C. elegans* at certain larval stages; however, such methods often utilize tedious, complex and low-throughput handling procedures of the nematodes. In the last part of this thesis, we demonstrate a PDMS microfluidic device for high-throughput, efficient and extremely rapid sorting of *C. elegans* at various life stages. Our device, which consists of three plasma-activated and bonded PDMS parts, empowers sorting of two consecutive larval stages in two minutes with a sorting purity of 73 - 100%. In parallel, we could retain the remaining population in the chip, providing collection of two sorted larval stages at both outputs of the device. In addition, we employed the equivalent of a standard bleaching procedure for embryo harvesting on-chip and showed that egg extraction and a synchronized L1 population could also be easily obtained. We think that our device can potentially find further use as a tool for *C. elegans* synchronization and rapid egg extraction.

Keywords: *C. elegans*, microfluidics, Lab-on-a-chip, high-content phenotyping, high-resolution, high-throughput, multiplexed, larvae, embryo, culture, long-term imaging, sorting, automation

Résumé

En raison de son court cycle de vie, de sa petite taille, son hermaphrodisme et de son génome totalement séquencé, *C. elegans* est un organisme modèle important en biologie. Dans cette thèse, nous présentons de nouvelles plateformes microfluidiques qui permettent la culture sur le long terme, le phénotypage automatisé à haut contenu, l'imagerie à haute résolution et le multiplexage. Nous avons aussi développé un dispositif portable de tri des larves et des embryons de *C. elegans*.

Jusqu'à présent, les laboratoires sur puce pour la culture des nématodes ne permettent pas un phénotypage automatisé à haut contenu pendant le cycle de vie des vers. Notre plateforme microfluidique multiplexée à base de Polydiméthylsiloxane (PDMS) permet de réaliser un phénotypage rapide, à haut contenu et à différents moments du cycle de vie des populations mais aussi d'un seul exemplaire de *C. elegans*. Afin de réaliser une imagerie de fluorescence stable, les vers étaient confinés toutes les 35 minutes, de manière réversible, dans des canaux. En plus de l'imagerie nous avons pu extraire des paramètres sur la croissance et sur la mobilité des nématodes. Ces dernières informations ont été obtenues à partir d'enregistrements vidéo réalisés par intervalle de 7 heures. Les 19 paramètres phénotypiques qui ont été extraits, ont montré que la restriction alimentaire (DR) joue un rôle crucial dans la régression de la maladie de Huntington chez un modèle de *C. elegans*.

Afin de pouvoir analyser l'embryogenèse des nématodes sous l'application de différents composés chimiques nous avons réalisé une plateforme microfluidique automatisée et multiplexée qui permet de réaliser le phénotypage d'embryons à haut contenu. Notre expérience prévoit un temps de préparation de 35 minutes et nous pouvons analyser jusqu'à 800 embryons en même temps. L'expérience consiste en 12 heures d'imagerie (avec 5 et 10 minutes d'intervalle) suivies par un phénotypage automatisé en utilisant des approches de traitement d'images et d'apprentissage automatique. Notre étude sur l'osmosensation a indiqué que les embryons qui ont été exposés à des doses élevées (200 mM) de glucose et de NaCl présentent un retard du développement et une croissance du stress mitochondrial. En revanche, de petites doses de saccharose et de glucose ont accéléré le développement des embryons.

Les technologies microfluidiques pourraient être davantage exploitées afin d'analyser les caractéristiques phénotypiques d'un seul exemplaire de *C. elegans* à la fois, offrant ainsi un phénotypage 'personnalisé', tout en collectant des informations moyennées sur la population, comme dans les bioessais classiques. Notre plateforme microfluidique multiplexée permet l'analyse à haut débit et à haute résolution d'un seul individu de *C. elegans*, depuis le stade embryonnaire jusqu'au stade adulte. En plaçant des embryons dans des chambres de croissance

nous avons pu observer les principaux stades embryonnaires (avec des captures d'images faites à 5 minutes d'intervalle) et nous avons pu étudier ensuite le développement des larves (avec des enregistrements vidéo toutes les 4 heures). Les nématodes étaient exposés à 8 différentes concentrations, de 1 nM à 1 mM, d'un médicament anthelminthique tétramisole qui était dilué dans une solution alimentaire de *E. coli*. Nos résultats, obtenus à l'aide du phénotypage automatisé, montrent que le développement et la motilité des nématodes se trouvant déjà dans un stade de vie avancé sont fortement influencés par le tétramisole. Nous avons ainsi pu prouver que notre dispositif est capable de réaliser un phénotypage très précis de l'impact des produits chimiques sur *C. elegans*.

Ce nématode est très utilisé dans les études d'épigénétique. Jusqu'à présent ces études se sont focalisées sur l'analyse des variations phénotypiques sur plusieurs générations sans évaluer l'héritage épigénétique dans les premières étapes du cycle de vie des nématodes. Nous avons réalisé une plateforme microfluidique à haute résolution afin de pouvoir observer la transmission des gènes phénotypiques entre mère et progéniture, grâce à une automatisation significative et un degré élevé de parallélisation. Nous avons réalisé une culture de 24 heures de *C. elegans* à partir de larves L4 avec différentes concentrations et durées d'exposition de doxycycline. Ensuite, afin d'obtenir un indicateur sur le stress mitochondrial, nous avons quantifié l'expression du gène rapporteur de la réponse protéique mal pliée mitochondriale (UPR^{mt}) libérée par les premiers embryons *hsp-6 : :gfp* – en calculant l'intensité moyenne de la protéine fluorescente verte (GFP). A l'aide de nos algorithmes de phénotypage automatisés et personnalisés, nous avons pu analyser les différents phénotypes et nous avons constaté qu'avec une concentration minimale de doxycycline de 30 µg/mL et un temps d'exposition au médicament de 15 heures, les mères causent un stress mitochondrial chez les embryons.

Afin d'éviter tout type de données aberrantes dans les résultats, les analyses basées sur *C. elegans* nécessitent des populations avec des individus ayant le même âge. De nombreuses approches ont été proposées pour synchroniser les populations à différents stades larvaires. Cependant, ces méthodes utilisent souvent des procédures complexes et à faible débit de traitement des nématodes. Dans la dernière partie de cette thèse, nous présentons un dispositif microfluidique PDMS qui permet le tri de *C. elegans* à différentes étapes du cycle de vie à haut débit, efficace et extrêmement rapide. Notre appareil, constitué de trois parties en PDMS soudées entre elles et activées au plasma, permet le tri de deux stades larvaires consécutifs en deux minutes avec une pureté de tri entre 73 et 100%. Les deux stades larvaires sont collectés aux deux sorties de l'appareil. En outre, nous avons utilisé l'équivalent d'une procédure de blanchiment standard pour la collecte d'embryons sur puce et nous avons montré que l'extraction des œufs et d'une population L1 synchronisée peuvent être facilement obtenues. Nous pensons que notre appareil peut être commercialisé pour la synchronisation de *C. elegans* et l'extraction rapide des œufs.

Mots clés : *C. elegans*, microfluidique, laboratoires sur puce, high-content phenotyping, haute résolution, haut débit, multiplexé, larves, embryon, culture, imagerie à long terme, tri, automatisation

Contents

Acknowledgements	i
Abstract	iii
Résumé	v
List of Figures	xi
List of Tables	xv
1 Introduction	1
1.1 <i>Caenorhabditis elegans</i> - the model organism	1
1.2 Microfluidics as assisting technology	4
1.3 Thesis outline	6
2 Platform design and common procedures	9
2.1 Mask fabrication	9
2.2 Microfluidic chip fabrication	10
2.2.1 Fabrication of single-layer Si-SU8 molds	10
2.2.2 Fabrication of two-layer Si-SU8 molds	11
2.2.3 Fabrication of hybrid PDMS microfluidic chips	11
2.3 Materials and chemicals	11
2.4 Bacteria culture and preparation	13
2.5 Control of worm populations	13
2.6 Experimental setup	14
3 Automated high-content phenotyping over the life cycle of the nematode <i>Caenorhab-</i> <i>ditis elegans</i>	17
3.1 Introduction	19
3.2 Automated high-content phenotyping platform design and operation	20
3.2.1 Microfluidic chip design	20
3.2.2 Silanization of the microfluidic chip	21
3.2.3 Automated fluidic protocol	22
3.2.4 Platform working principle	22
3.3 Automated post-experiment image and video analysis	25
	vii

3.3.1	Growth parameters obtained from time-lapse imaging	25
3.3.2	Volume calculation and fluorescent intensity correction	28
3.3.3	Motility analysis from video recordings	30
3.3.4	Initial raw data after the post-experiment automated phenotyping . . .	32
3.4	High-content phenotyping of worms at various concentration of bacterial food	33
3.4.1	Egg release behavior of worms	34
3.4.2	Change of growth parameters	35
3.4.3	Induction of mitochondrial stress	36
3.4.4	Change of motility parameters	38
3.4.5	Clustergram analysis	39
3.5	Influence of DR on a Huntington's disease worm model	40
3.5.1	Change of growth parameters	41
3.5.2	Change of motility parameters	41
3.5.3	Clustergram analysis	43
3.6	Statistical analysis	44
3.7	3D microfluidic channel fabrication for accurate worm immobilization	45
3.8	Discussion and conclusion	46
4	Automated phenotyping of <i>C. elegans</i> embryos with a high-throughput-screening microfluidic platform	49
4.1	Introduction	50
4.2	Automated microfluidic phenotyping platform design and operation for <i>C. elegans</i> embryos	51
4.2.1	Microfluidic chip design	51
4.2.2	Automated fluidic protocol	52
4.2.3	Platform working principle	52
4.3	Automated detections of embryo state and embryogenesis stage transitions . .	55
4.3.1	Automatic location of embryo incubators	56
4.3.2	Automated detection of embryo states and embryo stage transitions . .	57
4.3.3	Automated fluorescent signal quantification	62
4.4	Osmotic influence on embryo development	63
4.5	Dominant influence of ionic molecules on the embryo development	68
4.6	Mitochondrial stress induction under osmotic stress	70
4.7	Statistical analysis	73
4.8	Discussion and conclusion	74
5	Automated platform for life-long and high-content phenotyping of single <i>C. elegans</i> worms	77
5.1	Introduction	78
5.2	Automated microfluidic phenotyping platform design and operation of single <i>C. elegans</i> worms	79
5.2.1	Microfluidic chip design	79
5.2.2	Silanization of the microfluidic chip	80

5.2.3	Platform working principle	81
5.2.4	Automated fluidic protocol	81
5.3	Tetramisole viability assay on <i>C. elegans</i>	82
5.3.1	Effect of tetramisole dose and bleaching treatment on the embryonic development	82
5.3.2	Effect of tetramisole dose on the larval development: growth parameters	85
5.4	Effect of tetramisole dose on the larval motility and correlation with the growth parameters	87
5.5	Effect of tetramisole dose on the larval motility by averaging the motility indices over the full experiment duration (80 hours)	91
5.6	Statistical analysis	93
5.7	Discussion and conclusion	94
6	The detection of early epigenetic inheritance of <i>C. elegans</i> with a microfluidic phenotyping platform	97
6.1	Introduction	98
6.2	Microfluidic phenotyping platform design and operation	99
6.2.1	Microfluidic chip design	99
6.2.2	Platform working principle	100
6.2.3	Fluidic experimentation protocol	101
6.3	Automated and operator-based post-experiment analysis	104
6.3.1	Mother nematode size tracking analyzed with time-lapse imaging	104
6.3.2	Operator-based phenotyping of L1 progenies	104
6.3.3	Embryo viability and fluorescent signal expression tracking	104
6.4	Parental generation development under doxycycline treatment	106
6.5	Doxycycline influence on the embryogenesis of first embryo progenies	109
6.6	Inheritance of mitochondrial stress as evidenced by the fluorescence expression of embryos	110
6.7	UPR ^{mt} expression of L1 larvae	111
6.8	Statistical analysis	112
6.9	Discussion and conclusion	113
7	PDMS filter structures for size-dependent sorting and on-chip egg extraction of <i>C. elegans</i>	117
7.1	Introduction	118
7.2	PDMS filter structures design and operation	119
7.2.1	Microfluidic chip design	119
7.2.2	Sorting protocol	121
7.3	Results of the sorting experiments	122
7.3.1	Population-based statistics of the sorted nematodes	125
7.3.2	Purity of the sorting	127
7.4	On-chip egg extraction	128
7.4.1	Egg extraction via a standard bleaching procedure	128

Contents

7.4.2 Egg extraction via mechanical compression of PDMS	129
7.5 Discussion and conclusion	129
8 Conclusions	133
8.1 Future outlook	135
 Acronyms	 139
Bibliography	141
Curriculum Vitae	157
List of Publications	159

List of Figures

1.1	Schematic overview of the drug discovery pipeline.	2
1.2	Schematic development cycle of the nematode <i>C. elegans</i> at 22 °C.	3
1.3	Overview of the designed microfluidic platforms and the related chapters of the thesis.	6
2.1	Details of the Cr mask fabrication process.	9
2.2	Details of the fabrication process of single-layer Si-SU8 molds and the microfluidic chip.	10
2.3	Details of the fabrication process of two-layer Si-SU8 molds and the microfluidic chip.	12
2.4	Details of the fabrication process of hybrid PDMS microfluidic chip.	13
2.5	Schematic protocol of the bleaching procedure.	14
2.6	Schematic diagram of the experimental setup.	15
3.1	Details of the microfluidic platform for automated high-content phenotyping of <i>C. elegans</i>	21
3.2	Fluidic protocol of the microfluidic chip.	23
3.3	Operation modes of the microfluidic chip.	24
3.4	Real-time confinement images of <i>C. elegans</i> at several larval stages.	26
3.5	The dynamic background creation approach used in the confinement analysis.	27
3.6	Details of the automated image analysis of the bright-field images for the worms confined in the tapered channels.	28
3.7	Details of the automated fluorescent image intensity analysis for the worms confined in the channels.	29
3.8	Details of the automated fluorescent image aggregate analysis for the <i>punc-54::Q40::YFP</i> worms confined in the channels.	30
3.9	The dynamic background creation approach used in the motility analysis.	31
3.10	Details of the automated motility analysis for worms that are freely moving in a growth chamber.	33
3.11	Automated image and video analysis for extraction of worm phenotypes.	34
3.12	Study of the effect of <i>E. coli</i> concentration on the fertility of <i>hsp-6::gfp</i> worms.	35
3.13	Study of the effect of <i>E. coli</i> concentration on the worm development of <i>hsp-6::gfp</i> worms.	36

List of Figures

3.14	Study of the effect of <i>E. coli</i> concentration on the fertility of <i>hsp-6::gfp</i> worms. .	37
3.15	The normalized average fluorescent intensity expression of <i>hsp-6::gfp</i> worms under four different <i>E. coli</i> feeding concentrations.	37
3.16	Study of the effect of <i>E. coli</i> concentration on the motility of <i>hsp-6::gfp</i> nematodes.	38
3.17	The dose-dependent motility behavior for four different <i>E. coli</i> feeding of <i>hsp-6::gfp</i> worms at 57 hours.	39
3.18	Clustergram comparison of <i>hsp-6::gfp</i> nematodes of motility and development parameters.	40
3.19	Study of the effect of <i>E. coli</i> concentration on the longitudinal growth of the <i>p_{unc-54}::Q40::YFP</i> mutant worms, a model for HD.	42
3.20	Study of the effect of <i>E. coli</i> concentration on the aggregate growth of the <i>p_{unc-54}::Q40::YFP</i> mutant worms, a model for HD.	42
3.21	Study of the effect of <i>E. coli</i> concentration on the motility parameters of <i>p_{unc-54}::Q40::YFP</i> mutant worms.	43
3.22	Clustergram comparison of <i>p_{unc-54}::Q40::YFP</i> nematodes of motility and development parameters.	44
3.23	Schematic representation of an experimental configuration, as defined by the number of worms distributed over the different chambers and the applied feeding conditions.	45
3.24	Schematic diagram for microfabrication of variable-height three-dimensional confinement channel master structures in silicon.	46
3.25	SEM images of the confinement channels and the resultant surface profile of the etched Si wafers.	47
4.1	Details of the high-throughput microfluidic platform for automated phenotyping of <i>C. elegans</i> embryos.	53
4.2	Operation modes of the microfluidic chip.	54
4.3	Pressure and particle velocity simulations along all the embryo incubators in a microfluidic lane.	55
4.4	Stitched image covering 8 microfluidic lanes each of which having 100 embryo incubators.	56
4.5	Details of the automated detection of the position of the embryo incubators. .	57
4.6	Schematic representation of the algorithms used for the automated phenotyping of <i>C. elegans</i> embryos.	59
4.7	Automatic detection of the onset of the twitching stage of an embryo using the mobility function (MF).	60
4.8	Block diagram of the automated embryo phenotyping protocol.	61
4.9	Real-time images of six embryo incubators in a timespan of 12 hours.	61
4.10	Automated image analysis for fluorescent signal expression of <i>C. elegans</i> embryos.	62
4.11	Characterization of the bleaching procedure to obtain a massive amount of <i>C. elegans</i> embryos.	65

4.12 Study of the influence of various chemical compounds on the development time of “Normal” wild-type <i>C. elegans</i> embryos.	66
4.13 Study of the influence of various chemical compounds on the development time of “Normal” wild-type <i>C. elegans</i> embryos quantified by manual classification.	67
4.14 Study of the effect of various chemical compounds with different molarities on the development of wild-type <i>C. elegans</i> embryos.	70
4.15 Study of the effect of various 200 mM chemical compounds on the development of “Normal” <i>hsp-6::gfp C. elegans</i> embryos.	72
5.1 Single-animal resolution multiplexed microfluidic platform for phenotyping of the nematode <i>C. elegans</i>	80
5.2 Schematic illustration of the operation modes of the microfluidic chip.	83
5.3 Pressure and velocity simulations at the position of all the embryo pockets in front of the growth chambers.	84
5.4 Real-time images of the development of N2 wild-type nematodes starting from the experiment’s initiation up to 3 days.	85
5.5 Study of the development of N2 wild-type embryos under various tetramisole doses.	85
5.6 Study of the life cycle development of N2 wild-type nematodes under various tetramisole doses.	87
5.7 Example of real-time images of the development of N2 wild-type nematodes under various tetramisole dilutions.	88
5.8 Dose-dependent development and motility percentage response of N2 wild-type nematodes under various tetramisole concentrations at 36 hours in their life.	90
5.9 Dose-dependent development and motility percentage response of N2 wild-type nematodes under various tetramisole concentrations at 48 hours in their life.	91
5.10 Central velocity and head amplitude variation of N2 wild-type nematodes under various tetramisole concentrations.	92
5.11 Beating frequency and tail amplitude variation of N2 wild-type nematodes under various tetramisole concentrations.	93
5.12 Dose-dependent development and motility percentage response of N2 wild-type nematodes under various tetramisole concentrations.	94
6.1 Details of the mother-to-progeny development platform for the automated phenotyping of the larvae and embryos of <i>C. elegans</i>	101
6.2 Schematic representation of a worm culture chamber (left) and a serpentine with embryo traps (right) with zooms on key features.	102
6.3 Real-time images of the experimental protocol from the beginning of an experiment until the end.	103
6.4 Overview of the image processing approaches employed for the phenotyping of <i>C. elegans</i>	105
6.5 Details of the automated location detection of the embryo traps and the binary mask creation for embryos’ fluorescent intensity detection.	107

List of Figures

6.6	Influence of doxycycline on the development of the mother nematodes.	108
6.7	Study of the effect of doxycycline treatment on the embryo release parameters of mother nematodes.	109
6.8	The development time of first embryo progenies released from the mother nematodes under MET, OMT, OET and CNT conditions.	110
6.9	Illustrative images taken during an embryo development.	112
6.10	Normalized average embryo intensity profile of the first embryo progenies under MET, OMT, OET and CNT conditions and 15, 30 and 60 $\mu\text{g/mL}$ doxycycline concentrations.	113
6.11	Influence of doxycycline on the size (length, diameter) and UPR ^{mt} expression of L1 progenies.	114
6.12	Influence of doxycycline on the maximum UPR ^{mt} expression of L1 progenies. .	114
7.1	Details of the PDMS filter structures for size-dependent sorting and on-chip egg extraction of the nematode <i>C. elegans</i>	120
7.2	Details of the experimental protocol used during the sorting procedure.	122
7.3	Real-time images illustrating the sorting procedure, the target worms of the sorting are highlighted by red circles.	124
7.4	Measured diameter values of worms before and after sorting from different mixed populations.	125
7.5	Results from the sorting experiments.	126
7.6	Characterization of worm populations on NGM agar plates prior to sorting experiments.	128
7.7	Schematic illustration and real-time images of the experimental protocol for on-chip egg extraction via bleaching.	130
7.8	Schematic illustration and real-time images of the experimental protocol for on-chip egg extraction via PDMS deflection.	131

List of Tables

2.1	Experimental method to obtain L1, L2, L3, L4 and young adult (YA) <i>C. elegans</i> at a designated time point (hour <i>X</i>) from an initially characterized L1 larval population.	15
4.1	The embryo state classification obtained from the automated phenotyping script for wild-type nematodes.	64
4.2	Comparison of the automated phenotyping data to the manually classified data for the embryo states of wild-type worms.	68
4.3	Sensitivity of the automated phenotyping algorithm on the embryo states and stage transitions.	69
4.4	The embryo state classification obtained from the automated phenotyping script for <i>hsp-6::gfp</i> nematodes.	71
4.5	Comparison of the automated phenotyping data to the manually classified data for the embryo states of <i>hsp-6::gfp</i> worms.	73
4.6	Sensitivity of the automated phenotyping algorithm on the <i>hsp-6::gfp</i> embryo states and stage transitions.	73

1 Introduction

1.1 *Caenorhabditis elegans* - the model organism

The drug discovery pipeline constitutes of standardized steps that pharmaceutical companies execute to discover potential 'hits' among tens of thousands of compounds targeting a certain disease [1]. The main objective of the entire drug discovery pipeline is to find a synthetic or natural compound that may either cure or ameliorate the target disease [2]. This process consists of various phases but, simply speaking, it can be grouped into 4 main stages, namely, the drug discovery, pre-clinical, clinical trials and approval phases (Figure 1.1). In the drug discovery phase, a great deal of compounds (in the range of 10000) are screened by performing high-throughput *in vitro* assays. These assays are generally based on biochemical or cell-based drug studies. While cell-based assays provide predictability, possibility of automation, multiplexing and miniaturization [3], fluorescence-based readout methods in biochemical assays are advantageous due to their high sensitivity. After having performed one of these methods in a period of 3 to 5 years, the amount of compounds for the related disease is reduced from approximately 10000 to 250. The next step is to further reduce the amount of compounds in pre-clinical trials by using animal models. This step is pivotal to bridge the translational gap between drug discovery and clinic trials [4]. The selection of the animal model in this part remains crucial, therefore, a critical evaluation of the predictive validity of this model is important. This phase allows a reduction in the total number of possible compounds to a few and, following the identification of these compounds, the trials on humans start. In Phase I of the clinical trials, a small number of healthy volunteers is used to assess drug safety. In Phase II, a large number of patients (typically in the range of several hundred) with the targeted disease are included to test the efficacy of a drug. Phase III involves randomized test of a drug on several hundred or thousands of patients. This phase is also the transition stage to demand an approval to the market. If the outcome has turned out to be positive after this drug trial period, an approval can be obtained from the appropriate drug regulation organization. While the drug discovery pipeline is a well-established methodology, it possesses certain disadvantages. The total duration of the aforementioned drug discovery pipeline is extremely lengthy, it can also be quite expensive [5], and existing animal models are not perfectly fit for

the purpose.

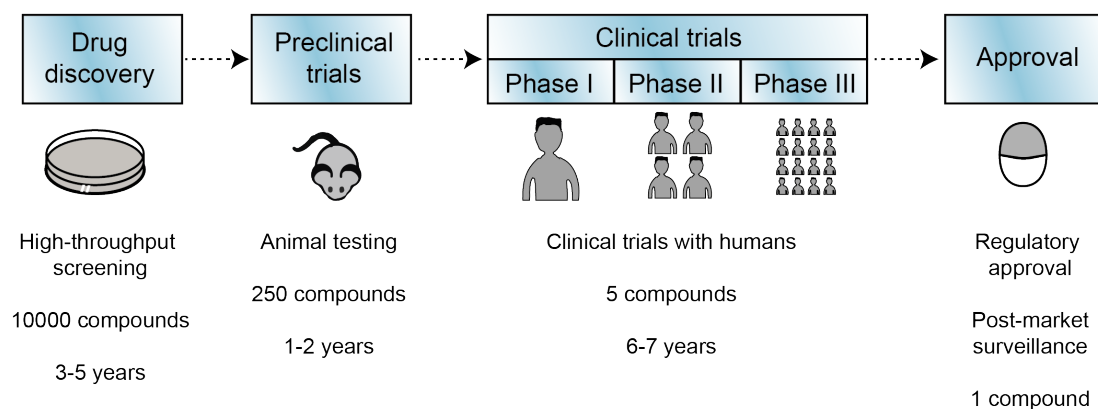


Figure 1.1 – Schematic overview of the drug discovery pipeline. Starting from a few thousands of compounds, the initial high-throughput drug screening is performed in an *in vitro* environment to reduce the compound library to 250 compounds. During the preclinical trials with rodents, a few critical compounds are selected and the clinical trials with humans are commenced. After identifying a potential compound, the regulatory approval is required for a more general drug application. The entire drug discovery process can take up to 15 years.

For initial drug screening, pharmaceutical industry increasingly relies on alternative biological models instead of rodents in order to identify potential hits in a more cost-effective and ethical way [6]. Despite the high interest in using mice for drug testing due to their close genetic match with humans [7], such studies are laborious, expensive and are challenging for generating large data sets. The nematode *Caenorhabditis elegans*, (also known as *C. elegans*) proved to be a highly advantageous biological model for pharmaceutical and drug testing applications at the initial phases of the drug discovery process [8, 9]. *C. elegans* can fit nicely in the drug discovery pipeline between the drug discovery phase with cell-based assays and the preclinical trials with animal testing, as whole animal-level phenotypic data at high-throughput can be obtained. Even though nematodes possess a comparatively lower genomic match to humans than laboratory mice, many of the disease genes are common to that of humans, while worms have certain advantages.

First introduced by Dr. Sydney Brenner in 1974, the roundworm *C. elegans* has proven its worth as an experimental model system in which fundamental questions on cellular processes such as cell division, embryo development, aging and cell death can be answered [10]. Since then, this model organism has never lost its charm, as it provides more content than too simple unicellular model organisms (bacteria, etc.) and it is less complicated than higher-order animals (rodents, etc.). By using *C. elegans*, biological problems both at the entire organism and the level of single cell can be identified.

An adult worm typically has a length of 1 mm and their transparent behavior allows high-resolution imaging of its anatomy. The development of cells and organs, nervous system, gene expression and signaling pathways can be visualized easily indeed. Worms also provide further advantages, such as having a short life cycle (~3 days) and an average lifespan (~2 weeks).

1.1. *Caenorhabditis elegans* - the model organism

This short developmental cycle permits rapid phenotypic data collection in a matter of days whereas, in other model organisms, this procedure can take up to weeks and even months. Their hermaphrodite behavior, with only 0.1% male worms, also enables culture of the worm population without an additional effort, thereby providing affordable culture conditions in any type of research laboratory. Hermaphrodite adult worms contain 959 somatic cells and the complete cell lineage has been traced [11]. The nervous system of *C. elegans* is highly simple and it has been well-characterized. The nematode has a very well-annotated genome [12]. Worms also pose no ethical issue, meaning that these model organisms could be adapted to any kind of chemical exposure study without being involved in any kind of regulations. There have also been a vast amount of *C. elegans* mutants for disease models, such as Alzheimer's, Parkinson's and Huntington's diseases, diabetes and cancer [13, 14, 15]. *C. elegans* culture traditionally is based on growth on nematode growth medium (NGM) agar plates that are pre-coated with *Escherichia coli* bacteria for feeding [16]. Typically, *C. elegans* pass through four larval stages (L1-L4), each of which ends with a molting event, and reach to an adult stage in 2 to 3 days (Figure 1.2; [16]). Subsequently, adult nematodes lay embryos – which hatch in 10-12 hours – and the developmental cycle reinitiates with the development of larvae progeny.

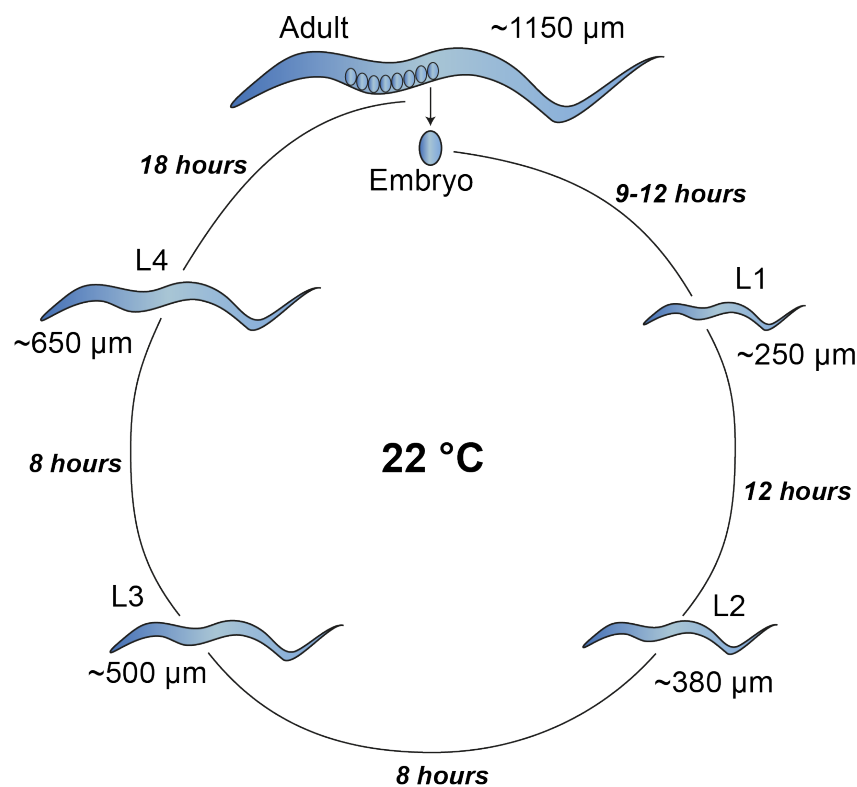


Figure 1.2 – Schematic development cycle of the nematode *C. elegans* at 22 °C. The development duration between two stages and the average length of the worms at each larval stage are noted.

A regular operator-based maintenance of NGM agar plates is required to regulate the exponentially increasing worm population. Commonly used methods to handle *C. elegans* include tedious manual manipulation, while also assisting tools for nematode manipulation exist. An assisting machinery for worm manipulation and phenotyping was released with the name COPAS Biosort [17, 18]. This device showed the possibility of screening over 14 thousand compounds and identifying 300 active molecules in *C. elegans* [19]. While such assisting tools can be highly useful, they are expensive, bulky, and lack the connection with worm culture and the possibility of complex phenotyping. Alternative tools such as microfluidic devices, solve many challenges encountered during various model organism handling procedures.

1.2 Microfluidics as assisting technology

Recent advances in microfluidics, electronics, and material sciences have enabled the miniaturization of bioanalytical applications into Lab-on-a-chip (LoC) systems [20, 21]. LoC systems provide powerful solutions for bioanalytical applications and microfluidic technologies have shown to enable automated studies of many complex biological systems. Extensive phenotypic data were collected during experimentation with uni- or multi-cellular organisms. LoC devices are conveniently applicable to cell-based and single organism studies, as they can easily be fabricated in an adaptable size, depending on the biological sample of interest [22, 23]. This feature together with the opportunity for parallel analysis and enabling high-throughput studies has allowed the design of various drug delivery platforms for living multicellular organisms.

The μ -liter flow regime brings certain advantages considering the consumption of low volumes of reagents, less waste production and low-cost in the experimentation. Meanwhile, microsystems have a very high surface area-to-volume ratio, thereby surface forces become dominant [24]. The Reynolds number Re is used to best characterize the flow regime in a fluidic environment and it is defined as the ratio of inertial forces to viscous forces as shown in Equation 1.1:

$$Re = \frac{V_{avg} L \rho}{\mu} \quad (1.1)$$

where V_{avg} , L , ρ and μ are the average flow velocity, the channel diameter, the fluid density and the fluid viscosity, respectively.

If Re is much less than 100, which is the case in microfluidic circuits with μm channel dimensions, the flow is completely laminar and no turbulent flow is observed. Such a laminar flow regime allows a relatively predictable and controlled molecule transportation. This phenomenon turns quite useful during the transfer of biological particles. On the other hand, if the Re is around 2000, as is the case on a macro scale, turbulent flow is apparent and the well-characterized flow control is no longer possible. The fluid actuation in microfluidics mostly arise from pressure-driven flow, in which the fluid is pumped in the microfluidic device by means of an external equipment such as a syringe pump. Such a flow is well-controlled and reproducible and additionally it is adoptable to miniaturization too.

A proper characterization of the motion of the fluid requires Newton's second law applied

together with mass conservation, leading to the Navier-Stokes equation is described for a Newtonian fluid (Equation 1.2):

$$\frac{\partial \mathbf{u}}{\partial t} + (\mathbf{u} \cdot \nabla) \mathbf{u} = -\frac{1}{\rho} \nabla p + \gamma \nabla^2 \mathbf{u} + \frac{1}{\rho} \mathbf{F} \quad (1.2)$$

where \mathbf{u} , p , ρ , γ and \mathbf{F} are the fluid velocity field, the pressure field, the fluid density, the kinematic viscosity and the external acceleration field, respectively.

As mentioned earlier, at low Re numbers, the turbulent flow is obsolete – as in the case of microfluidic flow – and Equation 1.2 can be simplified to Equation 1.3:

$$\gamma \nabla^2 \mathbf{u} = \frac{1}{\rho} \nabla p - \frac{1}{\rho} \mathbf{F} \quad (1.3)$$

The solution of the velocity field in Equation 1.3 leads to a regular and parallel streamline-based flow in microfluidic channels.

Based on the laminar flow profile and hence the opportunities in bio-material transfer, microfluidics has proven to be an interesting enabling technology for *in vivo* culture and phenotyping of *C. elegans* in a controlled manner, replacing many of the tedious traditional manipulation procedures by automated steps [25, 26, 27]. Microfluidic chips did not only facilitate handling and manipulation, but also provided very controlled and reliable phenotypic results for assaying drugs and chemicals indeed. A well-controlled concentration of any compound can be dispensed in a microfluidic device and the flow can be controlled by means of a syringe pump.

The high motility of *C. elegans* necessitates a temporary immobilization method for accurate imaging. Some common methods include the utilization of anesthetics for this purpose [28]. Different approaches with LoC platforms have been reported for arraying, culturing and immobilizing highly mobile *C. elegans* in a microfluidic chip for automated manipulation and long-term imaging. One such approach used “behavior” and “olfactory” chips, to effectively trap young adult nematodes, but the monitoring of spontaneous locomotion was somehow hindered by this design [29]. Another study developed a microfluidic chip that performed high-speed sorting and could also isolate and immobilize the nematodes for screening phenotypic features [30]. Alternatively, deflecting polydimethylsiloxane (PDMS) membranes were utilized to temporarily immobilize and capture time-lapse images of green fluorescent protein (GFP) expression of different nematode strains [31]. This technology was also combined with on-chip culturing and high-resolution imaging, although the initial worm distribution was tedious and the chip was low-throughput [32]. Long-term immobilization over multiple worm development stages was demonstrated at high imaging resolution [33]. Droplet encapsulation was also used as an alternative method to isolate and immobilize *C. elegans* at the L1 stage [34], while gel-based techniques were employed to temporarily arrest nematodes at various larval stages [35, 36]. Gel-based techniques were also proven to be ideal platforms for high-resolution longitudinal imaging and long-term culture, but without a microfluidic approach, they lacked an adequate bacterial replenishing system and automated late progeny wash off [37, 38, 39].

1.3 Thesis outline

In this thesis, I present various microfluidic platforms emerged from our laboratory for long-term imaging, automated high-content phenotyping and sorting of *C. elegans* larvae and embryos. This thesis consists of an introduction chapter (Chapter 1), a common experimental procedures part in Chapter 2, five major projects which are discussed in Chapter 3 to 7 and finally a conclusion chapter with the future outlook of *C. elegans* research (Chapter 8). Additionally, each of the five major project chapters encompasses an introduction part with the relevant state-of-the-art and a conclusion.

High-throughput, high-content, high-resolution and multiplexed experimentation was targeted in four of the chapters (Chapter 3-6) of this thesis and one chapter (Chapter 7) was dedicated to the design of assisting technologies using microfluidics (see an illustration in Figure 1.3). The former required four different microfluidic designs, as each of them needed unique features for the related experimental cases. For example, in Chapter 5, single worm tracking was enabled, which was not provided by any other design. Key features of each design are noted below or next to the images of the different microfluidic chips filled with liquid dye solution in Figure 1.3.

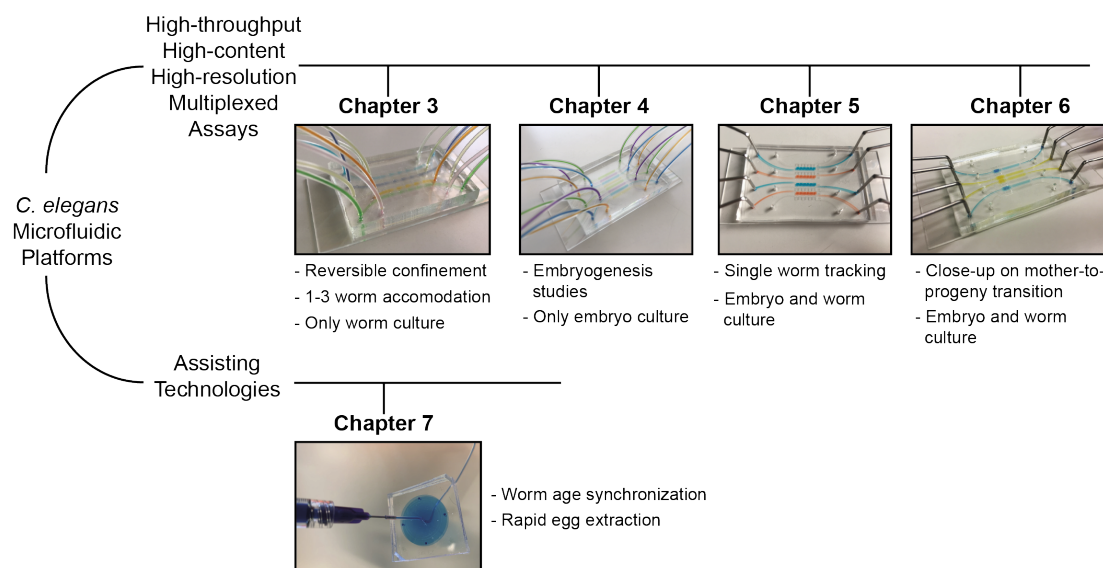


Figure 1.3 – Overview of the designed microfluidic platforms and the related chapters of the thesis. Key features of each microfluidic design are noted below or next to the images of microfluidic chips filled with liquid dye solution.

In Chapter 2, common procedures used in the experiments and the platform designs are explained. The standard cleanroom fabrication protocols are shown. These procedures include the development of a Cr mask and three different versions of microfluidic chip fabrication starting from a Si wafer level. In addition, the typical materials and chemicals used, the basics of the bacteria culture and preparation, the in-depth details of the age control of worm populations and the standard experimental setup for the accomplished projects were illustrated.

After the methodology- and technology-oriented Chapter 2, the first chip for the automated high-content phenotyping over the life cycle of *C. elegans* was described in Chapter 3. We presented an automated microfluidic platform that can obtain up to 19 phenotypic parameters from a single worm culture study. This platform, which enabled regular and reversible confinement of nematodes for stable fluorescent and bright-field imaging along with regular bright-field video-recording for the motility assay, allowed multiplexing of experimental studies and brought moderate throughput. We employed the effect of bacteria dilution on a worm model of Huntington's disease and demonstrated the disease regression by caloric restriction. In Chapter 4, a high-throughput microfluidic platform for automated phenotyping of *C. elegans* embryos was described. We showed the possibility of multiplexed chemical compound testing on up to 800 embryos. After 12 hours of time-lapse imaging, we obtained single embryo phenotypes through machine learning and image processing approaches. We exposed the embryos to various concentrations of chemical compounds and interestingly, we noticed a similar trend of tested compounds as priorly observed on the nematode.

Chapter 5 describes an automated microfluidic platform for life-long and high-content phenotyping of single *C. elegans* worms. We further improved the microfluidic platform illustrated in Chapter 3 and enabled single animal motility tracking, thereby, providing experimental opportunities at high-resolution and in a parallel fashion from the early embryo stage to the adult stage. The worms were exposed to an anthelmintic drug, tetramisole, at various dilutions to obtain dose-response curves on the associated growth and motility parameters.

We presented a microfluidic platform for the detection of early epigenetic inheritance in *C. elegans* in Chapter 6. We observed mother-to-progeny heritable transmission of mitochondrial stress at high-resolution, under significant automation and in a parallel fashion. We extracted development phenotypes of parental generation and the progenies at high-content and in an automated manner. We investigated the stress induction in embryos that were released from both stress-induced and stress-free parental generation with the proposed microfluidic device.

In Chapter 7, we demonstrated a PDMS microfluidic device for high-throughput, efficient and extremely rapid sorting of mixed larval populations of *C. elegans*. The microfluidic device which was realized by combining three plasma-activated and bonded PDMS parts enabled a sorting purity in the range of 73 to 100% of two consecutive larval stages at both the input and the output of the device. In parallel, we adopted the proposed microfluidic chip for on-chip high-throughput egg extraction, thereby eliminating the usage of expensive hardware.

In the last chapter of this thesis, Chapter 8, we provided the reader a conclusion of the work in this thesis and an outlook on the applications that can be realized on *C. elegans* in the future.

2 Platform design and common procedures

In this part of the thesis, we share common procedures that were employed for most of the experiments. In particular, this chapter consists of the design and fabrication of a Cr mask and single-layer and two-layer molds for the fabrication of various PDMS microfluidic chips, typical materials and chemicals used, bacteria culture and preparation, control and culture of worm populations and the experimental setup that was utilized.

2.1 Mask fabrication

Each microfluidic chip design required a dedicated Cr mask for the fabrication process. Therefore, standard fabrication techniques were applied to create a patterned Cr mask. The structured layout of the design was realized using CleWin and the fabrication processes took place at the EPFL CMi. A 5" × 5" blank mask was obtained by covering a transparent glass plate with a Cr layer and subsequently, with a positive photoresist layer (Figure 2.1a). The design-of-interest was transferred on the photoresist layer by a high-power laser beam ($\lambda = 355$ nm; Figure 2.1b). The exposed Cr blank was developed using a standard positive photoresist developer (Figure 2.1c). The Cr layer was etched by a Cr etchant (Figure 2.1d). The remaining positive photoresist layer was removed by a positive photoresist stripper (Figure 2.1e).

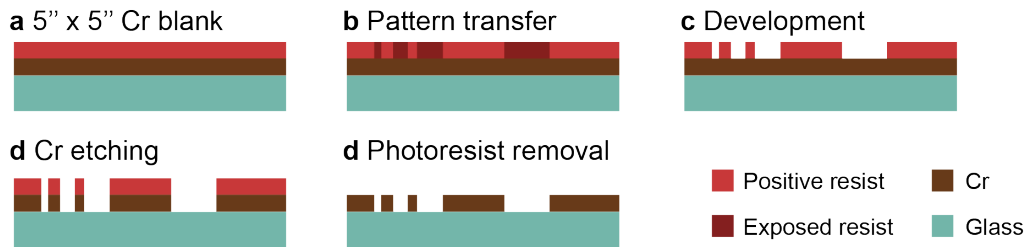


Figure 2.1 – Details of the Cr mask fabrication process. (a) A 5" × 5" Cr blank with a thin positive photoresist layer was obtained. (b) The design was transferred on the Cr mask. (c) The exposed photoresist was developed. (d) The Cr layer was etched. (e) The photoresist was stripped.

2.2 Microfluidic chip fabrication

In this part, we illustrate the three different fabrication methods that were used to realize the microfluidic chips. The first two sections illustrate the design protocol used for the culture and phenotyping of *C. elegans* larvae and embryos. The last section is dedicated to the fabrication of the filter structures for size-dependent sorting of *C. elegans* larvae.

2.2.1 Fabrication of single-layer Si-SU8 molds

Our wafer fabrication process for PDMS casting was composed of a single-layer fabrication protocol. SU8 was coated on the wafer in order to form either 40 or 80 μm high structures in PDMS (Figure 2.2a). Hereafter, the design was exposed (Figure 2.2b) and developed (Figure 2.2c). The surface of the wafer was TMCS treated for 15 minutes (Figure 2.2d) to provide easy PDMS demolding. A liquid PDMS mixture (base-to-curing agent ratio 10:1) was poured on the mold, degassed and cured at 80 $^{\circ}\text{C}$ for 2 hours (Figure 2.2e). Once the PDMS mixture was cured, we removed the PDMS solid part from the SU8 mold (Figure 2.2f) and punched 1.5 mm inlets and outlets using a biopsy punch (Figure 2.2g). Both PDMS device and 75 mm \times 38 mm glass slide were plasma-activated and sealed together (Figure 2.2h). The bonded microfluidic chip was kept on a hotplate at 80 $^{\circ}\text{C}$ for at least 10 minutes to enhance the bonding.

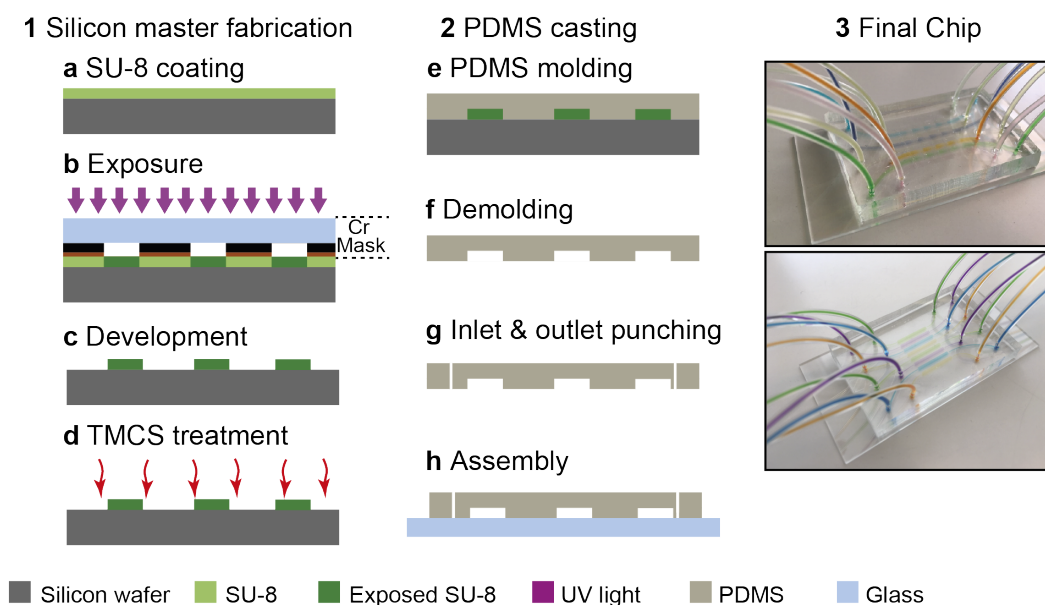


Figure 2.2 – Details of the fabrication process of single-layer Si-SU8 molds and the microfluidic chip. (a-c) Conventional photolithography was utilized to deposit 40 or 80- μm thick layer of SU8. (d) The mold was treated with TMCS in a vacuum chamber for 15 minutes to prohibit adhesion of PDMS during molding. (e) Once PDMS was cured on the wafer, (f) it was peeled off, (g) inlets and outlets were punched, and (h) the PDMS chip and a glass slide were bonded by oxygen plasma treatment.

2.2.2 Fabrication of two-layer Si-SU8 molds

Our wafer fabrication process for PDMS casting was composed of a two-layer fabrication protocol. Positive photoresist was spin-coated on a clean Si wafer (Figure 2.3a), the design was exposed (Figure 2.3b) and developed (Figure 2.3c). The wafer was etched with the Bosch process at $\sim 40\text{ }\mu\text{m}$ depth to realize the fluidic serpentine structures (Figure 2.3d), which was followed by photoresist stripping with acetone, isopropyl alcohol and oxygen plasma treatment (Figure 2.3e). For the second layer fabrication, SU8 was coated on the wafer in order to form later $80\text{ }\mu\text{m}$ high growth chambers in PDMS (Figure 2.3f). After, the design was exposed (Figure 2.3g) and developed (Figure 2.3h). The surface of the wafer was FOTS-treated (Figure 2.3i) to provide easy PDMS demolding. A liquid PDMS mixture (base-to-curing agent ratio 10:1) was poured on the mold, degassed and cured at $80\text{ }^{\circ}\text{C}$ for 2 hours (Figure 2.3j). Once the PDMS mixture was cured, we removed the PDMS solid part from the Si-SU8 mold (Figure 2.3k) and punched 1.5 mm inlets and outlets using a biopsy punch (Figure 2.3l). Both PDMS device and $75\text{ mm} \times 38\text{ mm}$ glass slide were plasma-activated and sealed together (Figure 2.3m). The bonded microfluidic chip was kept on a hotplate at $80\text{ }^{\circ}\text{C}$ for at least 10 minutes to enhance the bonding.

2.2.3 Fabrication of hybrid PDMS microfluidic chips

Starting from clean Si wafers, a $80\text{ }\mu\text{m}$ thick SU8 layer was spin-coated (Figure 2.4a), exposed and developed to realize three different designs on three different wafers (Figure 2.4b). Following a TMCS silanization of the three molds, a 10:1 PDMS polymer-to-curing agent mixture was poured on the wafers, degassed and cured for 2 hours at $80\text{ }^{\circ}\text{C}$ (Figure 2.4c). After peeling off the PDMS parts, inlets and outlets were punched with a biopsy punch (Figure 2.4d), and in a first step the patterned side of Layer 1 and the backside of Layer 2 were plasma-activated and bonded (Figure 2.4e). The fabrication was finalized by bonding the patterned side of the previously bonded part to the punched Layer 3 (Figure 2.4f).

2.3 Materials and chemicals

4-inch $550\text{ }\mu\text{m}$ thick Si wafers were purchased from the Center of Micro- and Nanotechnology of EPFL (CMi, Lausanne, Switzerland). MicroChem SU8-3050 1 L negative photoresist was bought from Micro Resist Technology GmbH (Berlin, Germany). PDMS Sylgard 184 was acquired from Dow Corning (Wiesbaden, Germany). 1 mL borosilicate H-TLL-PE syringes were obtained from Innovative Labor Systeme (Stutzerbach, Germany). Corning microscope slides ($75\text{ mm} \times 38\text{ mm}$), sodium hydroxide, *1H,1H,2H,2H*-Perfluorooctyl-trichlorosilane (FOTS), Trimethylchlorosilane (TMCS), sodium hypochlorite solution 10-15%, and mPEG5K-silane were bought from Sigma-Aldrich (Buchs, Switzerland). Microline ethyl vinyl acetate tube with 0.51 mm inner and 1.52 mm outer diameters was purchased from Fisher Scientific (Wohlen, Switzerland). L-Broth bacterial culture medium was obtained by adding 10 g of Bacto-tryptone, 5 g of Bacto-yeast, and 5 g of NaCl in 1 L of H_2O . S-Basal was obtained by

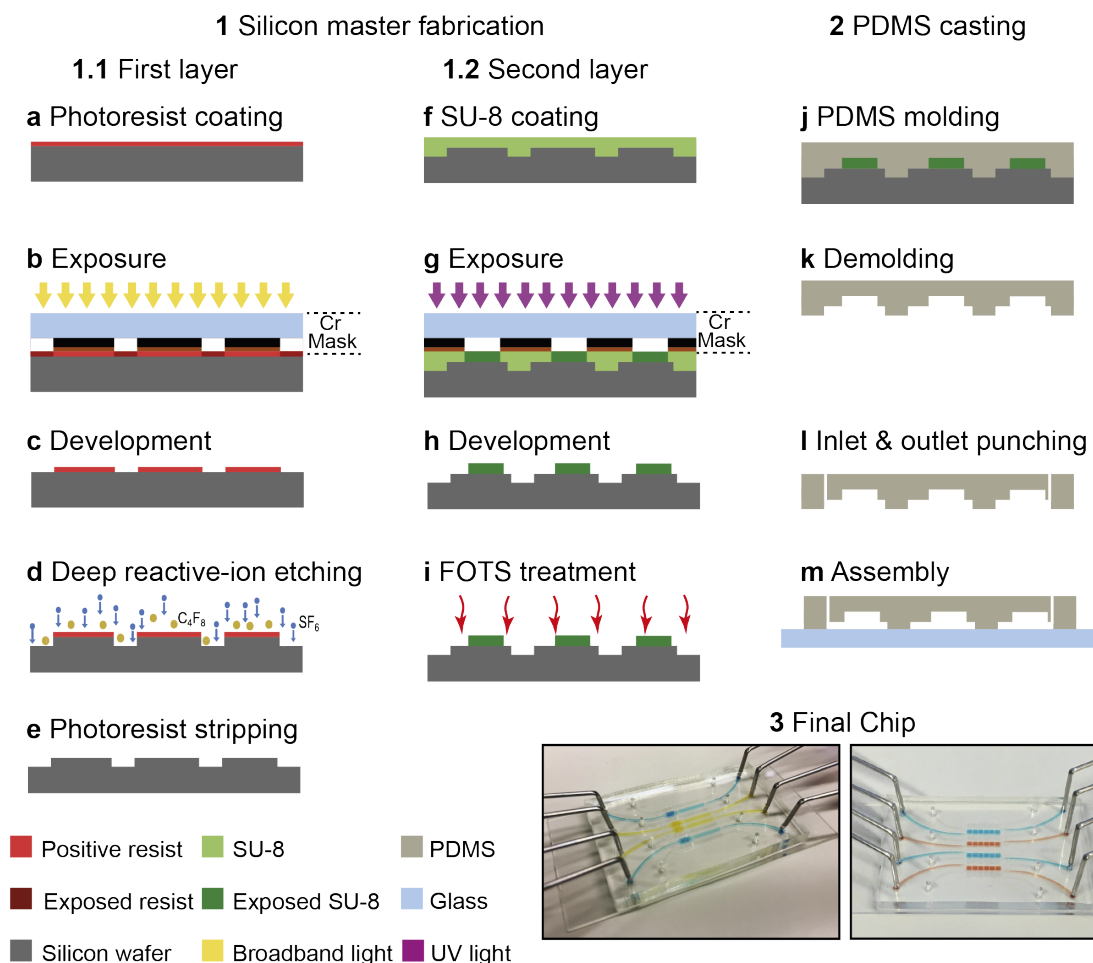


Figure 2.3 – Details of the fabrication process of two-layer Si-SU8 molds and the microfluidic chip. (a-e) On a 4-inch wafer, the first layer of the mold was patterned by a 2- μm thick positive photoresist, AZ1512 HS, and the wafer was etched using deep reactive-ion etching (Bosch process) to obtain 40- μm deep structures. (f-h) Conventional photolithography was utilized to deposit 40- μm thick layer of SU8 on the growth chambers. (i) The mold was treated with FOTS in a vacuum chamber for 12 hours to prohibit adhesion of PDMS during molding. (j) Once PDMS was cured on the wafer, (k) it was peeled off, (l) inlets and outlets were punched, and (m) the PDMS chip and a glass slide were bonded by oxygen plasma treatment.

adding 5.85 g of NaCl, 1 g of K_2HPO_4 , 6 g of KH_2PO_4 , and 1 mL of cholesterol (5 mg/mL in ethanol) in 1 L of H_2O . S-medium was obtained by adding 0.5 mL of 1 M potassium citrate (pH 6), 0.5 mL of trace metal solution, 0.15 mL of 1 M CaCl_2 , and 0.15 mL of 1 M MgSO_4 in 50 mL of S-Basal. S-Basal, L-Broth and S-medium were sterilized by autoclaving. mPEG5K-silane solution was prepared by diluting 200 mg of mPEG5K-silane in 10 mL of 95% ethanol. The bleach solution was prepared by combining 0.33 mL of 4 M sodium hydroxide, 3.66 mL of DI water and 1 mL of 7-10% sodium hypochlorite solution.

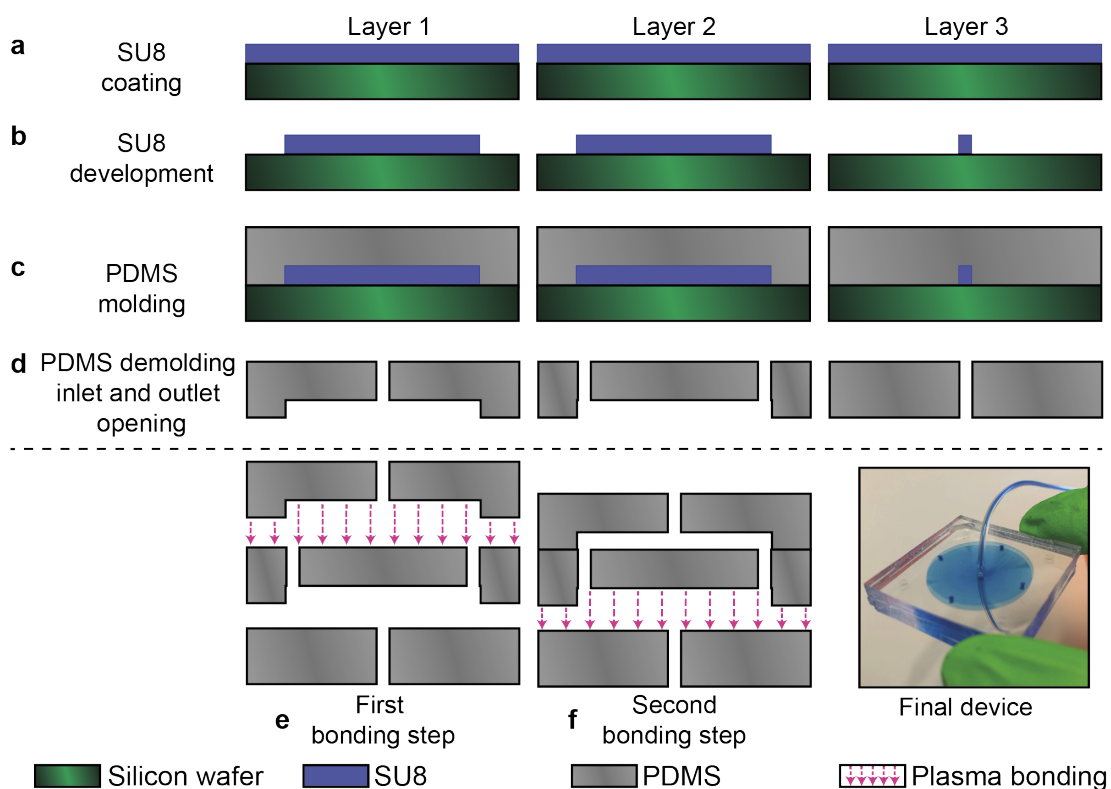


Figure 2.4 – Details of the fabrication process of hybrid PDMS microfluidic chip. Conventional photolithography was utilized to (a) deposit 80- μm thick layer of SU8 and (b) develop on three Si wafers. (c) After a TMCS treatment in a vacuum chamber for 15 minutes, PDMS was cured on the wafers, (d) PDMS parts were peeled off and inlets and outlets were punched. (e, f) Three different PDMS parts were sealed consecutively to each other by oxygen plasma treatment.

2.4 Bacteria culture and preparation

A single colony of *Escherichia coli* strain OP50 was used from the streak plate and injected into L-Broth. The injected cultures were shaken at 37 °C overnight. The L-Broth medium was removed after the overnight culturing by centrifuging. Freshly prepared and filtered S-medium was added and the suspension was vortexed to obtain uniform bacterial distribution. A typical bacteria concentration was in the range of $1-4 \times 10^9$ cells/mL. This bacteria source was utilized to aliquot NGM agar plates for standard worm culture. Same procedure was also applied to obtain *E. coli* strain HT115 for the bacterial feeding of worms inside the microfluidic chip. Occasionally, an optical cell density meter was used to realize a stock concentration.

2.5 Control of worm populations

A NGM plate with a mixed larvae population was suspended in a 1.5 mL Eppendorf tube. After 2-3 minutes, the top 100 μL of this suspension was extracted. As the older larval stages sink

faster in a suspension, the extracted suspension contained mostly L1 nematodes. In order to keep track of a L1 population regularly, a synchronized population of around 500-600 L1 stage worms were distributed on a *E. coli*-seeded NGM plate. After two days, when the population reached the adult stage and when embryos were observed on the plates, NGM plates were bleached to extract the embryos (see Figure 2.5). For certain studies, these freshly obtained embryos and also the L1 progenies hatched from these embryos were used, otherwise the worm population was kept under control by repeating this cycle and continuously supplying L1 nematodes.

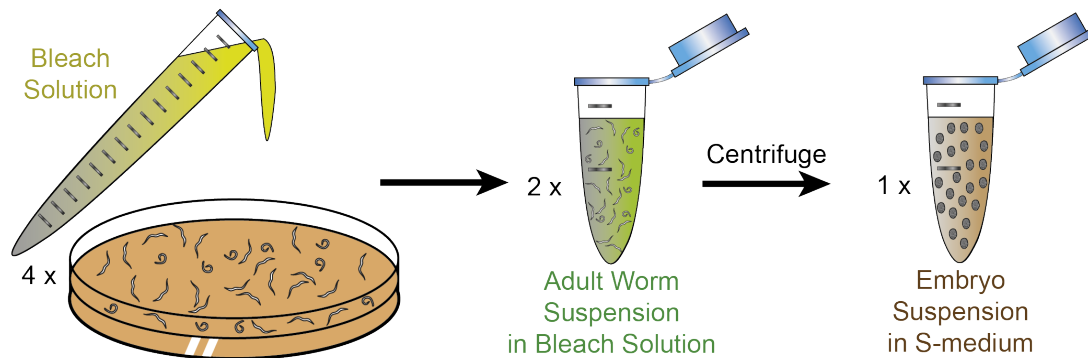


Figure 2.5 – Schematic protocol of the bleaching procedure. 5 mL of bleach solution – 0.33 mL of 4 M sodium hydroxide, 3.66 mL of DI water and 1 mL of 7-10% sodium hypochlorite solution – is distributed on adult worm plates. The solution is suspended in 1.5 mL Eppendorf tubes, and then centrifuged 4 times to replace bleach solution with S-medium.

The development and onset of larval stages of *C. elegans* strongly depend on temperature conditions during culture, a faster development being reported for higher temperatures [40, 41]. Based on these prior works, we adopted an experimental approach that allows collection and testing of each of the *C. elegans* larval stages at a designated time point for use in the sorting experiment. We distributed a synchronized population of around 500-2000 L1 worms on a NGM plate after adjusting the density of the worms by counting the number of worms in a 2 μ L suspension on a glass slide. The exact time and temperature of culture was adjusted to obtain a synchronized population at a certain larval stage for use at a fixed experimental starting time *X* (see Table 2.1). We used an incubator to stabilize the temperature either at 16 °C or adopted room temperature (22 °C) culture conditions. When the population reached to the desired larval stage, the NGM plate was washed with S-medium and worms were suspended in an Eppendorf tube. N2 wild-type, *hsp-6::gfp* and *p_{unc-54}::Q40::YFP* strains were used too and were provided by the Caenorhabditis Genetics Center (University of Minnesota).

2.6 Experimental setup

The schematic diagram of the experimental setup is illustrated in Figure 2.6. The microfluidic chip was mounted on the motorized stage of a microscope setup (Axio Imager M2, Zeiss,

Table 2.1 – Experimental method to obtain L1, L2, L3, L4 and young adult (YA) *C. elegans* at a designated time point (hour X) from an initially characterized L1 larval population. For example, to have a population of synchronized YA, a synchronized L1 population needs to be cultured during 52 hours at 22 °C.

Targeted synchronized population at experimental starting time X	YA	L4	L3	L2	L1
L1 seeding time	($X-52$)	($X-28$)	($X-20.5$)	($X-19$)	
and culture	hours	hours	hours	hours	-
temperature	(22 °C)	(22 °C)	(22 °C)	(16 °C)	

Germany). The microscope was utilized to acquire both bright-field and fluorescence images via a camera on the microscope (pco.edge 4.2, PCO, Germany). The inlets of the microfluidic chip were connected to a 12-port rotary valve placed on a Kloehn pump (V6 48K Syringe Drive Pump, IMI Precision, the USA). Two inlets of the 12-port valve were connected to a S-medium and a waste reservoir, respectively. Typically, a Python script deployed from a computer was used to control both the motorized stage of the microscope setup and the syringe pump via serial port commands. In Chapter 7, only the microscope part of this experimental setup was used.

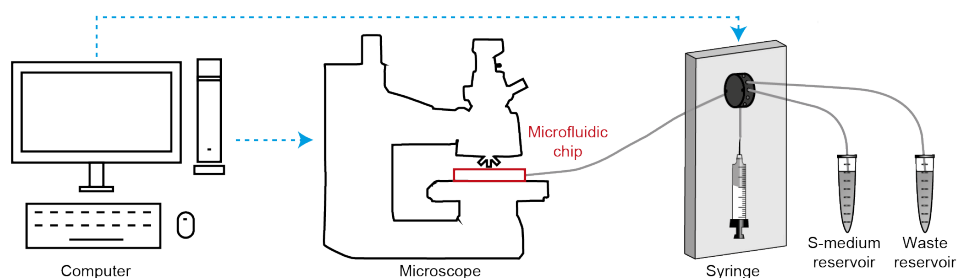


Figure 2.6 – Schematic diagram of the experimental setup. A computer, microscope setup with a microfluidic chip mounted and a syringe pump was linked together for experimental studies.

3 Automated high-content phenotyping over the life cycle of the nematode *Caenorhabditis elegans*

The nematode *Caenorhabditis elegans* is increasingly used as a model for human biology. However, *in vivo* culturing platforms for *C. elegans* allowing high-content phenotyping during their life cycle in an automated fashion are rare. Here, a multiplexed microfluidic platform for the rapid high-content phenotyping of populations of *C. elegans* down to single animal resolution is presented. Nematodes are (i) reversibly and regularly confined during their life inside tapered channels for imaging fluorescent signal expression and to measure their growth parameters and, (ii) allowed to freely move in microfluidic chambers, during which swimming behavior was video-recorded. The obtained data sets are analyzed in an automated way and 19 phenotypic parameters are extracted. Our platform is employed for studying the effect of bacteria dilution, a form of dietary restriction (DR) in nematodes, on a worm model of Huntington's disease and demonstrates the influence of DR on disease regression.

This chapter is an adapted version of the following publications:

- **H. B. Atakan**, M. Cornaglia, L. Mouchiroud, J. Auwerx and M. A. M. Gijs, “Automated high-content phenotyping from the first larval stage till the onset of adulthood of the nematode *Caenorhabditis elegans*”, *Lab on a Chip*, vol. 19, no. 1, pp. 120-135, 2019.
- **H. B. Atakan**, M. Cornaglia, L. Mouchiroud, J. Auwerx and M. A. M. Gijs, “A microfluidic platform for automated phenotyping during full lifespan of *Caenorhabditis elegans* at high-throughput”, in *21st International Conference on Miniaturized Systems for Chemistry and Life Sciences*, pp. 50-51, 2017.
- **H. B. Atakan**, R. Xiang and M. A. M. Gijs, “Variable-height microfluidic channels for accurate immobilization of *C. elegans* worms by using a single dry etching step”, in *22nd International Conference on Miniaturized Systems for Chemistry and Life Sciences*, pp. 630-631, 2018.

Chapter 3. Automated high-content phenotyping over the life cycle of the nematode *Caenorhabditis elegans*

- **H. B. Atakan**, M. Cornaglia, L. Mouchiroud, J. Auwerx and M. A. M. Gijs, “Slow-down of Huntington's disease progression in a *Caenorhabditis elegans* worm model by decreasing bacterial food supply on-chip”, in *22nd International Conference on Miniaturized Systems for Chemistry and Life Sciences*, pp. 1543-1545, 2018.

3.1 Introduction

Microfluidics provides an opportunity for parallelized analysis and hence is well adapted for the design of various drug delivery platforms for living multicellular organisms. For example, microfluidic gradient generators were developed for drug application on zebrafish [42, 43], while other work on *Drosophila* larvae included application of gradients of airborne chemical cues [44]. Drug delivery platforms were also developed for droplet-based mammalian cells [45].

It has become clear that rapid and high-content phenotyping of *C. elegans* is essential to obtain significant amounts of data that allow conclusions to be drawn on a solid statistical basis. Image and video processing approaches are commonly used to obtain phenotypic data by quantifying the development and the motility of *C. elegans* [46, 47]. Yet, most of the studies focused on short-term behavior without culturing the nematodes for the long-term [48, 49, 50]. Some previous aging and drug screening platforms had nematode growth chambers but lacked immobilization [51], had good lateral confinement but were missing early larval stage development and phenotyping [52, 53] and exhibited confinement for a larval stage but were missing on-chip culturing [54] or had less precise initial worm distribution [55]. Other microfluidic approaches also provided long-term culture and phenotypic analysis, either in populations or down to single worm resolution, but these papers did not report multiplexing of experimental parameters or automated high-content phenotyping results [56, 57, 58, 59]. To the best of our knowledge, there has been no *C. elegans* platform before that (i) enables life cycle on-chip culturing, (ii) includes features for reversibly immobilizing worms at all different life stages, and (iii) has an integrated image and video processing approach to extract multiple swimming gait and development properties.

Here, we present an automated, multiplexed, rapid and high-content phenotyping platform for the quantification of growth, fluorescence and motility of a statistically relevant *C. elegans* population down to single worm resolution. Our microfluidic chip has ~30 culture and immobilization chambers that enable culturing several worms in parallel, ranging from one to three worms per chamber, and include only passive hydrodynamic filter structures that are straightforward in operation by applying pressure-pulsed liquid flows. We performed life cycle culturing and phenotyping, which allowed us to observe the motility and development parameters of the nematodes starting from their first larval stage. Besides video recordings, we provided tapered channels to reversibly immobilize worms with a high accuracy at all stages for high-resolution imaging. We think that our platform is one of the most advanced systems out there, providing in-depth disease progression studies on nematodes with its unique features of high-content phenotyping, multiplicity, automation and ease of use, all at once. In order to validate our approach, we focused on the effects of DR in a *C. elegans* model of Huntington's disease (HD). DR is defined as the restriction of nutrients without malnutrition and has been shown to extend the lifespan in a wide variety of species [60, 61]. DR not only prolongs the lifespan but also delays a variety of age-related diseases [62, 63]. In *Caenorhabditis elegans*, a broad range of DR regimens have been proposed and they all extend the lifespan to various degrees by separate or partially overlapping molecular pathways [64, 65].

However, little is known about the effect of DR on proteotoxic stress and neurodegenerative diseases. Additionally, DR studies on worms cultured on agar plates have been extremely tedious to perform due to the lack of a suitable food control system. We first identified the optimal food dosing for normal development and for studying DR on wild-type *C. elegans*, and subsequently analyzed the effects of DR on protein aggregation, in a worm model for HD that expresses Yellow Fluorescent Protein (YFP)-tagged poly-glutamine repeats in body-wall muscle [66]. We present a comprehensive study that correlates worm motility, development and aggregate formation behavior, depending on the food concentration.

3.2 Automated high-content phenotyping platform design and operation

3.2.1 Microfluidic chip design

Our platform enables reversible immobilization for high-resolution imaging of *C. elegans* nematodes with, as additional features, the possibility of multiplexed studies and full automation. Thereby the user interaction can be reduced to a minimum level during the whole execution of the experiment. The system is based on passive hydrodynamics, without requiring additional active components on-chip. The latter contains eight lanes for performing multiplexed experiments, each lane having four unit cells, each of which consists of a growth chamber and thirteen tapered channels (Figure 3.1a). Each of these microfluidic lanes has one inlet, which is connected to a syringe pump through a distributing valve, and one outlet, which is connected to either a worm or a bacterial reservoir. Each of the unit cells has a rectangular shape of $4100\text{ }\mu\text{m} \times 1410\text{ }\mu\text{m}$ (Figure 3.1b). The growth chamber size is carefully chosen such that up to three worms have enough space to be successfully cultured throughout their life cycle. These spacious growth chambers facilitate accommodating enough bacterial food for the growth of the worms. The tapered channels were optimally designed so that the minimum channel length ($2500\text{ }\mu\text{m}$) was two times longer than the largest observed adult worm ($\sim 1200\text{ }\mu\text{m}$) to ensure full coverage of the nematode during imaging (Figure 3.1c). We designed our channel entrances with a certain angle ($\sim 30^\circ$) such that worms easily find their way inside the channels for immobilization with the least microfluidic flow increase. Thirteen channels are conjugated side-by-side to increase the possibility of confinement during high-resolution imaging (see details in Figure 3.1d). We carefully selected all the geometrical parameters so that we could have spacious growth chambers that can accommodate up to three worms, angled entrances of the tapered channels to provide good immobilization rates, large enough channel entrances to confine all the stages of worms, short enough tapered channel exit points to block the small larvae during confinement and to provide bacterial passage. We also included alignment markers to line up the camera position perfectly on the confinement channels. The PDMS part has a size of $35\text{ mm} \times 53\text{ mm}$, so that a $38\text{ mm} \times 75\text{ mm}$ -sized glass microscope slide can be used as the sealing part (Figure 3.1e).

3.2. Automated high-content phenotyping platform design and operation

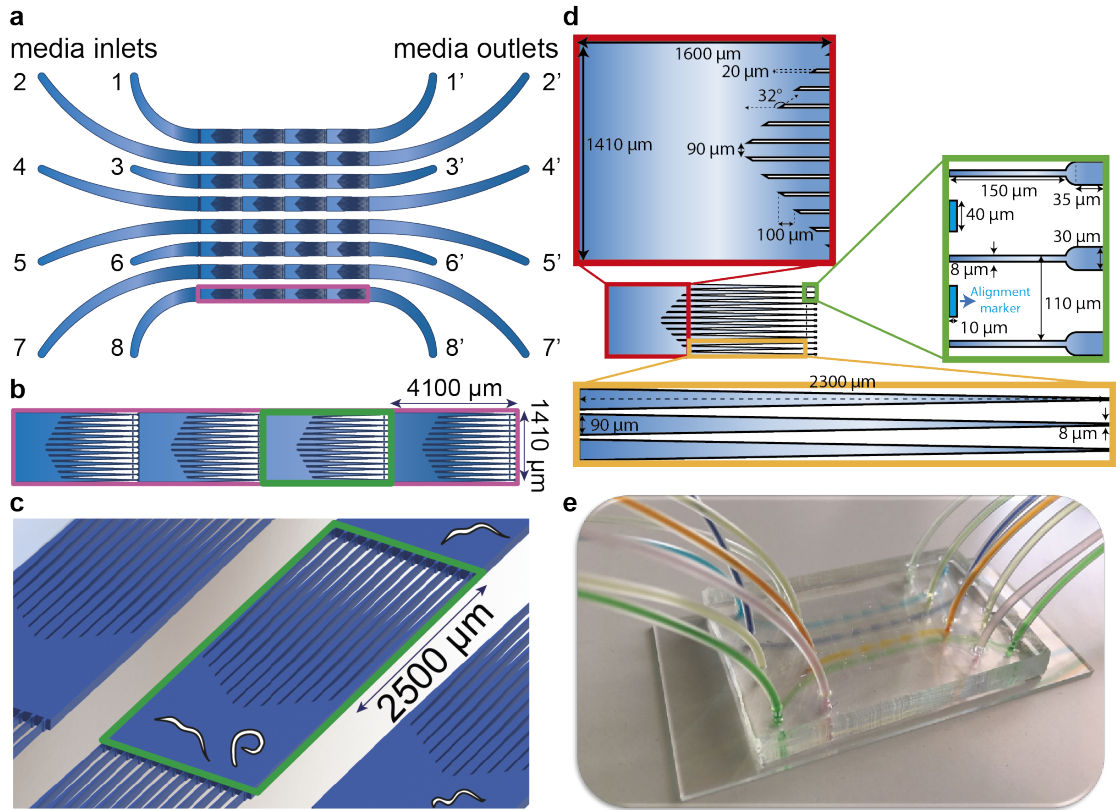


Figure 3.1 – Details of the microfluidic platform for automated high-content phenotyping of *C. elegans*. (a) Schematic representation of the microfluidic chip with eight lanes, having each four unit cells, consisting of a growth chamber and tapered channels. Each lane has a media inlet (1 to 8) and outlet (1' to 8'). (b) Zoom on one microfluidic lane consisting of four growth chambers and tapered channels, each unit cell being of rectangular shape (4100 μm × 1410 μm). (c) Three-dimensional schematic view on one unit cell, including young adult worms for size comparison, displaying the shortest tapered edge channel of 2500 μm. (d) The schematic representation of a unit cell (consisting of a growth chamber and thirteen tapered channels) with zoom on certain areas including the specific dimensions. (e) Picture of the microfluidic chip (35 mm × 53 mm) bonded on a standard glass microscope slide (38 mm × 75 mm).

3.2.2 Silanization of the microfluidic chip

After plasma-bonding the PDMS device and 38 mm × 75 mm-sized glass microscope slide, and keeping the bonded microfluidic chip on a hotplate at 80 °C for 10 minutes to enhance the bonding, the chip was removed from the hotplate to continue silanization process to prevent bacteria adhesion during life cycle culturing. All inlets and outlets of the chip were connected by tubing such that the whole 8-inlet and 8-outlet device was converted into a single inlet and single outlet version. A 1 mL borosilicate syringe was filled with 500 μL of mPEG5K-silane solution and connected to the microfluidic chip. An initial flow of 3 μL/s was set to remove bubbles and after having two thirds of the solution washed off at this speed, we dropped the flow rate to 4 nL/s and kept in this configuration for 1.5 hour. These microfluidic operations

were performed with Nemesys syringe pumps. We, then, flushed the microfluidic device with 1 mL of 95% ethanol and dried with an air gun. This cycle was repeated three times to be sure that there were not any silane crystals left. Subsequently, all the tube connections were removed and the microfluidic chip was placed inside a vacuum chamber for 1.5 hour. After removing the chip from the vacuum chamber, it was gently cleaned with an ethanol washed cleanroom wipe and it was ready for the experiment.

3.2.3 Automated fluidic protocol

All types of studies had similar semi-automatic operation (Figure 3.2). Initially, filtered S-medium was used to fill the microfluidic chip at around 1.67 $\mu\text{L/s}$. The same flow rate was utilized to degas the microfluidic chip having the outlet tubes clamped for approximately 15 minutes. After a successful degassing step, the clamps were released and tubes were placed inside worm suspension. Synchronized L1 worms in S-medium with a concentration of 10-15 L1 worms per 200 μL of suspension were first injected into the chip through the media outlet of each microfluidic lane with a flow rate of 0.6 $\mu\text{L/s}$ (Figure 3.2a). In particular, L1 worms were collected in front of the first filter set and short injection pulses – by suction from the syringe side with a flow rate of 3.33 $\mu\text{L/s}$ – were then utilized to distribute them among the chambers using passive hydrodynamics (*i.e.* not using active valves on the chip) as shown in Figure 3.2b. When needed, we pushed the nematodes back to their prior chambers – by S-medium push from the syringe side – in order to get an even worm distribution among the chambers. As soon as the desired numbers of worms per chamber were reached, any worms remaining in front of the first filter set were pushed back at a flow rate of 42 nL/s (Figure 3.2c). This flow rate was carefully chosen as at this point, trapped worms inside the chambers might move to the neighboring chambers, causing a deviation in the distribution. After having all the excessive worms pushed backed to the worm reservoirs, the bacteria reservoir containing 600 μL of *E. coli* suspension was plugged in to the media outlet. The same flow rate was used to cover the entire microfluidic lane with uniform *E. coli* HT115 solution of 25 μL , having a direction from bacteria reservoir to waste reservoir (Figure 3.2d). We developed an automation script with Python to control the bacterial feeding amount and flow rates, confinement pushback amount and flow rates, stage positions, image and video acquisition time instants throughout the experiment. After the first trigger of this Python script, the user did not need to communicate through the experiment anymore with the only exception of filling the bacteria reservoirs every night. The first confinement and image acquisition step took place with fresh S-medium pushed from the media inlet towards the media outlet (Figure 3.2e), and after it was terminated, video recording started. This was followed by the first bacterial feeding and then continued with further confinement and feeding steps.

3.2.4 Platform working principle

There are two operation modes after the initiation of an experiment (Figure 3.3a). In the first part, *E. coli* injection is carried out from the media outlets, during which the worms

3.2. Automated high-content phenotyping platform design and operation

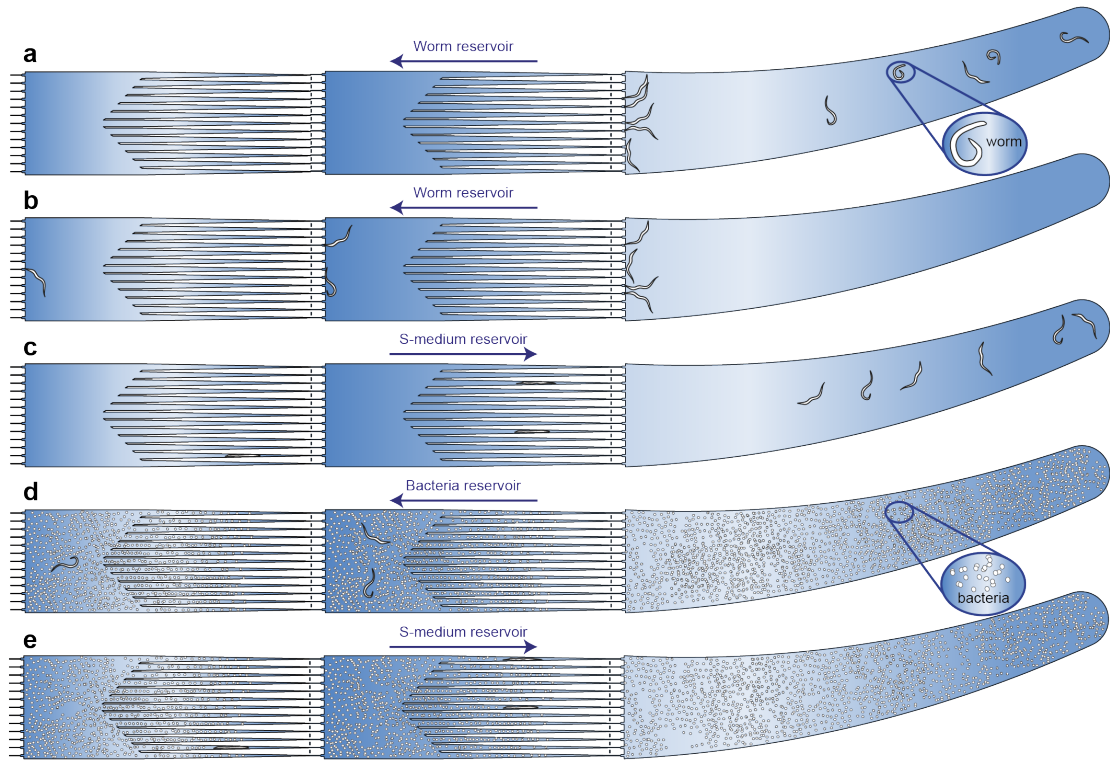


Figure 3.2 – Fluidic protocol of the microfluidic chip. (a) A 200 μL suspension of synchronized L1 worms in S-medium is injected from the media outlet of a lane towards the media inlet. (b) After successfully collecting L1 worms in front of the first filter set, the worms are distributed over all unit cells by applying short injection pulses. (c) When the desired worm distribution among the growth chambers is reached, excessive worms are gently pushed back towards the media outlet. (d) A 25 μL suspension of *E. coli* is injected from the media outlet until it completely fills the microfluidic chip. (e) The automated imaging protocol starts with a first cycle of worm confinement in the tapered channels.

are pushed towards the passive filters. Once this step is finalized, worms are left inside the growth chambers for some dedicated amount of time to continue their development with the fresh bacterial solution. This operation mode is termed “Culture” mode. During this operation, every 7 hours, videos were recorded for our motility study. In the second operation mode, namely “Confinement”, roughly every 35 minutes, the worms are pushed towards the tapered channels for imaging and phenotyping. A pulsed microfluidic flow with one-second interruptions is utilized to confine the worms temporarily. If the Confinement flow rate was too high ($> 417 \text{ nL/s}$), the flow-induced viscous drag force exerted on the later stage larvae and adult nematodes moved them towards the end of the $8 \mu\text{m}$ -wide tapered channels. Hence, the nematodes were either tightly squeezed, which hindered their development, or they could inadvertently move to the neighboring growth chamber. Instead, pulsed flow with one-second interruptions during the confinement enabled the worms to grow adequately and provided smooth repositioning of the worms inside the tapered channels.

Chapter 3. Automated high-content phenotyping over the life cycle of the nematode *Caenorhabditis elegans*

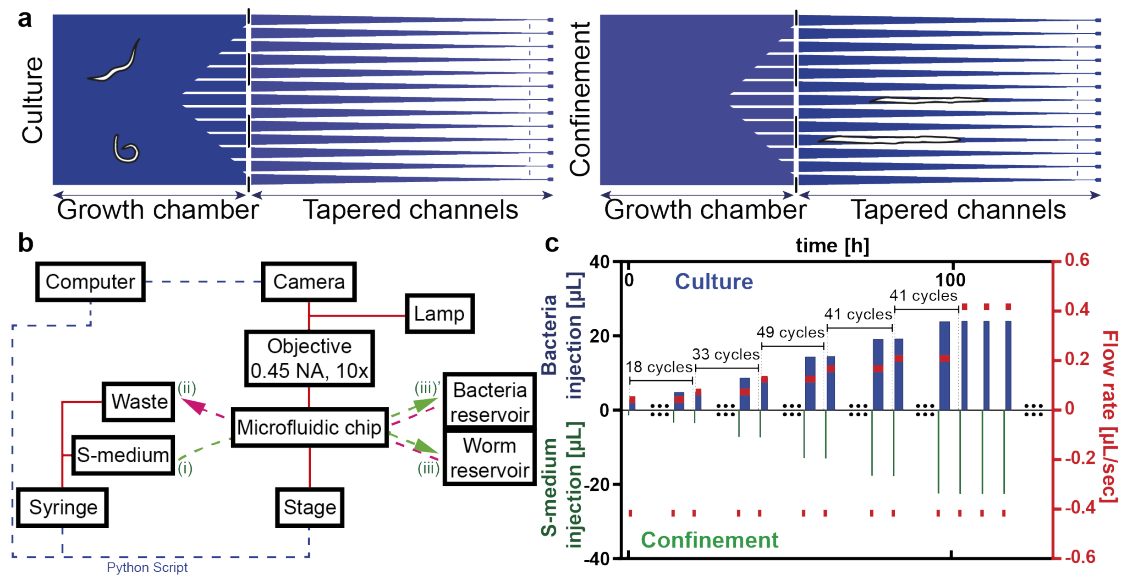


Figure 3.3 – Operation modes of the microfluidic chip. (a) The two operation modes of the unit cell. Nematodes are kept in “Culture” mode after the suction of fresh *E. coli* from the media outlets. In “Confinement” mode, they are confined in the tapered channels for imaging and phenotyping. (b) Block diagram of the overall platform with indication of different connections made to the inlets ((i), (ii)) and outlets ((iii), (iii)') (see text). (c) S-medium injection volumes during Confinement (lower part of plot and left axis) and bacteria injection volumes during Culture (upper part of plot and left axis) and the corresponding flow rates (red symbols and right axis). For example, in the first confinement step, 1.4 μL of S-medium is injected at a flow rate of 417 nL/s. This step is followed by a 2.9 μL bacteria injection at a flow rate of 42 nL/s in the first culture step. The S-medium injection volume is gradually increased during worm development. Bacteria injection is always kept 1.5 μL more than the previous S-medium injection volume to retain *E. coli* uniformity. 18 cycles were applied with the same flow rate during Culture, after which the flow rate increases. After 100 hours, the flow rate during Culture no longer is increased and kept constant.

A block diagram of the experimental setup is displayed in Figure 3.3b. A custom Python script was written to automate and synchronize the operations of the camera, the syringe pump and the motor stage with the microfluidic chip. This permits the full automation of the experiment with no need of user intervention, potentially throughout the whole duration of the worms' life cycle. Chip connections (i) – (iii)', (i) – (iii), (ii) – (iii)', (ii) – (iii) are used for confinement with fresh S-medium injection, gentle L1 push back after initial L1 distribution and fresh S-medium loading, *E. coli* injection and worm injection - distribution, respectively. We represent the used flow profiles over time in Figure 3.3c. Although having more than 200 confinement-culture cycles in an experimental run, for illustrative purposes, we only represent the experimental flow profile during a few of the cycles. Initially, we selected the ideal confinement S-medium flow rate (417 nL/s) and injection volume (1.4 μL) by manual operator tests for L1 worms, so that the latter were laterally confined but at the same time not be pushed to the neighboring chamber (lower bars of Figure 3.3c). If the Confinement flow rate was higher than the chosen

417 nL/s, we observed that late stage larvae and adult nematodes would be squeezed through the 8 μ m filters. When applying the same S-medium flow rate and injection volume to the other larval stages, we could not force larger worms any more to enter into the confinement channels. We therefore linearly increased the injection volume over time but did not increase the Confinement flow rate. Consequently, the duration of the confinement progressively increased in a linear fashion, starting from around 1 minute from the first confinement cycle (= width of the first green bar). After 100 hours, when worms had reached their largest size, we no further increased the S-medium injection volume per cycle. After each Confinement cycle, a Culture cycle started during which bacteria were injected from the other side of the chip (upper bars of Figure 3.3c). We used initially a flow rate of 42 nL/s and kept in each cycle the bacteria injection volume 1.5 μ L higher than the previous S-medium injection volume to ensure everywhere a uniform *E. coli* concentration. Therefore the duration of the bacteria injection (= width of a blue bar) was increasing too over time, starting from an initial duration of 10 minutes. After bacterial injection, nematodes were left in culture during 24 minutes until next Confinement cycle. The flow rates of bacteria injection during Culture were increased in steps from 42 nL/s to 73, 125, 167, 208 and 417 nL/s after 18, 33, 49, 41 and 41 cycles, respectively. Our approach enabled successful confinement during all life stages of *C. elegans* (see Figure 3.4).

3.3 Automated post-experiment image and video analysis

We developed an automated image and video analysis script with Matlab (MathWorks, Natick, MA, U.S.A.), including a custom-made GUI, to allow the user to extract the phenotyping results rapidly. The above-mentioned Matlab script and GUI served three purposes, namely bright-field confinement studies, fluorescence and motility analysis. Depending on the computational power of the computer, the processing times can vary significantly. In average, confinement and fluorescent analysis can be finished in less than 8 hours for an average computer, whereas, it will take 1-2 days for the motility analysis.

3.3.1 Growth parameters obtained from time-lapse imaging

The length and area of a worm were obtained from the raw bright-field images that were captured during the confinement of nematodes in the tapered channels. The first step was to create a dynamic background that provided the best result for the isolation of the confined worms (see details in Figure 3.5a-c) and subtract it from the raw image. Therefore, the real-time image of interest (Figure 3.5a), the previous three frames and the following three frames (Figure 3.5b) were merged by taking the median (Figure 3.5c). Any captured real-time image (Figure 3.6a) was first cropped to reduce the data size (Figure 3.6b) and then slightly blurred to reduce the false detections (Figure 3.6c). The previously created dynamic background was subtracted from the modified image (Figure 3.6d) and then the resultant image was first pixel intensity-adjusted (Figure 3.6e) and then binarized. After the binarization

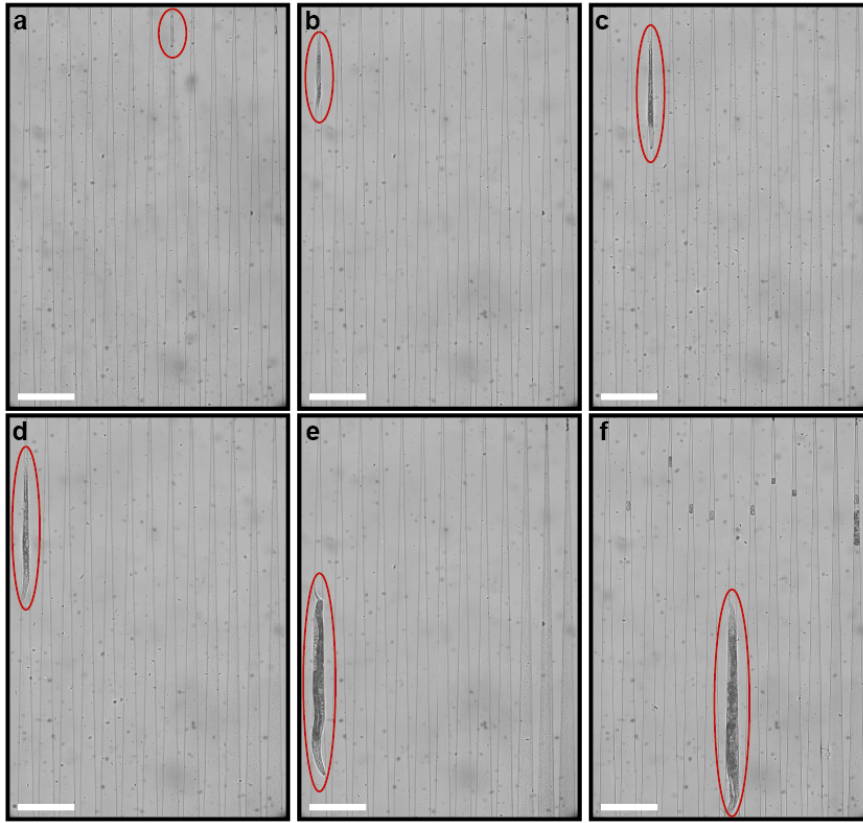


Figure 3.4 – Real-time confinement images of *C. elegans* at several larval stages. Confinement images of (a) L1, (b) L2, (c) L3, (d) L4 larvae, (e) young adults, and (f) adults. Scale bars: 300 μm .

of the intensity values, the confined worms and the remaining background clusters were marked. The brightness-adjusted image was thresholded (Figure 3.6f) in order to remove background clusters and the largest connected components matching the number of worms accommodated in the related chamber were automatically detected (Figure 3.6g). The total pixel number of each component was scored as the area. Morphological operations were applied to obtain the splines that were spatial fits to the worms. The total pixel number of the spline that was corresponding to a worm was scored as the length of the latter.

We analyzed two different strains, having slightly different fluorescent signal detection approaches, *i.e.* the mitochondrial unfolded protein response reporter *hsp-6::gfp* strain [67] – which essentially behaves like a wild-type (WT) strain of worms – and the HD model *p_{unc-54}::Q40::YFP* [66]. Along with bright-field images, at each confinement instance, we also acquired fluorescent images. In the first part, we wanted to observe the maximum and average fluorescent signal expression inside the nematodes. For this purpose, we dilated the resultant image from the bright-field image analysis and used it as a mask for the fluorescent image (Figure 3.7a-d). Our goal was to not unintentionally discard the fluorescent intensity values for *hsp-6::gfp* or aggregate clusters for *p_{unc-54}::Q40::YFP* nematodes on the nematode edges,

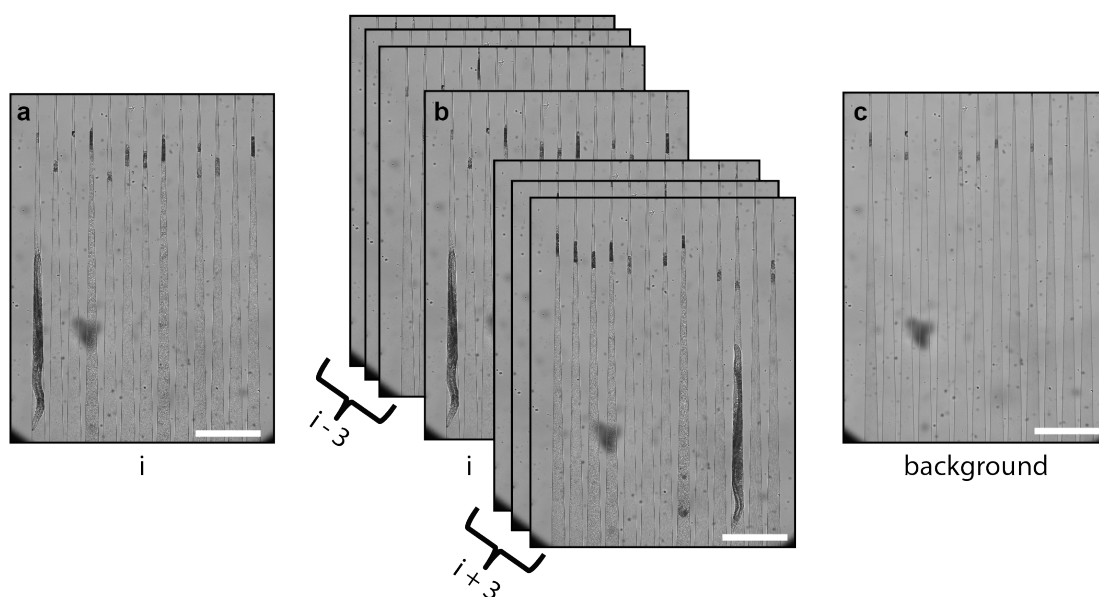


Figure 3.5 – The dynamic background creation approach used in the confinement analysis. (a) An image is acquired during the confinement cycle when all the worms in the chambers are immobilized in tapered channels. (b) The image of interest, the previous three frames and the following three frames are merged by taking the median. (c) The resultant median filtered image is worm-free and takes into account the bacteria clusters in the tapered channels for a more accurate worm shape extraction. Scale bars: 400 μm .

when the mask would be chosen too tight. We directly multiplied those two images so that we would only locate the worm of interest and avoid false fluorescent signal detection from the background (Figure 3.7e). An inverted version of the worm mask was also multiplied with the raw fluorescent image separately to quantify the average background intensity and to calculate the actual intensity value (Figure 3.7f-h). The average fluorescent intensity value was calculated by taking the median of all non-zero intensity values inside each identified worm mask. Likewise, the average of all non-zero intensity values were calculated and scored as the average background intensity for the second part.

A similar approach was adapted for the HD model in which a quantification of the protein aggregates was required (see details in Figure 3.8). A fluorescent image was captured (Figure 3.8a) and multiplied with a dilated version of the confinement result converted to a mask (Figure 3.8b-d). Hereon, we applied a Laplacian of Gaussian filter ($\sigma = 10$) as depicted in Figure 3.8e, which was followed by an image binarization step [52]. Over the resultant image in Figure 3.8f, a connected component search was performed to count the number of aggregates and record the total aggregate area by counting the total number of non-zero pixels. As the worms were confined in the tapered channels, some clusters that were in different focal planes were not easily detected; however, the resultant image provided accurate results to observe the significant aggregates.

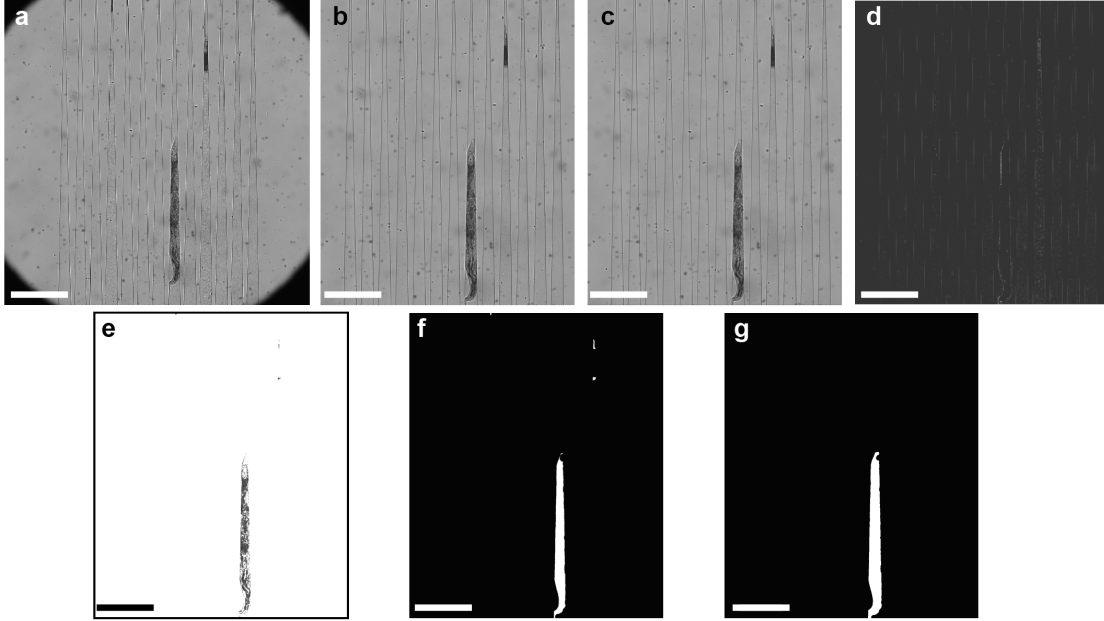


Figure 3.6 – Details of the automated image analysis of the bright-field images for the worms confined in the tapered channels. (a) All worms in the growth chambers are confined and a 2048 by 2048 pixel image is acquired. (b) The image is cropped to reduce the data storage, leaving only thirteen channels in the field of view. (c) The image is slightly blurred to reduce the false detections. (d) The dynamic background was subtracted from the slightly blurred image. (e) Image intensity values are adjusted such that background saturates towards white, the worms and outliers towards zero. (f) The image is thresholded. (g) The largest connected components matching to the number of worms accommodated in that chamber are detected. Scale bars: 400 μm .

3.3.2 Volume calculation and fluorescent intensity correction

We employed further data analysis to the initial phenotypic data to approximate volume for all the worms and corrected fluorescent intensity for *hsp-6::gfp* worm strain.

For the volume calculation, assuming that worms were approximately radially symmetric, we utilized the following formula in Equation 3.1 [68]:

$$Volume = \frac{\pi}{4} \times \frac{Area}{Length} \quad (3.1)$$

We determined the corrected value of the average fluorescent intensity with the following Equation 3.2:

$$I_{SBR} = \frac{(I_{ROI} - I_{BG})}{I_{BG}} \quad (3.2)$$

where, I_{SBR} and I_{ROI} are the corrected and the average intensity values of the fluorescence in the worm region of the image, respectively, while I_{BG} is the average background intensity value. We followed an initial background noise removal and then a standard signal-to-noise

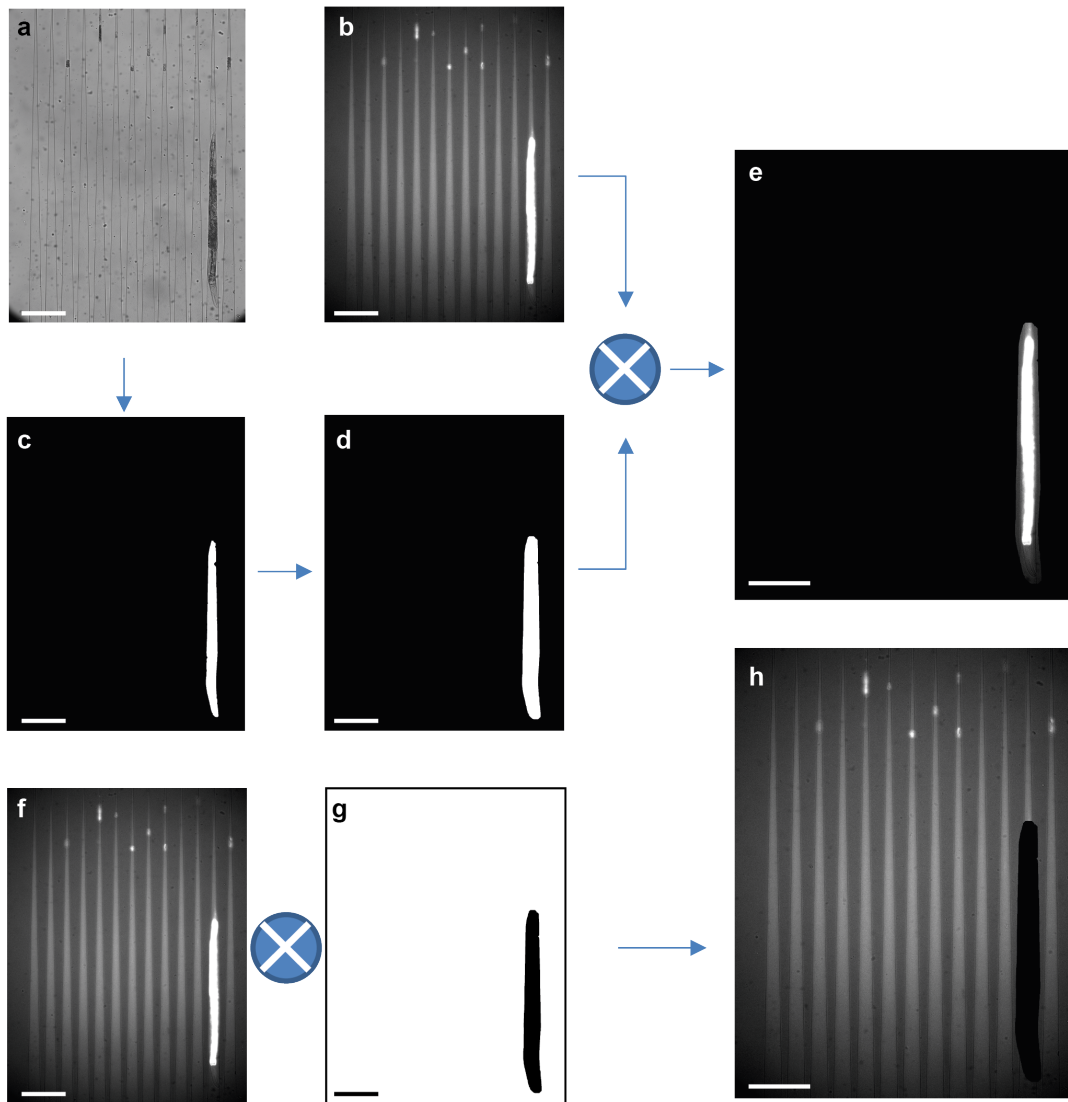


Figure 3.7 – Details of the automated fluorescent image intensity analysis for the worms confined in the channels. All worms in the growth chambers are confined and a bright-field image (a) and a fluorescent image (b) are acquired. (c) The bright-field image is turned into a binary mask as explained in Figure 3.6. (d) This mask is dilated to ensure the full coverage of the worm during the multiplication with the fluorescent image in (b). (e) The resultant image is used to quantify the fluorescent signal expression only inside the worms. (f) The same fluorescent image is also processed to quantify the background intensity. (g) The inverted version of binary mask in (d) is used to exclude all the worms in the image. (h) These two images are multiplied to obtain a worm-free background fluorescent image to quantify the average background fluorescent intensity expression. Scale bars: 300 μm .

ratio (SNR) correction method.

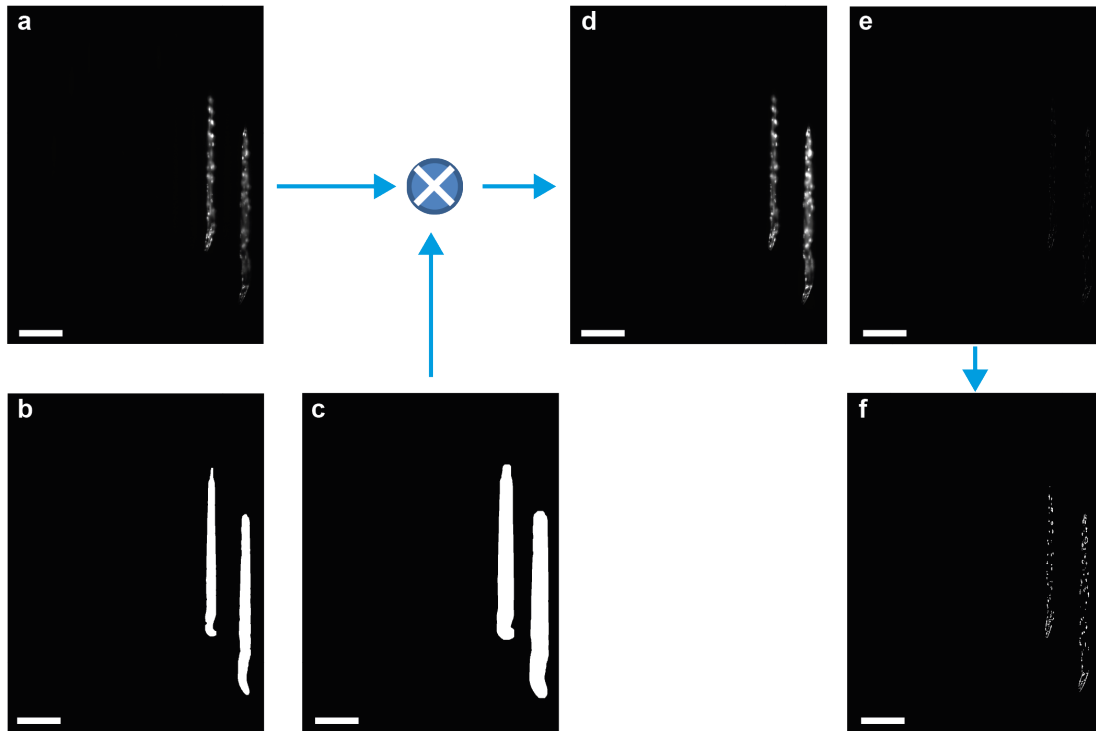


Figure 3.8 – Details of the automated fluorescent image aggregate analysis for the *p_{unc-54::Q40::YFP}* worms confined in the channels. (a) A fluorescent image is captured while the worms are confined in tapered channels. (b) The resultant image from the bright-field confinement analysis is loaded, (c) and dilated so that it covers the worms of interest after the image multiplication. (d) The resultant multiplied image is background-free and contains only the worms. (e) The image is passed through a Laplacian of Gaussian filter ($\sigma = 10$) to detect the aggregates. (f) It is, then, thresholded to observe the aggregates clearly. Scale bars: 300 μm .

3.3.3 Motility analysis from video recordings

For video analysis, we adjusted a motility tracking algorithm for *C. elegans* in M9 buffer for our study [48]. Further details in the calculation of these phenotypes can be found in the related research of the same authors [69, 70]. Similar to the bright-field confinement image processing, a dynamic background subtraction was required to isolate the nematodes in the chambers. For this, we created a dynamic background image combining the median of the video frames of interest and the median of all the video frames (Figure 3.9). This step provided the best results for the worm isolation in the growth chambers. For a single frame of a video set of 50 frames (Figure 3.9a), we merged two different backgrounds together to create a single background for subtraction. We took median of all 50 frames in a video set (Figure 3.9b) and acquired a background, namely, “video set” background (Figure 3.9c). We also combined “video set” backgrounds of 15 sets (Figure 3.9d) by taking the median to obtain the second background, namely, “overall” background (Figure 3.9e). To construct the “final” background for the subtraction from the raw video frames, we combined these two backgrounds with the

3.3. Automated post-experiment image and video analysis

Equation 3.3 (Figure 3.9f):

$$B_{final} = \frac{(2 \times B_{videoset} - B_{overall})}{3} \quad (3.3)$$

where, B_{final} , $B_{videoset}$ and $B_{overall}$ are the “final” background, “video set” background and “overall” background, respectively.

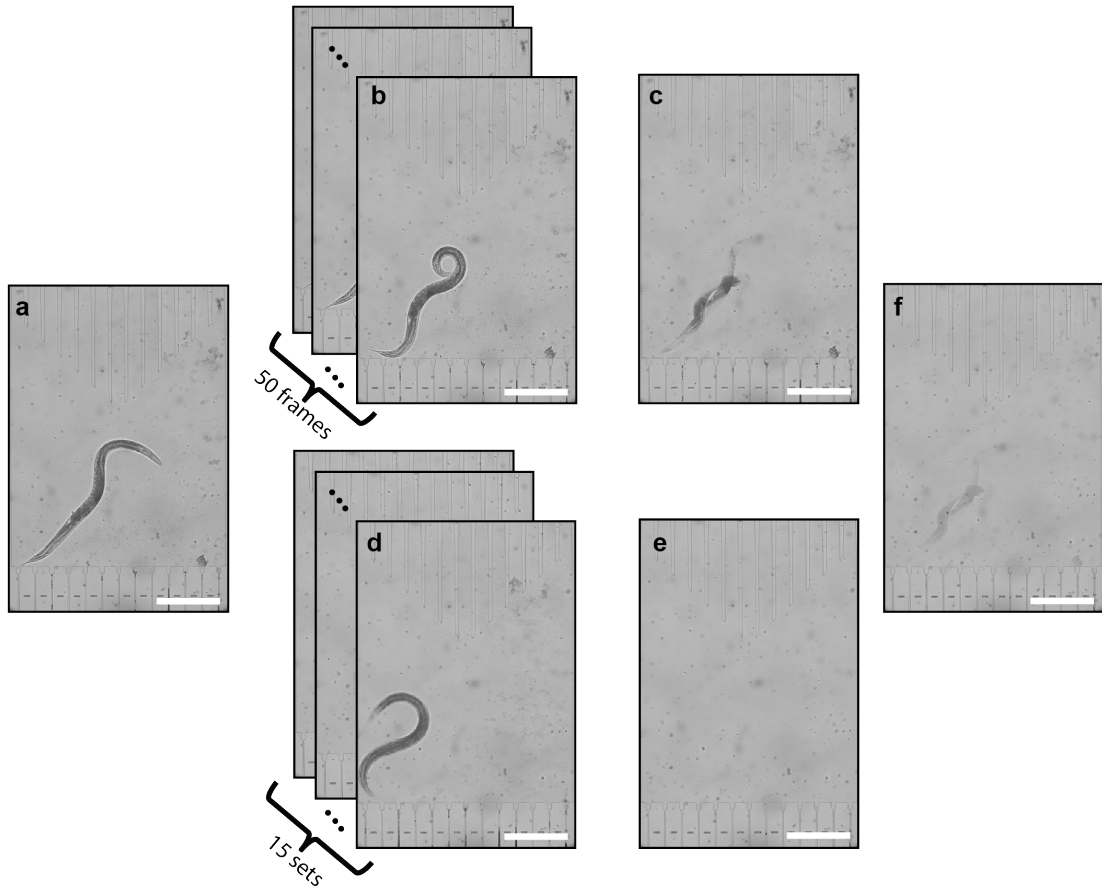


Figure 3.9 – The dynamic background creation approach used in the motility analysis. (a) An image is acquired during the worm motion in the growth chamber. (b) The images of each video set, having 50 frames typically, are merged together to obtain the “video set” background (c). (d) The 15 sets of “video set” background are merged together to obtain the “overall” background (e). (f) For each video set, two units of “video set” background and one unit of “overall” background are averaged to obtain one “final” background, which results in the best distinction of the worms in the chambers from the environment. Scale bars: 400 μ m.

Approximately every 7 hours, videos at 5 Hz for 10 seconds were recorded. A frame of the video stack is shown in Figure 3.10a. As explained in Figure 3.9, a dynamic background was created for each video set (Figure 3.10b). After the background removal (Figure 3.10c), each frame was thresholded (Figure 3.10d), smoothed and forced to detect the number of the largest connected components matching to the worms accommodated in that chamber. A worm in the chamber

was randomly detected (Figure 3.10e) and hereon, our algorithm was divided into two parts. In the first part, the first detected worm's mask was dilated (Figure 3.10f) and multiplied with the binarized version of the consecutive frame to keep track of the same worm (Figure 3.10g). A spline is fit, tangential and perpendicular components of the spline are marked for further data extraction. Among the two end points of the spline, the higher curvature point was assumed to be the head and the other end to be the tail. In the second part, we wanted to detect other neighboring worms in the same growth chamber. An inverted version of mask in Figure 3.10f (Figure 3.10h) is multiplied with the first frame of the same video set (Figure 3.10d) in order to keep track of the other worms in the chambers (Figure 3.10i). The same approach as in Figure 3.10g is pursued to obtain all the necessary components for data extraction. If there were more than two worms in the same growth chamber, we combined the dilated and inverted versions of the first tracked frame with a logical OR. All these data were combined to extract central velocity, beating frequency (also known as "locomotor frequency"); head, center and tail beating amplitudes; minimum, mean and maximum curvature; bending wavelength and bending wave amplitude change in time (wavespeed), bending force and mechanical power.

3.3.4 Initial raw data after the post-experiment automated phenotyping

For each of the recorded results, we also annotated the first egg release times, which were obtained from the confinement images by operator-observation of the first egg that was trapped in the tapered channels. We present a single worm phenotypic analysis in Figure 3.11a-d. The raw data from each algorithm required some post-adjustment to obtain reliable data that prevented incorrect detection. Our method was to check the closeness of neighboring data points. For this purpose, we computed the difference of a measurement point of interest to the three previous time point measurements. If three different difference values were in a certain interval, the data point was counted as a reliable measurement; otherwise, it was classified as an outlier and discarded. Our method discarded, in average, 72% of the overall data. The main reason of such a high discarding rate is due to mainly (i) low confinement accuracy for the adults after 100 hours of experiments, and (ii) to ensure that no false data were included, which eventually results in correct measurements to be discarded as well. During development of our platform, we therefore systematically performed operator-based visual controls to assure the correctness of our method. The resultant data was recorded (Figure 3.11a) and used later to combine with other worms grown under the same conditions. Similarly, we discarded incorrect average fluorescent intensity values by deselecting eventual outliers at any time scale (Figure 3.11b). Remaining average fluorescent intensity data was plotted and a semi-log line was fit. This raw data was again, combined with the other raw data of the worms that were grown under the same conditions. By identifying the incorrect length and fluorescence measurements and, hence, by excluding the related measurement times with our method, we obtained the corrected aggregate count plot in time (Figure 3.11c). A sigmoidal fit was performed on the corrected data. The worm's center velocity and beating frequency required a manual approach to correct the raw data, as worms could alternate

3.4. High-content phenotyping of worms at various concentration of bacterial food

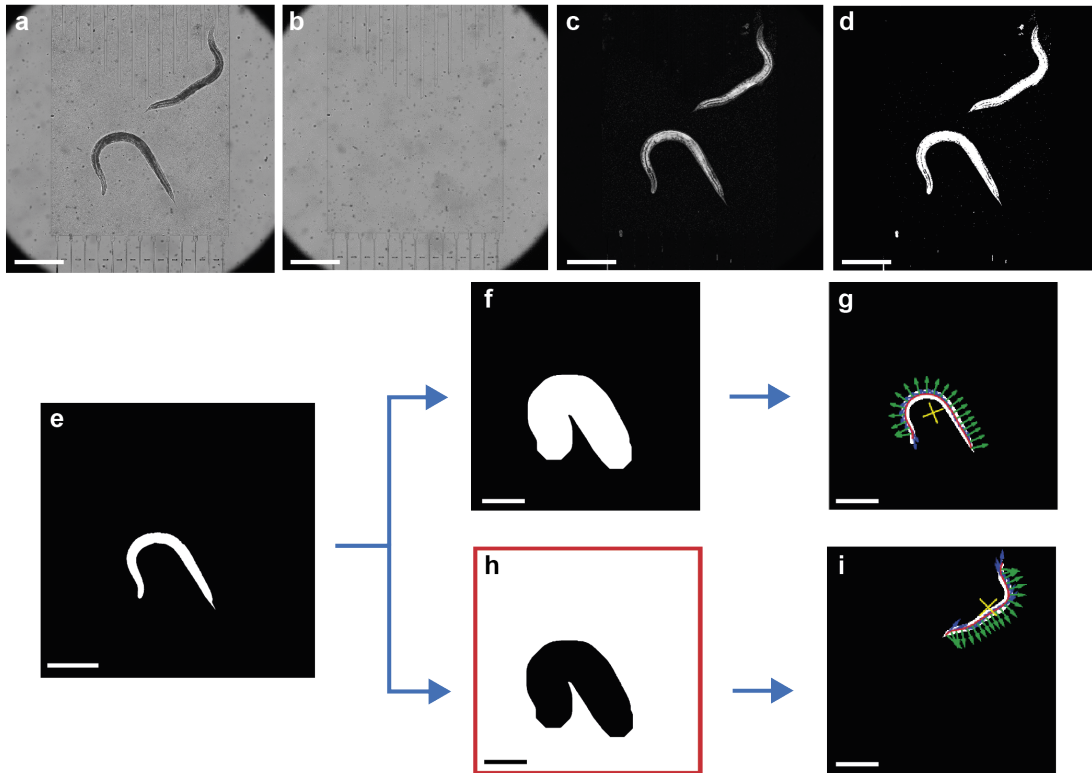


Figure 3.10 – Details of the automated motility analysis for worms that are freely moving in a growth chamber. (a) Video frames at 5 Hz for 10 seconds are recorded. (b) The previously created dynamic background (c) is subtracted from the video frames. (d) The subtracted image is thresholded and smoothed. (e) One of the largest connected components is detected. (f) The dilated version of the binary worm mask was used to keep track of the same worm. (g) The worm is skeletonized, the center point of the worm (shown as yellow), the tangential (shown as blue) and perpendicular components (shown as green) of each skeleton point are denoted. (h) The inverted version of worm mask in (f) is multiplied with (d) to locate the other residing worm. (i) Same procedure as in (g) is applied to keep track of the neighboring worm. Scale bars: 400 μm .

periods of activity and rest (Figure 3.11d). We plotted all data in time and whenever the spline fit was rather poor in a single video recording, we manually discarded these data.

3.4 High-content phenotyping of worms at various concentration of bacterial food

In many animal species, such as rats, monkeys, yeast cells, *Drosophila melanogaster*, *C. elegans*, mice that were tested so far, DR has been shown to slow down the aging process, resulting in longer maintenance of health and an extended mean and maximum lifespan [60, 62, 71, 72, 73, 74]. Interestingly, DR not only promotes lifespan extension but also decreases the occurrence

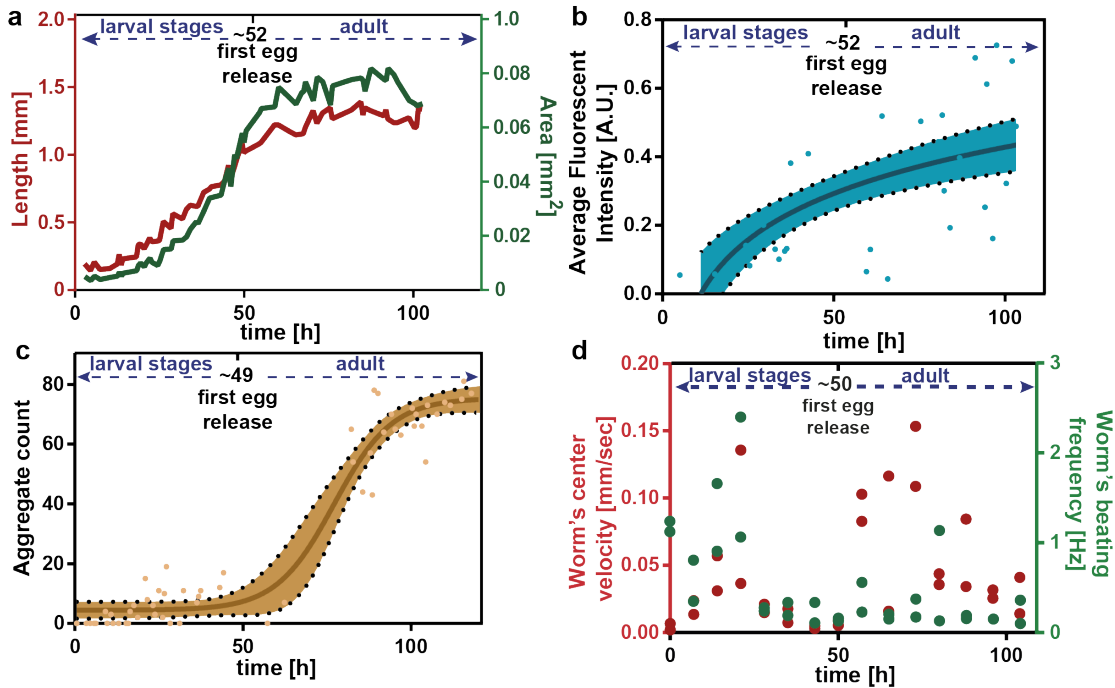


Figure 3.11 – Automated image and video analysis for extraction of worm phenotypes. (a-d) Typical results obtained for a single worm's length and area, average fluorescent intensity, aggregate count, worm's center velocity, and beating frequency, after analysis of the cases introduced in Figure 3.6, Figure 3.7, Figure 3.8, and Figure 3.10, respectively. Semilog and sigmoidal interpolation lines are used for average fluorescent intensity ($R^2 = 0.43$) and aggregate count ($R^2 = 0.95$) measurements, respectively, in order to remove outliers.

of age-dependent diseases, including neurodegeneration [75]. Among all the model organisms employed in this field, *C. elegans* continues to serve as a powerful model of longevity induction caused by DR [76]. As a proof-of-concept for our technology, we intended to use *C. elegans* and our microfluidic platform in order to better define the effect of DR on neurodegenerative diseases.

3.4.1 Egg release behavior of worms

We first wanted to determine the ideal bacterial dilution that could be provided in the microfluidic platform for establishing proper DR conditions on *C. elegans* growth and motility (Figure 3.12). We have selected four different *E. coli* concentrations, namely, 4×10^9 – which corresponds to the *ad libitum* (AL) feeding condition –, 2×10^9 , 1×10^9 and 5×10^8 cells/mL [64, 77]. DR is known to delay the growth rate and to reduce the fertility in numerous organism including *C. elegans* [61], but very little is known about the timing resolution of DR effects during the development. In order to explore the impact of DR during development, we first investigated the timing of first egg laying by visually checking the tapered channels for presence of a first confined egg. The first temporal instance an egg observed was recorded and

3.4. High-content phenotyping of worms at various concentration of bacterial food

compared for different *E. coli* feeding concentrations (Figure 3.12a). The first egg release time demonstrated a similar profile for the highest two feeding conditions and a 5% time increase was obtained for the lowest feeding condition. In addition, we quantified the embryo release rate by subtracting number of embryos trapped in the initial frame that embryo laid was first noticed from the fifth following frame, then dividing by number of worms accommodated and the time interval between those two frames (Figure 3.12b). This extrapolated data delivered an estimation on the progeny release rate under various feeding conditions. In accordance with previous works done on NGM plates, we observed that DR increases the egg release rate [78].

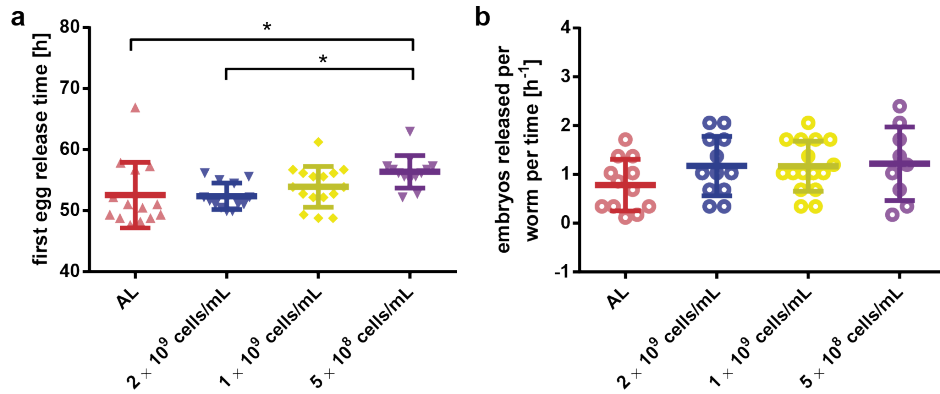


Figure 3.12 – Study of the effect of *E. coli* concentration on the fertility of *hsp-6::gfp* worms. (a, b) The first egg release time and embryos released per worm per time results obtained from the embryo collection inside tapered channels. Data are expressed as mean \pm SEM, * $p \leq 0.05$. All measurements are based on $N = 18$ to 24 worms.

3.4.2 Change of growth parameters

By merging the corrected data from the confinement in tapered channels (both bright-field and fluorescent), we observed the influence of bacterial dilution on length, area and volume. The maximum worm length decreases with bacterial food dilution in a dose-dependent manner (Figure 3.13a). Interestingly, the area of the worms demonstrated a different growth dynamics (Figure 3.13b). For AL *E. coli* feeding, 2×10^9 cells/mL and 1×10^9 cells/mL concentration, the maximum area reached by the worms at the adult stage was similar. However, a 10 hours time delay in the worm area growth was typically observed for the 1×10^9 cells/mL condition. This piece of information would have been missed if we could not follow the full dynamics of area increase as enabled by our platform. Moreover, for the 5×10^8 cells/mL feeding condition, worms were much smaller at all stages compared to any other feeding condition. The maximum area a worm could cover with this feeding was in fact almost half of that of a properly fed worm. A similar trend was also detected for the worm volume (Figure 3.13c). In comparison to previous studies [77], we could confirm a similar length and volume profile, and hence, possibly the same area results.

We extracted the dose-dependent curves of length (Figure 3.13d), area (Figure 3.13e) and

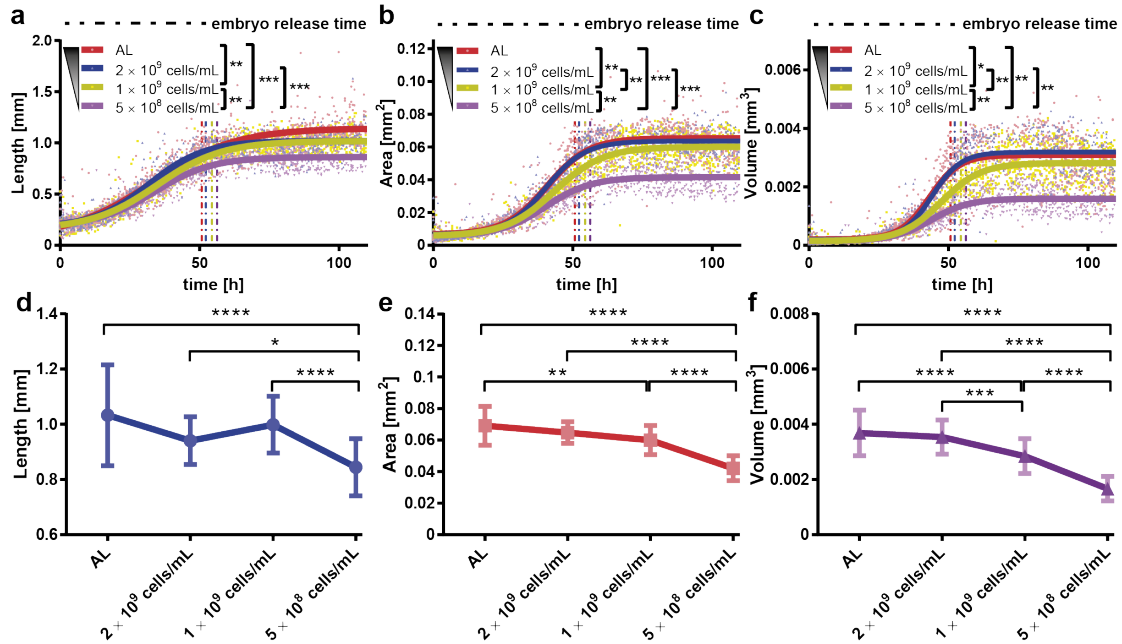


Figure 3.13 – Study of the effect of *E. coli* concentration on the worm development of *hsp-6::gfp* worms. (a-c) Length, area and volume obtained by feeding with different bacteria concentrations. A sigmoidal fit is utilized for length, area and volume estimation. R^2 values representing the quality of sigmoidal fits are calculated to be [0.87, 0.92, 0.93, 0.89], [0.89, 0.94, 0.92, 0.87], [0.81, 0.89, 0.87, 0.81]; for the feeding conditions [AL, 2×10^9 cells/mL, 1×10^9 cells/mL, 5×10^8 cells/mL] from panel (a) to (c), respectively. The average first embryo release time was also plotted as a vertical dashed line to indicate the transition from the larval stages to adult stage. (d-f) The dose response curve of length, area and volume obtained at 80 hours by feeding with different bacteria concentrations. Data are expressed as mean \pm SEM, * $p \leq 0.05$, ** $p \leq 0.01$, *** $p \leq 0.001$, **** $p \leq 0.0001$. All measurements are based on $N = 18$ to 24 worms.

volume (Figure 3.13f) at 80 hours of development. Besides the length curve, we observed a dose-dependent sigmoidal decrease in the parameters, which demonstrates the effect of *E. coli* concentration on the worms' growth. Real time-images of growth chambers at 65 hours were captured and detailed to demonstrate the developmental difference of worms under different feeding conditions (Figure 3.14a-d). At the time, where all the worms reached the adult stage and laid embryos, there was a significant size difference among the worms that were raised under different feeding conditions.

3.4.3 Induction of mitochondrial stress

In order to extract more information about the impact of DR on the worm physiology, we monitored the modulation of the mitochondrial unfolded protein response (UPR^{mt}) upon DR treatment. The mitochondrial function and its associated stress response is today considered

3.4. High-content phenotyping of worms at various concentration of bacterial food

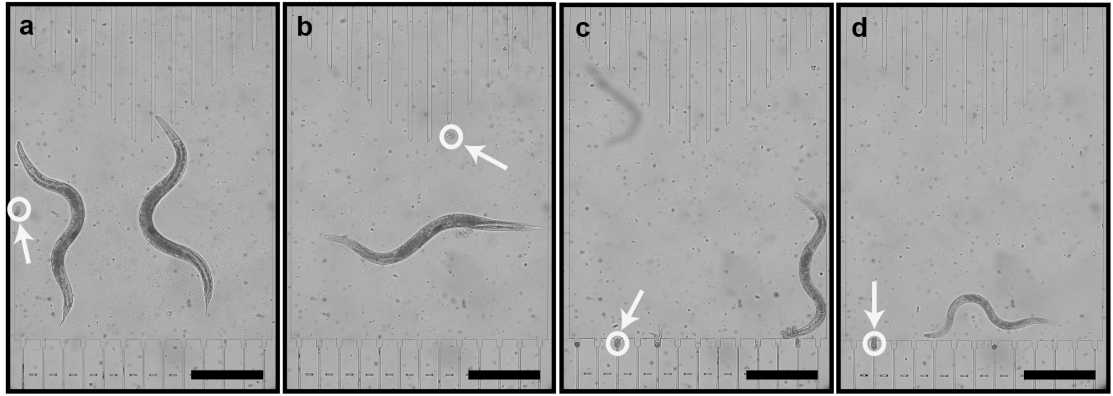


Figure 3.14 – Representative real-time growth chamber images of wild-type *hsp-6::gfp* nematodes under (a) 4×10^9 cells/mL (AL), (b) 2×10^9 cells/mL, (c) 1×10^9 cells/mL, and (d) 5×10^8 cells/mL *E. coli* concentration at 65 hours with eggs laid indicated. Scale bars: 400 μ m.

as a pivotal player for aging regulation, but the role of the so-called UPR^{mt} in DR is not well understood so far. We employed our automated fluorescent image analysis algorithm to quantify the expression of the *hsp-6::gfp* reporter for evaluating the induction of the UPR^{mt} (see details in Figure 3.15). Interestingly, DR has no significant effect on UPR^{mt}, confirming previous observation using a genetic model of DR in *C. elegans* [79]. At the early larval stages, the worms did not have a significant variance in the mitochondrial stress for different amounts of feeding; however, to the later stages of their life cycle, mitochondria were stressed more for a higher feeding concentration than for lower amounts. Of note, we observed 50% reduction in the intensity of the fluorescent signal in the adult population submitted to the lowest concentration of food, indicative for less stress in mitochondria.

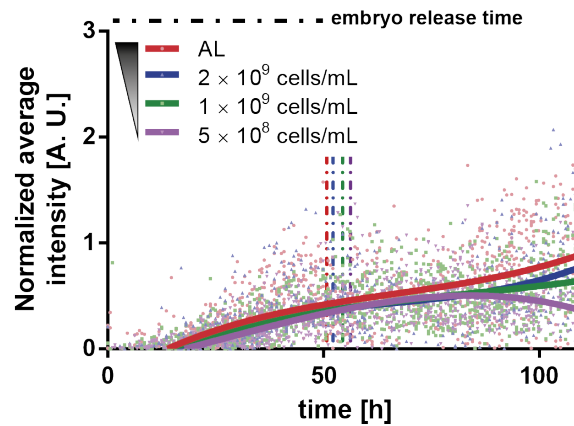


Figure 3.15 – The normalized average fluorescent intensity expression of *hsp-6::gfp* worms under four different *E. coli* feeding concentrations. A third order polynomial fit is utilized for estimating the normalized average fluorescent intensity in time. R^2 values representing the quality of polynomial fits are calculated to be [0.37, 0.51, 0.59, 0.57] for the feeding conditions [AL, 2×10^9 cells/mL, 1×10^9 cells/mL, 5×10^8 cells/mL], respectively.

3.4.4 Change of motility parameters

DR is also reported to have an effect on motility behavior [80]. The central velocity (Figure 3.16a) and the beating frequency (Figure 3.16b) of the worms were rather invariant at the early larval stages. The influence of different feeding became more significant after 20 hours of development. At 1×10^9 cells/mL feeding, worms were more inclined to move around inside their chamber, likely pushed by the need of more food. In line with this speculation, at AL and 2×10^9 cells/mL feeding, worms were not so mobile. A variation of the motion at 5×10^8 cells/mL feeding was observed. Because of poor feeding, worms remained smaller at this *E. coli* concentration and, similarly, their movement speed was reduced compared to 1×10^9 cells/mL feeding condition, when movement was most intense. The head (Figure 3.16c) and center (Figure 3.16d) beating amplitudes were also detected and showed a similar effect that confirmed this phenomenon. The variation in the beating amplitudes was more pronounced after 35 hours. We also performed a feeding dose-dependence analysis for these four motility parameters (Figure 3.17) to observe the effect of DR on the motility. For all the selected motility parameters, there was a gaussian trend. As the food amount decreased, worms tended to increase their motility till a certain point. After that, due to insufficient food provision, worms suffered from caloric restriction.

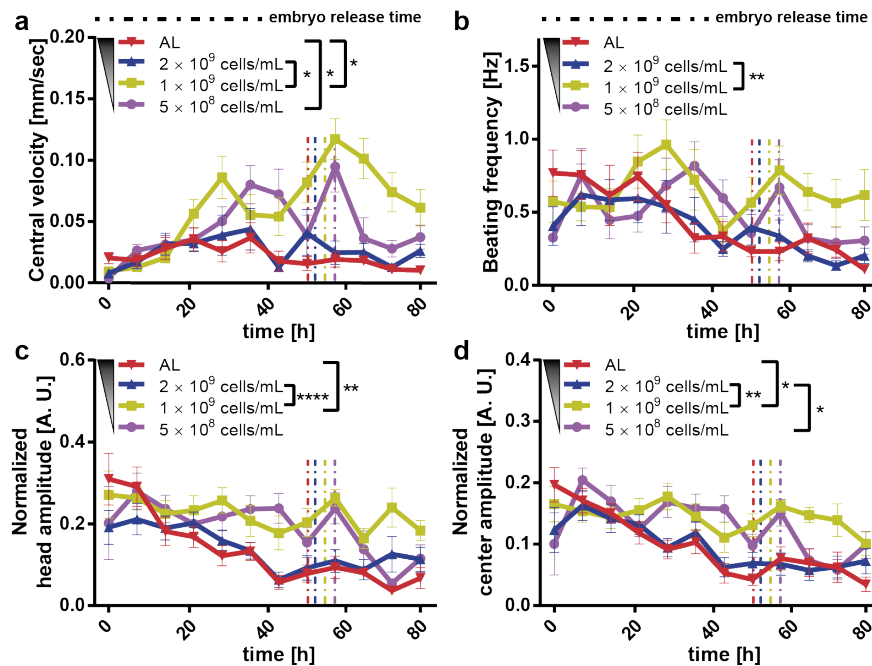


Figure 3.16 – Study of the effect of *E. coli* concentration on the motility of *hsp-6::gfp* nematodes. (a-d) Comparison of four motility parameters, namely the worms' center velocity, beating frequency, and normalized head and center beating amplitude after feeding with different *E. coli* concentrations. The average first embryo release time was also plotted as a vertical dashed line to indicate the transition from the larval stages to adult stage. Data are expressed as mean \pm SEM, * $p \leq 0.05$, ** $p \leq 0.01$, **** $p \leq 0.0001$.

3.4. High-content phenotyping of worms at various concentration of bacterial food

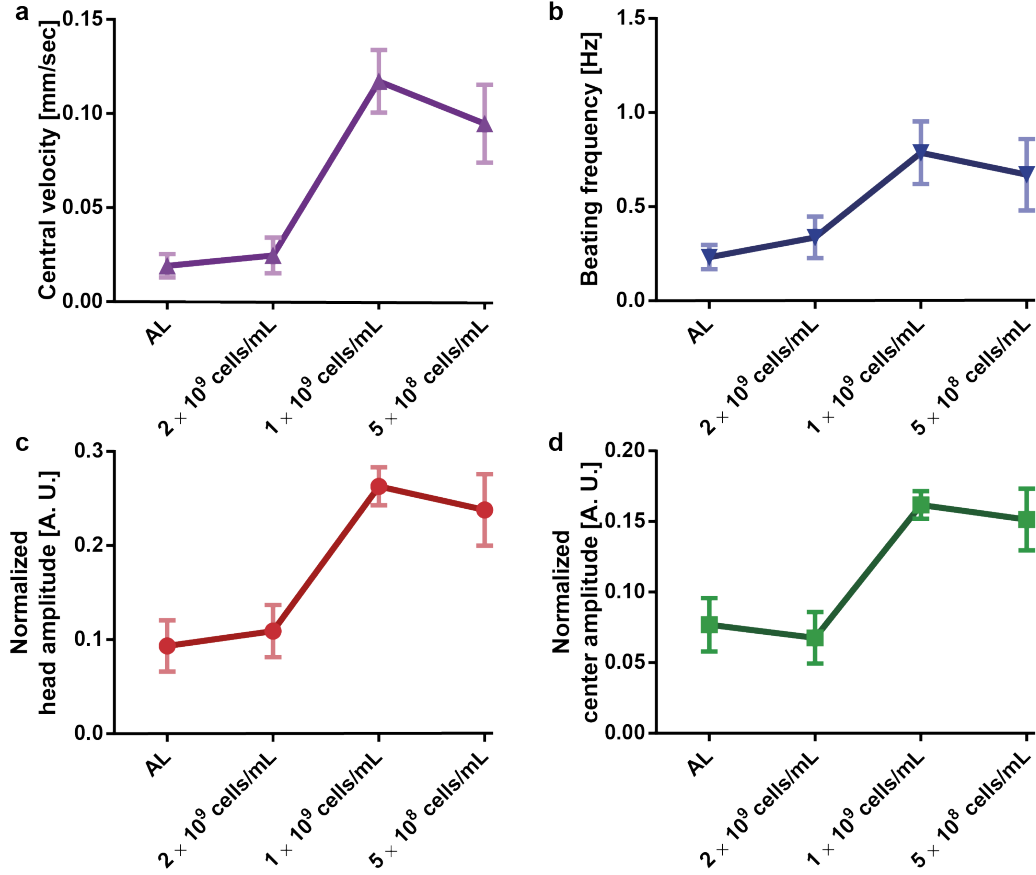


Figure 3.17 – The dose-dependent motility behavior for four different *E. coli* feeding of *hsp-6::gfp* worms at 57 hours. (a) Central velocity, (b) beating frequency, (c) normalized head beating amplitude and (d) normalized center beating amplitude results compared for four different feeding concentrations are demonstrated.

3.4.5 Clustergram analysis

In order to compile all together the generated data and facilitate the visualization of eventual variations in the motility and growth parameters in time, we built clustergram profiles with the normalized data with the Equation 3.4 (Figure 3.18):

$$P_{OI} = \frac{P_{IN}}{P_{CNT}} - 1 \quad (3.4)$$

where, P_{OI} , P_{IN} and P_{CNT} are the normalized parameter of interest, the parameter of interest and the corresponding control parameter, respectively.

At 21 hours, no significant changes were detected yet, compared to the condition of maximum feeding (Figure 3.18a). Nevertheless, the dendrogram related to the lowest *E. coli* concentration started to show distinct features from the other concentrations. The first significant change was detected at 35 hours (Figure 3.18b). The dendrogram related to the lowest *E. coli* concentration demonstrated that there was a clear separation from the other feeding concentrations. At

43 hours, the lowest *E. coli* concentration condition and the 1×10^9 cells/mL concentration were coupled together, resulting in a similar behavior of motility parameters and they were separated from the other coupled 2×10^9 cells/mL and AL concentrations (Figure 3.18c). At 65 hours of development, the isolation of different feeding conditions was not significantly different except for the 1×10^9 cells/mL concentration (Figure 3.18d). The 5×10^8 cells/mL feeding condition's movement parameters approached the remaining two feeding conditions around this time point. We hence speculate that the relatively small size of worms under the most severe DR conditions caused an alteration in the swimming motion (Figure 3.18a-c). From these data, it was clear that DR has a significant impact on motility parameters and adverse influence on the growth and fertility parameters.

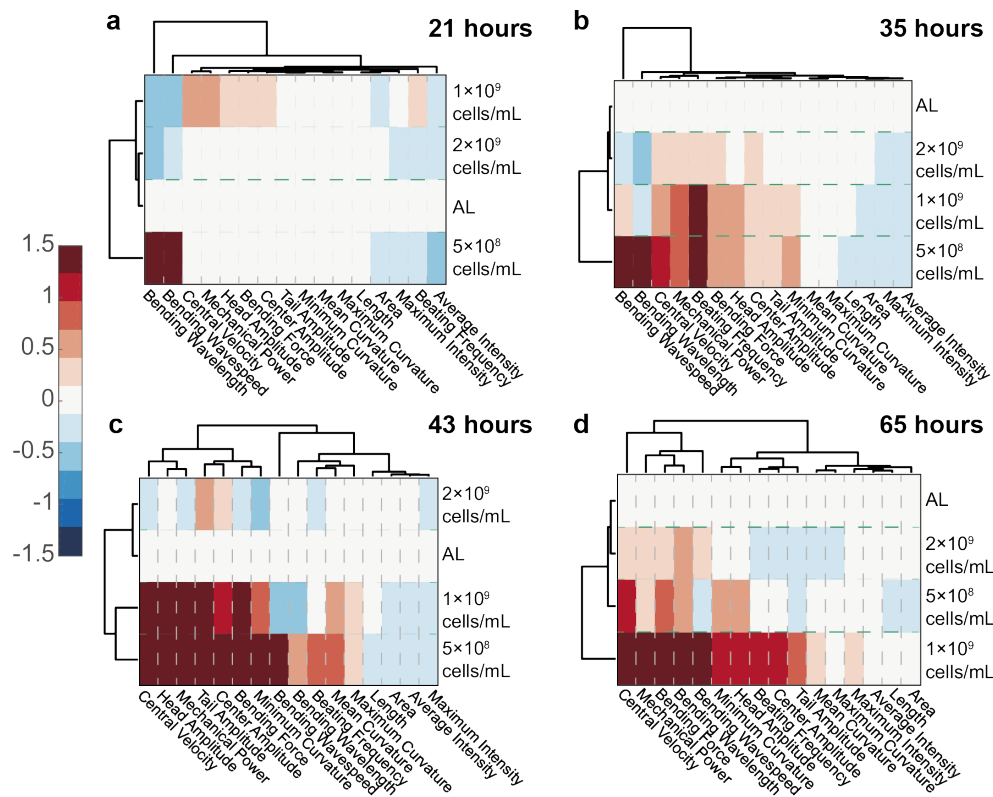


Figure 3.18 – Clustergram comparison of *hsp-6::gfp* nematodes of motility and development parameters. The comparison plots obtained at (a) 21, (b) 35, (c) 43 and (d) 65 hours after the first bacteria injection on the chip, respectively, as obtained for different *E. coli* concentrations. All measurements are based on N = 18 to 24 worms.

3.5 Influence of DR on a Huntington's disease worm model

DR is a relevant intervention to increase the resistance of the nervous system to age-related neurodegenerative disorders [81]. Based on previous observations, we wanted to analyze the effect of DR on a worm model of neurodegenerative disease. HD is one of the most common

3.5. Influence of DR on a Huntington's disease worm model

genetically determined neurodegenerative diseases, with approximately 90% of HD cases being hereditary and transmitted in an autosomal dominant fashion [82]. This disease belongs to a group of neurological disorders caused by expanded cytosine-adenine-guanine (CAG) triplet repeats encoding self-aggregating polyglutamine (polyQ) tracts in their respective proteins. In the case of HD the polyQ expansion is in the *huntingtin* gene [83]. In order to model HD in worms, we used a *C. elegans* strain that carries the transgene *p_{unc-54}::Q40::YFP* resulting in the expression of the fusion protein Q40::YFP specifically in worm muscle cells, causing an age-dependent aggregation phenotype whose readout is a progressive motility deficiency [66]. Based on the results obtained in WT worms, we selected two *E. coli* feeding conditions, *i.e.* 4×10^9 cells/mL (*ad libitum* AL) and 5×10^8 cells/mL (DR), which demonstrated the most significant difference between proper feeding and settling the DR condition. The feeding at 5×10^8 cells/mL yielded more phenotypic changes to the worms as opposed to the feeding at 1×10^9 cells/mL, in which worms were smaller but still active. Therefore, a 5×10^8 cells/mL feeding concentration was chosen as the ideal condition for DR studies.

3.5.1 Change of growth parameters

We extracted the growth and motility parameters and studied the polyQ aggregation in a time-dependent manner (see growth parameters' details in Figure 3.19 and Figure 3.20). The length (Figure 3.19a), area (Figure 3.19b) and the volume (Figure 3.19c) of the HD worms displayed a similar profile as in the WT strain. The HD worms fed with the AL concentration were longer and larger in area and volume throughout the whole study compared to the worms that were on DR. The total aggregate number (Figure 3.20a) and the total aggregate size (Figure 3.20b) were then quantified. Interestingly, HD worms submitted to a DR regimen have a significant reduction of the total aggregate number and total aggregate size compared to HD worms fed AL. Furthermore, the average aggregate size in time (Figure 3.20c), which was calculated as total aggregate area size divided by total number of aggregates, showed a similar behavior. Indeed, the average aggregate size of the worms under DR were all the time, except during the initial few hours, smaller than the ones under AL conditions. We also calculated the aggregate number per length, which corresponds to the total number of aggregates divided by the length of the worm (Figure 3.20d). This plot established that, as the worms grow in time, the feeding has less of an influence and the aggregate number per length saturates. We thereby demonstrated that DR has a progressive influence on the delay of protein aggregation and size for HD worms, suggesting that the disease is significantly attenuated by food restriction.

3.5.2 Change of motility parameters

The progressive loss of motility in the HD worm model is a well-established phenotype [84]. We observed that the central velocity (Figure 3.21a) and the beating frequency (Figure 3.21b) of the HD worms were significantly improved under the DR regime. Indeed, the restricted worms were moving faster and with a greater beating frequency than the ones that were fed with higher *E. coli* concentration. Interestingly, head (Figure 3.21c) and center (Figure 3.21d)

Chapter 3. Automated high-content phenotyping over the life cycle of the nematode *Caenorhabditis elegans*

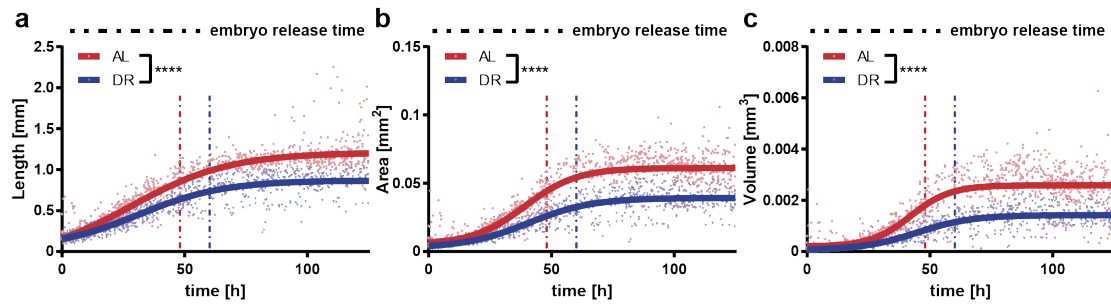


Figure 3.19 – Study of the effect of *E. coli* concentration on the longitudinal growth of the *p_{unc-54::Q40::YFP}* mutant worms, a model for HD. (a-c) Length, area and volume obtained by feeding worms with two different bacteria concentrations. The average first embryo release time was also plotted as a vertical dashed line to indicate the transition from the larval stages to adult stage. A sigmoidal fit is utilized for all the plots. R^2 values representing the quality of sigmoidal fits are calculated to be [0.86, 0.84], [0.85, 0.84], [0.76, 0.78]; for the feeding conditions [AL, DR] from panel (a) to (c), respectively. Data are expressed as mean \pm SEM, **** $p \leq 0.0001$. All measurements are based on $N = 18$ to 20 worms.

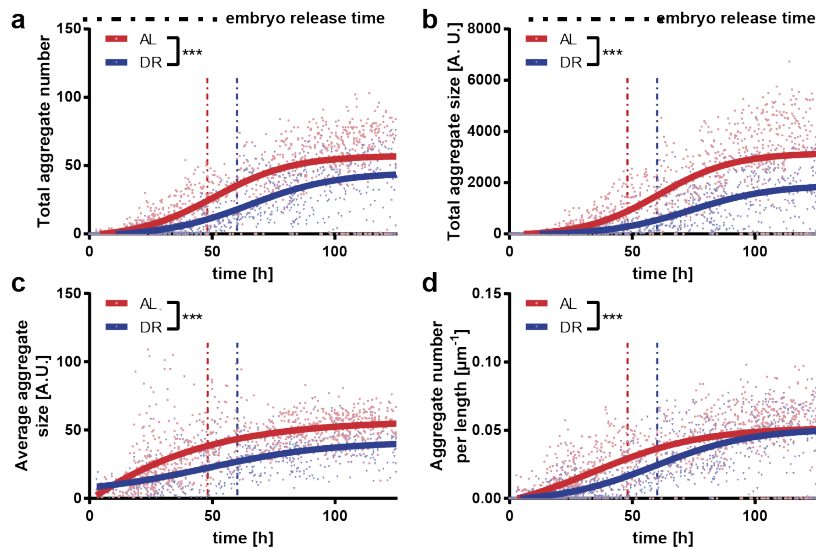


Figure 3.20 – Study of the effect of *E. coli* concentration on the aggregate growth of the *p_{unc-54::Q40::YFP}* mutant worms, a model for HD. (a-d) Total aggregate number, total aggregate size, average aggregate size and aggregate number per worm's length, obtained by feeding with two different bacteria concentrations. The average first embryo release time was also plotted as a vertical dashed line to indicate the transition from the larval stages to adult stage. A sigmoidal fit is utilized for all the plots. R^2 values representing the quality of sigmoidal fits are calculated to be [0.66, 0.66], [0.64, 0.58], [N/A, 0.34], [0.57, 0.63]; for the feeding conditions [AL, DR] from panel (a) to (d), respectively. Data are expressed as mean \pm SEM, *** $p \leq 0.001$. All measurements are based on $N = 18$ to 20 worms.

beating amplitudes did not show much of a difference. In the early larval stages, the beating amplitudes were similar and only between 20 and 60 hours were the worms fed with the low *E.*

3.5. Influence of DR on a Huntington's disease worm model

coli concentration more mobile. After 60 hours, the worms with low *E. coli* concentration were disturbed and the beating amplitude patterns became invariant once more. This indicated that the curvature of the body remains similar whereas the movement speed and beating frequency increases under DR regimen. Similar as for the aggregation, motility was also improved with less feeding, reflecting the attenuated development of the disease.

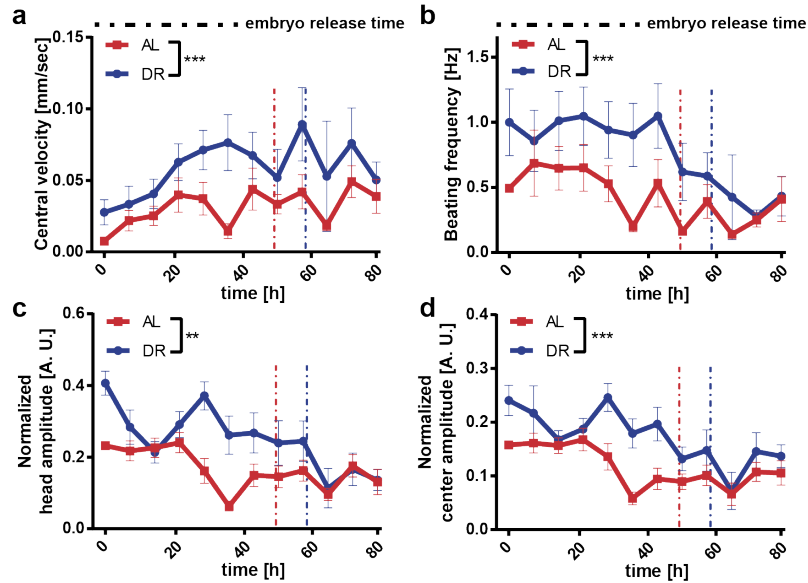


Figure 3.21 – Study of the effect of *E. coli* concentration on the motility parameters of *punc-54::Q40::YFP* mutant worms. (a-d) Comparison of four motility parameters including, central velocity, beating frequency, normalized head and center amplitude of the nematodes for two different *E. coli* concentrations. The average first embryo release time was also plotted as a vertical dashed line to indicate the transition from the larval stages to adult stage. Data are expressed as mean \pm SEM, ** $p \leq 0.01$, *** $p \leq 0.001$. All measurements are based on $N = 18$ to 20 worms.

3.5.3 Clustergram analysis

We again decided to look at clustergram plots in time to spot the variance of motility, development and aggregate parameters for the two feeding conditions. The AL feeding concentration was used as the control source and DR results were normalized accordingly, hence only normalized DR results were displayed. At 21 hours (Figure 3.22a), there were not yet enough features to distinguish the worms under two different *E. coli* concentrations. The first distinguishable features were seen at 35 hours (Figure 3.22b), when HD worms under DR feeding have greater mechanical power, central velocity, beating frequency, bending force and fewer aggregates compared to the AL condition. At 43 hours (Figure 3.22c), the DR worms demonstrated an increase in all motility parameters, which could be considered as an improvement in the disease attenuation. Central velocity, beating frequency and aggregate clusters were most distinctive among the worms under DR at 65 hours (Figure 3.22d). Additional development

in Figure 3.23.

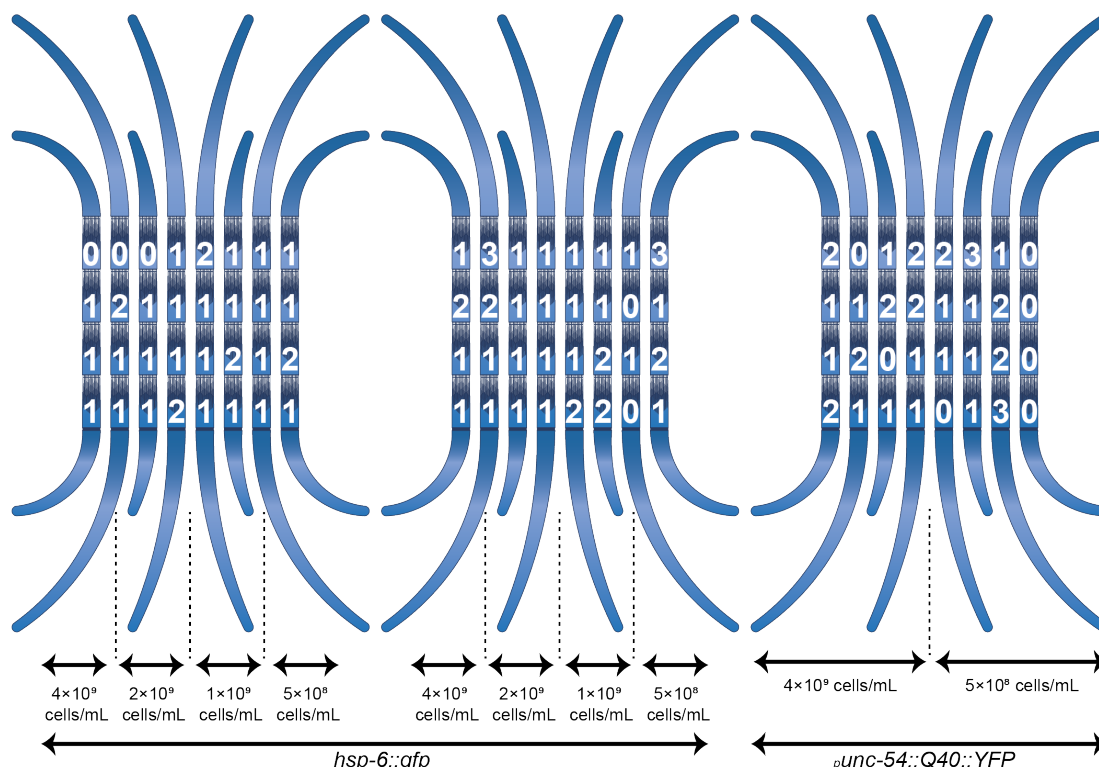


Figure 3.23 – Schematic representation of an experimental configuration, as defined by the number of worms distributed over the different chambers and the applied feeding conditions. For *hsp-6::gfp* nematode experiments, 4×10^9 cells/mL, 2×10^9 cells/mL, 1×10^9 cells/mL, and 5×10^8 cells/mL were required; therefore two lanes were selected per feeding condition. These experimental conditions were repeated on a second identical chip in order to obtain significance in worm phenotyping. For *punc-54::Q40::YFP* nematode experiments, 4×10^9 cells/mL and 5×10^8 cells/mL were required; therefore four lanes were used per feeding condition. A single chip was capable of significant worm phenotyping.

3.7 3D microfluidic channel fabrication for accurate worm immobilization

We attempted to improve confinement accuracy by optimizing the channel geometry for future studies. Therefore, we developed a novel idea for a more accurate *C. elegans* immobilization. We benefited from aspect ratio dependent etching (ARDE) method, utilizing the Bosch dry etching process of silicon. We worked on creating the optimal silicon master microstructures for replication of PDMS microchannels that allow immobilizing *C. elegans* worms at all sizes during their full life cycle.

We came up with a novel microfabrication process to fabricate so-called 3D microchannels without using gray-scale lithography. A positive photoresist layer was spun on a Si wafer,

exposed and developed (Figure 3.24). Hereafter, we utilized the Bosch process, which enables the wider parts of the channels to be etched deeper than the narrower parts. To benefit from ARDE, we had to etch deeper than our target depth. The excessive etching depth was subsequently removed by front-side surface grinding.

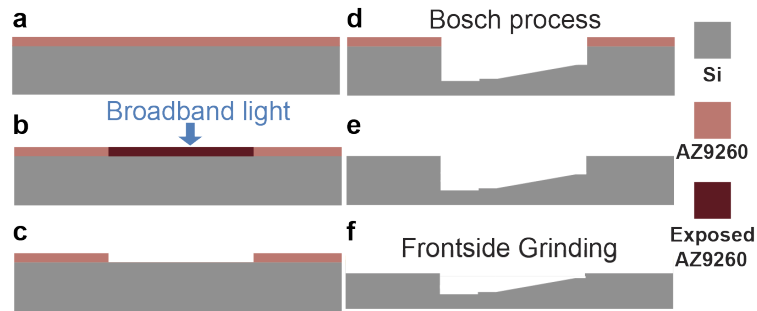


Figure 3.24 – Schematic diagram for microfabrication of variable-height three-dimensional confinement channel master structures in silicon. (a) A Si wafer is spin-coated with positive photoresist. (b) The layout is exposed through a Cr mask. (c) The exposed design is developed. (d) The patterned photoresist and the Si wafer are inserted in a dry etchant tool to initiate the Bosch process and hence, the ARDE. (e) The positive photoresist is stripped to provide surface profiling with Scanning Electron Microscopy (SEM). (f) Once the desired surface profile is reached, the excessive Si depth is removed by front-side grinding of the wafer.

We have characterized the effect of three different etching times on the etching profile of our channels (Figure 3.25). The results indicated that we were obliged to remove approximately 100 μm of Si from the front side of our wafers via grinding. The final surface scan demonstrated that we can achieve our desired profile by utilizing the ARDE of the Bosch process. The final version of our wafer includes 80 μm -wide growth chambers that are large enough to let the worms and larvae freely move and tapered channel profiles, starting from 60 μm in height and narrowing down to 10 μm height, to successfully confine nematodes at all larval stages. In order to invert our design, the silicon etching step is followed by PDMS casting to establish the pattern of our Si wafer to PDMS chips.

We successfully managed to reach our desired surface profile within 35 minutes of Bosch process etching. However, further optimization in the microfabrication process is required to integrate the single worm culture-enabling features.

3.8 Discussion and conclusion

Here we described a new microfluidic platform for multiplexed high-content phenotyping studies in a fully automated way. To the best of our knowledge, no other platform provided such automated phenotyping over the worm life cycle. Different microfluidic chambers were independently configured for different conditions, which allowed to study multiple cases side-by-side. The platform's high-resolution imaging capacity furthermore enabled to accurately extract 19 phenotyping results almost in real time. We optimized the experimental

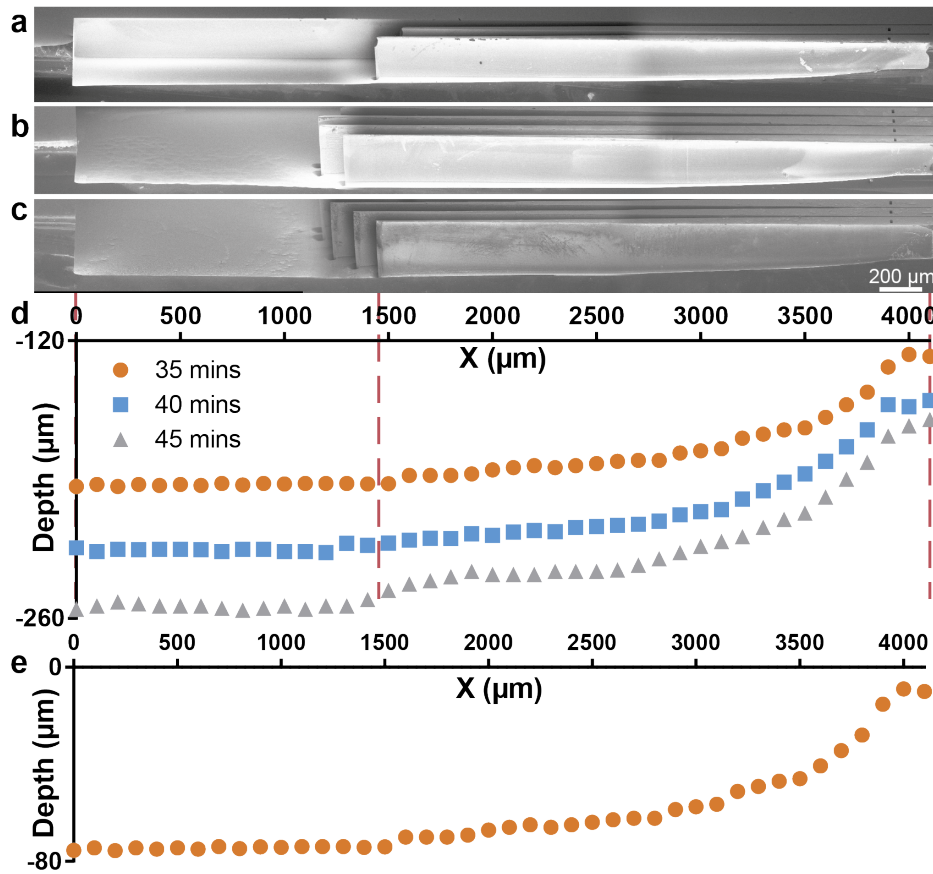


Figure 3.25 – SEM images of the confinement channels and the resultant surface profile of the etched Si wafers. The resultant SEM stitched images obtained after (a) 35 min, (b) 40 min and (c) 45 min etching are shown. (d) The initial depth profile of three different etching times illustrates that the etching depth is deeper than it is required. (e) The excessive Si depth is removed by utilizing front-side grinding and hence the final surface profile is reached.

conditions such that worms could be kept for more than 120 hours on a chip without any bacterial clogging. The initial silanization process and the parallel integration of multiple filter channels were key to the well-controlled bacterial concentrations in the microfluidic chip. This feature enabled the culture and phenotyping of the worm population during the entire larval development and several days after the adult stage – more particularly up to around three days of the adult stage – without any problem and any human intervention. As an average over all experiments, we observed a 30% confinement rate. Thanks to the adequate bacterial supply, we did not observe any stress-related phenotypes such as larval death, bagging or arrest among animals. Additionally, we did not notice any L1 injury during initial L1 distribution and all the nematodes completed their life cycle. We retained all animals from the beginning of the experiment till the end. We had an average of 88% occupancy rate of chambers in all experiments; with 71%, 24%, and 5% of the chambers occupied by a single worm, two and three worms, respectively. The high microfluidic flow rates and injection

Chapter 3. Automated high-content phenotyping over the life cycle of the nematode *Caenorhabditis elegans*

volumes during the adult stage confinement enabled us moreover to easily wash off late L1 progeny at 100% efficiency and thereby allowed to keep track of the identity of the same worm from the very beginning.

A significant advantage of our platform is that it does not include any active on-chip components. We avoided also complex micro-fabrication steps to provide a reliable and easy-to-operate microfluidic chip. Instead of using alternative immobilization approaches that required, on-chip valves or chemical treatment, we integrated tapered confinement channels for the temporary and reversible immobilization of the worms. Unlike previously proposed microfluidic platforms with integrated tapered channels, we optimized channel size such that we could confine all larval stages in a single channel geometry.

Furthermore, our platform allowed to reduce the need of user interaction with very limited requirements for experimental setup. Once the user initiated the experiment with semi-automated commands, there was no longer need of any communication with the only exception of bacteria refilling if needed. The semi-automated experimental pipeline also diminished external operator-based variations in the experiments and increased the reproducibility. Also, we built an integrated, automated and fast image and video analysis tool. We extracted up to twelve swimming gait properties, three development properties, two fertility parameters and up to four fluorescent phenotypes of the worms. We could combine all the phenotypic data obtained from bright-field and fluorescent image acquisition and video recording to create clustergrams to provide in-depth analysis at each time point of worm development. Thanks to the clustergrams, we were able to isolate the most or least dominant parameters of different feeding conditions.

In order to validate our platform and its applicability to biomedical research, we studied the effect of an environmental challenge (*i.e.*, food concentration) on the development of a complex neurodegenerative disease. For this purpose, we employed a *C. elegans* model of HD, which is shown to mimic the disease progression in humans [85]. By combining the possibility to accurately control the food concentration in our system and to perform high-content analysis, we monitored the change in growth, reproduction, protein aggregation, motility and disease progression by feeding the worms with four different concentrations of *E. coli*. As previously reported, DR increased worm motility, and retarded growth and fertility. In addition, DR delayed the onset and progression of protein aggregation disease in a HD worm model that we used, highlighting the potential utility of dietary interventions in the setting of proteotoxic neurodegenerative diseases.

We provided an integrated, automated, multiplexed, long-term culturing platform with automated image and video analysis tools for the collection, extraction, and analysis of phenotypic data. Our platform hence allowed high throughput and high-content phenotypic analysis of *C. elegans* strains. We expect that such a platform, will stimulate the use of *C. elegans* as a model organism for longitudinal and dynamic studies, starting from the early larval stages onwards.

4 Automated phenotyping of *C. elegans* embryos with a high-throughput-screening microfluidic platform

The nematode *C. elegans* has been extensively used as a model multicellular organism to study the influence of osmotic stress conditions and toxicity of chemical compounds on developmental and motility-associated phenotypes. However, still the several days long culture time of nematodes needed for such studies has directed researchers to explore alternatives. *C. elegans* embryos in particular, due to their shorter development time and immobile nature, could be exploited for this purpose, although classically their harvesting and handling is tedious. Here, we present a multiplexed, high-throughput and automated embryo phenotyping microfluidic approach to observe *C. elegans* embryogenesis under application of different chemical compounds. After performing experiments with up to 800-embryo per chip and up to 12 hours of time-lapse imaging per embryo, the individual phenotypic development data are collected and analyzed through machine learning and image processing approaches. Our proof-of-concept platform indicates developmental lag and induction of mitochondrial stress in embryos exposed to high doses (200 mM) of glucose and NaCl, while small doses of sucrose and glucose accelerate development. Overall, our new technique has potential for large-scale developmental biology studies and opens new avenues for very rapid high-throughput and high-content screening using *C. elegans* embryos.

This chapter is an adapted version of the following publications:

- **H. B. Atakan**, M. Cornaglia, T. Alkanat, R. Trouillon and M. A. M. Gijs, “Automated on-chip phenotyping of *Caenorhabditis elegans* embryos: a developmental study as function of exposure to various compounds”, in *22nd International Conference on Miniaturized Systems for Chemistry and Life Sciences*, pp. 119-121, 2018.
- **H. B. Atakan**, T. Alkanat, M. Cornaglia, R. Trouillon and M. A. M. Gijs, “Automated phenotyping of *C. elegans* embryos with a high-throughput-screening microfluidic platform”, *Microsystems & Nanoengineering*, under review, 2019.

4.1 Introduction

Survival in osmotic conditions and the ability to repair osmotic stress-induced damage is crucial for the long-term maintenance of cellular life [86]. *C. elegans* has since long emerged as a suitable model organism for osmo-sensing studies [87]. These nematodes bring several advantages for an in-depth understanding of the mechanisms behind animal cell adjustment to osmotic conditions. It has been previously demonstrated that high levels of osmotic changes in the environment induce the formation of mitochondrial reactive oxygen species (ROS) [88] and an accumulation of osmolytes such as glycerol in *C. elegans* [89]. Additionally, hypertonic or hyperosmotic conditions cause loss of water, which triggers an intracellular ionic imbalance and hence protein aggregation [90]. Therefore, an insight into the molecular mechanisms of osmotic damage on *C. elegans* may be paramount to unravel complex human diseases too [91, 92].

Previous studies mostly focused on the influence of high chemical compound concentrations on the lifespan of *C. elegans* [93]. It has been claimed that glucose restriction extends the lifespan of *C. elegans*, while glucose levels of 2% in the nematode growth medium can significantly reduce it. The same tendency was observed for high doses of glycerol [94]. Lifespan reduction can also be induced by high molarities of NaCl [95], but can be recovered with the addition of sterilizing compounds such as 5-fluorodeoxyuridine (FUdR). Osmotic effects can also be created with sucrose, a molecule composed of two monosaccharides, glucose and fructose. On top of the osmotic influence of NaCl and sucrose, there might be additional toxic effects that cause lifespan reduction [96]. For instance, treatment with sorbitol – an acyclic polyol used as an osmotic stabilizer – can induce an adaptive osmotic response to compensate for the lifespan reduction. Hypertonic conditions provided by NaCl, sucrose and glucose can also reduce the survival rate of the nematodes in time and significantly alter the body size and shape [97, 98]. Additionally, the deleterious effects of NaCl are stronger than sucrose at the same molarity [99]. More phenotypic results also revealed that high doses of glucose severely affect the motility of the nematodes [100].

A wealth of designs and applications for *C. elegans* investigations, at the larval or adult stages, has been proposed utilizing microfluidic platforms. However, these technologies have been rarely utilized for embryo studies so far [1], despite advantages such as the fast embryo development time and their relatively immobile nature. It is well established that early life stage events can have a large impact on the nematode development and lifespan [101]. Interestingly, nematode morphologies in later life can also be predicted from early-embryo stage variations [102]. Hence, it is worth investigating if *C. elegans* embryos could be potentially exploited to perform toxicity or osmosensation studies.

Traditionally, embryo developmental imaging studies were conducted by mounting embryos on agar pads, which is highly laborious [103] and lacks a constant chemical aspiration system. Recent microfluidic developments facilitate the handling of *C. elegans* embryos. A microfluidic platform with microwells was used to host and observe early embryos obtained by dissecting adults [104]. An initial fluidic design for handling *Drosophila melanogaster* embryos [105] was later adapted and used for *C. elegans* embryos too, in particular an automated microfluidic

4.2. Automated microfluidic phenotyping platform design and operation for *C. elegans* embryos

platform with embryo incubators was created to observe embryogenesis of various strains [106]. Other researchers worked on drug delivery to embryos obtained from fertile nematodes [57], while observation of the first cellular division after mechanically compressing adult nematodes for embryo release was demonstrated [107]. Yet, all these platforms accommodated only a few embryos, worked under a single condition and lacked automated phenotyping of embryonic phenotypes.

In this work, we present a high-throughput multiplexed microfluidic platform for automated phenotyping of *C. elegans* embryos during their full development. We used wild-type and mitochondrial unfolded protein response reporter *hsp-6::gfp* embryos to evaluate the stress response. *C. elegans* embryos were obtained through a classical bleaching procedure of gravid adult animals for rapid and massive embryo extraction. The developmental influence of embryo exposure to various osmotic compounds was studied on-chip. Our automated phenotyping script that utilizes deep learning and image processing, displayed accurate results in a relatively short time, most of the time matching the results obtained by a human operator. We believe that this is the first report of a massive embryo handling protocol, combining high-throughput and multiplexed observations with automated phenotyping. The severe developmental lag and lethality of high molarities of glucose and NaCl on embryos was observed, in agreement with prior works on adult worms. Overall, our phenotypic embryo development results indicate that *C. elegans* embryos can represent an alternative to the use of adult worms, leading to comparable experimental conclusions in even shorter time periods.

4.2 Automated microfluidic phenotyping platform design and operation for *C. elegans* embryos

4.2.1 Microfluidic chip design

Our design and technology empowers massive amount of *C. elegans* embryo observation at high-resolution and permits highly-parallel studies. The semi-automated fluidic pipeline also allows dramatically diminishing the external operator influence on the experiments. Our device is solely based on passive hydrodynamics without integration of any active on-chip components, resulting in a robust and user-friendly device. The design consists of eight side-by-side microfluidic lanes to impose up to eight different conditions on embryos in parallel (Figure 4.1a). Each lane has a media inlet, that is connected to either an S-medium or waste reservoir, and a media outlet, that is connected to either an embryo suspension or chemical solution. During initial microfluidic chip filling and degassing, S-medium was dispensed from the media inlet towards media outlet, by means of a syringe pump. Otherwise, media outlets were used to draw either embryo suspension or chemical solution towards the media inlet, which was linked to a media reservoir. We based our design of embryo incubators on a previously proposed platform [106], which we configured with slightly larger – 10 μm – embryo incubator gates (Figure 4.1b). This was found to reduce the clogging due to worm debris generated by the bleaching procedure and hence increased the probability of

Chapter 4. Automated phenotyping of *C. elegans* embryos with a high-throughput-screening microfluidic platform

filling the embryo incubator correctly with a *C. elegans* embryo. All worm culture chambers and other redundant components from the previous design were removed to create a rapid embryogenesis observation platform. Each microfluidic lane consists of 100 concatenated embryo incubators such that up to 100 embryos can be observed under a single condition (Figure 4.1c). We used standard PDMS fabrication processes to create our microfluidic chips. A PDMS part (~35 mm × 50 mm in size) containing the microfluidic channel design is plasma-sealed on a standard 38 mm × 75 mm glass microscope slide (Figure 4.1d). Throughout our studies, we recorded images of 6 embryo incubators at once to save data space (Figure 4.1e). Unlike previous 63× oil immersion bright-field [108, 109] or differential interference contrast (DIC) imaging [110, 111] of *C. elegans* embryos, we found that 20× bright-field imaging is sufficient for our case studies. In order to further decrease the automated phenotyping time, we cropped 70 μm × 70 μm image patches around the embryo incubators and ran our image processing algorithm on these patches.

4.2.2 Automated fluidic protocol

After the initialization of the experiment, 150 μL of the embryo suspension – corresponding to ~800 embryos – are aspirated from the media outlet towards the media inlet with a flow rate of 625 nL/s (Figure 4.1). This step lasts normally around 2 minutes and it can be extended to ensure that at least 90% of all the embryo incubators in a microfluidic lane are occupied. Later, the embryo suspension reservoir is exchanged with the 600 μL chemical solution reservoir and the chemical of interest is aspirated from the media outlet towards the media inlet with a flow rate of 156 nL/s. After focus readjustment, a gentle flow velocity of 42 nL/s from the media outlet towards the media inlet is left for 12 hours to confirm the embryo stability inside embryo incubators. Hatched embryos and washed-off chemicals are collected in the waste reservoir. During this gentle flow, time-lapse images of every 6 embryo incubators are recorded every 5 minutes for only bright-field imaging studies and every 10 minutes for dual bright-field-fluorescent imaging studies.

4.2.3 Platform working principle

We designed a robust and repeatable experimental protocol to rapidly load *C. elegans* embryos in the incubators and initiate developmental monitoring. We aimed at reducing the operator's influence on the experiment to a minimum level, therefore identical serial port commands for the syringe pump were used during initialization of each experiment to set the same flow rates and injection amounts.

Through the experimental initialization protocol, the main steps are the embryo and chemical loadings. Eppendorf reservoirs, containing a dense population of *C. elegans* embryos suspended in filtered S-medium, were plugged to the media outlets (Figure 4.2a). We started loading embryos after the initial microfluidic chip filling and degassing steps. By passive fluidic dynamics, each embryo found its way to one of the embryo incubators. The liquid velocity profile and pressure distribution along embryo incubators were simulated to ob-

4.2. Automated microfluidic phenotyping platform design and operation for *C. elegans* embryos

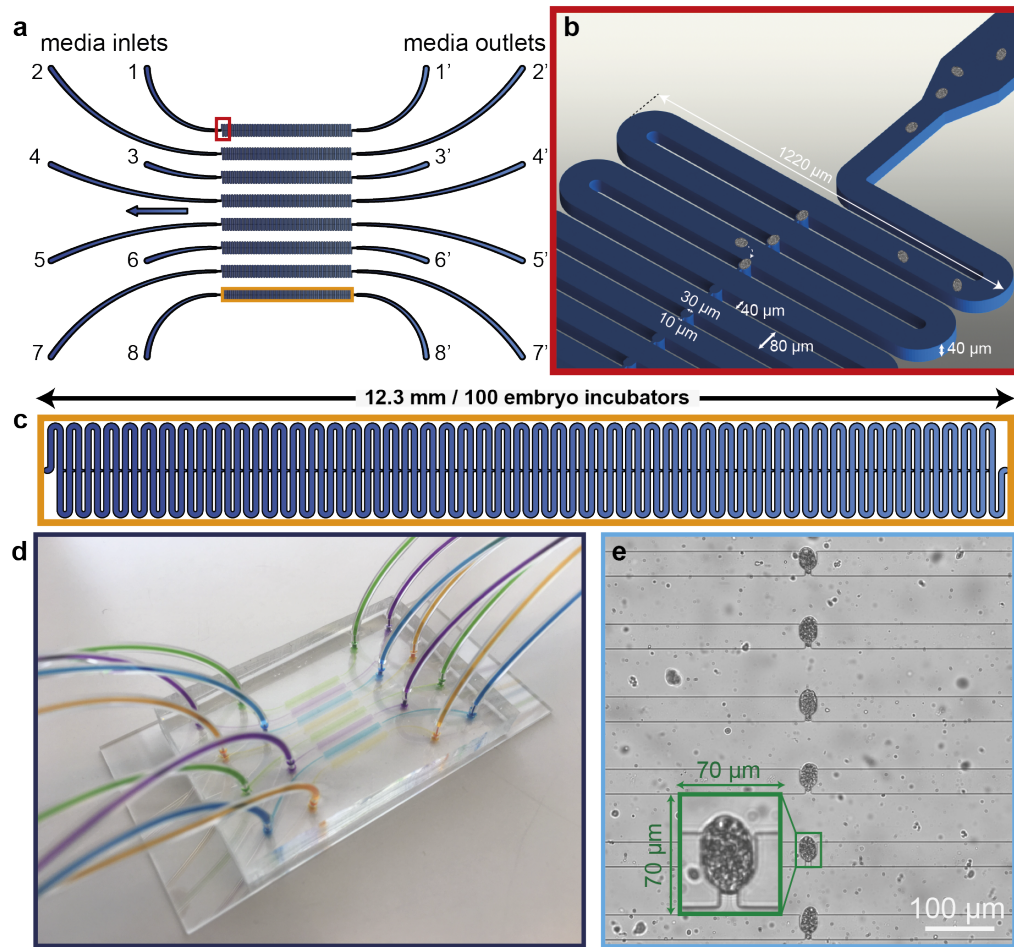


Figure 4.1 – Details of the high-throughput microfluidic platform for automated phenotyping of *C. elegans* embryos. (a) Schematic representation of the microfluidic chip with eight multiplexed lanes having one end connected to the media inlet and the other to the outlet. (b) Zoom on the entrance of a microfluidic lane with feature sizes marked. (c) Focus on a single lane that consists of 100 embryo incubators within 12.3 mm. (d) A picture of the PDMS chip (35 mm \times 50 mm) filled with dye solutions and bonded on a standard glass microscope slide (38 mm \times 75 mm). (e) An image of 6 embryo incubators visualized during time-lapse imaging; a single incubator containing an embryo (in green) is displayed and utilized in the automated script for phenotyping.

serve the influence of hydrodynamics on the incubator filling (Figure 4.3a, b). Embryos were transported by the high flow rates in the serpentine channel, enabling gradual filling of all embryo incubators. From time to time, debris resulting from the bleaching step occupied some embryo incubators but the high number of incubators per lane compensates for this loss. If the embryo suspensions were residue-free, up to 100 incubators could be filled in less than 2 minutes in each microfluidic lane. Following the embryo loading, the embryo suspension reservoirs were replaced with chemical solution reservoirs (Figure 4.2b). These solutions contained the chemical compound of interest at a certain concentration. The mi-

Chapter 4. Automated phenotyping of *C. elegans* embryos with a high-throughput-screening microfluidic platform

crofluidic lanes were fully filled with the solution in a microfluidic lane-alternating manner, as presented in Figure 4.2b, c. We divided the total chemical injection amount into 15 cycles. After completing the first chemical loading cycle for one microfluidic lane, the injection in the neighboring lane was started. Once the first cycle for all eight lanes was completed, the next cycle started with the chemical injection in the initial microfluidic lane. The idea was to synchronize the chemical exposure time of different embryos in parallel microfluidic lanes. In between embryo and chemical loading steps, the focal planes were adjusted (~5 minutes) as the reservoir plug in - plug out steps caused a focal plane shift (idle time in Figure 4.2c).

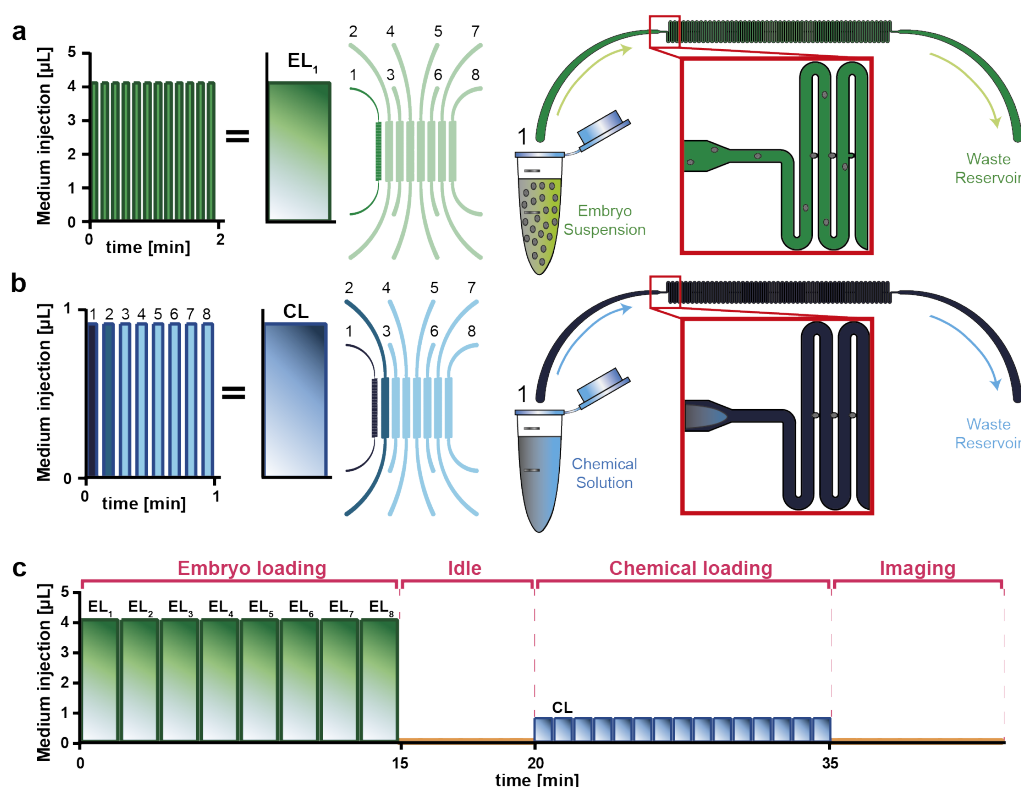


Figure 4.2 – Operation modes of the microfluidic chip. (a) In a basic embryo loading step, a 150 µL embryo suspension in S-medium was injected from the media outlet towards the media inlet during 2 minutes per each microfluidic lane, thereby filling almost all embryo incubators in that lane with *C. elegans* embryos. (b) In a basic chemical loading step, all microfluidic lanes were filled with chemical solution of interest using again a flow directed from the media outlet towards the inlet, during one minute for the 8 microfluidic lanes. (c) The overall experimental protocol contained a period of basic embryo loading steps of approximately 15 minutes to fill 800 embryo incubators with embryos, a step of 5 minutes idle time for focus re-adjustments, a period of basic chemical loading steps of around 15 minutes for chemical solution loading and finally, 12 hours of imaging.

Under ideal conditions, we could fill up to 800 embryo incubators in 15 minutes (see an example of the device during an experiment in Figure 4.4). The total experimental preparation time can be reduced to ~35 minutes. Our easy-to-use and semi-automated platform can

4.3. Automated detections of embryo state and embryogenesis stage transitions

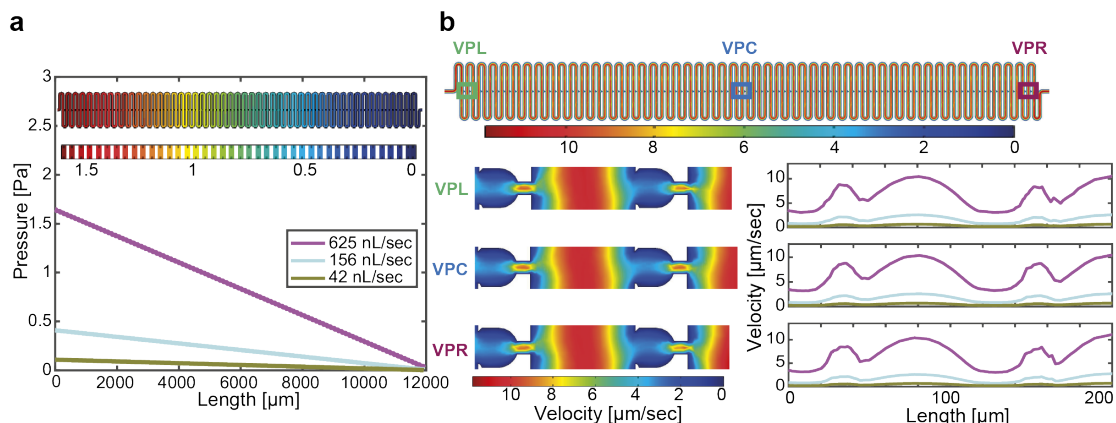


Figure 4.3 – Pressure and particle velocity simulations along all the embryo incubators in a microfluidic lane. (a) Pressure distribution profile along a microfluidic lane at three main flow rates used in the experiment (42, 156, 625 nL/s). The fluidic pressure is adequate to keep embryos in their incubators. (b) Liquid velocity profile at the closest point to the media outlet (VPL), center point of the microfluidic lane (VPC), and at the closest point to the media inlet (VPR) at the three main flow rates used in the experiment.

therefore set up a large number of *C. elegans* embryos for development studies in an extremely short time. Our fluidic protocol was finalized by leaving a gentle 42 nL/s flow to maintain embryos in the incubators for 12 hours of time-lapse imaging. Such a flow was required to retain embryos inside incubators.

4.3 Automated detections of embryo state and embryogenesis stage transitions

The nematode *C. elegans* has been a well-established model organism in terms of rapid data extraction through automated phenotyping studies [46]. Previously, various tracking methods were applied to the nematodes to provide high-content phenotypic data [47, 48, 112]. However, very few automated phenotyping methods have been proposed for *C. elegans* embryos. An embryo phenotyping approach that automatically locates and segments cells and nuclei from video recordings was presented [113]. Alternatively, cell shape analysis was also conducted using image processing with cell membrane segmentation [114]. Another approach showed the possibility of automated cell lineage tracing [115]. During *C. elegans* embryogenesis, cell movement, division and death were automatically detected. However, no platform so far provided (i) an assessment on the physiological state (alive or dead) of the embryo and, (ii) a detection of the embryogenesis stage in a systematic and fully automated manner at high-throughput.

We developed an automated embryo stage detection and a fluorescent signal quantification algorithm for rapid, high-content phenotyping of *C. elegans* embryos. We processed bright-field and fluorescent images that we acquired during 12 hours time-lapse imaging – with 5-minute

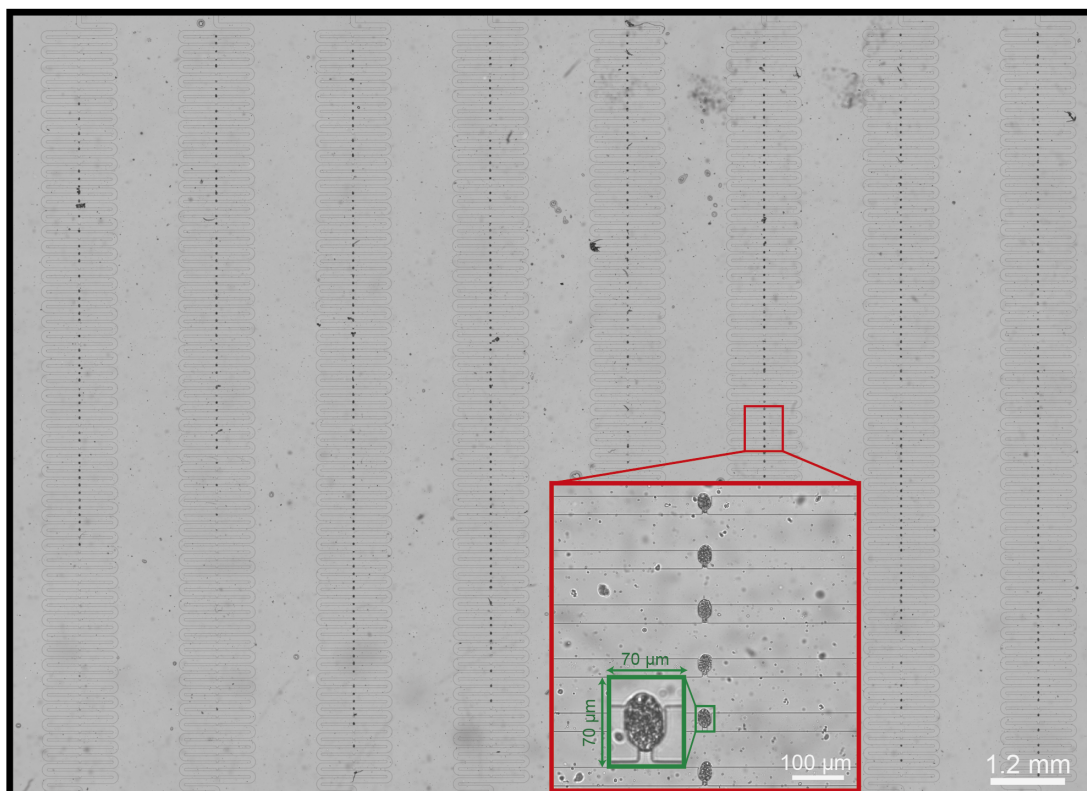


Figure 4.4 – Stitched image covering 8 microfluidic lanes each of which having 100 embryo incubators. Real-time images containing six embryo incubators (in red) are collected during time-lapse imaging and 70 μm by 70 μm image patches, centered around each individual embryo incubator (in green) are provided to the automated phenotyping script for feature extraction.

intervals for embryogenesis and 10-minute intervals for mitochondrial stress expression studies. The automated embryo development analysis algorithm consisted of three main parts, namely, i) detection of the locations of the different embryo incubators, ii) analysis of the embryo states, and iii) detection of the stage transitions during embryogenesis.

4.3.1 Automatic location of embryo incubators

Detection of the embryo incubator locations took place once for each relevant position of our motorized microscope stage, whereby each physical position provided an image of a unique set of incubators in the microfluidic chip. By selecting a single image from each position, our algorithm relied on classical methods of computer vision to get the spatial location of incubators. To achieve this, we chose a sample bright-field image from the image stack (Figure 4.5a), and we utilized Canny edge detector [116] due to its ability to merge weak edges with strong edges in their vicinity leading to more robust extraction of edge information (Figure 4.5b). After edge detection, we applied a morphological closing operation on the

4.3. Automated detections of embryo state and embryogenesis stage transitions

resulting edge map to reveal all incubator boundaries without disruptions (Figure 4.5c). Next, to find the y-coordinate corresponding to a horizontal boundary, we summed all pixels in a row of Figure 4.5c. The resulting one-dimensional set of line-averaged pixel values allowed to allocate the horizontal PDMS boundaries (two for each incubator). For each incubator, the lower PDMS boundary was selected (red line). A similar procedure was followed for finding the x-coordinate corresponding to the embryo incubators (green line). After revealing x- and y-coordinates of each embryo incubator for each position of our motorized stage, we cropped image patches of $70\ \mu\text{m} \times 70\ \mu\text{m}$ (corresponding to 200×200 pixels) around each embryo incubator to be used for subsequent stages of our algorithm (Figure 4.5d).

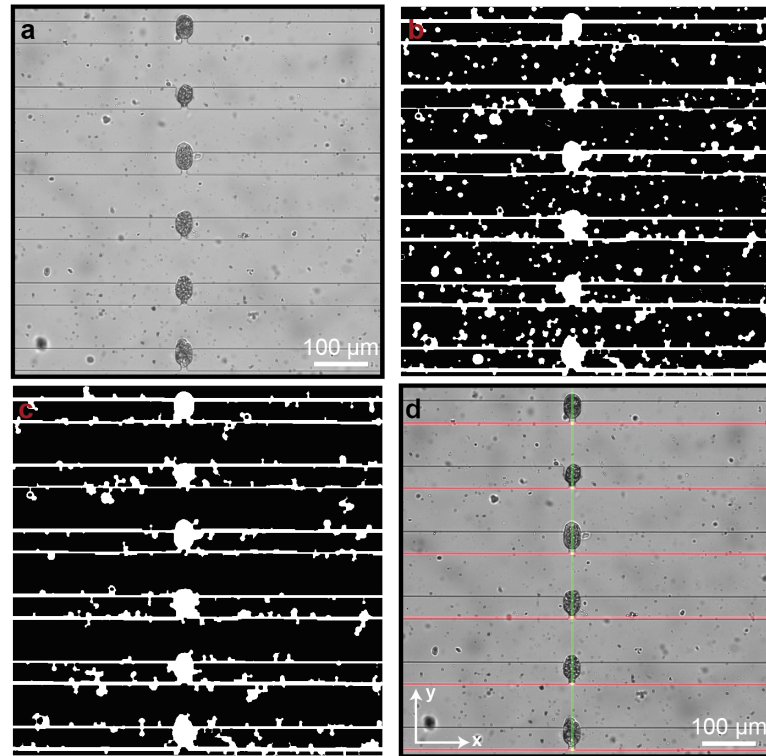


Figure 4.5 – Details of the automated detection of the position of the embryo incubators. (a) A sample real-time bright-field image during time-lapse imaging was utilized. (b) Canny edge detector was run to reveal the edge map. (c) After edge detection, we revealed all incubator boundaries without disruptions. (d) For each incubator, the lower PDMS boundary (red line) and the corresponding x-coordinate (green line) were selected. Image patches of $70\ \mu\text{m} \times 70\ \mu\text{m}$ (corresponding to 200×200 pixels) around each embryo incubator were cropped to be used for the following parts of our algorithm.

4.3.2 Automated detection of embryo states and embryo stage transitions

After preliminary observations of embryogenesis, we established a classification of different embryo development steps. *C. elegans* embryos pass through several embryogenesis stages

and we focused on detecting some of the most significant ones, namely the bean, twitching and hatching stages [106]. During the experiments, some embryos were dead, some embryos had visually unclear bean phases (already passed the bean stage or due to embryo orientation in the incubator), some embryos did not hatch within 12 hours and some embryos developed normally and had a clear appearance of bean, twitching and hatching stages. Additionally, some embryo incubators were empty during the course of the experiments because of debris accumulation or low embryo concentration in the suspension. The above-mentioned states were named as, “Dead”, “Unclear Stage”, “Late Hatching”, “Normal” and “Empty Embryo Incubator”, respectively. Our goal was just to classify experimental image patches in these different categories.

We employed a combination of convolutional neural network (CNN) and standard image processing techniques to detect the above-mentioned three embryogenesis stage transitions and the five embryo or incubator states. We made use of features extracted using CNN, which was based on the well-established AlexNet [117] architecture (Figure 4.6a) along with mean temporal difference information on the image patches.

AlexNet is one of the most well-known CNN architectures. First, a sample image is resized to $224 \times 224 \times 3$ pixels (the factor 3 represents the 3 color channels). The resized image is filtered through five convolutional layers to extract features from it. Basically, a convolution layer is used to divide the input image into small tiles, on which a convolution operation is applied (multiplying the pixel intensity values of the tile with those of a small matrix window that represents a predefined feature and is slid over the tile). The tiles obtained from the input image that are used in the five subsequent convolution layers are convolved with matrix windows with different weights of the matrix elements, also known as Kernels, and having sizes of 11×11 , 5×5 , 3×3 , 3×3 and 3×3 pixels, respectively. After each convolution operation, a feature map with the most significant features that are actually present in the original image is created, such as edges, blobs, shapes, etc.. Moreover, after each convolution, a rectified linear unit (ReLU) is used to set all negative values in the feature map to zero. Then, only the largest values in the feature map are stored, also known as a Max Pooling operation, meaning that the size of the feature map is reduced by down-sampling. After the convolutional layers, three so-called fully connected layers perform a classification based on the features extracted by the former. The fully connected layers generate a probability for each of the classification options the model is trying to predict. Initially, during training of the network, known images are fed to the network and all learnable parameters of the fully connected layers are changed such that the network at the end gives the desired classification results.

We simplified the AlexNet architecture for our case study (Figure 4.6b). We used AlexNet convolutional layers, while we removed the fully connected layers. Instead, we used two fully connected layer branches: one to determine whether an incubator contains an embryo or not and another to detect if the embryo is either in the “Pre-bean” or “Bean Stage” of embryogenesis. Outputs of both branches are two-dimensional vectors, where the value of each field represents the probability of its associated status. For training of the network, we provided three types of image patches corresponding to the “Empty Embryo Incubator” (4096 images), “Pre-bean Stage” (10165 images) and “Bean Stage” (6090 images) states (Figure 4.6c).

4.3. Automated detections of embryo state and embryogenesis stage transitions

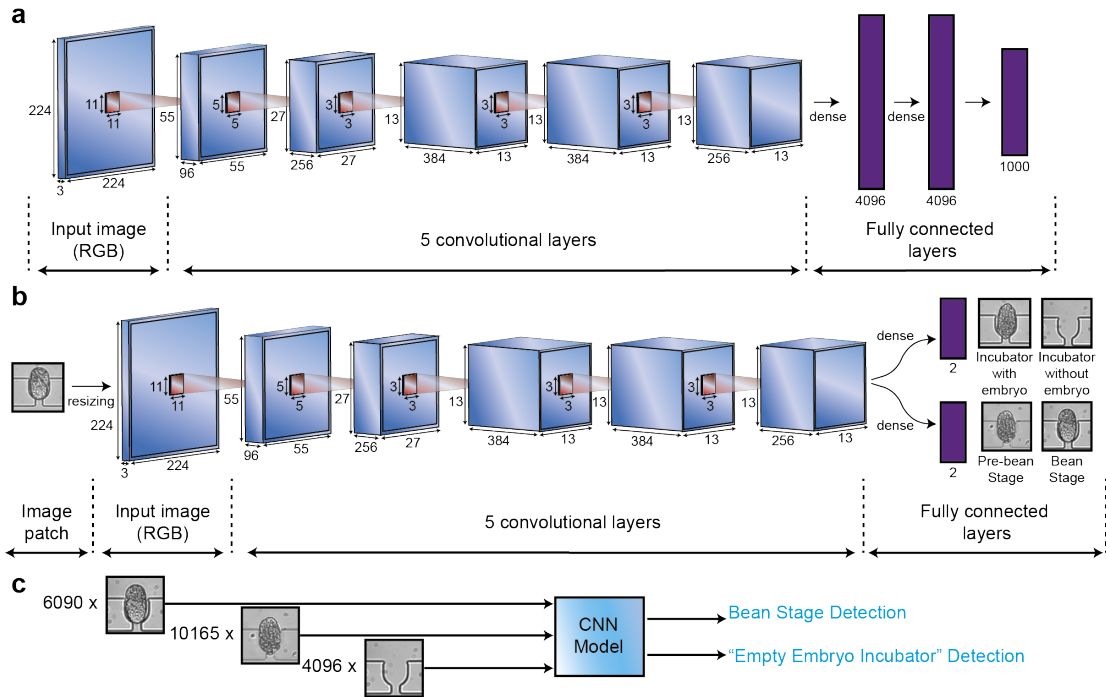


Figure 4.6 – Schematic representation of the algorithms used for the automated phenotyping of *C. elegans* embryos. (a) Original AlexNet architecture. (b) Our specific architecture used for embryo classification, based on AlexNet. (c) An initial training data set of 6090 pre-labeled embryos in the bean stage, 10165 pre-labeled embryos prior to the bean stage, and 4096 images pre-labeled as "Empty Embryo Incubator" were provided.

In parallel, we benefited from mean temporal information of pixel intensities in the image patches. The differences of the intensity values of all pixels present in two consecutive embryo image patches of a time-lapse sequence are averaged, representing the mobility function (MF) of the embryo (Figure 4.7a). The MF is median-filtered (Figure 4.7b). Only the median-filtered MF before the hatching time is considered and averaged. The time point, at which this Average function intersects with the median-filtered MF defines the start of the twitching stage (Figure 4.7c). Examining the mobility data for individual embryos, we noticed only a slightly varying mobility profile. This was caused by (i) the presence of background pixels within the incubator image patches and (ii) the similar spatial brightness appearing for embryos in the different stages (Figure 4.7d).

We illustrate our method with the block diagram of Figure 4.8. Our algorithm was engaged as follows. Initially, our CNN model was utilized to determine if the image patch contained an embryo or if it was embryo-free. If an embryo did not exist, the embryo incubator under consideration was classified as "Empty". In case it contained an embryo, the algorithm calculated the variance of the mobility function. If the latter was lower than a pre-determined threshold, this indicated that the twitching stage was not present and the embryo incubator under consideration contained a "Dead" embryo. Otherwise, a twitching stage was detected and then the embryo under consideration was a living embryo with a twitching stage (we

Chapter 4. Automated phenotyping of *C. elegans* embryos with a high-throughput-screening microfluidic platform

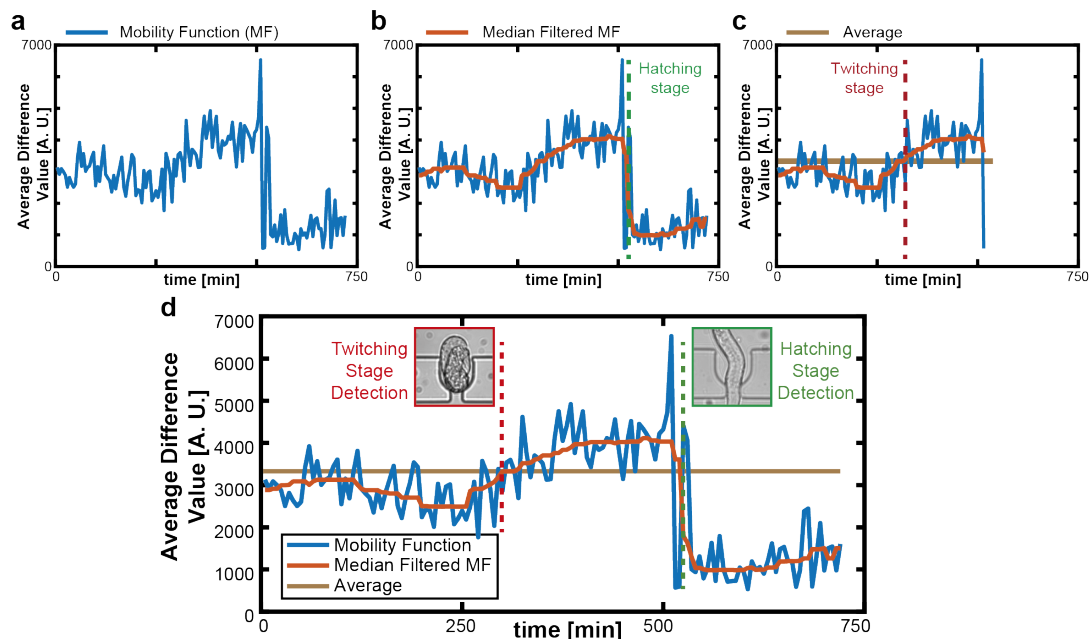


Figure 4.7 – Automatic detection of the onset of the twitching stage of an embryo using the mobility function (MF). (a) The average of the differences of all pixel-intensity values in two consecutive embryo image patches are represented as MF of the embryo. (b) The MF is median-filtered. (c) The time point, at which this Average function intersects with the cropped and median-filtered MF defines the start of the twitching stage. (d) MF, Average and Median Filtered MF are represented with the indicated twitching and hatching transition stages.

classified them in “Normal”, “Unclear Stage”, or “Late Hatching” states). The CNN model was also used to check whether a hatching stage was present. The hatching stage transition was identified by checking embryo presence and detecting the time at which the embryo was no longer present according to the trained CNN. If the hatching stage could not be recorded in the time-lapse sequence of 12 hours, the embryo state was assigned as “Late Hatching”. Lastly, we used the trained network to detect the transition from pre-bean to bean stage of the embryo, if it existed. If a clear visual transition could not be determined, then we concluded that we had an embryo with an “Unclear Stage”. Otherwise, we had a “Normal” embryo where visual cues of stage transitions were clear.

We created a reduced mobility function by cropping the median-filtered mobility data to a timeframe limited by the time of the hatching stage transition (see Figure 4.7d). Our experimental observations revealed that the transition time from the bean stage to the twitching stage could be modeled as the instance where the reduced mobility function intersected with its mean. In the case of a “Late Hatching” embryo, the twitching stage was determined by utilizing the non-cropped mobility data. We provided a few typical experimental examples of classification in Figure 4.9. From top to down (Figure 4.9a-f), the algorithm categorized the embryos as; “Empty Embryo Incubator”, “Normal”, “Late Hatching”, “Unclear Stage” “Dead” and “Dead”. The “Normal” embryo had bean, twitching and hatching stage detections at 185,

4.3. Automated detections of embryo state and embryogenesis stage transitions

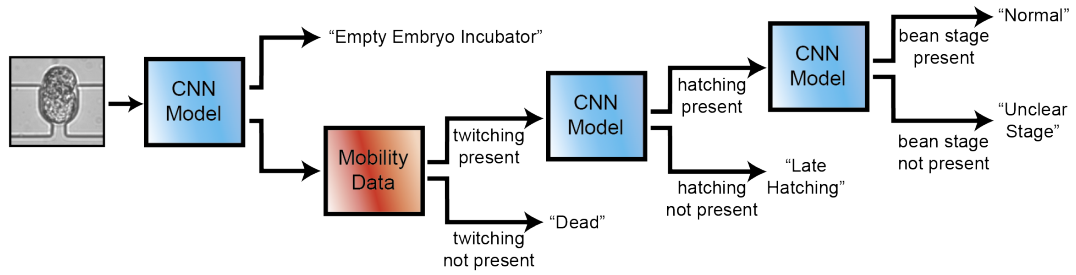


Figure 4.8 – Block diagram of the automated embryo phenotyping protocol. For detecting an “Empty Embryo Incubator”, the hatching stage transition and the bean stage transition, we used the CNN model. The mobility data was used to determine if an embryo was alive or “Dead”.

270 and 565 minutes, respectively. The “Late Hatching” embryo had twitching stage detection at 440 minutes. The “Unclear Stage” embryo had twitching and hatching stage detections at 260 and 565 minutes, respectively. We noticed that the 5th embryo incubator was classified as “Dead” even though the correct result was “Empty Embryo Incubator”. Likewise, corrected values for the bean stage of “Normal” embryo and the twitching stage of “Late Hatching” embryo were 210 and 465 minutes, respectively.

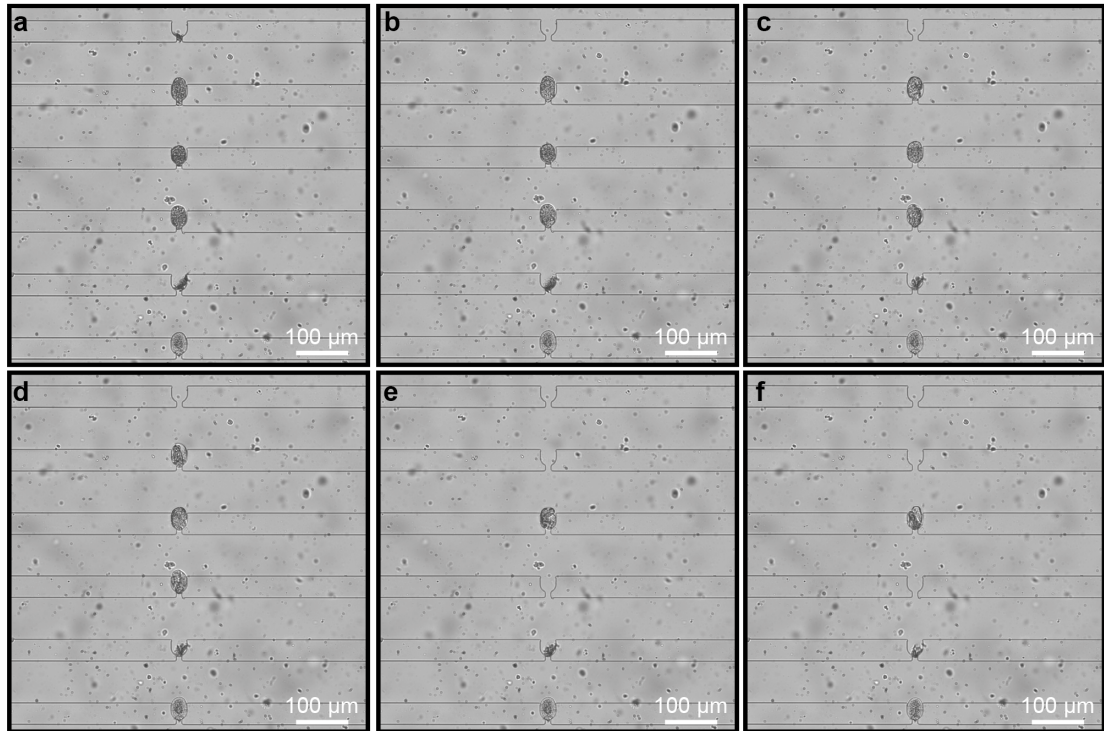


Figure 4.9 – Real-time images of six embryo incubators in a timespan of 12 hours. A real-time bright-field image in (a) the beginning, after (b) 145 minutes, (c) 290 minutes, (d) 435 minutes, (e) 580 minutes, and (f) 720 minutes of the experiment.

4.3.3 Automated fluorescent signal quantification

We followed a straightforward image processing approach to quantify the GFP expression of *hsp-6::gfp* *C. elegans* embryos. We first created a binary mask from one of the embryo-free patch images, which was extended and mapped on the fluorescent image (see Figure 4.10). This mask isolated the fluorescent signal of the embryo from the background and took into account only the pixel values originating from the embryo. After the multiplication of these two patches, the irrelevant background was excluded with the only exception of background openings on top and bottom of the embryo. However, as the total pixel number of these openings was just around 4% of the total pixel number in the unmasked part of the image patch, by simply taking the non-zero median intensity value of this image patch, we obtained a meaningful average fluorescent signal expression. Additionally, a $70\ \mu\text{m} \times 7\ \mu\text{m}$ background window was cut from the top part of an image patch (see Figure 4.10) and the average fluorescent intensity in this window was utilized to normalize the fluorescent signal intensity expression of an embryo with the Equation 4.1:

$$I_{SBR} = \frac{I_{ROI}}{I_{BG}} \quad (4.1)$$

where, I_{SBR} , I_{ROI} and I_{BG} are the normalized average embryo intensity (region of interest: ROI), the average embryo intensity expression, and the average background fluorescent intensity values, respectively.

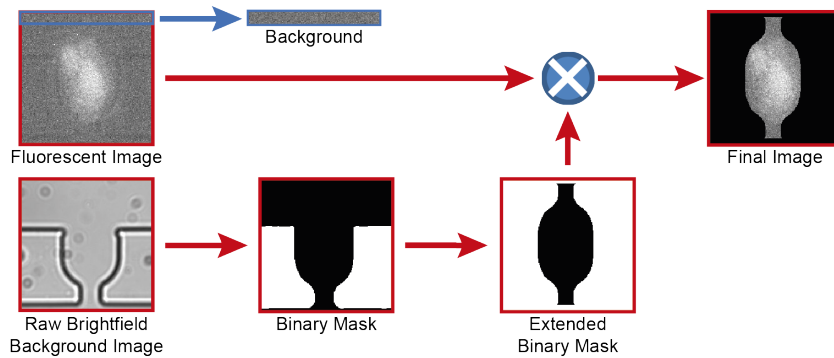


Figure 4.10 – Automated image analysis for fluorescent signal expression of *C. elegans* embryos. For the fluorescent signal analysis, a binary mask was created, extended and mapped on the fluorescent image to target only the background-free embryo. The median intensity value inside the final image was calculated to compute the embryo’s fluorescent intensity. This result was corrected using a $70\ \mu\text{m} \times 7\ \mu\text{m}$ background window cut from the top part of an image patch to take into account eventual variations in lamp intensity.

4.4 Osmotic influence on embryo development

We studied the influence of various compounds and osmotic conditions that were previously reported as significant on the lifespan, survival, life expectancy, body shape and the stress induction on *C. elegans* worms. Our goal here was to investigate if the *C. elegans* embryo could be suitable for predicting the behavior of the adult nematode. For this purpose, we exposed wild-type embryos to 200, 20, 2 mM concentrations of L-glucose, D-glucose, sucrose, glycerol, and NaCl and characterized the influence of these compounds on the embryo development and survival at room temperature with our automated script. We observed a variation in the embryo lethality rate for control conditions of different chemical studies (Table 4.1). Albeit having identical media exposure (filtered S-medium with no other chemical) across different experiments, such variations might result from the adult worm population on a plate, local *E. coli* distribution profile on a plate and hence slightly advanced or developmentally lagging worms, minor variations in the exact bleaching duration, and operator-based influences during bleaching. During the bleaching procedure, we regularly checked the embryo suspension and, if all the adult body fragments had disappeared, we centrifuged the solution. Otherwise, any remaining adult body fragments would likely clog the microfluidic lanes and incubators. We performed an off-chip characterization of the embryo suspension one day after the egg harvesting and we display the resulting data in Figure 4.11.

Immediately after the bleaching protocol, only embryos kept their integrity. The larvae seen in Figure 4.11a and Figure 4.11b hence result from the hatching of embryos, confirming the viable status of the latter after bleaching. Dead embryos are still visible as such. The variability in the embryo development can be due to indeed the hazardous effects as a consequence of the toxic bleaching procedure (Figure 4.11c). The variability in the number of L1 larvae and embryos in a 2 μ L sample was considered as an indicator of the variations in the initial gravid adult worm populations on the agar plate (Figure 4.11d). We additionally noticed a dead embryo percentage variation between 20-60% after the bleaching procedure.

D-glucose, usually referred to as glucose, is an important energy source and L-glucose is its laboratory-synthesized enantiomer. L-glucose is not biologically active and such type of compound affects the nematode differently. Previous researches covered the different impacts of these two enantiomer compounds on lifespan [94], motility [100], egg laying rate [118] and the nematode sensitivity [119].

We observed a development time increase, especially for the twitching-to-hatching duration at high molarities of L-glucose (Figure 4.12a). More specifically, at 200 mM concentration, the average bean-to-twitching interval was 48 minutes and the twitching-to-hatching interval was 40 minutes more than the control condition. This was also complemented by a 55% increase in “Dead” embryo percentage and a 36% decrease in “Normal” embryo over the alive embryo – sum of “Normal”, “Late Hatching”, “Unclear” – population (Table 4.1). This means that extreme doses of L-glucose were hazardous, as they increased both the development time and the “Dead” embryo rate, along with a reduction in the successful detection of “Normal” embryos. Interestingly, a similar development time profile was also observed for D-glucose (Figure 4.12b), with a more severe impact on the survival of the embryos. The twitching-to-

Chapter 4. Automated phenotyping of *C. elegans* embryos with a high-throughput-screening microfluidic platform

Table 4.1 – The embryo state classification obtained from the automated phenotyping script for wild-type nematodes. The fraction of “Dead” embryos over all embryos and of the “Normal” embryos over the alive embryo population results are illustrated for 200 mM, 20 mM, 2 mM and Control (0 mM) conditions of L-glucose, D-glucose, sucrose, glycerol and NaCl for wild-type *C. elegans* embryos.

Compound	Dose	Dead embryo [%]	Normal embryo over alive embryo [%]
L-glucose	200 mM	59.8	29.7
	20 mM	36.3	28.5
	2 mM	22.2	34.3
	Control	38.5	46.7
D-glucose	200 mM	56.1	20.8
	20 mM	52.7	47.9
	2 mM	37.2	56.5
	Control	48	47.2
Sucrose	200 mM	19.4	35.9
	20 mM	25.7	36.2
	2 mM	27.4	31.5
	Control	30.1	33.6
Glycerol	200 mM	37.1	37.1
	20 mM	29	30.7
	2 mM	44.9	32.6
	Control	36.5	23.5
NaCl	200 mM	42.8	22.3
	20 mM	32.6	38.7
	2 mM	29.3	34.9
	Control	18.5	43.3

hatching development interval was elevated by 60 minutes compared to the control at 200 mM concentration. 17% and 10% increase of “Dead” embryo rate was also noticed for 200 and 20 mM concentrations, respectively (Table 4.1). We also observed a severe drop (~55%) in “Normal”-classified embryo rate only for the highest concentration of glucose. Embryos treated with 200 mM D-glucose concentration created a problem for the bean stage detection due to the embryo deformation at this dose. L-glucose cannot be used by living organisms as a source of energy, though showed a similar trend to D-glucose. The effect of these enantiomers on embryos was therefore expected to be mostly osmotic rather than arising from specific biochemical mechanisms. However, the 47.9% and 56.5% rate of “Normal” embryos at 20 and 2 mM D-glucose concentrations, respectively, may indicate a limited role at these concentrations, with the toxicity being more prevalent at more extreme doses.

Sucrose, a molecule composed of glucose and fructose, was utilized to create hypertonic conditions for *C. elegans*. Former studies demonstrated a decaying trend in nematode survival by a rise in the osmotic stress created by an increment in sucrose dose [97, 99]. We found parallel results of sucrose dose influence on *C. elegans* embryos compared to the adult nematode. We

4.4. Osmotic influence on embryo development

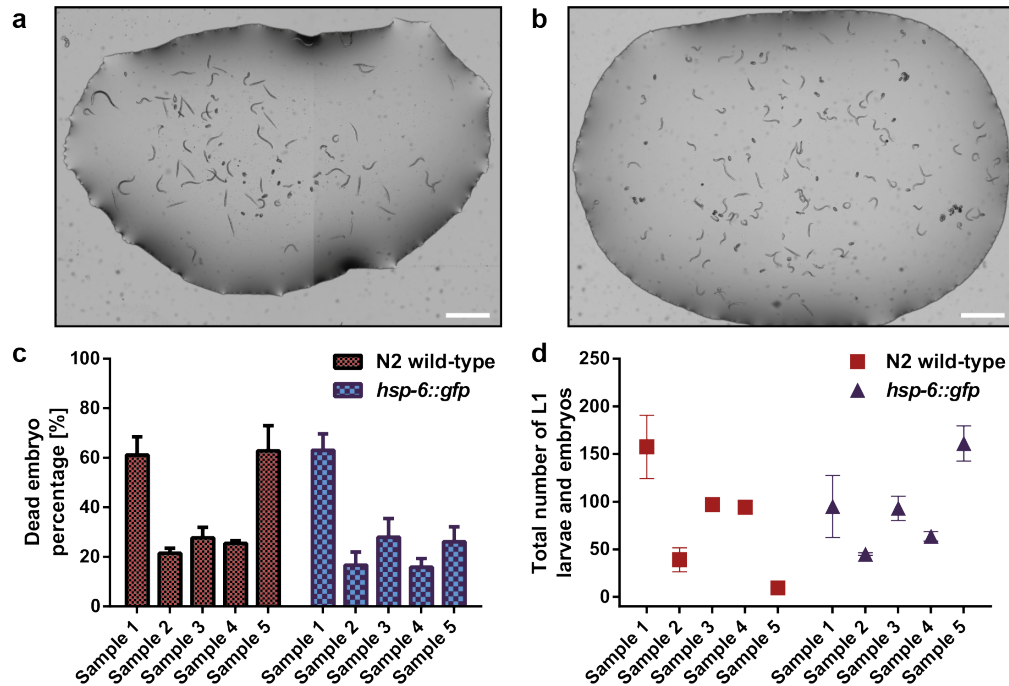


Figure 4.11 – Characterization of the bleaching procedure to obtain a massive amount of *C. elegans* embryos. Photographs of (a) N2 wild-type and (b) *hsp-6::gfp* worms and embryos in 2 μ L samples obtained one day after the bleaching protocol. Scale bars: 500 μ m. (c) Dead embryo percentage of five different samples for N2 wild-type and *hsp-6::gfp* strains. (d) Total number of L1 larvae and embryos in the same 2 μ L samples shown in (c).

detected an almost linear development time increase along with an increase in the molarity (Figure 4.12c). Indeed, the average twitching-to-hatching time interval increased from 216 minutes (for the control condition) to 292 minutes (for 200 mM sucrose) in a rather linear fashion on a log scale. Nonetheless, a vigorous effect, namely a decline in “Dead” embryo percentage as molarity rises was noted (Table 4.1). The lethality rate dropped by 36%, 15% and 9% for 200 mM, 20 mM and 2 mM concentrations, respectively. There was no influence of sucrose molarity on the detection of “Normal” embryos. We concluded that osmotic conditions created by sucrose resembled the osmotic influence with glucose, if not identical. There was less lethal outcome for embryos in sucrose than glucose.

Previous studies with two types of glucose and sucrose revealed that the influence of these compounds could be due to either a toxic or an osmotic effect. The main influence of these chemical compounds on embryo development has not yet been established. For this reason, we performed an osmotic study on embryos using the non-toxic polyol compound glycerol. Prior research with glycerol [94] reported a lifespan reduction of the nematodes and an adaptive response of the nematode to osmotic glycerol conditions [120]. We performed an osmotic study on *C. elegans* embryos with logarithmic dilutions of glycerol and our results showed that there was not a significant impact of osmotic conditions created by glycerol on the development time (Figure 4.12d). We noticed a dose-independent variation in the “Dead” embryo

Chapter 4. Automated phenotyping of *C. elegans* embryos with a high-throughput-screening microfluidic platform

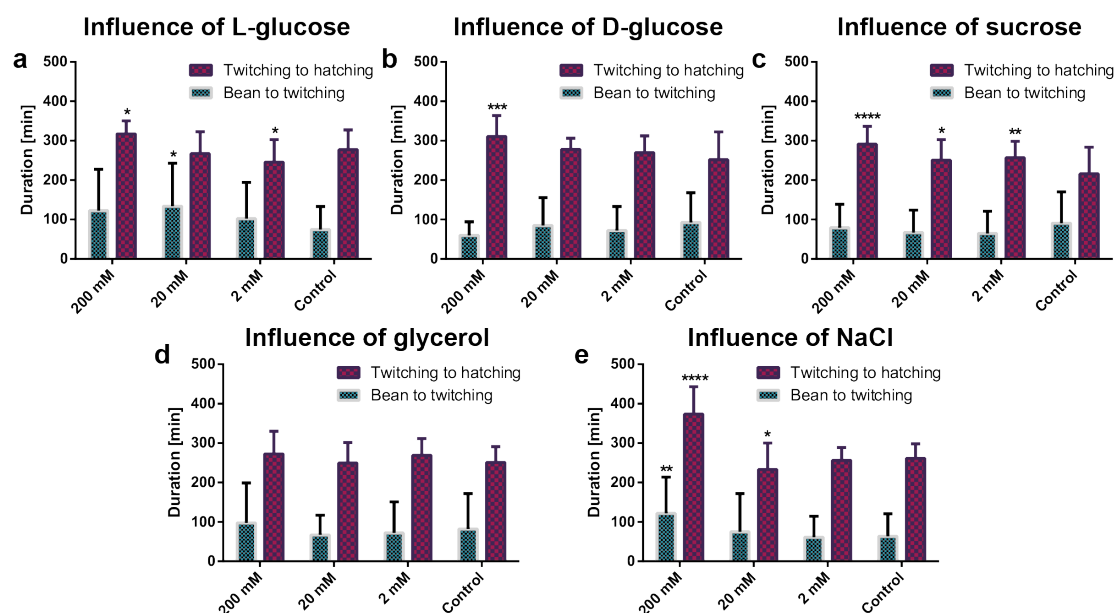


Figure 4.12 – Study of the influence of various chemical compounds on the development time of “Normal” wild-type *C. elegans* embryos. Influence of (a) L-glucose, (b) D-glucose, (c) sucrose, (d) glycerol, and (e) NaCl on the bean-to-twitching and twitching-to-hatching time intervals, respectively. Data are expressed as mean \pm SEM, * $p \leq 0.05$, ** $p \leq 0.01$, *** $p \leq 0.001$, **** $p \leq 0.0001$. All measurements were based on $N = 15$ to 65 embryos.

percentage and interestingly, a beneficial influence to detect “Normal” embryos at high molarities (Table 4.1). The “Normal” embryo detection percentage increased in the range of 31 to 58% with the addition of glycerol during embryo development. We established that the non-toxic compound glycerol had a different outcome on the embryo development then on the nematode development.

NaCl is known to be a highly toxic and ionic component that severely affects the nematode *C. elegans*, although nematodes have some tolerance to a certain extent [121]. NaCl has been demonstrated to have a dramatic impact on the survival [86, 89] lifespan [95, 96] aging [98] and body volume [99] of the nematode. We spotted a highly toxic dose on the development time at 200 mM concentration (Figure 4.12e). The twitching-to-hatching development time was almost 50% more than any other condition; even the bean-to-twitching time was around 60% more at this dose than at any other one. Another toxic indication was the “Dead” embryo rate (Table 4.1). We noticed a dose-dependent behavior, such as the lethality rate increase by 58%, 76% and 131% for the NaCl concentrations of 2 mM to 200 mM, respectively. In parallel, the “Normal” embryo percentage was severely influenced at the 200 mM dose. It dropped almost 50% compared to the successful detection in the control condition. These findings correlated with the previous research on *C. elegans* embryo survival under hypertonic conditions created by NaCl [122].

We additionally investigated the power and accuracy of our phenotyping algorithm for each osmotic study visually. We classified embryo states and embryogenesis stage transitions for

4.4. Osmotic influence on embryo development

all embryos. Our results demonstrated a close match between manually classified states and CNN and mobility function script results (Figure 4.12, 4.13 and Table 4.2). A “Dead” embryo detection problem occurred for 200 mM NaCl. At this dose, the algorithm classified some manually classified “Late Hatching” embryos as “Dead”. However, this is understandable, as unhatched embryos after 12 hours of culture may indicate indeed that the embryo or the first larval stages are dead. We noticed a sensitivity decrease in accordance between the manually classified and the automated script-based detection of the bean stage (in the range of 43 to 67%, see details in Table 4.3). The main explanation for this decrease was the inclusion of zero tolerance between manual and automatic classification. This means that the manual classification of a stage transition, as evidenced by observing two consecutive images in a time-lapse sequence, must be the same as in the automated classification, *i.e.* the stage change should be detected exactly in the same frame of the time-lapse sequence. In the future, bean stage detection could be improved by adding more and clearer bean stage images to the CNN training data.

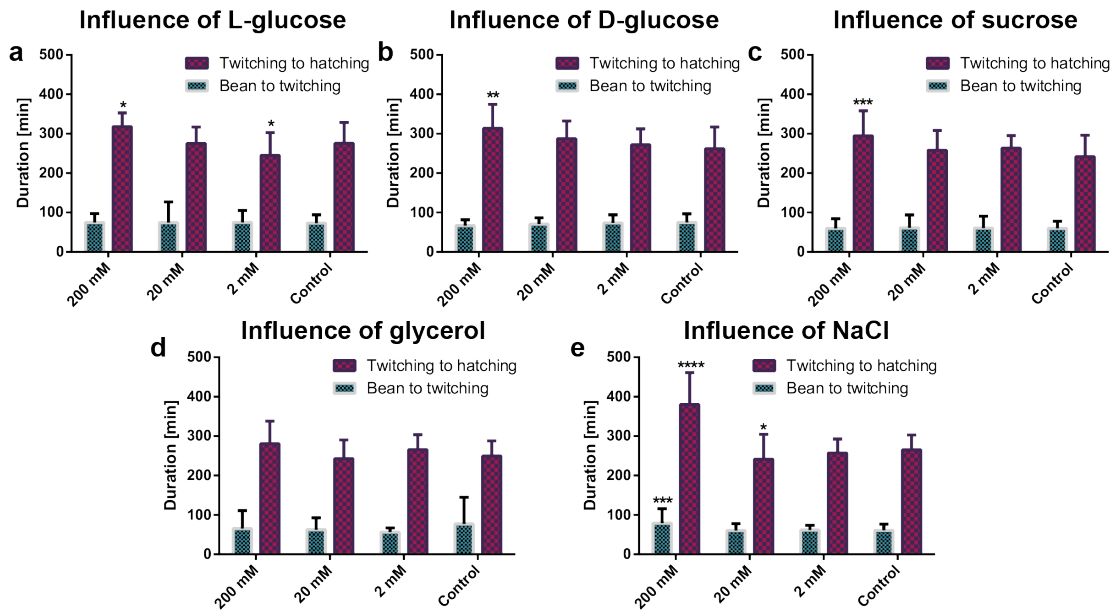


Figure 4.13 – Study of the influence of various chemical compounds on the development time of “Normal” wild-type *C. elegans* embryos quantified by manual classification. Influence of (a) L-glucose, (b) D-glucose, (c) sucrose, (d) glycerol, and (e) NaCl on the bean-to-twitching and twitching-to-hatching time intervals, respectively. Data are expressed as mean \pm SEM, * $p \leq 0.05$, ** $p \leq 0.01$, *** $p \leq 0.001$, **** $p \leq 0.0001$. All measurements were based on $N = 12$ to 63 embryos.

Chapter 4. Automated phenotyping of *C. elegans* embryos with a high-throughput-screening microfluidic platform

Table 4.2 – Comparison of the automated phenotyping data to the manually classified data for the embryo states of wild-type worms. Percentage comparison of the automated phenotyping algorithm to our manually classification based on Dead, Unclear Stage, Empty Embryo Incubator, Late Hatching and Normal Embryo for 200, 20, 2 mM and the Control (0 mM) conditions of L-glucose, D-glucose, sucrose, glycerol and NaCl of wild-type *C. elegans* embryos.

Compound	Dose	Dead embryo [%]		Unclear stage embryo [%]		Empty embryo incubator [%]		Late hatching embryo [%]		Normal embryo [%]	
(C)ode / (M)anual		C	M	C	M	C	M	C	M	C	M
L-glucose	200 mM	59.8	58.7	25.2	26.5	18.9	20.9	3.1	1.6	12.0	13.5
	20 mM	36.3	35	45.1	50.1	8.5	11.1	0.6	0	18.1	14.1
	2 mM	22.2	27.9	48.9	45.9	10	14	2.2	1.2	26.7	25
	Control	38.5	42.3	30.5	30.4	13	16	2.3	0	28.7	27.4
D-glucose	200 mM	56.1	56.6	26.2	27.7	18	20.5	8.5	8.2	9.1	7.5
	20 mM	52.7	54.2	22	21.8	25	29	2.7	0.7	22.7	23.2
	2 mM	37.2	44.4	22.4	18.9	8.5	15.5	4.9	0.6	35.5	36.1
	Control	48	58.9	24	16.6	14.5	18.5	3.5	1.2	24.6	23.3
Sucrose	200 mM	19.4	22.3	51.1	48.6	10	10.5	0.6	0.6	28.9	28.5
	20 mM	25.7	27.1	45.7	47.6	12.1	17	1.7	0	26.9	25.3
	2 mM	27.4	29.8	49.1	48.5	10.7	14.5	0.6	0	22.9	21.6
	Control	30.1	34.9	45.2	46.1	17	24	1.2	0	23.5	19.1
Glycerol	200 mM	37.1	34.4	38.1	46.7	1.5	2.5	1.5	1	23.4	18
	20 mM	29	35.5	48.7	43	3	7	0.5	0	21.8	21.5
	2 mM	44.9	46.9	35.3	35.6	16.5	20	1.8	0	18.0	17.5
	Control	36.5	35.3	45.9	50.6	9	15	2.8	0	14.9	14.1
NaCl	200 mM	42.8	33.6	13.3	19	10	10.5	31.1	35.2	12.8	12.3
	20 mM	32.6	40.5	37	34.8	8	11	4.3	1.1	26.1	23.6
	2 mM	29.3	30.8	42.7	43.4	25	28.5	3.3	2.1	24.7	23.8
	Control	18.5	22.4	45.1	43.2	8	8.5	1.1	0	35.3	34.4

4.5 Dominant influence of ionic molecules on the embryo development

We previously analyzed the influence of various osmotic compounds on the lifespan, survival and development of *C. elegans* embryos. One study of interest would be the comparative influence of these compounds at the same molarities. Therefore, we created a clustergram profile from the normalized mean values of our measurement results with the Equation 3.4. Such a clustergram approach provides a normalized comparison of various chemicals together with eliminating intra-control variations and leading to an assessment of the most important phenotypes that highlight a chemical's influence on the embryo longevity. Our clustergram also reports two more parameters that we did not display previously (parameters "Normal/Total" and "Total Time" in Figure 4.14). The "Normal" embryo over all embryos ratio

4.5. Dominant influence of ionic molecules on the embryo development

Table 4.3 – Sensitivity of the automated phenotyping algorithm on the embryo states and stage transitions. Sensitivity results of the automated phenotyping script for 200, 20, 2 mM and the Control (0 mM) conditions of L-glucose, D-glucose, sucrose, glycerol and NaCl of wild-type *C. elegans* embryos.

Compound	Dose	Embryo State [%]	Bean Stage [%]	Twitching Stage [%]	Hatching Stage [%]
L-glucose	200 mM	95.4	58.8	93.4	100
	20 mM	86.9	62.5	92.7	100
	2 mM	87	65.1	86.9	98.3
	Control	84	63.6	87.4	100
D-glucose	200 mM	93.5	66.7	89.6	100
	20 mM	89	51.5	93.4	100
	2 mM	85	52.5	87.9	98.9
	Control	85	63.2	81	96.9
Sucrose	200 mM	94.5	48.1	79.3	98.5
	20 mM	87.5	73.8	87.1	98.3
	2 mM	88.5	56.8	78.1	96.5
	Control	83.5	65.5	73.9	95.8
Glycerol	200 mM	88.5	42.9	81	97.4
	20 mM	86.5	62.5	80	94.1
	2 mM	91.5	50	84.5	100
	Control	80	45.8	84.7	96.9
NaCl	200 mM	87.5	45.5	78.8	100
	20 mM	86	54.8	85.6	99
	2 mM	91	55.9	84.5	97.9
	Control	92.5	52.4	85.7	100

was included in addition to the “Normal” embryo over alive embryo ratio. In fact, we did not notice significant variation in these two parameters. The other parameter was the total development time, which was calculated as the average bean-to-twitching development time plus the average twitching-to-hatching development time. From this clustergram, we noticed that 2, 20 and 200 mM sucrose, 20 mM glycerol and 2 mM D-glucose concentrations revealed a positive stimulus on the health of embryos (in the blue rectangle). In these conditions, the “Dead” embryo percentage was reduced and the “Normal” embryo observation percentage was increased. In parallel, there was not a significant variation in the twitching-to-hatching and total development times. While 200 mM glycerol concentration did not have a significant impact on embryos, 200 mM of L-glucose, D-glucose and NaCl showed toxic effects, thereby reducing the “Normal” embryo percentage, increasing the “Dead” embryo rate and the development time (in the red rectangle). More specifically, NaCl as an ionic compound severely impacted embryos at all molarities. We presumed that ionic compounds could penetrate inside the eggshell as the bleaching step weakens the outer embryo shell layers [104, 123]. The thus weakened eggshell allowed ionic compounds dissolved in S-medium buffer to easily pass

Chapter 4. Automated phenotyping of *C. elegans* embryos with a high-throughput-screening microfluidic platform

inside the egg and influence the embryo development. NaCl also alters the ionic strength of the buffer, thus creating a gradient across the embryo membrane and worsening the water loss induced by the hyperosmotic environment. By observing the dendrograms of the clustergram, NaCl at 200 mM concentration appeared to be isolated from the rest of the conditions and hence, had the most pronounced influence.

Thanks to the clustergram analysis, we concluded that the most crucial phenotypes to evaluate embryo longevity were the “Normal” and “Dead” embryo population percentage. Interestingly, we noticed that a healthy embryo development indicator was the shortening of the bean-to-twitching stage duration. The twitching-to-hatching time interval and the total development time did not display any significant distinguishable features. This clustergram demonstrated to be a method to illustrate all data in a graphical fashion, highlighting the key phenotypes and the most influential chemicals on the embryo development.

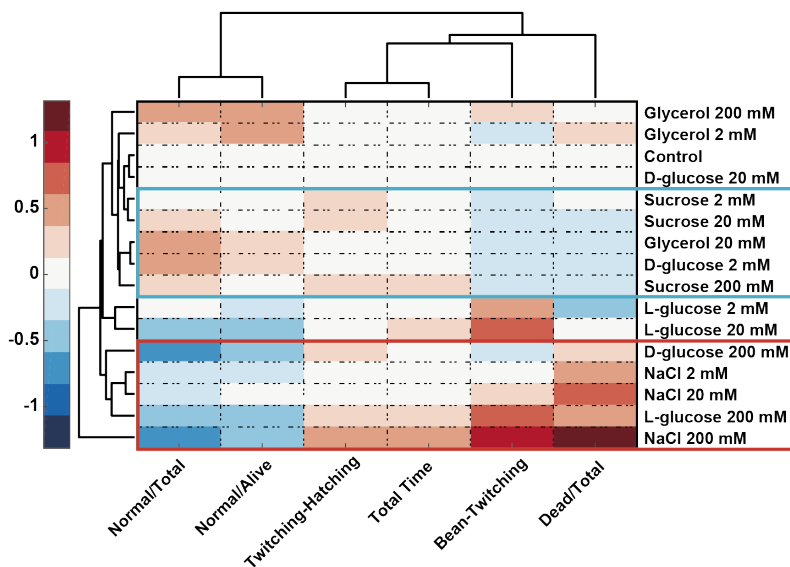


Figure 4.14 – Study of the effect of various chemical compounds with different molarities on the development of wild-type *C. elegans* embryos. Zones in the clustergram that correspond to conditions that are in favor or disfavor of longevity are marked with blue and red rectangles, respectively. All measurements were based on N = 15 to 65 embryos.

4.6 Mitochondrial stress induction under osmotic stress

Osmotic stress causes loss of water, which leads to an intracellular ionic imbalance and hence protein aggregation in the nematode [92]. It is also the origin of the formation of methylglyoxal-modified mitochondrial proteins and ROS [88]. From these indications, osmotic conditions likely alter the function of mitochondria in the nematodes. In this part, we focused on mitochondrial behavior of *C. elegans* embryos under osmotic conditions. We analyzed the development of UPR^{mt} reporter *hsp-6::gfp* strain [67] and evaluated the induction of the

4.6. Mitochondrial stress induction under osmotic stress

UPR^{mt} under a hyperosmotic environmental condition. UPR^{mt} is one of the stress responses deployed by the cells to maintain mitochondrial functions [124].

We selected the three most influential compounds at 200 mM concentration (L-glucose, D-glucose and NaCl) from our development study on the wild-type embryos. We analyzed the developmental behavior of “Normal” *hsp-6::gfp* embryos under hyperosmotic conditions (Figure 4.15a). All three compounds were the source of a lagging development time, as already observed in the wild-type embryo study. The highest impact resulted from ionic NaCl at 200 mM. The average twitching-to-hatching development time for NaCl increased by 89 minutes compared to the control condition. We noticed an opposing profile for the bean-to-twitching stage compared to the twitching-to-hatching stage. The main reason of such a behavior is the narrow error tolerance due to the automated phenotyping with 10-minute intervals and the rather short development duration of the bean-to-twitching duration compared to the twitching-to-hatching stage duration (which was more error-tolerant due to a larger development time). This was confirmed after obtaining manually classified data (see Figure 4.15b). The “Dead” embryo percentage was elevated for all osmotic conditions, and similarly, NaCl produced the highest lethality rate with 72% increase compared to the control condition (Table 4.4). We noticed a 50% drop in the “Normal” embryo rate for 200 mM NaCl. Yet, this influence was not that much apparent for two glucose types. We saw a decline in the accuracy of “Dead” embryo classification for 200 mM NaCl, as before in wild-type embryo study (see accuracy results in Tables 4.5 and 4.6). The drop in the accordance between manual and automated classification results was most likely due to 10-minute intervals.

Table 4.4 – The embryo state classification obtained from the automated phenotyping script for *hsp-6::gfp* nematodes. The fraction of “Dead” embryos over all embryos and of “Normal” embryos over the alive embryo population results are illustrated for 200 mM NaCl, 200 mM D-glucose, 200 mM L-glucose and the Control condition (0 mM) of *hsp-6::gfp C. elegans* embryos.

Compound	Dose	Dead embryo [%]	Normal embryo over alive embryo [%]
NaCl	200 mM	77.1	18.8
D-glucose	200 mM	51.6	35.5
L-glucose	200 mM	52.4	33.9
Control	0 mM	44.7	37.0

For the “Normal” embryos, we investigated the population-averaged time-dependent UPR^{mt} expression profile (Figure 4.15c-e). We focused on the initial 300 minutes of the experiment, as most of the embryos were present in an incubator in this time interval. The data corresponding to the entire duration of the experiment can be found in Figure 4.15f-h. Here too, after 300 minutes we noticed an increasing intensity profile in parallel with the advancement of embryo development, just like in Figure 4.15c-e. The drop that is observed in the curves after 400 minutes corresponds to the onset of embryo hatching events, lowering the average intensity results due to the significantly reduced intensity contributions from embryo-free incubators. From the latter, we calculated the fold induction of these compounds on the fluorescent

Chapter 4. Automated phenotyping of *C. elegans* embryos with a high-throughput-screening microfluidic platform

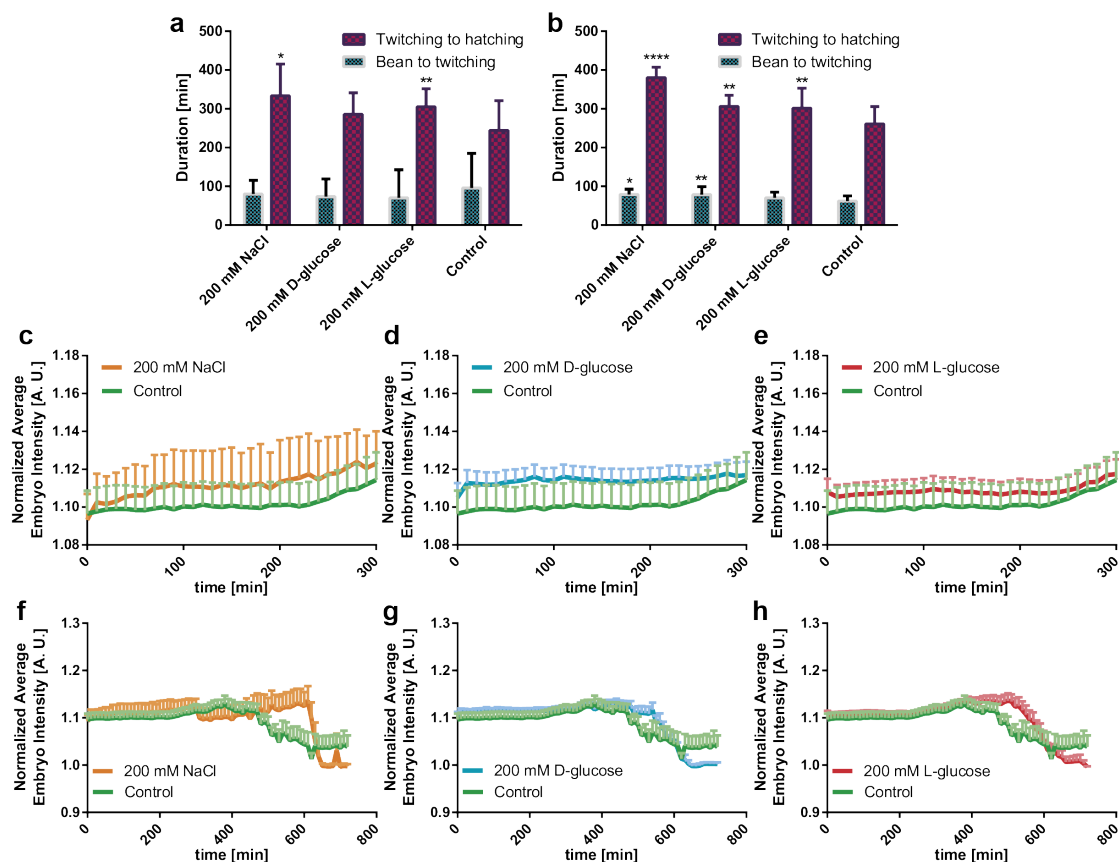


Figure 4.15 – Study of the effect of various 200 mM chemical compounds on the development of “Normal” *hsp-6::gfp* *C. elegans* embryos. Influence of NaCl, D-glucose and L-glucose on the bean-to-twitching and twitching-to-hatching time intervals quantified by (a) automated and (b) manual classification. Mitochondrial stress induction in embryos is evidenced by the background-corrected fluorescence, during the initial 300 minutes of embryogenesis for (c) 200 mM NaCl, (d) 200 mM D-glucose and (e) 200 mM L-glucose compared to the control condition; and during the entire course of the experiment for (f) 200 mM NaCl, (g) 200 mM D-glucose and (h) 200 mM L-glucose compared to the control condition. Data are expressed as mean \pm SEM, * $p \leq 0.05$, ** $p \leq 0.01$, **** $p \leq 0.0001$. All measurements were based on N = 6 to 27 embryos.

intensity as an additional phenotype. Our results revealed a fold induction of 1.009, 1.011 and 1.006 for 200 mM NaCl, 200 mM D-glucose and 200 mM L-glucose, respectively. We noticed that mitochondrial stress induction in this period was the highest for D-glucose, which was followed by NaCl and then by L-glucose.

The *hsp-6::gfp* embryos were previously demonstrated to generate a rather weak fluorescent signal [106]. We noticed that the basal intensity expressed by an average embryo under the control condition was around 1.1-1.2 A. U. (see Figure 4.15c-e), because of the development of the weakly fluorescent larva inside the eggshell. The exposure to various chemical compounds at 200 mM exhibited no significant > 1-fold induction. Although all three compounds triggered

4.7. Statistical analysis

Table 4.5 – Comparison of the automated phenotyping data to the manually classified data for the embryo states of *hsp-6::gfp* worms. Percentage comparison of the automated phenotyping algorithm to our manually classification based on Dead, Unclear Stage, Empty Embryo Incubator, Late Hatching and Normal Embryo for 200 mM NaCl, 200 mM D-glucose, 200 mM L-glucose and the Control condition (0 mM) of *hsp-6::gfp C. elegans* embryos.

Compound	Dose	Dead embryo [%]		Unclear stage embryo [%]		Empty embryo incubator [%]		Late hatching embryo [%]		Normal embryo [%]	
		C	M	C	M	C	M	C	M	C	M
(C)ode / (M)anual											
NaCl	200 mM	77.1	45.7	10	14.3	30	30	8.6	32.9	4.3	7.1
D-glucose	200 mM	51.6	38.3	29.3	42.9	21.1	23	1.9	1.9	17.2	16.9
L-glucose	200 mM	52.4	43.9	27.4	31.7	38	38.5	4	8.1	16.1	16.3
Control	0 mM	44.7	42.1	31.8	39.7	34	39.5	3	0	20.5	18.2

Table 4.6 – Sensitivity of the automated phenotyping algorithm on the *hsp-6::gfp* embryo states and stage transitions. Sensitivity results of the automated phenotyping script for 200 mM NaCl, 200 mM D-glucose, 200 mM L-glucose and the Control condition (0 mM) of *hsp-6::gfp C. elegans* embryos.

Compound	Dose	Embryo State [%]	Bean Stage [%]	Twitching Stage [%]	Hatching Stage [%]
NaCl	200 mM	71.5	50	88	94.1
D-glucose	200 mM	86.5	50	93.2	100
L-glucose	200 mM	90.5	35	83.6	100
Control	200 mM	87.5	77.3	87.7	98.4

a slight increase in UPR^{mt} expression, the signal was not very significant (p-values > 0.05). From previous research, we know that the impaired mitochondria respiration increases UPR^{mt} signal expression as an indicator of a stress response to promote lifespan [125, 126]. We believe that the slight induction we observe might be the result of such stress response that strives to reach homeostasis under hypertonic conditions. Osmotically stressed embryos also remained in the basal fluorescent intensity level of 1.1-1.2 A. U., which is an additional indicator of the weak disturbance generated during their development.

4.7 Statistical analysis

Data from raw images were extracted to fill an array for statistical tests using Graphpad Prism. Development duration data were analyzed for statistical significance with ordinary one-way ANOVA (and Dunnett's multiple comparison test). Average embryo intensity data were analyzed for statistical significance with Repeated Measures two-way ANOVA (and Dunnett's

Chapter 4. Automated phenotyping of *C. elegans* embryos with a high-throughput-screening microfluidic platform

multiple comparison test). For the study of the influence of L-glucose on wild-type embryos, we had 19, 33, 48, 50 embryos for 200 mM, 20 mM, 2 mM and control conditions, respectively. For the study of the influence of D-glucose on wild-type embryos, we had 15, 34, 65, 42 embryos for 200 mM, 20 mM, 2 mM and control conditions, respectively. For the study of the influence of sucrose on wild-type embryos, we had 52, 47, 40, 39 embryos for 200 mM, 20 mM, 2 mM and control conditions, respectively. For the study of the influence of glycerol on wild-type embryos, we had 46, 42, 30, 27 embryos for 200 mM, 20 mM, 2 mM and control conditions, respectively. For the study of the influence of NaCl on wild-type embryos, we had 23, 48, 37, 65 embryos for 200 mM, 20 mM, 2 mM and control conditions, respectively. For the study of the mitochondrial stress induction on *hsp-6::gfp* embryos, we had 6, 27, 20, 27 embryos for 200 mM NaCl, 200 mM D-glucose, 200 mM L-glucose and control conditions, respectively.

4.8 Discussion and conclusion

In this work, we presented a new multiplexed and automated phenotyping microfluidic platform for high-throughput *C. elegans* embryogenesis studies. To the best of our knowledge, no other platform demonstrated such level of throughput combined to parallel and automated experimental protocols for embryogenesis studies. We configured each microfluidic lane for different parallel conditions to observe simultaneously the influence of various compounds on embryo development. Thanks to the integration of microfluidics, we continuously perfused well-characterized doses of compounds in the microchannels, guaranteeing an experimental control that is unseen with the traditional methods on agar plates. We can incubate up to 100 embryos in a single microfluidic lane, extract five phenotypes for the incubator occupancy and detect three important life stage points of embryogenesis. We observed the experiment for up to 12 hours from the initial embryo placement, and this in an automated manner. We intentionally designed our microfluidic platform to contain only simple, passive components and we followed standard soft-lithographic fabrication procedures. The simplicity of the design and the user-friendliness of the semi-automated protocol are aimed at a larger use by researchers, beyond the microsystem community and including biologists who are active in nematode research. The traditional 63× oil immersion imaging was replaced by 20× imaging in our protocol to reduce computational time and data storage space but 63× imaging can still be effortlessly fitted to the system.

Our platform reduced the user interaction to a minimum level, thanks to the semi-automated experimental pipeline and the simple handling of the embryos throughout the experiment. We created repeatable serial port commands for the syringe pump, which generated a simple experimental preparation pipeline and reduced the laborious operator involvement. The initial setup time of the experiment was reduced to 35 minutes. Additionally, an experiment demanded no active involvement of the user, once it was initiated, in sharp contrast with the embryo studies on agar plates. A significant amount of data was efficiently collected in a short time, while still providing high-content datasets.

As a proof-of-concept, we performed a case study, which was the development of *C. elegans* embryos under osmotic conditions. We loaded several chemical compounds that are known to induce hyperosmotic conditions, which are toxic for the adult nematode. We noticed a high toxicity for wild-type embryos of all NaCl concentrations, as well as 200 mM doses of L-glucose and D-glucose, by observing an increased dead embryo percentage and development time. A favorable stimulus for the embryo health was observed at 2, 20 and 200 mM sucrose, 20 mM glycerol and 2 mM D-glucose concentrations by counting of an increased number of healthy embryos. NaCl at 200 mM concentration demonstrated the greatest variation in the phenotypic properties in comparison and had a dominant effect, as revealed by the clustergram analysis. This phenomenon was understood as a consequence of higher osmolarities of the buffer that sets an osmotic gradient across the eggshell, as the outer embryo layers were already compromised by bleaching.

We also demonstrated how embryos try to adjust to osmotic environments. We performed an embryogenesis study with the *hsp-6::gfp* worm strain that exhibits mitochondrial stress expression under 200 mM doses of NaCl, D-glucose and L-glucose. Our results revealed that UPR^{mt} expression and hence, mitochondria function slightly increased by 0.6 to 1.1% to compensate for the osmotic stress. Furthermore, extreme molarities of these compounds had a higher killing rate (in the range of 15 to 72%) on embryos with respect to the control condition. Specifically, 200 mM of NaCl had an extreme lethality rate.

Beyond the technical advancements of the work, this study supports the use of *C. elegans* embryos for osmosensing studies instead of adult worms. The short development time of the embryos, and their similar behaviors to that observed in the adult nematodes under osmotic conditions, opens new experimental avenues for more case studies. Further bioanalytical studies formerly performed on the nematode can be directed to the embryo of *C. elegans* to obtain abrupt but rapid answers to bioanalytical questions. We therefore believe that our new microfluidic approach will pave the way for new research opportunities utilizing embryo as a new model for biochemical and development investigations.

5 Automated platform for life-long and high-content phenotyping of single *C. elegans* worms

The nematode *Caenorhabditis elegans* is a suitable model organism in drug screening. Traditionally worms are grown on agar plates, posing many challenges for long-term culture and phenotyping of animals under identical conditions. Microfluidics allows for ‘personalized’ phenotyping, as microfluidic chips permit collecting individual responses over worms’ full life. Here, we present a multiplexed, high-throughput, high-resolution microfluidic approach to culture *C. elegans* from embryo to the adult stage at single animal resolution. We allocated single embryos to growth chambers, for observing the main embryonic and post-embryonic development stages and phenotypes, while exposing worms to up to 8 different well-controlled chemical conditions. Our approach allowed eliminating bacteria aggregation and biofilm formation-related clogging issues, which enabled us performing up to 80 hours of automated single worm culture studies. Our microfluidic platform is linked with an automated phenotyping script that registers organism-associated phenotypes at high-throughput. We validated our platform with a dose-response study of the anthelmintic drug tetramisole by studying its influence through the life cycle of the nematodes. In parallel, we could observe development effects and variations in single embryo and worm viability due to the bleaching procedure that is standardly used for harvesting the embryos from a worm culture agar plate.

This chapter is an adapted version of the following publications:

- **H. B. Atakan**, R. Xiang, M. Cornaglia, L. Mouchiroud, J. Auwerx and M. A. M. Gijs, “Automated high-content phenotyping of the nematode *C. elegans* at single animal resolution with a microfluidic platform”, in *20th International Conference on Solid-State Sensors, Actuators and Microsystems (TRANSDUCERS)*, pp. 2209-2212, 2019.
- **H. B. Atakan**, R. Xiang, M. Cornaglia, L. Mouchiroud, E. Katsyuba, J. Auwerx and M. A. M. Gijs, “Automated platform for long-term culture and high-content phenotyping of single *C. elegans* worms”, *Scientific Reports*, vol. 9, 14340, 2019.

5.1 Introduction

C. elegans in their natural habitat live in colonies, therefore, it is easy to collect large data sets with statistical relevance, but in traditional worm culture on agar plates, monitoring individual responses and identifying eventual heterogeneity in response within a population is difficult. Microfluidic chips are utilized to facilitate handling and manipulation, and also they provide very controlled and reliable phenotypic results for assaying drugs and chemicals. However, the majority of the proposed *C. elegans* microfluidic platforms were designed for studying of nematodes at the whole population level, leading to averaged results and omitting the study of any relevant individual response and eventual intra-population heterogeneity [35, 112, 127, 128]. Microfluidics proved also to be promising for high-resolution and high-throughput imaging, for example for detecting subtle aging phenotypes [59] or for assaying of poly-glutamine aggregates as indicators of disease progression [52]. Previously, platforms that targeted single nematode handling included agarose micro chambers as a culturing environment [37, 129]. Yet, the experimental preparation was time-consuming with little automation and these platforms were lacking automated and continuous food replenishing systems during the worms' life. A hybrid approach, in which PDMS microfluidic chips were combined with an agarose gel substrate, permitted single nematode manipulation and culture [38, 39]. However, the lack of a continuous food supply, tedious procedures for the initial single worm or embryo placement, and problems with late progeny removal disfavored such approaches for automation. Other microfluidic approaches included the generation of droplets [130, 131], in which a single L1 or L4 stage nematode was trapped to isolate and culture worms individually. However, the complexity of the microfluidic chip fabrication and challenges in delivering food or drugs disfavored usage of droplet generators for drug screening.

Full-PDMS microfluidic approaches were impeccable candidates to tackle automation and systematic needs to handle nematodes at single animal resolution. Microfluidic platforms for single worm culture starting from L1 [32, 36] or L4 [55] stages were proposed, but they were operating at low-throughput and required an integration of on-chip components like pressure-activated valves that increased the complexity of the microfabrication. Some microfluidic designs showed that single nematode loading in individual growth chambers was possible at higher throughput, but worm feeding was performed through single nozzle entrances [51, 53, 56, 58]. This design feature was susceptible to bacteria aggregation in the later life stages of the nematodes. Another study demonstrated the possibility of life cycle culturing, starting from the embryo stage, but, similarly, single-point entrances of growth chambers were susceptible to bacteria accumulation and biofilm formation and experimental parallelization was limited [57]. In addition, these devices still lacked the degree of automation needed to collect and analyze a significantly large amount of data, as required for high-throughput applications. Besides studying phenotypic parameters such as length or fertility, researchers realized the importance of motion analysis of *C. elegans*. Previous motility phenotyping methods mostly focused on the single larval stage motion of the nematodes inside a buffer solution [46, 47, 48, 49], but integration of these phenotyping algorithms over the nematodes' full life cycle at single worm-resolution was not reported so far.

5.2. Automated microfluidic phenotyping platform design and operation of single *C. elegans* worms

We propose here a simple and easy-to-use microfluidic system for automated long-term culturing and phenotyping of *C. elegans* at single-organism resolution. After obtaining a large amount of embryos from an agar plate through a standard bleaching procedure, we automatically distributed embryos and observed the embryonic and post-embryonic development stages under a chemical treatment in an automated fashion. Our microfluidic chips have 48 culture chambers providing multiplexed and high-throughput study opportunities, while providing six single worm growth chambers per single chemical test condition. Five minute interval time-lapse images of each growth chamber were taken during 11 hours of experimentation and then automatically converted to 10 seconds videos, every 4 hours, until the end of the experiment. Operator-based observation was employed during the phenotyping of the embryonic development stages. Thereafter, high-content phenotypic results on larvae and adults were obtained automatically with our video processing script. To validate our microfluidic approach, we performed a case study with logarithmic dilutions of tetramisole in *E. coli* solution to observe its influence on the life cycle of the nematodes. Tetramisole is an anthelmintic drug that is known to have harmful effects on internal parasites [132] and anthelmintic drugs are also used to paralyze *C. elegans* temporarily for imaging applications [133]. However, little is known about how these compounds affect the various embryonic and larval developmental life stages of *C. elegans*. Our platform simultaneously allowed studying the effects of a standard bleaching procedure on the health of embryos and worms.

5.2 Automated microfluidic phenotyping platform design and operation of single *C. elegans* worms

5.2.1 Microfluidic chip design

We designed spacious growth chambers allowing observation of *C. elegans* during their life cycle (Figure 5.1). Our microfluidic chip has 8 lanes with media inlets and 8 media outlets (Figure 5.1a); each microfluidic lane has 6 growth chambers (Figure 5.1b). While media inlets were utilized to draw fresh S-medium in the lanes, media outlets were used to load either embryo or *E. coli* solution. Each growth chamber was designed large enough ($1280\text{ }\mu\text{m} \times 1280\text{ }\mu\text{m} \times 80\text{ }\mu\text{m}$) such that nematodes could go through all developmental stages. Each growth chamber has 24 filter structures both on the right and the left (Figure 5.1b), which are coupled to so-called embryo incubators and to one so-called embryo pocket, the latter being situated at the media inlet side. The configuration of 24 filters in parallel provides uniformity in the bacteria distribution and avoids any possible bacteria aggregation and associated clogging problems. The embryo pocket in the middle of the filter structures on the left-hand side is used for initial embryo trapping and subsequent dispensing to distribute *C. elegans* embryos individually in their chambers. The wing-shaped design of the embryo pocket allows easy injection by just an increase in the flow rate via a pressure pulse of the S-medium, once the embryos were positioned in the embryo pockets. Additional key features were also noted. The molded PDMS part containing all microfluidic features had an approximate size of 35 mm

Chapter 5. Automated platform for life-long and high-content phenotyping of single *C. elegans* worms

× 53 mm, so that a standard 38 mm × 75 mm-sized glass microscope slide could be used as the sealing part (Figure 5.1c).

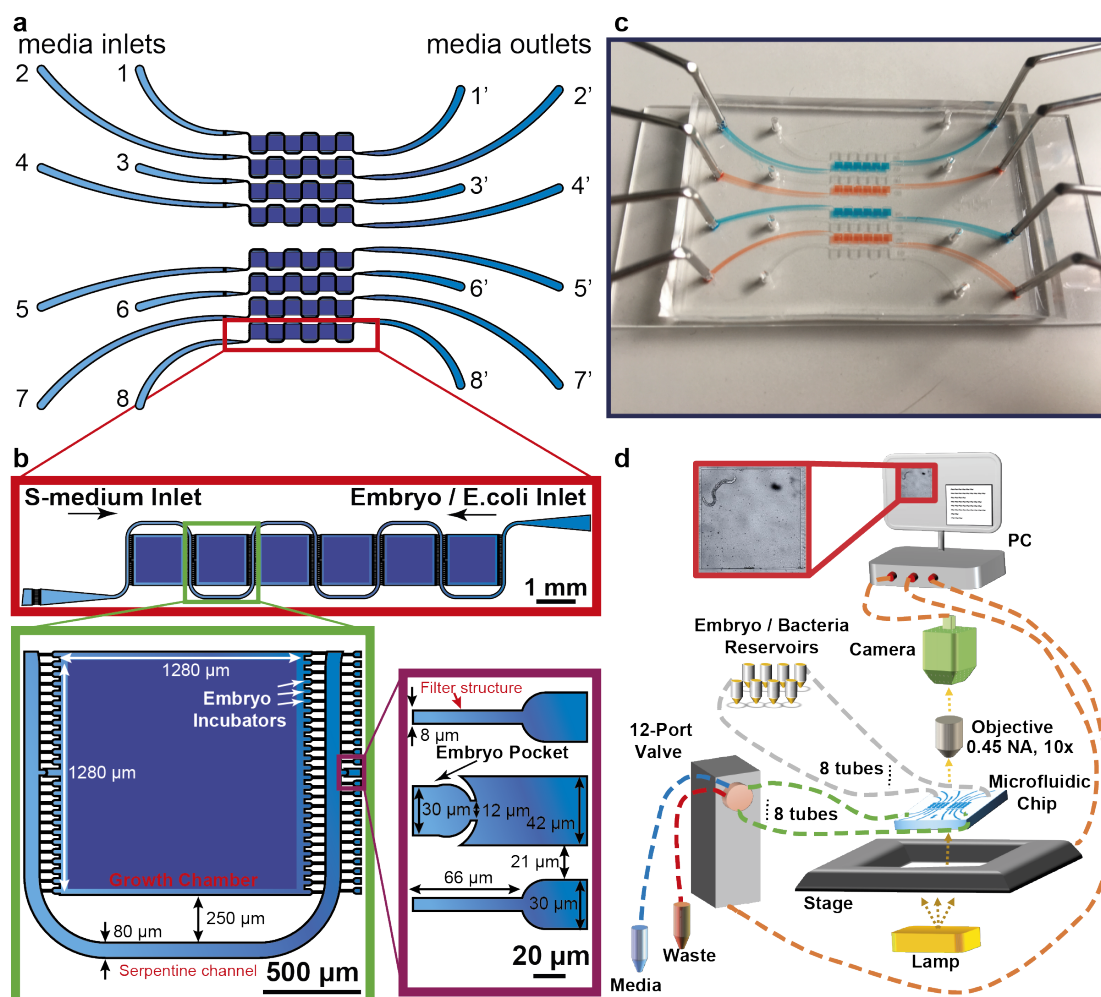


Figure 5.1 – Single-animal resolution multiplexed microfluidic platform for phenotyping of the nematode *C. elegans*. (a) Schematic drawing of the microfluidic chip consisting of eight lanes, each lane having six culture chambers. (b) Each growth chamber has a single embryo pocket to trap and push a single *C. elegans* embryo inside in a controlled manner. (c) An image of the microfluidic chip filled with liquid dye solutions. (d) Illustration of the overall platform.

5.2.2 Silanization of the microfluidic chip

We employed the same silanization procedure as explained in the Subsection 3.2.2, which is the reason we do not duplicate this text here.

5.2.3 Platform working principle

A 12-port rotary valve was connected to a Kloehe syringe pump and it was coupled to the microfluidic device (Figure 5.1d). The microfluidic device was mounted in a microscopy control system (Visitron, Puchheim, Germany). For each microfluidic lane, we have 8 interchangeable embryo and bacteria reservoirs connected to the media outlets. In parallel, 8 media inlets were linked to 8 ports of the 12-port valve. The two additional ports of the 12-port valve were linked to waste and clean media reservoirs, respectively. The excessive media coming from these reservoirs were dispensed into a waste reservoir. During the chip filling, the initial embryo trapping, dispensing and embryo imaging, fresh S-medium was loaded from the media reservoir into the microfluidic lanes. 48 different chamber positions were located through the GUI of the microscope after mounting the microfluidic chip on a motorized stage. Our camera was triggered to capture images every 5 minutes during embryogenesis and recorded videos for 10 seconds at 5 Hz every 4 hours through a $10 \times (0.45 \text{ NA})$ objective. The operation method of the platform was semi-automated in order to provide the most reliable and repeatable results with the least human interaction. Therefore, we customized fluidic scripts that were repeated at each experiment to load embryos, dispense the embryos, and load the *E. coli* solution. Recorded videos were analyzed with our automated motility analysis script on a computer.

5.2.4 Automated fluidic protocol

We first obtained a large amount of embryos by bleaching synchronized gravid adult worms. Initially, the embryos were injected into the chip from the media outlet and collected by the filters on the media inlet side (Figure 5.2a). After approximately 10 embryos were collected in front of the filter set on the media inlet side, an S-medium flow was initiated from the media inlet side to position the embryos in the embryo pockets in front of each growth chamber with a flow rate of 625 nL/s (Figure 5.2b). Due to the high pressure in front of the embryo pockets in comparison to the adjacent filters, embryos were trapped individually in the embryo pockets awaiting entry into the chambers. After all of the pockets were filled, and extra embryos were washed off through the media outlet, the channel was quickly deformed via a short but powerful S-medium pulsed flow (in a range from 6 $\mu\text{L/s}$ to 30 $\mu\text{L/s}$) to permit embryos to enter the chambers (Figure 5.2c). With the increase of the flow rate and hence the increase of the fluidic pressure, we verified through a fluidic simulation that the pressure drop along each embryo pocket was powerful enough to push embryos inside the growth chambers (Figure 5.3). We also validated the uniform velocity profile along each embryo pocket by simulation and verified experimentally that our fluidic commands provided consistent trapping of embryos. The wing-shaped embryo pockets enabled to briefly enlarge their section at the narrowest part during a pressure pulse and thereby injected all embryos in their growth chamber. Hereafter, the embryo reservoir was replaced by the bacteria reservoir and we filled each channel with a 100 μL fresh suspension of *E. coli* HT115 with different tetramisole concentrations at a flow rate of 0.1 $\mu\text{L/s}$, having a direction from the bacteria reservoirs to the waste reservoir (Figure 5.2d). Then, we injected 20 nL S-medium at 21 nL/s from the media reservoir into each channel

every 5 minutes in an attempt to trap the embryos in one of the embryo incubators inside the growth chambers, and images of each chamber were captured every 5 minutes for 11 hours during the embryo development study (Figure 5.2e). After 11 hours, the camera switched to recording videos of the chambers every 4 hours for the nematode growth and motility study. An automation script with Python was utilized to control the stage positions and image/video acquisition throughout the experiment. After 20 hours, a fresh *E. coli* HT115 bacteria solution with different tetramisole concentrations was injected into the channels at 42 nL/s with an injection amount of 3.13 μ L, followed by an S-medium injection from the media reservoir at 42 nL/s with an injection amount of 1.04 μ L. This protocol prohibited early larval stage escape through the embryo pockets. The bacteria injection volume was kept at least 2 μ L higher than the medium injection volume in order to retain bacteria uniformity in the chip. This feeding was continued in 15-minute cycles until the control worms reached to the adult stage. After, the *E. coli* injection amount and flow rate were changed to 6.25 μ L and 83 nL/s, respectively. Similarly, the S-medium injection amount and flow rate were changed to 2.08 μ L and 83 nL/s, respectively. This feeding was carried out in 15-minute cycles until the end of the experiment. Since tetramisole hindered the development of *C. elegans*, the bacteria injection flow rate varied (in the range of 21 nL/s to 83 nL/s) depending on the size of worms. S-medium injection at 667 nL/s was utilized to wash off the late progenies. This experimental procedure enabled continuous *C. elegans* culture for several days (Figure 5.4).

5.3 Tetramisole viability assay on *C. elegans*

C. elegans has been demonstrated to be a valuable model organism for anthelmintic drug testing studies [134]. Several approaches were proposed to quantify anthelmintic effects. A thrashing assay was illustrated as an important phenotype to assess the level of motility change by levamisole [135]. While a levamisole dose of 100 nM did not alter the motility behavior, a concentration of 1 mM significantly affected the worm motion. Other researchers developed an electropharyngeogram (EPG) system to capture an anthelmintic effect and additionally, they noticed a change in EPG waveform at 10 mM levamisole concentration [136]. While the effect of anthelmintic drugs on larvae and adult worms have been widely studied [137], *C. elegans* embryos have not been explored thoroughly in an anthelmintic viability assay [138]. Moreover, the development lag during all stages of life due to life-long exposure to tetramisole of the nematodes remains unknown.

5.3.1 Effect of tetramisole dose and bleaching treatment on the embryonic development

We first exploited our platform for studying the dose-dependent influence of tetramisole on the embryonic health and development. We selected a maximum tetramisole concentration of 1 mM [136] and used logarithmic dilutions of this concentration down to 1 nM. For accurate imaging, we aimed at keeping embryos as steady as possible in the embryo

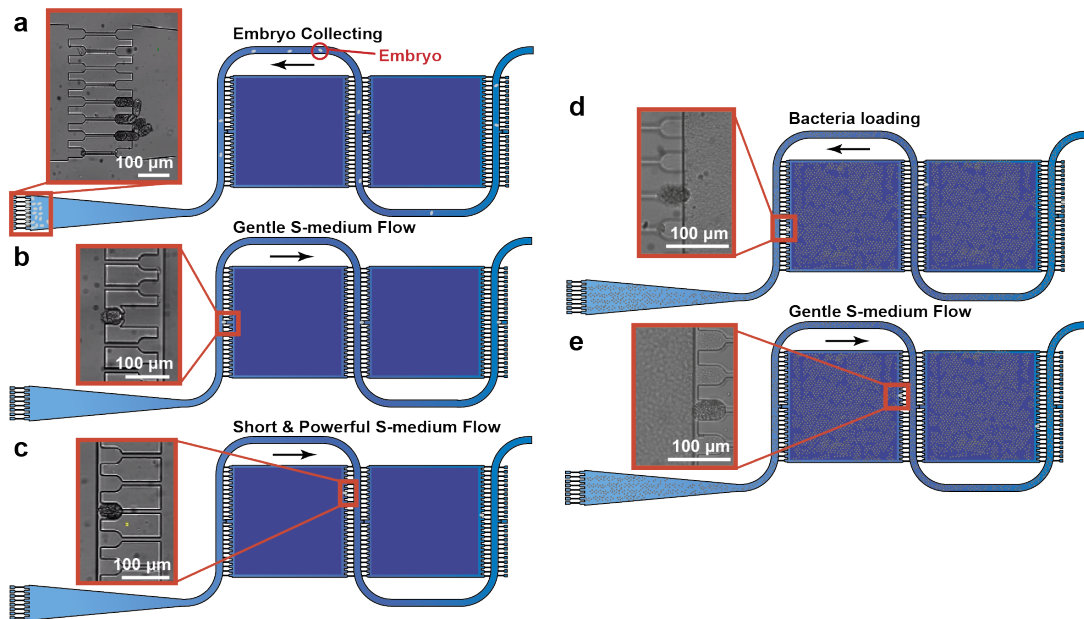


Figure 5.2 – Schematic illustration of the operation modes of the microfluidic chip. (a) Initially, embryos were collected in front of the filter set towards the media inlet side. (b) S-medium was pushed from the syringe side towards the media outlets and one embryo was placed in the embryo pocket in front of each growth chamber, while the remaining ones were disposed off. (c) The fluidic pressure was increased to push all the embryos in the same microfluidic lane into the growth chambers simultaneously. (d) Tetramisole-diluted bacteria solution loading was initiated. (e) An S-medium flow rate from media inlets towards outlets was utilized to trap each embryo in one of the embryo incubators inside the growth chambers temporarily for imaging.

incubators inside the growth chambers during embryogenesis. Yet, even when embryos were not firmly positioned in the incubators, embryo-related phenotypes could still be extracted. The provided tetramisole concentrations were diluted in *E. coli* solution to guarantee proper feeding after embryo hatching. We visually analyzed time-lapse images that were captured every five minutes and we investigated the development of embryos. We observed that there was not an osmotic or a toxic influence at all tetramisole doses on the twitching-to-hatching developmental time of embryos (Figure 5.5a). Similarly, we quantified the successful hatching rate of embryos into the L1 stage (Figure 5.5b). We observed that the tetramisole dose does not correlate with the hatching rate, despite an observed 50% decrease at 10 μ M tetramisole concentration compared to the control. As there was no clear dose-effect trend of tetramisole on the hatching rate, we believe that this variation in the hatching rate was probably related to small variations in the bleaching procedure, which is known to be quite aggressive to *C. elegans* embryos, although nominally all bleaching protocols were identical [139]. 1 nM, 10 nM, 100 nM, 100 μ M and 1 mM concentrations demonstrated a non-monotonous 5-20% nematode killing rate after the initial hatching of L1 nematodes (Figure 5.5c). This phenomenon was due most likely again, owing to a lack of correlation with the tetramisole dose, to the post-effects

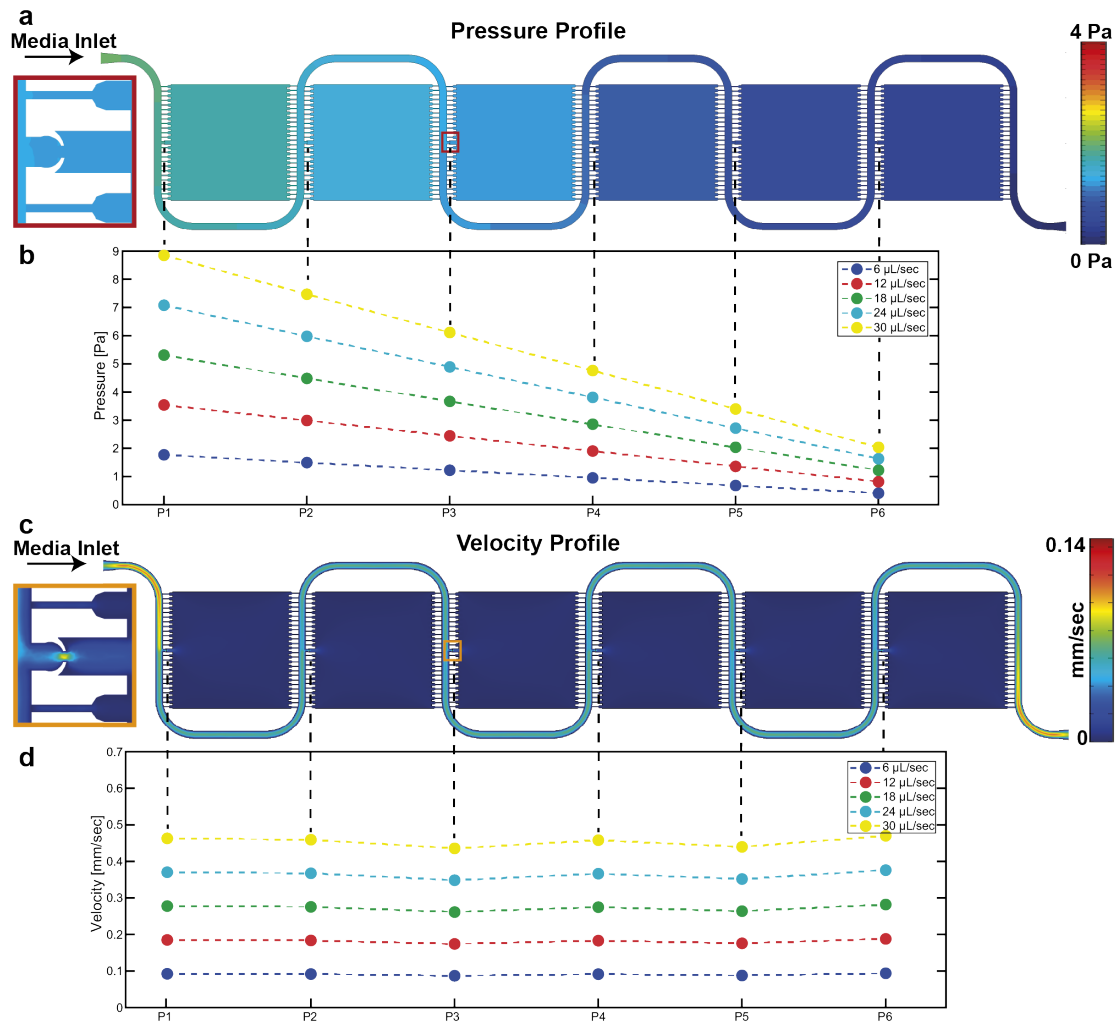


Figure 5.3 – Pressure and velocity simulations at the position of all the embryo pockets in front of the growth chambers. (a) The pressure distribution profile colored along a microfluidic lane. (b) Six different flow rates that were supplied from the media inlet demonstrated the pressure drop from the embryo pocket of the first growth chamber to the last one. (c) Color-coded local velocity distribution profile along a microfluidic lane. (d) Six different flow rates that were supplied from the media inlet illustrate the local similar velocity profile around the embryo pockets in front of the growth chambers.

of the bleaching step that damaged the embryos' integrity. We presume that the distribution of extracted embryos within the bleaching solution yielded more viable conditions for some embryos than for others. Single embryo and worm resolution of our platform has thereby been key for identifying these variations in response. We concluded therefore that there was no systematic anthelmintic dose effect on the development and the health of embryos. Thanks to the single embryo tracking enabled by our platform, we could however accurately quantify the development duration and the hatching rate of embryos and the initial dead L1 nematode rate.

5.3. Tetramisole viability assay on *C. elegans*

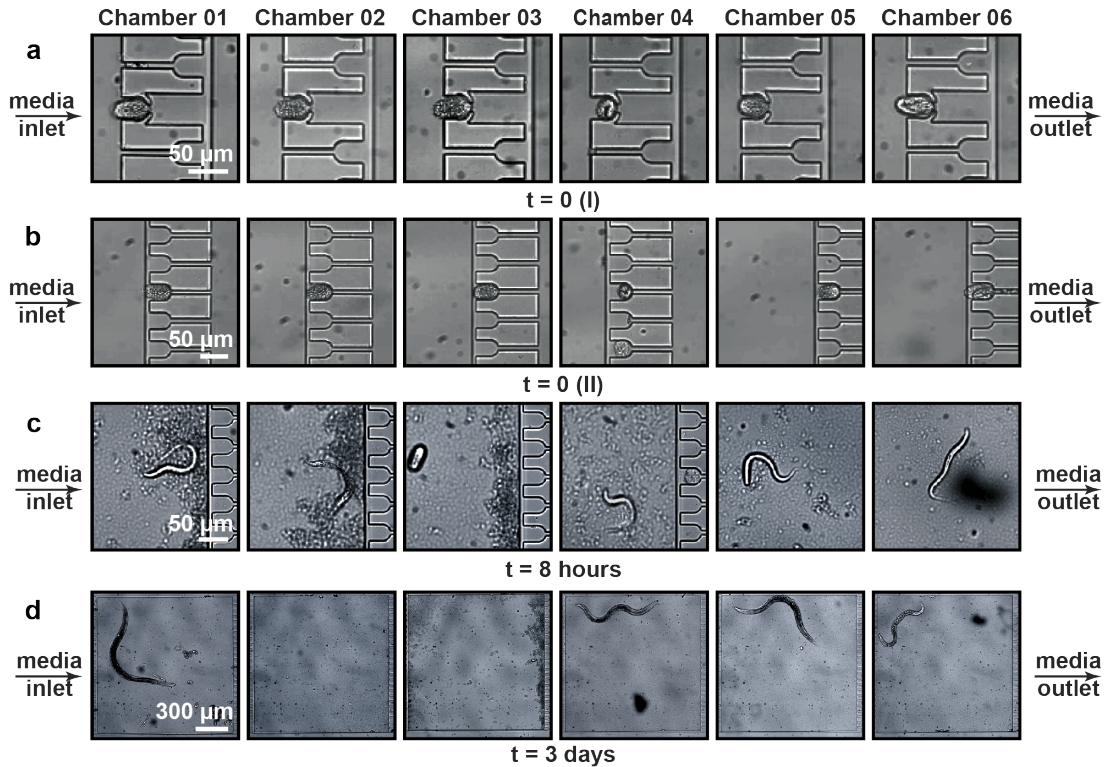


Figure 5.4 – Real-time images of the development of N2 wild-type nematodes starting from the experiment's initiation up to 3 days. (a) Embryos were trapped in the embryo pockets in front of the growth chambers. (b) After having embryos dispensed inside the growth chambers and the chemical of interest loaded in the microfluidic lane, a gentle flow rate was utilized for 11 hours to retain the embryos in the embryo incubators as close as possible to observe embryogenesis. (c) After 8 hours, the majority of the embryos hatched. (d) After 3 days, most of the worms reached their adult stage, while some others were dead.

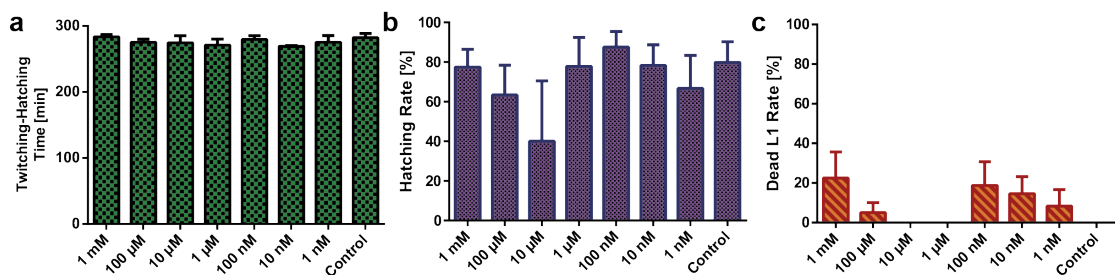


Figure 5.5 – Study of the development of N2 wild-type embryos under various tetramisole doses. (a-c) Influence of tetramisole doses on the twitching-to-hatching development time, the hatching rate of embryos and the lethality of the tetramisole dose on the initially hatched L1 worms. All measurements are based on N = 5 to 12 embryos per experimental condition.

5.3.2 Effect of tetramisole dose on the larval development: growth parameters

Levamisole and other anthelmintic chemicals were established to behave as cholinergic agonists on *C. elegans* [140, 141]. The nematodes typically exhibit certain distressed responses

to such agonist compounds, in particular at elevated concentrations [142, 143]. We observed the growth dynamics of N2 wild-type nematodes in their chambers, when exposed to 1 nM to 1 mM tetramisole concentrations. Our automated video processing script allowed us to accurately quantify longitudinal phenotypes (as explained in the Subsection 3.3.3). From the spline fits of the larval body during post-analysis of the images, we derived the influence of tetramisole dose on the worm length from the initial L1 stage until 80 hours of nematode development. We utilized partial agonist fits on our data to illustrate the correlation between different tetramisole doses to the control condition. We saw that doses in the range of 1 nM - 10 μ M did not cause any development lag, as determined from the length of the worms (Figure 5.6a, b). However, extreme doses of 100 μ M and 1 mM of tetramisole demonstrated a severe effect – as seen by a drop of the maximum length of 62% and 72%, respectively – evidencing a lag in the worms' development (Figure 5.6c). A similar study was also performed taking the worm area as a phenotypic parameter. There too, tetramisole doses in the range of 1 nM - 10 μ M confirmed no significant area-wise change compared to the control condition (Figure 5.6d, e), while 100 μ M and 1 mM conditions indicated, once again, a drop of 62% and 72% in the maximum worm area compared to the worms under control condition, respectively (Figure 5.6f). Hence, we could confirm that high concentrations of tetramisole (100 μ M and 1 mM) caused considerable development lag during the nematode life cycle.

A significant advantage of our microfluidic platform was to isolate single nematodes and observe individual phenotype changes under logarithmic tetramisole concentrations. Our approach empowers visual tracking of the single nematode development at various time points of the experimentation at high-resolution. Therefore, we categorized the real-time high-resolution images of the nematodes – extracted from the video recordings – at designated time points and created a comparative image as an example (Figure 5.7). After the initial hatching of the embryos – labeled as 0 hours – we perceived a growth behavior variation depending on the tetramisole concentration. From 12 hours up to 48 hours, the distinction of the growth profile between nematodes exposed to 0 - 10 nM and 100 nM - 1 mM doses became apparent. We noticed that, after 48 hours of development, the control, 1 nM and 10 nM tetramisole concentrations, permitted the nematodes to reach the adult stage (as evidenced by the first embryo progeny development observed inside the nematodes). On the other hand, the developmental lag of the nematodes exposed to 100 μ M and 1 mM concentrations is clear from Figure 5.7. Our study thereby allowed determining the whole development dynamics of single nematodes under different chemical conditions thanks to the high-resolution imaging and this in a longitudinal fashion at selected time points during their development. By simply changing the video recording interval, we eventually could obtain real-time images in a more frequent way.

5.4. Effect of tetramisole dose on the larval motility and correlation with the growth parameters

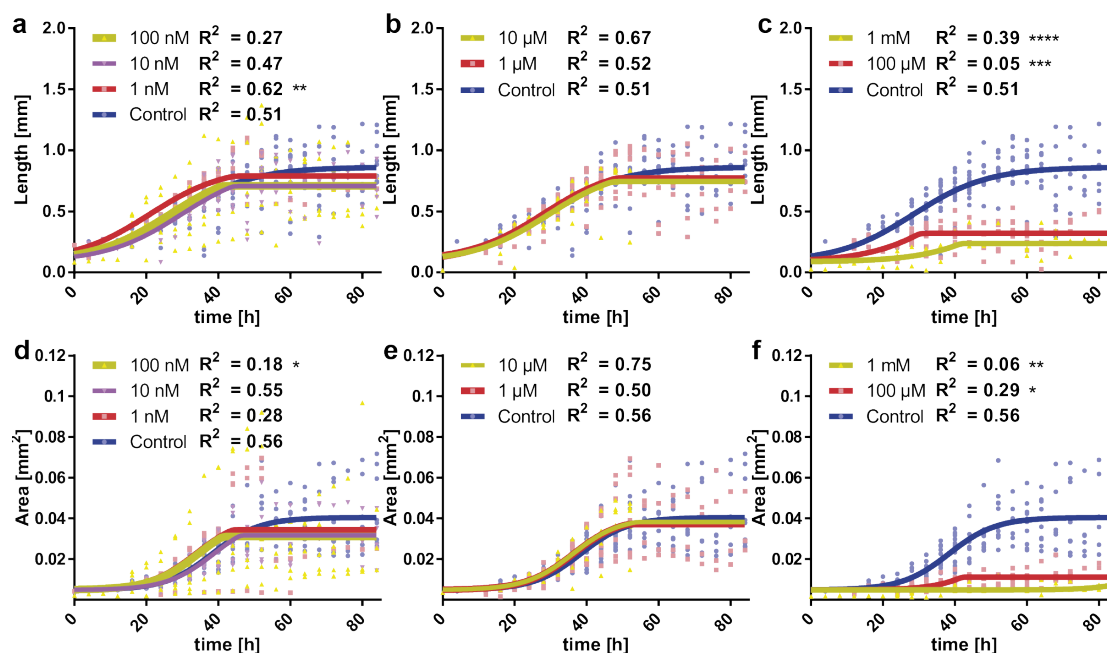


Figure 5.6 – Study of the life cycle development of N2 wild-type nematodes under various tetramisole doses. (a-c) Influence of tetramisole on the length of wild-type nematodes with doses of (a) 1-100 nM, (b) 1, 10 μM and (c) 100 μM, 1 mM compared to the control condition. (d-f) Influence of tetramisole on the area of wild-type nematodes with doses of (d) 1-100 nM, (e) 1, 10 μM and (f) 100 μM, 1 mM compared to the control condition. Partial agonist fits are used and R² values are noted. Data are expressed as mean ± SEM, * p ≤ 0.05, ** p ≤ 0.01, *** p ≤ 0.001, **** p ≤ 0.0001. All measurements are based on N = 5 to 12 worms per experimental condition.

5.4 Effect of tetramisole dose on the larval motility and correlation with the growth parameters

Anthelmintic compounds are also known to exhibit significant changes in the motility behavior of nematodes or parasites [144]. Previous research on this phenomenon demonstrated that in addition to the influence of levamisole on the velocity of *C. elegans* and *Oesophagotomum dentatum*, there was a significant drop in the response. Technically a worm is defined responsive if the area covered by a worm's travel is larger than the area of a circle with a radius equal to the worm's body length [145]. The levamisole sensitivity of *Oesophagotomum dentatum* was also established by capturing motility phenotypes such as propagation velocity, wavelength, wave amplitude and oscillation frequency [146]. The half-maximal effective concentration (EC₅₀) of anthelmintic compounds that was derived from lifespan, survival or motility phenotypes also proved to be valuable to quantify an anthelmintic drug's influence on the nematode [147]. In addition to the larval development parameters, we selected therefore four phenotypic motility parameters, namely, central velocity, head amplitude, beating frequency and tail amplitude, to study the tetramisole dose-effect on *C. elegans* as a function of development

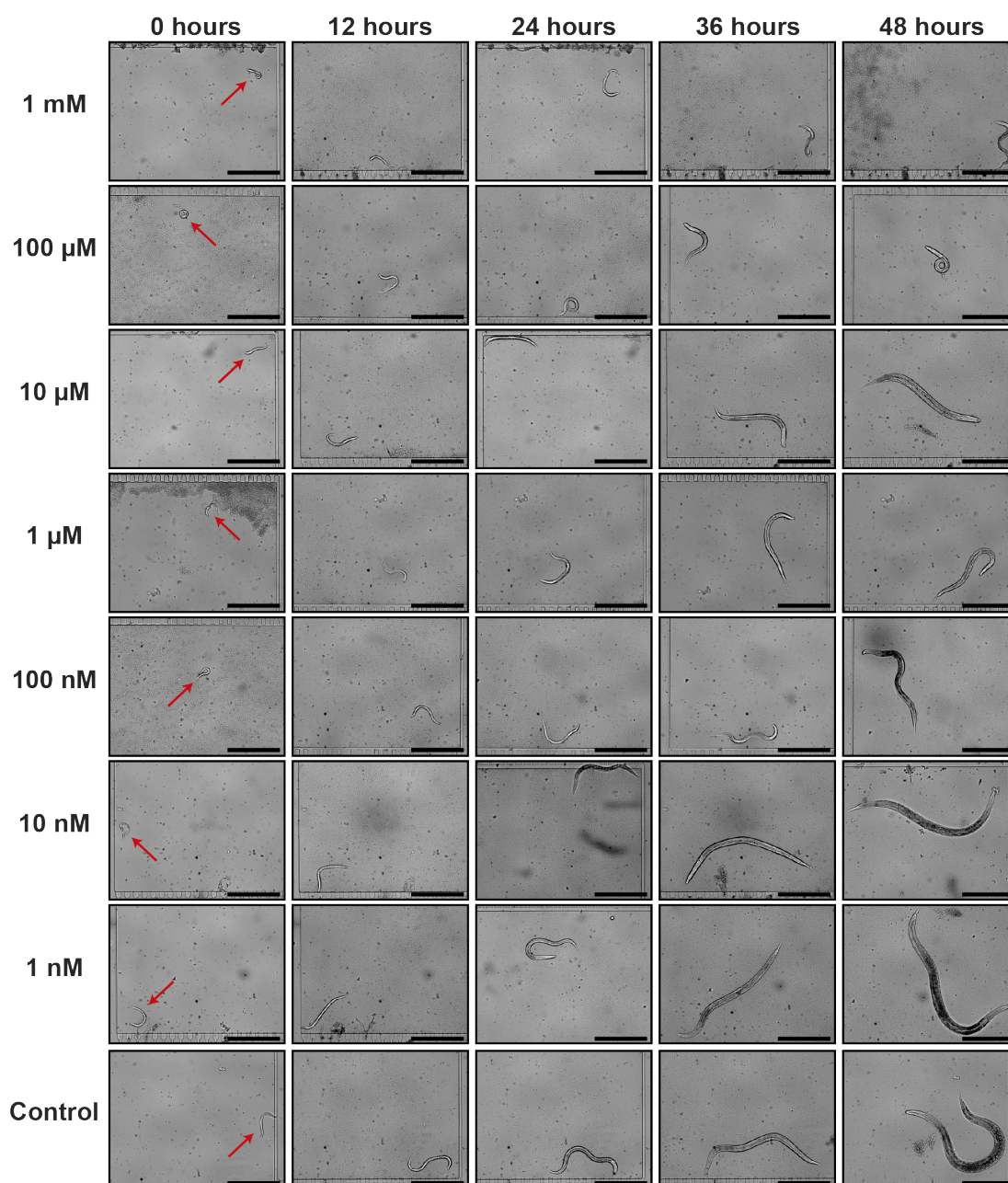


Figure 5.7 – Example of real-time images of the development of N2 wild-type nematodes under various tetramisole dilutions. Worm development under 1 mM, 100 μ M, 10 μ M, 1 μ M, 100 nM, 10 nM, 1 nM and control (0 mM) tetramisole concentrations diluted in *E. coli* solution at 0, 12, 24, 36 and 48 hours after the hatching of the embryo. Scale bars: 300 μ m.

time. We analyzed the dose-dependent effect of tetramisole by focusing on a few time points in the nematodes' life and generating percentage response curves – relative to the control – in order to characterize the time-dependent effect of tetramisole. Therefore, we normalized all the phenotypic data by their corresponding mean control value, and we focused in particular

5.4. Effect of tetramisole dose on the larval motility and correlation with the growth parameters

on two time points, namely 36 and 48 hours, at which the dose-response behavior was evident. Additionally, we quantified for each time point the half-maximal inhibitory concentration (IC_{50}) as an additional indicator for the dose-response curves.

Our device allows studying of several phenotypes on single worms at high precision, from which dose-response curves were created. No other platform to the best of our knowledge can provide such precise phenotyping of single worms in an automated manner. Based on our state-of-the-art device and approach, a clear response was obtained for all six phenotypes at 36 hours (Figure 5.8). The two growth parameters, length and area, indicated a behavior characterized by low deviations from an IC_{50} fit, with IC_{50} values of 46 and 43 μM , respectively (Figure 5.8a, b). For the motility parameters, although an evident percentage response for the central velocity (the average distance the worm travels within a video frame of 10 seconds) and the beating frequency (the number of worm thrashes within a second) was observed, the large standard deviations at certain tetramisole molarities, such as at 10 nM, caused an ambiguous fit and the algorithm could not deduce an IC_{50} value (Figure 5.8c, d). Interestingly, at this time point, the head and tail beating amplitudes (the total movement of the worm's head and tail within a video frame, respectively) were harshly affected at even lower concentrations (Figure 5.8e, f). Our analysis revealed IC_{50} values for these two phenotypes at 5 and 2 nM, respectively. Thanks to our platform, we could capture the whole dynamics of the worm development and motion in time and we found that the effect of tetramisole on the motility sets on earlier (at much lower concentrations) than when an influence on the growth parameters is noted. We should note that the large variations in the motility phenotypic parameters might also be affected by the random data sampling, as different worms might alternate arbitrarily between activity and resting periods, also known as sleep-like states [148]. Therefore, while IC_{50} values obtained from growth parameters can draw meaningful conclusions with percentage response curves, one should bear in mind that the presence of eating-sleeping cycle of worms complicates the analysis of the motility parameters. A significant phenotypic impact due to exposure to tetramisole was also observed at 48 hours (Figure 5.9). For the higher mentioned reason, though tetramisole results in an apparent influence on the worms, due to the relatively large variation of the phenotypic parameters, an IC_{50} value cannot be derived in most of the cases. Figures 5.9a and 5.9b show however that IC_{50} values should be in the range of a few 10 μM , consistent with Figure 5.8a, b. We could obtain from the percentage response behavior of Figures 5.9d and 5.9f an IC_{50} value of 2 and 14 μM , respectively. Such increasing IC_{50} value with respect to the 36 hours time point could be explained eventually by the nematodes having gained certain tolerance to the anthelmintic [149].

We detailed the longitudinal results of the motility phenotypes (over the full 80 hours of experimentation) in Figures 5.10 and 5.11. The central velocity displayed that worms' motion was not distinguishable from the control up to 10 μM tetramisole concentration (Figures 5.10), while worms were rather immobile at 100 μM and 1 mM tetramisole concentrations throughout the experiment. A similar behavior was also noted on the head amplitude profile. However, the beating frequency results did not display such behavior at high tetramisole concentrations and it revealed a dose-independent profile as a function of time (Figures 5.11). In parallel to the head amplitude study, the tail amplitude behavior up to 10 μM was not significantly

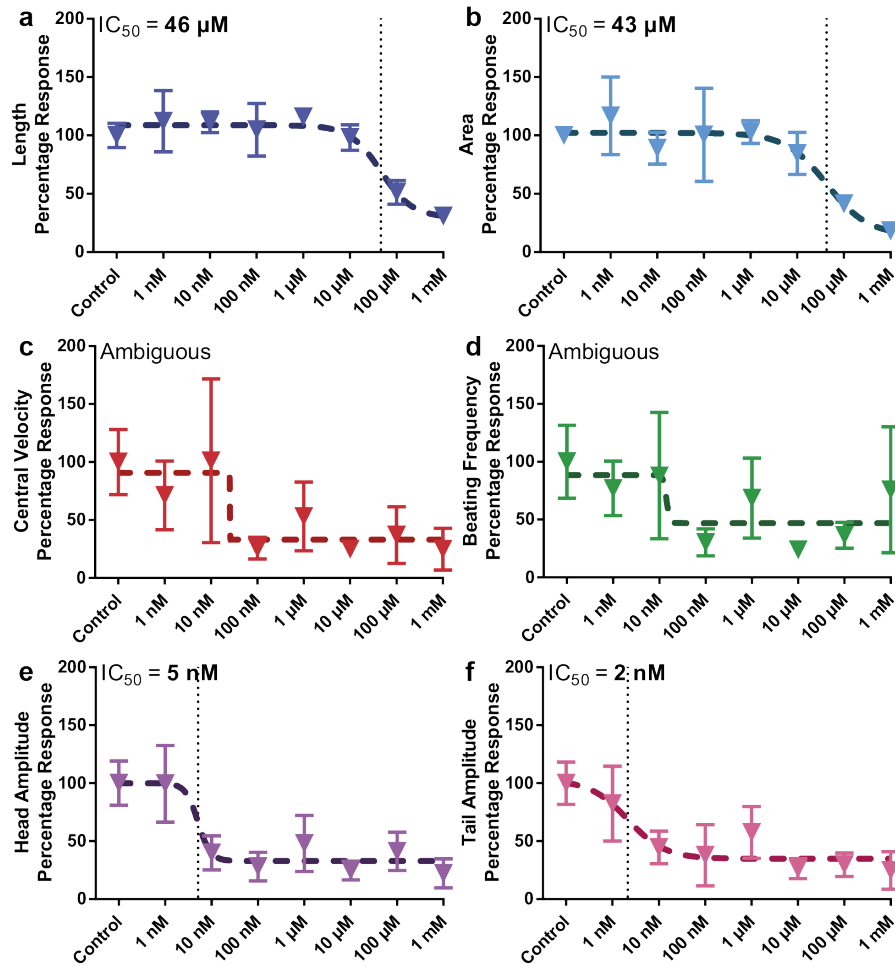


Figure 5.8 – Dose-dependent development and motility percentage response of N2 wild-type nematodes under various tetramisole concentrations at 36 hours in their life. Dose-dependent percentage response of (a) length, (b) area, (c) central velocity, (d) beating frequency, (e) head and (f) tail beating amplitude profile of wild-type nematodes are illustrated. All measurements are based on N = 5 to 12 worms. IC_{50} doses are noted. Data are expressed as mean \pm SEM.

different from the control, but at 100 μM and 1 mM tetramisole concentrations, the movement was reduced. Of note, a significant change in head and tail amplitudes ($p \leq 0.05$) were noticed at 1 mM tetramisole concentration compared to the control condition indicating a severe movement restriction at this concentration (Figures 5.10 and 5.11). Overall, the longitudinal phenotyping of the motility parameters did not clearly highlight an anthelmintic dose influence on the nematodes. As illustrated here, our platform however brings significant advantages in terms of tracking the whole dynamics of single worms under a chemical exposure and thus obtaining phenotypic data longitudinally or with a dose-response approach. We also studied a dose-response behavior at an earlier life stage of the nematode, more specifically at 24 hours and we noticed that there was not a significant dose effect on the nematodes. The fact that nematodes in their early life stage were not affected by tetramisole was also

5.5. Effect of tetramisole dose on the larval motility by averaging the motility indices over the full experiment duration (80 hours)

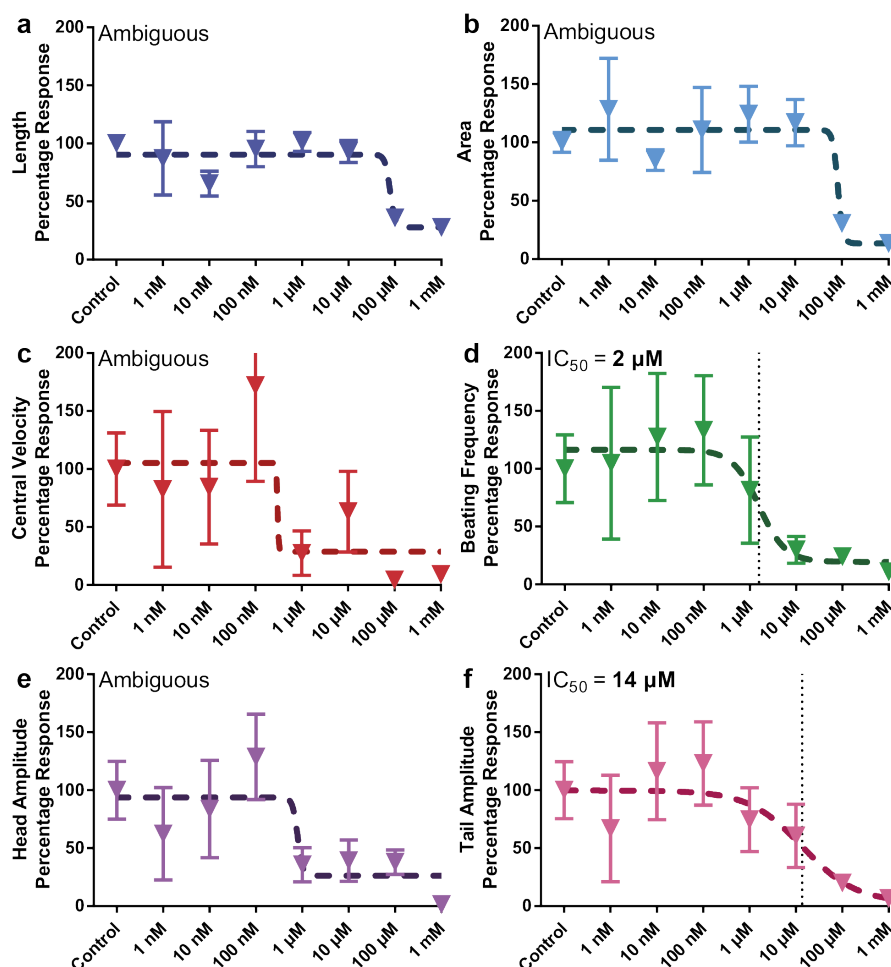


Figure 5.9 – Dose-dependent development and motility percentage response of N2 wild-type nematodes under various tetramisole concentrations at 48 hours in their life. Dose-dependent percentage response of (a) length, (b) area, (c) central velocity, (d) beating frequency, (e) head and (f) tail beating amplitude profile of wild-type nematodes are illustrated. All measurements are based on N = 5 to 12 worms. IC_{50} doses are noted. Data are expressed as mean \pm SEM.

previously demonstrated by observing the low sensitivity of larvae compared to adult worms to emodepside, an anthelmintic drug that is effective against gastrointestinal nematodes [150].

5.5 Effect of tetramisole dose on the larval motility by averaging the motility indices over the full experiment duration (80 hours)

As shown in previous section, the tetramisole dose-response analysis at the individual time points presented significant variation. Hence, a more time-invariant assessment could eventually better highlight the tetramisole influence on the nematodes. For this purpose, we focused

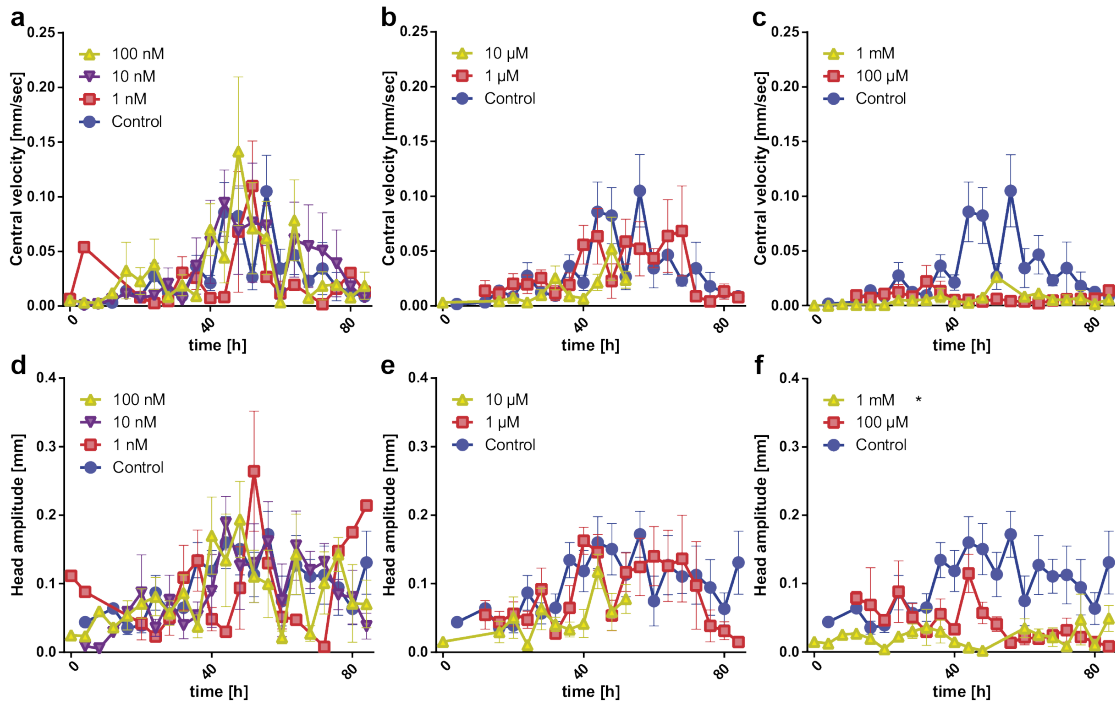


Figure 5.10 – Central velocity and head amplitude variation of N2 wild-type nematodes under various tetramisole concentrations. (a-c) Influence of tetramisole on the central velocity of wild-type nematodes with doses of (a) 1-100 nM, (b) 1, 10 µM and (c) 100 µM, 1 mM compared to the control condition. (d-f) Influence of tetramisole on the head beating amplitude of wild-type nematodes with doses of (d) 1-100 nM, (e) 1, 10 µM and (f) 100 µM, 1 mM compared to the control condition. Data are expressed as mean \pm SEM, * $p \leq 0.05$. All measurements are based on N = 5 to 12 worms.

on the time-averaged (80 hours of experimentation) motility indices and provided IC_{50} points corresponding to the different phenotypic parameters (Figures 5.12). For each phenotype, we averaged all the values at a certain concentration in time and then normalized by the corresponding control value. For the dose-response curve of length, we found the IC_{50} point to be at 38 µM (Figures 5.12a) and for the area at 27 µM (Figures 5.12b). We also fitted the central velocity data, one of the most important motility parameters, indicating an IC_{50} value of 5 µM (Figures 5.12c). The same analysis was also performed for the beating frequency, but we could not well deduce any IC_{50} value for this analysis due to the data point at 1 mM tetramisole concentration (Figures 5.12d). We additionally investigated the time-averaged percentage response of the head and tail beating amplitudes (Figures 5.12e, f) and found an IC_{50} value of 5 and 7 µM for the head and tail beating amplitudes, respectively. In summary, from the time-averaged data we find that while an IC_{50} value of 5 - 10 µM exists for the motility parameters, an IC_{50} value of 30 - 40 µM is obtained for the growth parameters. This difference between growth and motility phenotypes is probably due to sleep-like states of *C. elegans* that affect computation of the time-averaged motility phenotypes. Additional to our novel technology, the demonstrated case study shows that our device can be eventually used in

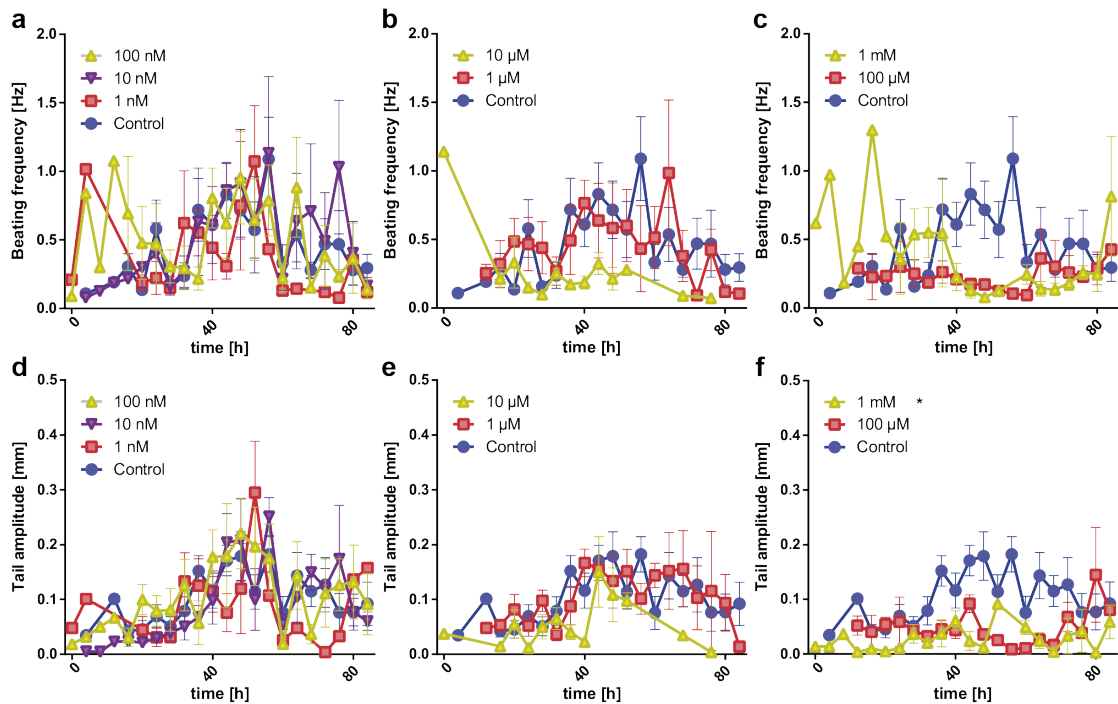


Figure 5.11 – Beating frequency and tail amplitude variation of N2 wild-type nematodes under various tetramisole concentrations. (a-c) Influence of tetramisole on the beating frequency of wild-type nematodes with doses of (a) 1-100 nM, (b) 1, 10 µM and (c) 100 µM, 1 mM compared to the control condition. (d-f) Influence of tetramisole on the tail beating amplitude of wild-type nematodes with doses of (d) 1-100 nM, (e) 1, 10 µM and (f) 100 µM, 1 mM compared to the control condition. Data are expressed as mean \pm SEM, * $p \leq 0.05$. All measurements are based on N = 5 to 12 worms.

future to capture the influence of sleep-like states on the nematode phenotypes.

5.6 Statistical analysis

Data from raw images were extracted to fill an array for statistical tests with Graphpad Prism. The embryo twitching-to-hatching development time, the hatching rate and the dead L1 rate data of N2 wild-type embryos and worms were analyzed for statistical significance using one-way ANOVA. The longitudinal larval development and motility parameters of N2 wild-type worms were analyzed for statistical significance using Repeated Measures one-way ANOVA by taking the mean of the values at every 4 hours. Mean values were computed to represent in graphs when measurements were repeated in multiple batches. For 1 mM, 100 µM, 10 µM, 1 µM, 100 nM, 10 nM, 1 nM and the control condition, we had 5, 7, 7, 7, 8, 7, 5, 12 worms, respectively. This distribution was obtained by combining four separate experiments together.

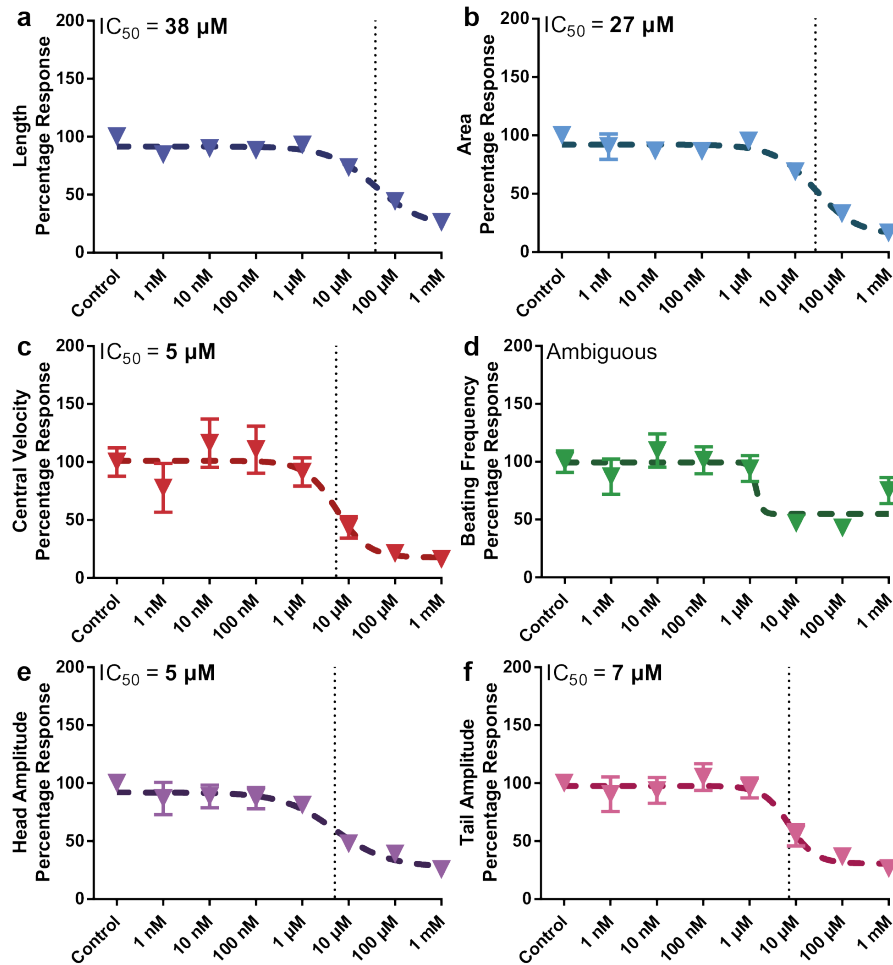


Figure 5.12 – Dose-dependent development and motility percentage response of N2 wild-type nematodes under various tetramisole concentrations. Time-averaged (a) length, (b) area, (c) central velocity, (d) beating frequency, (e) head and (f) tail beating amplitude index of wild-type nematodes are illustrated. All measurements are based on N = 5 to 12 worms. IC_{50} doses are noted. Data are expressed as mean \pm SEM.

5.7 Discussion and conclusion

In this work, we presented a new microfluidic platform, which empowered multiplexed, automated, potentially high-throughput, and high-resolution studies of *C. elegans* in both the embryonic and post-embryonic stages exposed to eight different tetramisole concentrations in parallel and allowing single worm phenotyping resolution. Additionally, we provided high-content phenotypic results of the larvae by our automated video analysis script and operator-based observations of the embryo development. We could culture the nematodes up to 80 hours with no problem of bacteria clogging or aggregation, as enabled by our 24 parallel filter structures in between growth chambers and the use of a silanization procedure. We tracked the same nematode from the embryonic stages to the late adult stage by utilizing

repeatable fluidic script commands that washed off late progenies. We traced the phenotypes associated to each single worm and obtained population-based statistics. Unlike previously proposed microfluidic platforms for single animal resolution, we removed all possible active on-chip components and designed an easy-to-use and easy-to-fabricate microfluidic platform. Utilizing just an inlet and outlet tube per microfluidic lane, we could load embryos inside growth chambers individually and simplify considerably nematode culture. Furthermore, we reported on two types of platform-associated automation processes. Considering the fluidic protocol, we delivered semi-automation for the initial embryo loading step, placement of the embryos in the embryo pockets, and pushing them into the individual chambers. Occasional manual fluidic commands were required to clear the serpentine from embryos. We adjusted our fluidic parameters such that there was a minimal worm loss during the worm culture and to establish rapid removal of late progenies. The other part of our automation was dedicated to the phenotyping by utilizing our video processing script, with which we could automatically study four motility and two development parameters.

We obtained our high-yield embryo collection through a standard bleaching procedure and we reduced the initial experimental preparation to a minimum level. After placement of these embryos inside the embryo incubators situated in the growth chambers, we observed the main embryonic stages clearly thanks to our time-lapse imaging. The development of larval stages were also conveniently detected with 10 seconds videos taken every 4 hours at high-resolution. Throughout all experiments that were conducted, we calculated an average growth chamber single embryo occupancy of 91%. Due to their natural sticky behavior, embryos sometimes attached strongly to the embryo pockets, after which they could not be dispensed easily inside the growth chambers. We computed an average embryo hatching rate of 70% in the growth chambers, the 30% loss most likely being due to the impact of the bleaching procedure used for embryo harvesting from the agar plate. Around 10% of the successfully hatched embryos died during the L1 larval stage. While these three phenomena lead to only 57% of all chambers having single worm occupancy, the actual value was calculated to be 50%. This drop was a result of worm departure through the embryo pockets, which happened from time to time during the first bacterial injection after embryo hatching.

To validate our microfluidic platform, we explored the influence of an anthelmintic drug, tetramisole, on the life cycle phenotypes of *C. elegans*. For this purpose, throughout the life stages of the nematodes, we provided logarithmic dilutions of tetramisole in *E. coli* solution to the embryos and worms. Our results revealed that, towards the late stages of the nematode life, tetramisole influence on the development and motility became more prominent, while a variable behavior in terms of IC_{50} values was observed at the different time points studied. We think that the variations in the motility phenotypic parameters might be affected by the random data sampling as obtained by recording of the 10-second video sequences, during which different worms might alternate arbitrarily between activity and resting periods. Additionally, we computed the time-averaged motility indices to obtain a more time-invariant influence of tetramisole on *C. elegans*, and we noted IC_{50} values in the range of 5 - 10 μM and 30 - 40 μM for the motility and growth parameters, respectively. We presume that such variation was due to the sleep-like states of worms at certain time points of the video recording.

Chapter 5. Automated platform for life-long and high-content phenotyping of single *C. elegans* worms

In short, we demonstrated an automated, integrated, multiplexed, long-term *C. elegans* culturing platform at single animal resolution, which was also equipped with an automated high-content phenotyping algorithm. Thanks to our platform, we could observe both embryonic and post-embryonic stages under various compound influences and provided rapid and high-content phenotypic results. Our device offers not only high precision to phenotype the impact of chemicals and drugs on *C. elegans*, but can also be used to characterize genetic (e.g. RNAi) interference to a high level of granularity.

6 The detection of early epigenetic inheritance of *C. elegans* with a microfluidic phenotyping platform

Fluctuations and deterioration in environmental conditions potentially have an impact on life that extends over generations. Epigenetics is the defined term for such transient inheritance, which is characterized by a non-alteration in the DNA sequence. The model organism *Caenorhabditis elegans* is exceptionally valuable to address epigenetics due to its short lifespan, well-mapped genome and hermaphrodite behavior. While the majority of the epigenetics on the nematodes focuses on generations-wide heritage, short-term and in-depth analysis of this phenomenon in a well-controlled manner has been lacking. Here, we present a novel microfluidic platform to observe mother-to-progeny heritable transmission in *C. elegans* at high imaging resolution, under significant automation, and enabling parallelized studies. After approximately 24 hours of culture of L4 larvae under various concentrations and application periods of doxycycline, we investigated if mitochondrial stress was transferred from the mother nematodes to the early progenies. Automated and custom phenotyping algorithms revealed that a minimum doxycycline concentration of 30 µg/mL and a drug exposure time of 15 hours applied to the mothers could induce mitochondrial stress in first embryo progenies indeed, while this inheritance was not clearly observed later in L1 progenies. We believe that our new device could find further usage in epigenetic studies modeled on *C. elegans*.

This chapter is an adapted version of the following publication:

- **H. B. Atakan**, K. S. Hof, M. Cornaglia, J. Auwerx and M. A. M. Gijs, “The detection of early epigenetic inheritance of mitochondrial stress in *C. elegans* with a microfluidic phenotyping platform”, *Scientific Reports*, under review, 2019.

6.1 Introduction

Certain experiences and stress during the life of an organism can have significant effects on the successive generations [151]. Especially maternal stress can precede phenotypic alterations over the next generations [152]. Heritable phenotypic changes without alterations of the genotype are known as epigenetics [153]. For example, in humans, prenatal exposure to famine causes significant epigenetic changes resulting in adult disease risk [154]. This human epidemiological study showcases the need for understanding the effect of maternal/prenatal stressors on epigenetic modifications. These modifications are widely acknowledged as a crucial factor in the control of gene expression, influencing the phenotypes of multicellular organisms [155]. Various model organisms are used for understanding of complex biological pathways and their epigenetic regulations [156], including plants, mice and *C. elegans* [157]. Although these model organisms show insight into the transmission of epigenetic information through the germline, the occurrence of this phenomenon in humans is inconclusive [158]. One of the main model organisms, *C. elegans*, offers the opportunity to study the mechanisms of epigenetics due to its fully sequenced genome, well-studied genetics, near exclusive hermaphrodite population and short lifespan [8, 159]. Therefore, a great deal of the research on the epigenetic inheritance has been performed on *C. elegans* as a model organism. Up to three generations of nematodes originating from famished mothers generated increased lifespan [160] and maternal food availability decreased progeny reproduction in food-sufficient environments [161]. Additionally, maternal age generated variations in the size at hatching, speed of development, growth rate and fecundity in the next generations [162]. Exposure of high glucose concentrations to *C. elegans* in the parental generation led to opposing effects on fertility, while providing protection against cellular stress in the descendent progenies [163]. Temperature-induced changes showed that for at least 14 generations, long-lasting epigenetic memory of environmental change can be stored [164]. Deficiency in the chromatin modifiers in the parental generation extended the lifespan of the descendants up until the third generation [165]. Most of these works focused on long-term and generation-wide epigenetic inheritance.

Short-term analysis of the effects of stressed mothers on development during the embryonic and first larval stages is a field of epigenetic inheritance research that is perfectly compatible with microfluidics. The main challenge in the short-term epigenetic studies in *C. elegans* is to establish a sustainable approach to obtain sufficient data of both the parental generation and the progenies at high-resolution. Such procedures require assisting tools, like offered by microfluidics and LoC technologies, to accomplish both tasks at the same time instead of standard agar plate-based methods [166]. While early *C. elegans* epigenetics has not been explicitly studied in microfluidic chips, several platforms have been proposed which could have been suitable for studies of parental generation's transition to the progenies. Combination of PDMS-based devices with agarose gels showed that single nematode resolution culture and first progeny tracking was possible, although these methods were laborious and a supply of a well-adjusted concentration and time profile in applying food or a drug could be problematic [37, 38, 39]. A microfluidic device with a built-in dissection board was de-

6.2. Microfluidic phenotyping platform design and operation

signed to extract embryos from adult nematodes [104]. The relatively low-throughput and laborious protocols of such devices, however, may dramatically disfavor their usage. Worm development studies in worm culture chambers in PDMS devices at single or multiple animal resolution have also been proposed. While these devices could be adapted for progeny studies too, they employ complicated micro-fabrication protocols [51, 55] or they were designed to start the worm culture from the onset of L1 larval stage [56, 112, 167], resulting in absence of data in the embryonic experimentation window. Alternative worm culture devices for controlled progeny evacuation [58] or counting [59] have also been demonstrated. However, considerable amount of modifications were required to enable high-resolution imaging and experimental parallelization. A PDMS design with embryo incubators has been proposed to observe embryogenesis of the first embryo progenies [106]. This design was further modified to obtain first embryo progenies by mechanically compressing adult nematodes [107] or studying the development of embryos released from the parental generation in worm culture chambers [57]. Embryo incubators have been demonstrated to be ideal construction features for embryogenesis studies, but they lacked a mechanism to trap embryos permanently as embryos floated freely in the fluidic serpentine due to the natural shape of the incubators. A long-term adult worm trapping and embryo collection chamber has also been reported [33]. However, this device had a rather complicated micro-fabrication procedure and the identity of embryos inside the chambers was not conserved.

In this work, we present a microfluidic device for the observation of mother-to-progeny epigenetic inheritance in *C. elegans*. This new device provides impeccable trapping and identity tracking of a single *C. elegans* embryo at high-resolution and in a parallel fashion, in combination with statistical analysis. We provided significant automation in experimentation and post-experiment data analysis, empowering recording of high-content data from the mothers, embryos and L1 progenies. As mitochondria play a central role in epigenetic alterations [168], epigenetic inheritance of mitochondrial stress in the early life stages of the progenies was selected as the platform's validation study. Using the UPR^{mt} reporter strain *hsp-6::gfp* allows to visualize mitochondrial stress, as this strain expresses GFP when mitochondrial function is destabilized. To mimic the mitonuclear imbalance, we have used doxycycline – an antibiotic drug that induces mitochondrial proteostasis – at different concentrations and application conditions in order to investigate if epigenetic inheritance of the mitochondrial stress occurs. Our results revealed that a dose-dependent maternal nematode treatment resulted in mitochondrial stress in the embryos of the next generation indeed and that this inheritance could possibly be maintained in L1 progenies.

6.2 Microfluidic phenotyping platform design and operation

6.2.1 Microfluidic chip design

Our main design requirements were (i) to minimize the need of fluidic control operations, and (ii) to track the transition of the parental generation to its progenies. We established a microfluidic design that allows the loading and culture of the mother nematodes, and isolation

Chapter 6. The detection of early epigenetic inheritance of *C. elegans* with a microfluidic phenotyping platform

and observation of the progenies. Our design consists of eight parallel microfluidic lanes, each lane having a single media inlet and a media outlet (Figure 6.1a). We integrated a worm culture chamber in each microfluidic lane to culture nematodes from the L4 larval stage to the adult stage. A fluidic serpentine, which was designed to accommodate embryos after being laid from the mother nematodes, was also incorporated next to a worm culture chamber. The worm culture chamber has a size of $1540\ \mu\text{m} \times 2385\ \mu\text{m} \times 80\ \mu\text{m}$, which was experimentally tuned to accommodate up to 30 nematodes (Figure 6.2). The media inlet side of the growth chambers consists of 32 constriction filters with a width of $10\ \mu\text{m}$ to prevent L1 progenies from escaping. The serpentine side of the growth chambers consists of 32 constriction filters with a width of $24\ \mu\text{m}$, which is tight enough to retain L4 larvae in the chamber and release embryos only upon a fluidic pressure increase from the worm culture chambers to the fluidic serpentine. A released embryo is located in one of the 25 embryo incubators and subsequently, forced to a tight confinement in the neighboring embryo trap. This microfluidic design is implemented in a PDMS part that has a size of $53\ \text{mm} \times 35\ \text{mm}$. A $75\ \text{mm} \times 38\ \text{mm}$ glass microscope slide is used as the sealing part to cover the entire PDMS surface (Figure 6.1b).

6.2.2 Platform working principle

We used a 12-port syringe valve during the experiments. We reserved two ports of the 12-port valve as a backup (in case of a clogging in any of the other ports), and connected one port to a waste reservoir and another to an S-medium reservoir (Figure 6.1c). Any waste generated during the worm and bacteria loading, was disposed in the waste reservoir. S-medium was supplied from its reservoir to transfer embryos out of the worm culture chambers and place them inside embryo traps. S-medium injection was also utilized to break any *E. coli* aggregate apart during the bacterial feeding of the nematodes. The remaining eight ports were linked to each media inlet of the microfluidic chip. This approach provided the maximum throughput that could be delivered with a 12-port valve. We relied on passive hydrodynamics – excluding any integration of on-chip components, such as pressure valves – during the course of the experimentation. The media outlets were interchangeably coupled to a L4 suspension, *E. coli* solution and S-medium solution reservoirs. While the L4 suspension contained L4 larvae suspended in S-medium solution, *E. coli* and S-medium solution reservoirs contained doxycycline at 0, 15, 30 or $60\ \mu\text{g}/\text{mL}$ concentrations. Three different objectives – $4\times$ (0.1 NA), $10\times$ (0.45 NA) and $20\times$ (0.4 NA) – were mounted on the setup and used, depending on the need of the experiment for high-resolution. A $4\times$ objective was selected while acquiring time-lapse images of the mother nematode development in the worm culture chambers, as it completely covered the observation of a worm culture chamber (Figure 6.1d). A $20\times$ objective was chosen to record the physiological properties and fluorescent intensity expression of L1 progenies by scanning through a worm culture chamber to collect data. A $10\times$ objective was seldom utilized for the same purpose. For the observation of embryogenesis and the progression of the mitochondrial stress in the embryos, a $20\times$ objective was found to be ideal to visualize two embryos in a single motorized stage position for time-lapse imaging (Figure 6.1e).

6.2. Microfluidic phenotyping platform design and operation

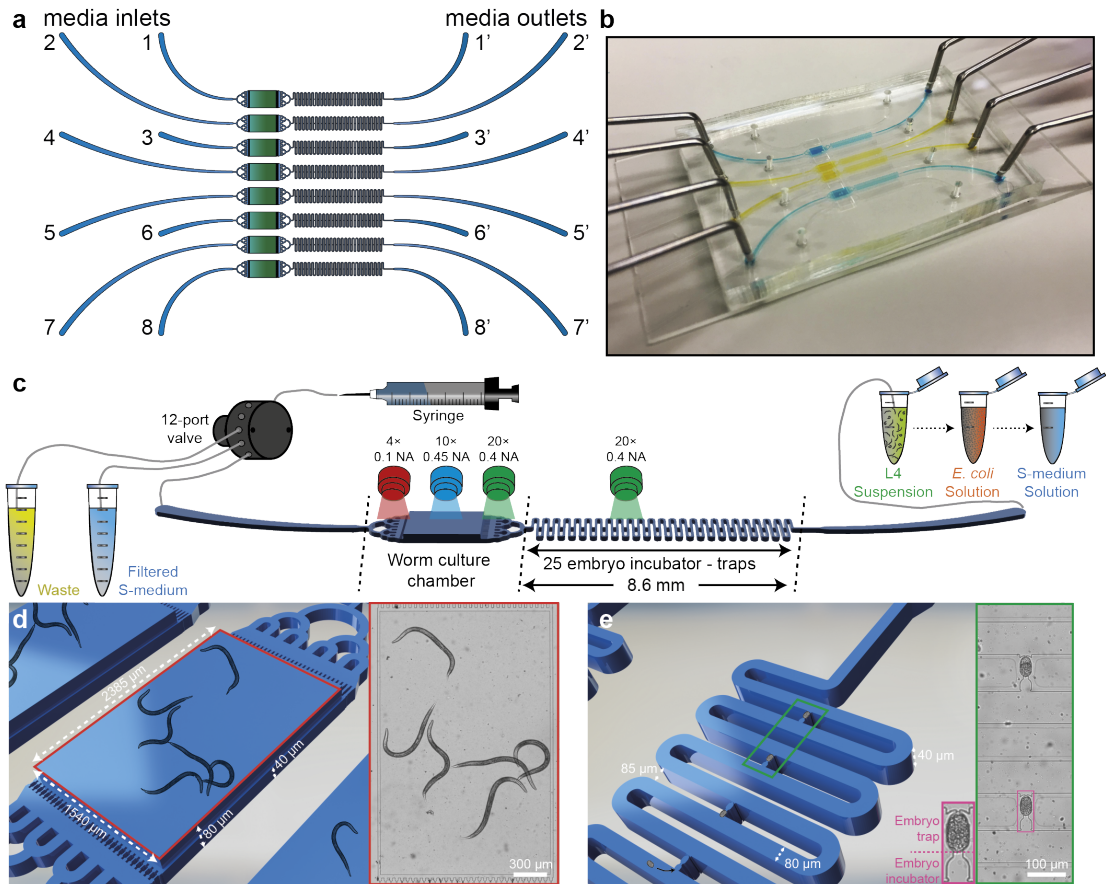


Figure 6.1 – Details of the mother-to-progeny development platform for the automated phenotyping of the larvae and embryos of *C. elegans*. (a) Schematic drawing of the microfluidic device, which consists of eight lanes, each of which having a culture chamber for the worm development from the L4 larval stage to the adult stage and a serpentine with 25 embryo incubators and traps for the first progeny imaging. (b) Real-time image of the microfluidic chip, which is filled with liquid dye solutions. (c) Representation of the platform operation. (d) Three-dimensional (left) and real-time (right) images of a worm culture chamber with the key feature sizes marked. (e) Three-dimensional (left) and real-time (right) images of a serpentine with embryo traps and incubators labeled and feature sizes marked.

6.2.3 Fluidic experimentation protocol

We created a semi-automated fluidic pipeline to reduce operator-based errors to a minimum level. Prior to the experiment initialization, all the tubing and the syringe pump were sterilized by injecting 70% ethanol solution into the whole fluidic system, after which the ethanol solution was flushed out using S-medium solution. An L4 suspension reservoir was plugged to a media outlet and the nematodes were loaded in the chip by a media injection from the media outlet towards the media inlet, collecting nematodes at the entrance filters of each worm culture chamber (Figure 6.3a). A media amount of 3 μL were injected at a flow rate of 625 nL/s with 2 second breaks from the media outlet to allow L4 larvae to pass through the filters

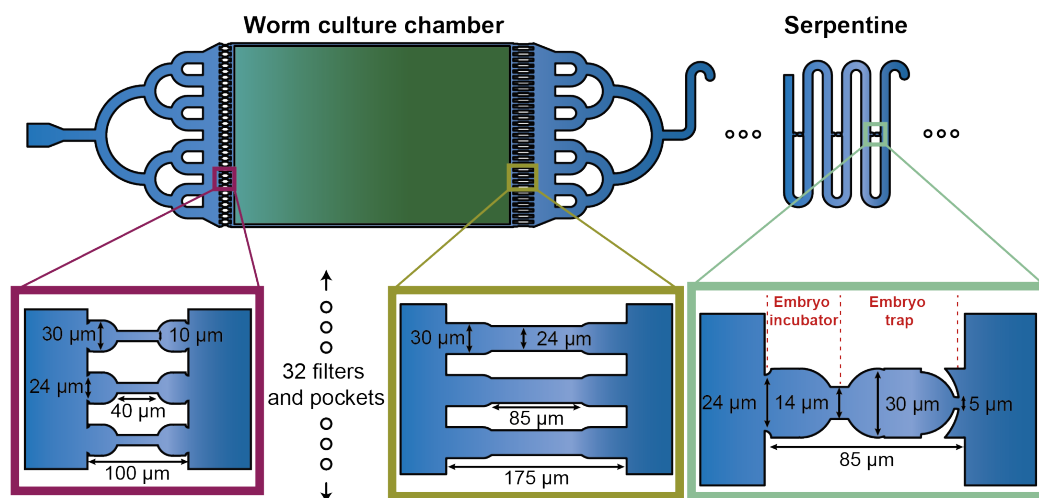


Figure 6.2 – Schematic representation of a worm culture chamber (left) and a serpentine with embryo traps (right) with zooms on key features. The right-hand side of the worm culture chambers consists of 32 parallel constriction filters with a width of 24 μm in order to be tight enough to (i) selectively capture all larval stages until up to the L4 larval stage and (ii) keep embryos inside the chamber. These filters are deformable to let embryos pass only under increased flow rates (2.3 $\mu\text{L/s}$). The serpentine is configured to act as a transfer layer for L4 larvae from the media reservoirs to the worm culture chambers and as an embryo transfer unit from the worm culture chambers to the embryo incubators.

and accommodate inside the chambers (Figure 6.3b). An L4 population of 5-30 worms could be cultured thanks to the optimized fluidic protocol and the well-tuned feature size of the worm culture chambers. Any possible early stage nematodes in a worm culture chamber and the excessive worms at the entrance of a culture chamber were washed off towards the media outlet by injecting S-medium from the media inlet at a flow rate of 104 nL/s (Figure 6.3c). The L4 suspension reservoir was then replaced by an *E. coli* solution reservoir and the bacterial solution was loaded from the media outlet at a flow rate of 156 nL/s. At the same time, a bright-field time-lapse imaging sequence was initiated with 30-minute intervals on the worm culture chambers until the first egg release. Every 15 minutes, S-medium was supplied from the media inlet at a flow rate of 104 nL/s to break any *E. coli* aggregate formation and then *E. coli* aspiration from the media outlet was resumed. The bacterial injection amount was kept 3.6 μL more than the S-medium supplied to ensure *E. coli* uniformity. The nematodes exhibited proper developmental behavior with this feeding protocol (see a worm culture image at 13 hours in Figure 6.3d). The feeding and the time-lapse sequence was terminated once worm culture chambers were occupied with first embryo progenies (Figure 6.3e). In a microfluidic lane-alternating manner, pulsed S-medium flow was supplied from the media inlet (an injection amount of 20 μL and a flow rate of 2.08 $\mu\text{L/s}$) and embryos in the culture chambers were first transferred to the embryo incubators (Figure 6.3f) and subsequently confined in the embryo traps (Figure 6.3g). After the finalization of the embryo trapping, the *E. coli* solution reservoir was replaced with an S-medium solution reservoir and 25 μL of solution

6.2. Microfluidic phenotyping platform design and operation

was aspirated. Hereafter, a time-lapse imaging sequence of 12 hours on two neighboring embryo traps with 10-minute intervals was initiated while providing a gentle flow of 104 nL/s from the media outlet side (Figure 6.3h). This sequence was employed in a dual bright-field and fluorescence imaging method to observe both embryogenesis and GFP expression of the embryos.

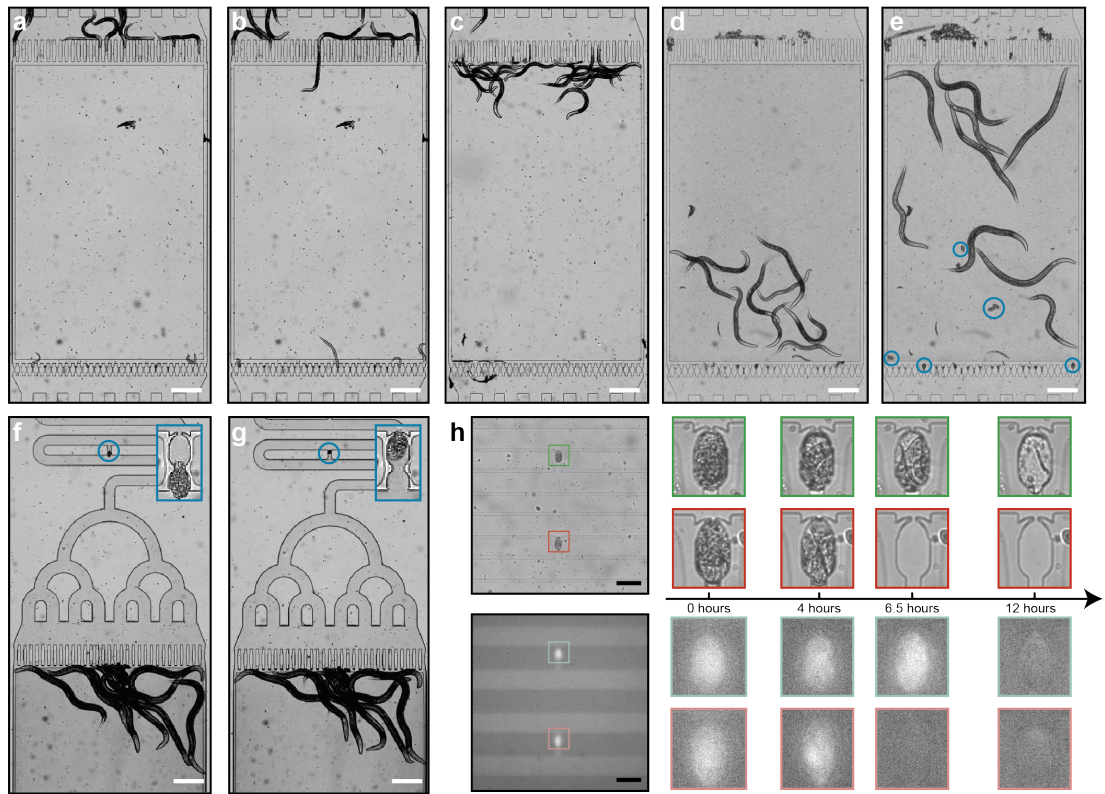


Figure 6.3 – Real-time images of the experimental protocol from the beginning of an experiment until the end. (a) Initially, L4 larvae are collected at the entrance of the worm culture chambers. (b) Nematodes are pulled inside the chambers via media aspiration by a pulsed media flow, whereby they pass tightly through the constriction filters. (c) Any young larvae located inside the chambers are pushed towards the media outlet. (d) The L4 larvae suspension reservoir is replaced by an *E. coli* solution reservoir and the bacterial feeding is initiated. An image after 13 hours of the experimental onset is shown. (e) The feeding is stopped when all culture chambers contain first embryo progenies (displayed in blue circles). A real-time image taken after 23 hours of the experimental onset is displayed. Hereafter, embryos are (f) first confined in an embryo incubator and right after, (g) they are placed inside an embryo trap where they will be analyzed. High-resolution images of embryo incubation and trapping sites are illustrated in the blue rectangles. (h) Time-lapse imaging starts during 12 hours of embryo development with 10-minute intervals (both bright-field and fluorescence imaging); the sample pictures represent two embryo traps in a single motorized stage position. Scale bars (a-g): 250 μm , scale bar (h): 100 μm .

6.3 Automated and operator-based post-experiment analysis

Automated analysis can reduce the human bias and speed up the data processing time as bioanalytical studies often require a large number of samples [169]. Various methods for high-throughput image acquisition and phenotyping of *C. elegans* have already been proposed [170]. In this work, we fashioned a novel approach for both automated and operator-based analysis of certain phenotypes of the nematode *C. elegans*. We employed three different image analysis algorithms after the finalization of an experiment (Figure 6.4).

6.3.1 Mother nematode size tracking analyzed with time-lapse imaging

We extracted phenotypes related to the mother nematodes and L1 progenies by utilizing images acquired on the worm culture chambers and first embryo progenies by using images obtained with time-lapse imaging on the embryo traps. The total area of the mother nematodes was computed from raw bright-field images that were captured during the time-lapse imaging (Figure 6.4a). Based on our work in Subsection 3.3.1, we applied background subtraction, standard morphological operations and image binarization to isolate the nematodes from the background. The resultant image constituted of only background-isolated nematodes with binarized pixel-intensity values, over which the total sum of non-zero pixels reported the total area of all the nematodes. The normalized area data was obtained by dividing the total area by the number of worms accommodated in the associated worm culture chamber. In parallel, operator-based observations were performed to extract embryo-related phenotypes, such as the first egg laying time, released embryo amount per worm and normalized egg release rate.

6.3.2 Operator-based phenotyping of L1 progenies

Another phenotype that could be obtained from the observation of the worm culture chambers was related to the L1 progenies (Figure 6.4b). Operator based measurements, utilizing open-source ImageJ software, were performed by tracing a spline through L1 larvae. The measurement result of the entire spline was noted as the length of the worm, while the diameter (or the width, as the worms were assumed cylindrical) was measured as the perpendicular line to this spline fit near the worm's vulva. Similarly, a worm was marked with a freehand line on its edges. By computing the average and the maximum pixel-intensity values within this geometry, the average (also noted as mean) and the maximum fluorescent intensity expressions, respectively, were deduced. These values were normalized by the background intensity, which was measured by computing the average pixel-intensity value on random circles drawn in the worm-free areas.

6.3.3 Embryo viability and fluorescent signal expression tracking

Another automation script was created to track the viability and fluorescent intensity expression of *C. elegans* embryos in the embryo traps (Figure 6.4c). We first detected the location

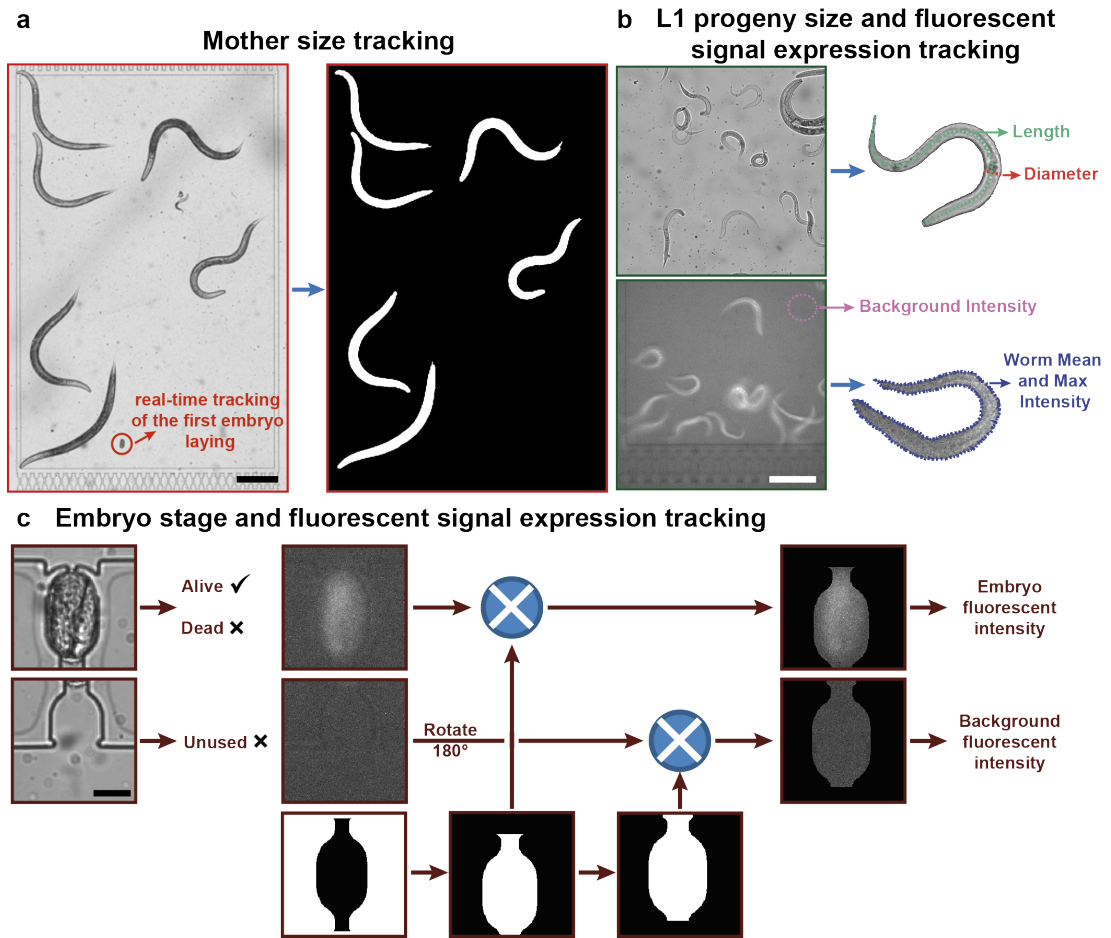


Figure 6.4 – Overview of the image processing approaches employed for the phenotyping of *C. elegans*. (a) For the size detection of the mother worms, we capture bright-field time-lapse images with 30-minute intervals. For each captured image, the background is subtracted, standard morphological operations are applied and a binary image is created for the area detection. Operator-based observations are additionally performed to detect first embryo laying time, amount of embryos released per worm and egg release rate. Scale bar: 250 μm . (b) L1 progeny size and fluorescent intensity expression tracking is performed to analyze morphological properties and fluorescence intensity expression of the nematodes. Scale bar: 150 μm . (c) The automated embryo development algorithm is initiated to locate alive embryos. A binary mask is created and mapped on the fluorescent image patch of an alive embryo in the trap and the average fluorescent intensity expression of an embryo is extracted. A spatially shifted version of the binary mask then quantifies the background fluorescent intensity in the incubator region. The two values are divided to assess the “normalized average embryo intensity” in time. Scale bar: 20 μm .

of embryo traps in an automated manner (see details in Figure 6.5a-e). After obtaining the x- and y- coordinates of the intersection between an embryo trap and an embryo incubator, we cropped 200 \times 200 pixel-sized images of each part. We utilized the automation script previ-

ously created in our work in Subsection 4.3 to distinguish alive embryos from the dead ones in the embryo traps (by using bright-field images of embryo traps). This script, additionally, generated the twitching-to-hatching development time. Although the bright-field images of embryo incubators were unused, the fluorescent set of embryo incubator images were required to calculate an average background fluorescent intensity. We modified a binary mask from our previous work (see Figure 6.5f) and then, the downward shifted version of this mask was mapped on the fluorescent set of images on embryo traps, while the upwards shifted version was used to cover only the embryo incubators. This approach provided a faultless capture of the fluorescent intensity of embryos and the background, excluding any false intensity values resulting from the PDMS part. In the last part, the average embryo fluorescent intensity was divided by the average background fluorescent intensity to compute the “normalized average embryo intensity”.

6.4 Parental generation development under doxycycline treatment

Mitochondria play a key role in the regulation of epigenetic mechanisms and it is known that an induction of mitochondrial stress extends lifespan and promotes longevity [171, 172, 173]. Doxycycline was chosen as the mitochondrial stress inducer compound as it is renowned for its blocking of mitochondrial translation, creating mitochondrial proteostasis and instigating UPR^{mt} [174]. We employed different types of doxycycline treatment for analysis of early inheritable mitochondrial stress. For some of the nematodes, we provided continuously doxycycline diluted in both *E. coli* solution and S-medium solution. This approach created a continuous doxycycline-induced stress on the mothers and embryos. We labeled this condition as Mother and Embryo Treated (MET). We also supplied doxycycline diluted in *E. coli* solution for only 15 hours for some other worms to observe if a temporary stress induction on the mother could transfer to the progeny, which was called as Only Mother Treated (OMT). For the rest, we delivered *E. coli* solution without doxycycline during the development of mother nematodes. For some of these worms, after embryo trapping, we presented doxycycline diluted in S-medium solution to detect if first embryo progenies can be stressed, while their mothers were not exposed to doxycycline. This condition was named as Only Embryo Treated (OET). Finally, we did not provide doxycycline for some worms, which was the control condition (CNT).

Firstly, we observed the developmental influence of doxycycline on the mother nematodes (Figure 6.6). Doxycycline as an antibiotic drug was demonstrated to show growth-delaying effects [174]. We noticed that, during the development of mother nematodes from the L4 larval stage to the adult stage, there was no significant influence of doxycycline as a developmental lag at 15, 30 and 60 $\mu\text{g}/\text{mL}$ concentrations (Figure 6.6a-c). The sigmoidal fits displayed that the development trend was similar in all case studies. We extracted the first egg release time – calculated after the onset of L4 larval stage – from the images of worm culture chambers. For 15 and 30 $\mu\text{g}/\text{mL}$ doxycycline concentrations (Figure 6.6d, e), there was a rather short delay between mother treated conditions (MET and OMT) compared to untreated conditions (OET and CNT). Surprisingly, for the MET condition at 60 $\mu\text{g}/\text{mL}$ of doxycycline, the egg

6.4. Parental generation development under doxycycline treatment

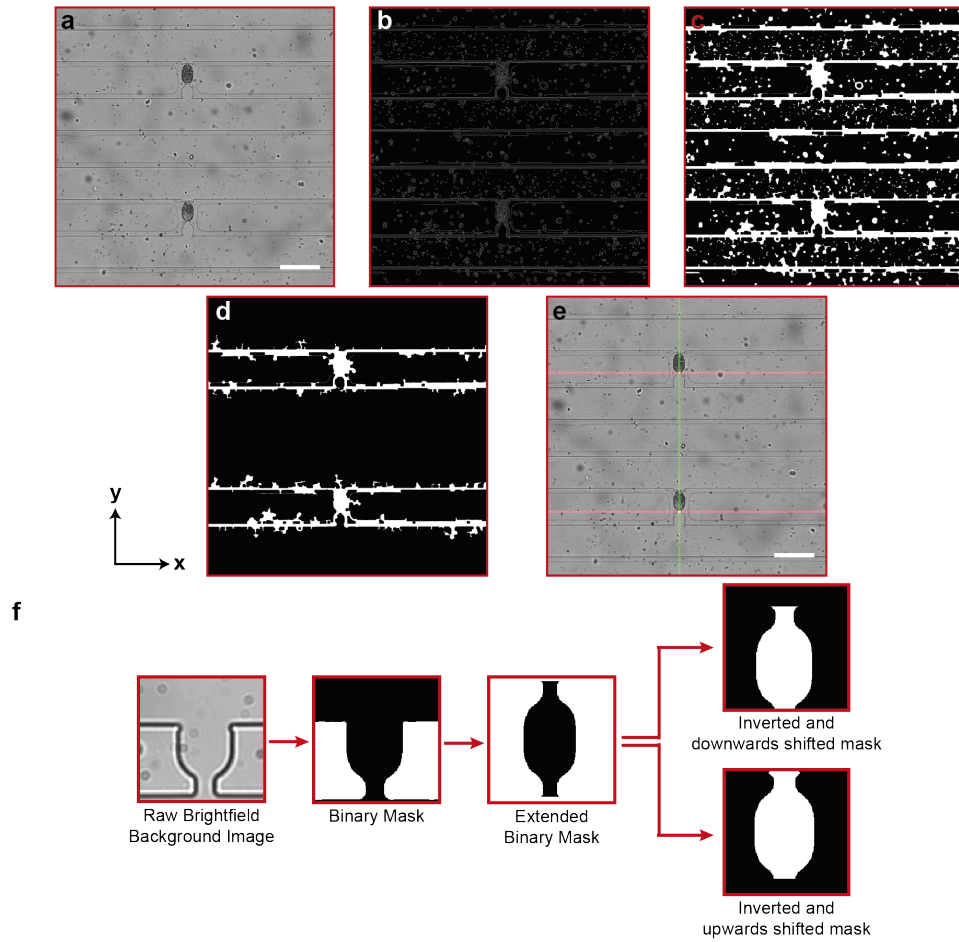


Figure 6.5 – Details of the automated location detection of the embryo traps and the binary mask creation for embryos' fluorescent intensity detection. (a) A sample image from the bright-field time-lapse sequence is used for the location detection of the embryo traps. (b) Canny edge detector is utilized to reveal the edge map information of the image of interest. (c) Morphological operations are applied on the resulting edge map image to reveal all embryo trap boundaries. (d) The largest two connected components are selected to discard the noise in the image. (e) In order to find the y-coordinate of the embryo traps, we sum all pixels in a row of (d), and the vicinity of the two maxima of the one-dimensional set of line-averaged pixel values allows to locate the horizontal PDMS boundaries of an embryo trap (red line). A similar approach is also performed to reveal the shared x-coordinate of the embryo traps (green line). After obtaining x- and y-coordinates for each embryo trap, 200×200 pixel images (corresponding to $70 \times 70 \mu\text{m}$) around each embryo trap was cropped for the subsequent embryogenesis observation and fluorescent intensity detection part of our algorithm. (f) An empty embryo incubator is binarized and extended by vertical duplication. During the post-processing of the embryo development analysis, this extended binary mask is inverted and shifted downwards or upwards to cover the embryo or the background regions, respectively. Scale bars: $100 \mu\text{m}$.

Chapter 6. The detection of early epigenetic inheritance of *C. elegans* with a microfluidic phenotyping platform

laying was significantly delayed (> 25 hours after the onset of L4 larval stage; Figure 6.6f). We waited for an additional 5 hours after the first egg release of the nematodes in the worm culture chambers of other test conditions (OMT, OET, and CNT); however, no egg laying was observed for the MET condition under 60 $\mu\text{g/mL}$ doxycycline concentration within this period. In order not to miss the observation of twitching onset of OMT, OET and CNT first embryo progenies and to have all conditions within the same experimental window, we proceeded to embryogenesis observation without MET embryos. Prior research on mitochondria targeting drugs showed that, at certain drug concentrations, fertility of the nematodes could be strongly altered [175]. At 60 $\mu\text{g/mL}$ doxycycline concentration, we observed this egg-laying alteration. As additional phenotypic parameters, we calculated the total number of embryos in the image of the time-lapse sequence that captured the first egg-laying event, and in the image of the time-lapse sequence that was captured one hour after the first egg-laying event normalized by the total number of worms accommodated (Figure 6.7a-f). We also obtained the normalized egg release rate by taking the time-derivative of the total number of embryos laid, averaged over the first two hours after the first egg-laying event (Figure 6.7g-i). We did not notice a noticeable trend for these parameters.

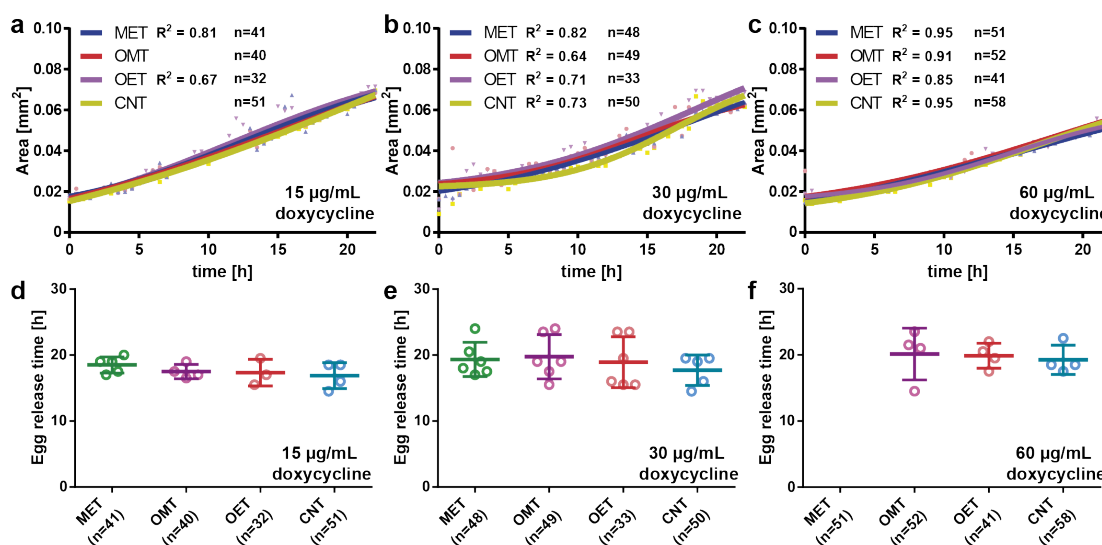


Figure 6.6 – Influence of doxycycline on the development of the mother nematodes. Mothers and embryos both doxycycline-treated (MET), only mothers doxycycline-treated for 15 hours (OMT), only embryos doxycycline-treated (OET), and no doxycycline treatment (CNT) conditions are studied. (a-c) The normalized area of the mother nematodes under (a) 15 $\mu\text{g/mL}$, (b) 30 $\mu\text{g/mL}$, and (c) 60 $\mu\text{g/mL}$ doxycycline solution. (d-f) The first egg release time of the mother nematodes under (d) 15 $\mu\text{g/mL}$, (e) 30 $\mu\text{g/mL}$ and (f) 60 $\mu\text{g/mL}$ doxycycline in *E. coli* solution. Data are expressed as mean \pm SD. All measurements are based on 2 to 3 experiments for each condition. The number in “n” is the total number of worms studied for a particular condition.

6.5. Doxycycline influence on the embryogenesis of first embryo progenies

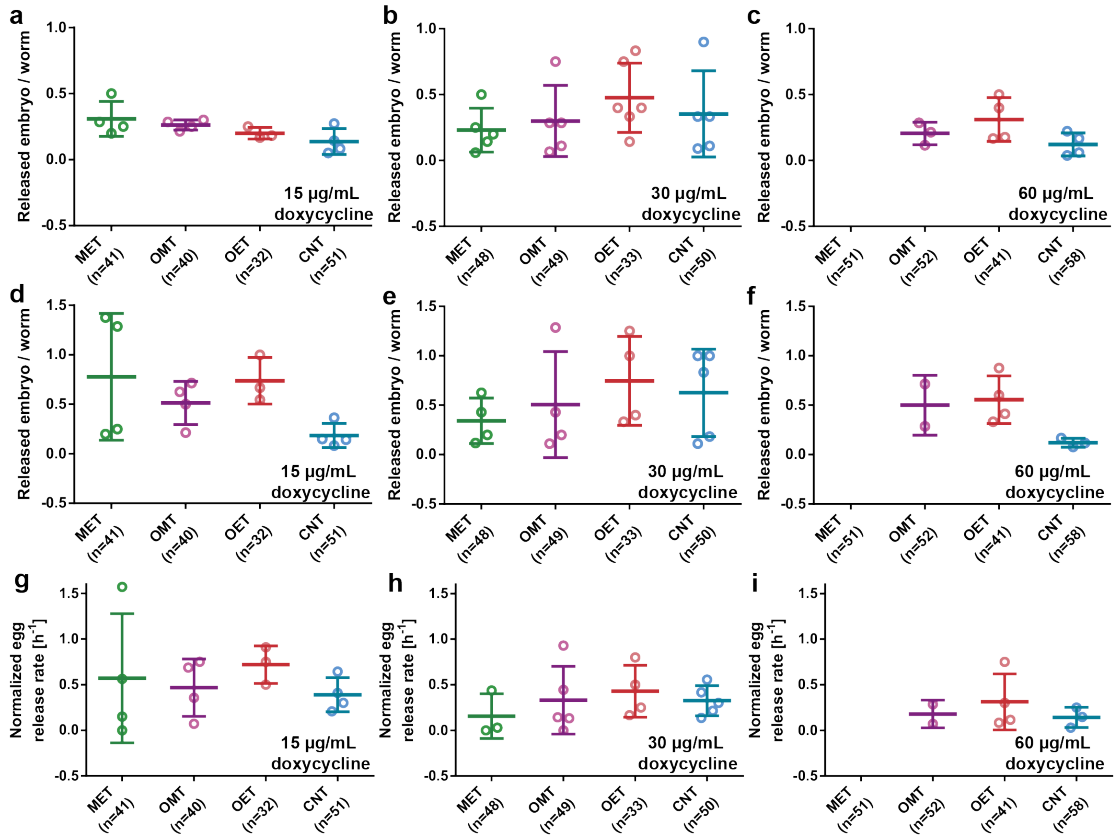


Figure 6.7 – Study of the effect of doxycycline treatment on the embryo release parameters of mother nematodes. (a-c) Total number of embryos in the image of the time-lapse sequence that captured the first egg-laying event normalized by the total number of worms accommodated in the worm culture chamber for (a) 15 µg/mL, (b) 30 µg/mL and (c) 60 µg/mL doxycycline solution. (d-f) Total number of embryos in the image of the time-lapse sequence that was captured one hour after the first egg-laying event normalized by the total number of worms accommodated in the worm culture chamber for (d) 15 µg/mL, (e) 30 µg/mL and (f) 60 µg/mL doxycycline solution. (g-i) Normalized egg release rate obtained by taking the time-derivative of the total number of embryos laid, averaged over the first two hours after the first egg-laying event for (g) 15 µg/mL, (h) 30 µg/mL and (i) 60 µg/mL doxycycline solution. Data are expressed as mean ± SD. All measurements are based on 2 to 3 experiments for each condition. The number in “n” is the total number of worms studied for a particular condition.

6.5 Doxycycline influence on the embryogenesis of first embryo progenies

After the successive trapping of *C. elegans* embryos inside the embryo traps, we could investigate the development of embryos using bright-field time-lapse imaging and automatically compute the development duration. The twitching and hatching development phases of embryos are some of the distinctive transition stages of embryogenesis [106] and tracking the time interval between these two stages would demonstrate whether the development duration

of embryos changed under doxycycline influence. We calculated the twitching-to-hatching phase duration of embryos treated with 15, 30 and 60 $\mu\text{g/mL}$ doxycycline concentrations in MET, OMT, OET and CNT conditions (Figure 6.8). Under 15 $\mu\text{g/mL}$ doxycycline concentration, the embryos laid from the treated mothers – MET and OMT conditions – displayed rather extended development behavior (Figure 6.8a). More specifically, a mother nematode treatment of 15 hours increased the twitching-to-hatching time by 4% compared to control, while continuous treatment showed that this duration increased by 6%. For treatments at 30 $\mu\text{g/mL}$ doxycycline concentration, this lagging effect became more dominant, increasing the development time for MET and OMT embryos by 9 and 7%, respectively (Figure 6.8b). Only 5% increase was noted for OMT embryos at 60 $\mu\text{g/mL}$ concentration, while, due to the significant delay in egg laying of MET mothers, there were no embryos to calculate the development time (Figure 6.8c). Additionally, for all the concentrations, there was no distinguishing developmental lag between OET and CNT embryos. It was previously reported that mitochondrial prohibition can result with a developmental arrest during embryogenesis [176]. Here, we observed a similar behavior. Mitochondrial stressed mothers produced developmentally lagging embryos under all doxycycline concentrations. The effect became more prominent when the drug application time was continuous rather than being limited to 15 hours.

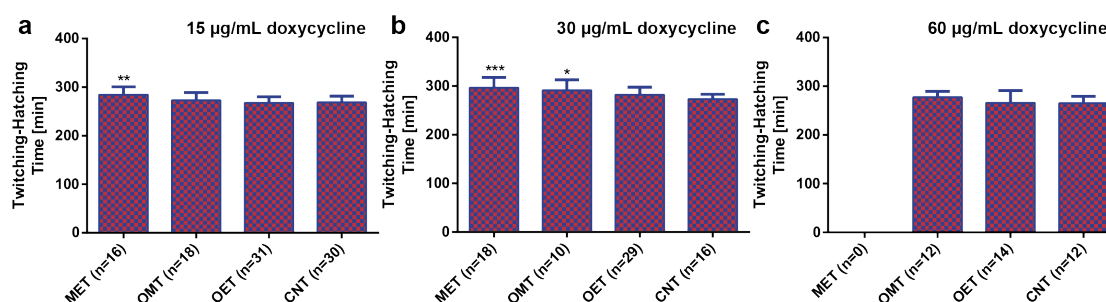


Figure 6.8 – The development time of first embryo progenies released from the mother nematodes under MET, OMT, OET and CNT conditions. Twitching-to-hatching development time of the first embryo progenies under (a) 15 $\mu\text{g/mL}$, (b) 30 $\mu\text{g/mL}$ and (c) 60 $\mu\text{g/mL}$ doxycycline solution. Data are expressed as mean \pm SD, * $p \leq 0.05$, ** $p \leq 0.01$, *** $p \leq 0.001$. All measurements are based on 2 to 3 experiments for each condition. The number in “n” is the total number of embryos studied for a particular condition.

6.6 Inheritance of mitochondrial stress as evidenced by the fluorescence expression of embryos

Certain epigenetic information is established during the sperm formation and consequently reprogrammed in *C. elegans* embryos [177]. The limit of early epigenetic transfer remains to be a motivating question however. In our case, we explored the early epigenetic inheritance of mitochondrial stress in *C. elegans*. In parallel to the bright-field embryogenesis observations, we acquired fluorescent time-lapse images of embryos in the embryo traps. Based on our

selection of the *hsp-6::gfp* strain [67], we could evaluate if the mitochondrial stress-induced mothers transferred such induction to the embryos. During our observations, we noticed that throughout the development of an embryo, the UPR^{mt} expression progressively increased over time (see a development example for a single embryo in Figure 6.9). We analyzed the normalized average fluorescent intensity expression of MET, OMT, OET and CNT first embryo progenies under 15, 30 and 60 µg/mL doxycycline concentrations (Figure 6.10). All intensity data after hatching were deleted (t=0 minutes was defined as the hatching event) and all the data were presented as the normalized average fluorescent intensity expression obtained from individual embryos. We noticed that UPR^{mt} could not be directly induced in the embryos once they were laid (OET, see Figure 6.10a-c), most likely attributed to *C.elegans*' eggshell impermeability to small molecule inhibitors [104]. However, we found a dose-dependent UPR^{mt} induction of OMT (Figure 6.10d-f) and MET (Figure 6.10g, h) embryos. While no UPR^{mt} induction was observed at 15 µg/mL for OMT embryos (Figure 6.10d), starting from a doxycycline concentration of 30 µg/mL, the UPR^{mt} was significant (Figure 6.10e, f). As expected, such a trend was also observed for MET embryos (Figure 6.10g, h). Since it was already demonstrated in Figure 6.10f with OMT embryos under 60 µg/mL doxycycline concentration and in Figure 6.10h with MET embryos under 30 µg/mL doxycycline concentration, we would expect a significant UPR^{mt} inheritance for MET embryos under 60 µg/mL doxycycline concentration too. Previous research in this field demonstrated that information from a mother's environment can be transferred to her offspring indeed [178]. Our results revealed that the embryos could express mitochondrial stress with the right selection of the timing and the drug concentration applied to the mothers. A doxycycline concentration of 30 µg/mL and a minimum application time of 15 hours to the mother nematodes seemed to be triggering UPR^{mt}.

6.7 UPR^{mt} expression of L1 larvae

Epigenetic inheritance is frequently disappearing at the start of a new generation cycle [179]. Whether the larval stages following the embryonic stage retain this inheritance remains an interesting question. Enabled by the 10 µm wide constriction filters of the worm culture chambers, we recollected the L1 larvae after the hatching of embryos in the embryo traps, which took place typically 12 hours after the initiation of embryogenesis studies. We evaluated there if such inheritance persisted and any developmental difference was obtained under various doxycycline conditions and exposure time (Figure 6.11). By monitoring the length and diameter of L1 progenies, we observed that there was no significant alteration under application of 15, 30 and 60 µg/mL doxycycline concentration (Figure 6.11a-c). Of note, we noticed L1 progenies of MET condition under 60 µg/mL doxycycline concentration, indicating that eggs were laid eventually during 12 hours time-lapse imaging. At the same time, we looked at the average fluorescent intensity expression of L1 larvae (Figure 6.11d-f). We noticed that for a 15 µg/mL doxycycline concentration (Figure 6.11d), the application of doxycycline (MET, OMT and OET) seemed to display a slightly less UPR^{mt} expression compared to the

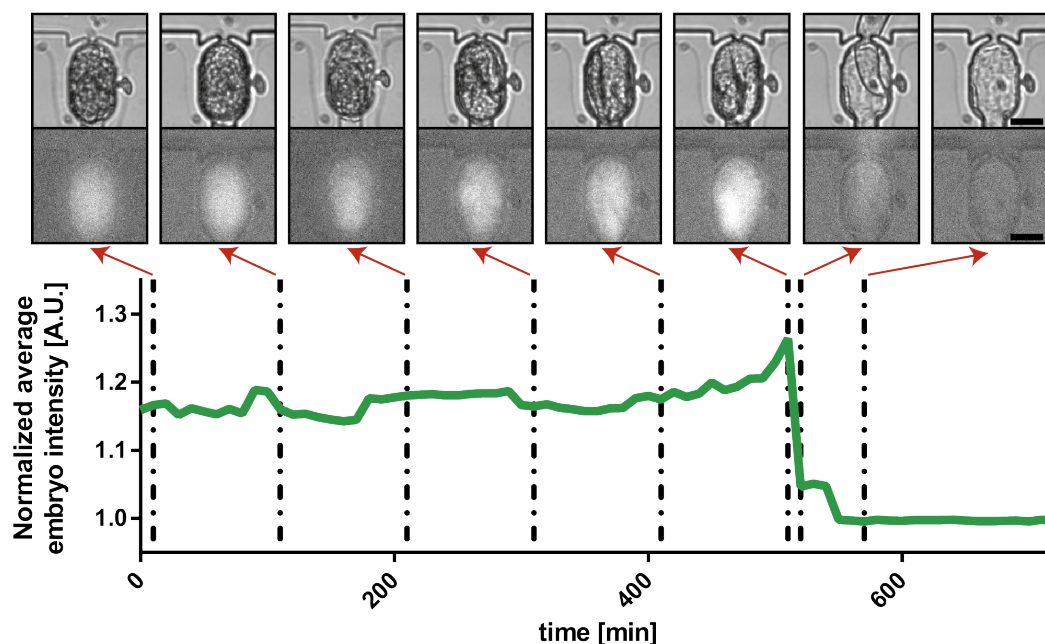


Figure 6.9 – Illustrative images taken during an embryo development. The normalized average embryo intensity during 12 hours of imaging, represented by both bright-field and fluorescent 200×200 pixel image patches at 10, 110, 210, 310, 410, 510, 520 and 570 minutes after the experiment initiation. Scale bars: $20 \mu\text{m}$.

control condition, which could however be caused by the data outliers in the control condition. This effect was absent with both 30 and $60 \mu\text{g/mL}$ doxycycline concentrations (Figure 6.11 e, f). In parallel, we calculated the normalized maximum UPR^{mt} expression of L1 progenies (Figure 6.12). Similar to the normalized average UPR^{mt} expression study, for all conditions, no significant trend was observed.

6.8 Statistical analysis

Data from raw images were extracted to fill an array for statistical tests using Graphpad Prism. The area of the mother nematodes and the normalized average fluorescent intensity of the *hsp-6::gfp* strain were analyzed for statistical significance using Repeated Measures two-way ANOVA. The rest of the data were analyzed for statistical significance using one-way ANOVA. For the study with 15 , 30 and $60 \mu\text{g/mL}$ doxycycline, we performed 2, 3 and 2 experiments for each condition, respectively. Mean values were computed to represent in graphs when measurements were repeated in multiple batches.

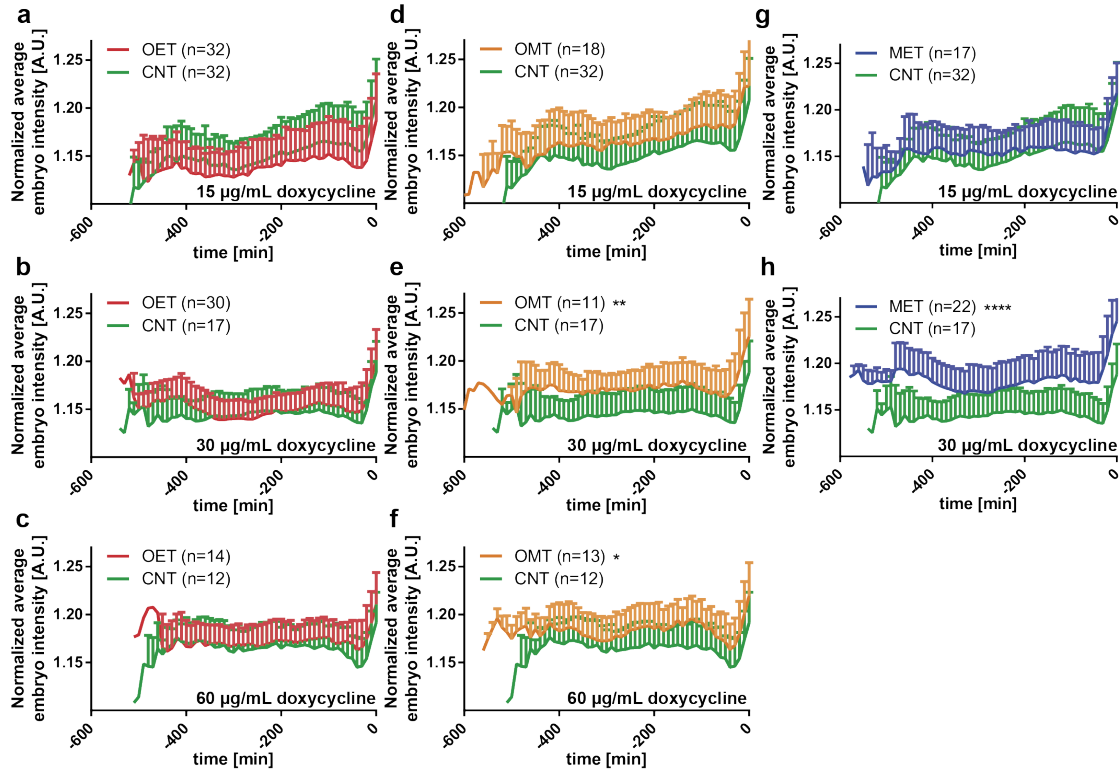


Figure 6.10 – Normalized average embryo intensity profile of the first embryo progenies under MET, OMT, OET and CNT conditions and 15, 30 and 60 $\mu\text{g/mL}$ doxycycline concentrations. $t=0$ min is defined as the hatching event of an embryo. Normalized average embryo intensity expression of the first embryo progenies of OET and CNT conditions under (a) 15 $\mu\text{g/mL}$, (b) 30 $\mu\text{g/mL}$ and (c) 60 $\mu\text{g/mL}$ doxycycline solution. Normalized average embryo intensity expression of the first embryo progenies of OMT and CNT conditions under (d) 15 $\mu\text{g/mL}$, (e) 30 $\mu\text{g/mL}$ and (f) 60 $\mu\text{g/mL}$ doxycycline solution. Normalized average embryo intensity expression of the first embryo progenies of MET and CNT conditions under (g) 15 $\mu\text{g/mL}$ and (h) 30 $\mu\text{g/mL}$ doxycycline solution. Data are expressed as mean \pm SD, * $p \leq 0.05$, ** $p \leq 0.01$, **** $p \leq 0.0001$. All measurements are based on 2 to 3 experiments for each condition. The number in “n” is the total number of embryos studied for a particular condition.

6.9 Discussion and conclusion

We reported here our novel microfluidic platform for automated phenotyping and high-resolution studies of the nematodes and the embryos of the animal model *C. elegans*. We targeted the fabrication of a simple and easy-to-operate device. Exclusion of any on-chip active components, such as pressure valves, facilitated the fabrication protocol and solved many production-related issues. Utilizing just a single media inlet and a media outlet, our device empowers rapid loading and culture of L4 larvae, single embryo trapping, embryogenesis observation and automated phenotyping of the maternal nematodes, embryos and L1 progenies. Such a design consideration also promotes opportunities for parallel case studies, having up to 8 different conditions at the same time. Our well-tuned design features allow the

Chapter 6. The detection of early epigenetic inheritance of *C. elegans* with a microfluidic phenotyping platform

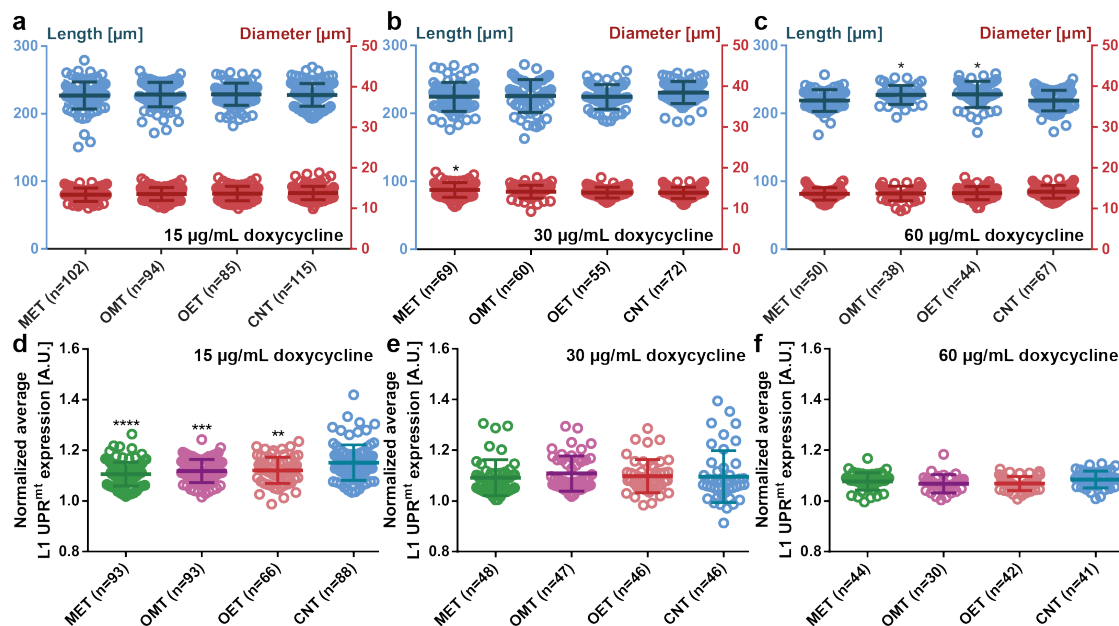


Figure 6.11 – Influence of doxycycline on the size (length, diameter) and UPR^{mt} expression of L1 progenies. (a-c) Length and diameter of the L1 progenies under (a) 15 µg/mL, (b) 30 µg/mL, and (c) 60 µg/mL doxycycline solution. (d-f) Normalized average UPR^{mt} expression of the L1 progenies under (d) 15 µg/mL, (e) 30 µg/mL and (f) 60 µg/mL doxycycline solution. Data are expressed as mean ± SD, * $p \leq 0.05$, ** $p \leq 0.01$, *** $p \leq 0.001$, **** $p \leq 0.0001$. All measurements are based on 2 to 3 experiments for each condition. The number in “n” is the total number of L1 progenies studied for a particular condition.

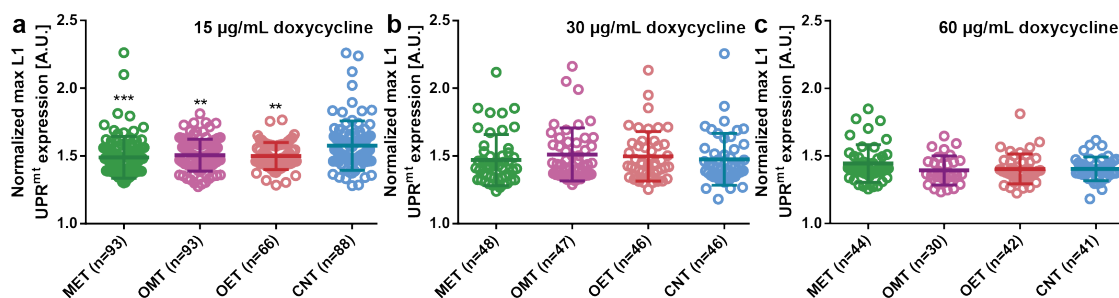


Figure 6.12 – Influence of doxycycline on the maximum UPR^{mt} expression of L1 progenies. Normalized maximum UPR^{mt} expression of the L1 progenies under (a) 15 µg/mL, (b) 30 µg/mL and (c) 60 µg/mL doxycycline solution. Data are expressed as mean ± SD, ** $p \leq 0.01$, *** $p \leq 0.001$. All measurements are based on 2 to 3 experiments for each condition. The number in “n” is the total number of L1 progenies studied for a particular condition.

culture of up to 30 nematodes in a single worm culture chamber where bright-field imaging can be performed. Typically, we culture nematodes for about 24 hours and move on to the embryo development studies. To this purpose, the fluidic serpentine contains 25 embryo traps to confine embryos accurately and enabling stable 12 hour-long embryogenesis observation using both bright-field and fluorescent imaging. Integration of three different sets of objectives

in our setup permits tracking the whole dynamics of the mother and progeny development and the transition between these two states. We employed simple and repeatable fluidic commands that were deployed to a syringe pump via serial port connection. Such an approach supported repeatable experimentation and reduced the possibilities of operator-based errors by keeping the operator's involvement during an experiment to a minimum level. An operator was involved in the experimentation only while changing the objective in use and the reservoir that was connected to a media outlet. In between experimental transitions, such as switching from the imaging of worm culture chambers to the imaging of embryo traps, a user was also required to terminate the prior stage and initiate a new one. Any possible intra-experiment variation was eliminated with this method.

We combined automated and operator-based image treatment techniques for data analysis. We created an automated script for rapid nematode size detection. In parallel, egg-release related phenotypes, the size and the fluorescent intensity expression of L1 progenies in the worm culture chambers were obtained by operator's observation. Utilizing an image processing script from our previous work described in Subsection 4.3, we could determine dead and alive embryos. After locating an alive embryo, an image patch with a size of 200×200 pixels was cropped around the embryo traps, background-corrected and the fluorescent intensity expression of an embryo during the embryogenesis was quantified. We studied heritable transmission of mitochondrial stress by exposing *C. elegans* to doxycycline. The *hsp-6::gfp* strain reporting mitochondrial unfolded protein response was chosen as a model. We applied various doxycycline concentrations with varying application times to the mothers (OMT: 15 hours, MET: continuous) along with only doxycycline-exposed embryos (OET) and untreated (CNT) cases. Our results revealed that the doxycycline treatment from the onset of L4 larval stage did not cause any lag in the nematode growth dynamics, while causing a significant delay in the first egg laying time for MET nematodes under $60 \mu\text{g/mL}$ doxycycline condition. In addition, embryos laid by doxycycline-treated mothers showed an extended twitching-to-hatching phase duration. A doxycycline concentration equal or higher than $30 \mu\text{g/mL}$ and an application period of 15 hours resulted in stressed embryos. However, the mitochondrial stress did not persist in the L1 larval stage.

In summary, we showed that our new microfluidic device provided extensive automation (in terms of both fluidic handling and imaging) and enabled high-resolution and multiplexed studies, so that we could capture subtle phenotypic transitions from a mother nematode to its early progenies. We believe that many more questions in the scientific community regarding inheritance from the mother-to-progeny could be answered utilizing our platform.

7 PDMS filter structures for size-dependent sorting and on-chip egg extraction of *C. elegans*

C. elegans-based assays require age-synchronized populations prior to experimentation to achieve standardized sets of worm populations, due to which age-induced heterogeneous phenotyping effects can be avoided. There have been several approaches to synchronize populations of *C. elegans* at certain larval stages, however many of these methods are tedious, complex and have low-throughput. In this work, we demonstrate a PDMS microfluidic filtering device for high-throughput, efficient, and extremely rapid sorting of mixed larval populations of *C. elegans*. Our device consists of three plasma-activated and bonded PDMS parts and permits sorting of mixed populations of two consecutive larval stages in a matter of minutes. After sorting, we also retain the remaining larval stage of the initially mixed worm population on the chip, thereby enabling collection of the two sorted larval populations from the device. Our approach is based on only passive hydrodynamics filter structures, resulting in a user-friendly and reusable tool. In addition, we employed the equivalent of a standard bleaching procedure that is practiced in standard worm culture on agar plates, for embryo harvesting on our chip and we demonstrated rapid egg extraction and subsequent harvesting of a synchronized L1 larvae population.

This chapter is an adapted version of the following publication:

- **H. B. Atakan**, F. Ayhan and M. A. M. Gijs, “PDMS filter structures for size-dependent larval sorting and on-chip egg extraction of *C. elegans*”, *Lab on a Chip*, under review, 2019.

7.1 Introduction

Frequently, age-synchronized populations of *C. elegans* at a designated larval stage are required to initiate an experimental sequence with a homogeneous set of worms. Any lagging or leading worms in the experimental set could potentially cause outliers in the resultant data. Synchronization methods to obtain age-synchronized worm populations to overcome this problem have been proposed, but these are often laborious and require operator's manual work [180]. Such methods consist of operator's regular involvement by transporting a few adult worms in between Petri dishes to isolate and culture released progenies. Thus, there has been an increasing interest in the development of more automated technologies and protocols to resolve many of the tedious steps in manual manipulation.

COPAS Biosort is a commercially available automated sorting system that provides high-throughput sorting based on recognition of fluorescent protein expression patterns and other optical signatures [17, 18]. While this system can also be applied to *C. elegans* for age-synchronization of mixed worm populations at moderate accuracy, it is still an expensive and bulky solution. While many of the reported microfluidic platforms allow automation in biological assays in terms of phenotyping, imaging and screening of *C. elegans* [9, 181], dedicated devices for age-synchronization and sorting applications have been developed too [182, 183, 184]. By means of electrotaxis, capitalizing on the nematode movement towards the cathodic side of an electrical field, and PDMS microfluidics, some researchers accomplished sorting of *C. elegans* larval stages. Some researchers employed age-based sorting using electrotactic response of the nematode with a selectivity of 90% [185]. While this method was automated and simple to use, it was working at low-throughput. Another work displayed the size-dependent sorting application within a few minutes by taking advantage of the worms' electrotactic skills [186]. PDMS-agarose hybrid platforms that allowed application of an electrical field was also illustrated for larvae sorting and for isolation of abnormally developing mutants [187]. Such a platform leveraged angular movement of nematodes in combination with the natural orientation of worms under electrotactic stimuli and isolated multiple larval stages. PDMS microchannels were also utilized as a feature in sorting applications based on electrotaxis [188]. However, longtime application of an electrical field to the nematode might have adverse effects [185, 186], therefore, alternative non-electrical approaches have been demonstrated for sorting applications. A continuous-flow-based microfluidic platform for sorting of *C. elegans* has been reported too [189]. This microfluidic approach, based on optical fiber detection and laminar flow switching, allowed sorting of fluorescent-labeled and wild-type worms at rather low-throughput. Another automated motility-based high-throughput chip was reported [190]. While this device was utilized to isolate mutants and can find potential use in genetic studies, it was again working at low-throughput and limited to its application range. A microfluidic device for high-speed sorting and immobilization of *C. elegans* was further modified to dispense screened worms to culture chambers for high-resolution time-lapse imaging [30]. Integrated PDMS pressure valves have also been reported as impeccable add-on features for size-dependent sorting of *C. elegans* [127]. In combination with pressure valves, researchers revealed a diode-like microfluidic chip for passive filtering

of a mixed nematode population, ultimately obtaining a size-dependent isolation of larval stages in separate sorting chambers [191]. These microfluidic chips have proven to be highly valuable for sorting applications, but their fabrication was complex and they did not allow egg harvesting directly on-chip. Another microfluidic platform reported early *C. elegans* larvae sorting via their encapsulation in droplets of a thermosensitive hydrogel [192]. Size-based separation using an array of geometrically optimized pillars [193], maze-like designs [194] that acted as sieves, or trapezoidal channels integrated in microfluidic spiral chips [195] were also demonstrated for sorting. The versatile set of introduced designs allowed accurate sorting of larval stages, but challenges in fabrication, ease-of-operation, reusability, application range and throughput of these devices might hinder employment by non-experienced users on the longer run.

In this work, we present a microfluidic chip for rapid and high-throughput sorting of the nematode *C. elegans*. We defined an experimental protocol with reusable microfluidic chips for size-dependent sorting of various combinations of mixed larval populations. Our device is a hand-held tool that requires no external pressure control, electrical field, complicated tubing, or use of a syringe pump. Resembling a common syringe-based solution filtering approach, our microfluidic chip can be attached to the tip of a standard 1 mL syringe and several hundreds of mixed larvae can be sorted in a matter of minutes. As a further enabling feature of our microfluidic chip, we demonstrated the usage of this device in the application of egg harvesting as obtained from a standard bleaching protocol. We demonstrated that the aforementioned applications can be employed with a minimum of external components, avoiding bulky and expensive experimentation.

7.2 PDMS filter structures design and operation

7.2.1 Microfluidic chip design

The main goal in the design and fabrication of the microfluidic sorting device was to create a user-friendly and simple device that could reach out to a broad user community. The main working principle of the sorting chip is based on allowing high-throughput and rapid sorting between multiple larval stages via passive hydrodynamic filter structures. In addition, the proposed device can be further exploited for egg extraction without any need of external hardware components. The microfluidic device is realized by combining three different PDMS parts that are labeled as the filtering, transmission and collection layers (Figure 7.1a). While the filtering layer is utilized for collecting a worm population and sorting out the target worm population by means of passive hydrodynamics, transmission and collection layers are used for the transfer and collection of the target worm population, respectively. Our device, which resembles a commercial syringe filter tip, can find potential use as a hand-held worm synchronization tool. The chip has a typical size of $36 \times 36 \times 9$ mm, it can be stored in an operator's hand while only requiring a borosilicate syringe and a desired length of tubing as additional items (Figure 7.1b).

The PDMS device has an outer radius of 12.5 mm and is designed to mimic the layout a

Chapter 7. PDMS filter structures for size-dependent sorting and on-chip egg extraction of *C. elegans*

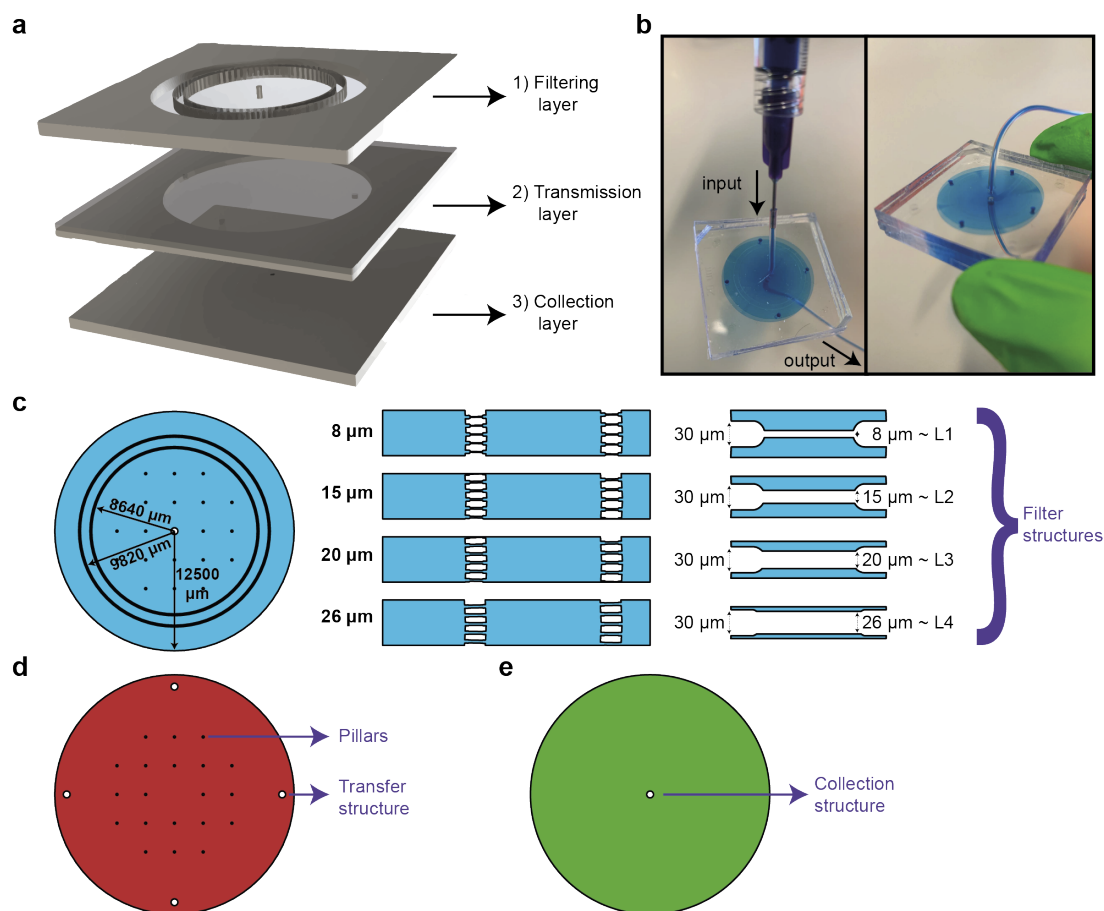


Figure 7.1 – Details of the PDMS filter structures for size-dependent sorting and on-chip egg extraction of the nematode *C. elegans*. (a) Schematic illustration of the design. A worm population is sorted in the filtering layer, transferred via the transmission layer, and finally collected at the collection layer. (b) Photograph of the device filled with liquid dye solution. (c) Details of the filtering layer. Two circular filtering layers with a radius of 8640 and 9820 μm , respectively, are placed in series to ensure accurate sorting of the worm population. A hole is punched in the center for sample injection. The width of the filter structures on a circle are adjusted for the sorting of the target population, i.e. 8, 15, 20 and 26 μm filter widths and 80 μm height for the sorting of L1, L2, L3 and L4 target populations, respectively. (d) Details of the transmission layer. Pillars are used to avoid collapse of the PDMS parts during plasma bonding. Four hole transfer structures allow the transfer of a worm population down to the collection layer. (e) Details of the collection layer, which is simply a single hole collection structure, via which the sorted population is fetched.

standard syringe filter (Figure 7.1c). The filtering layer contains a primary and a secondary ring of sorting filters with a radius of 8640 and 9820 μm , respectively. The outer filter set acts as a fail-safe in the event of PDMS-to-PDMS bonding issues – which might result in a local collapse of a filter set – or an accidental transfer of an undesired worm during an over inflation of filter structures, the inner filter ring is integrated as a second insurance to avoid any failure

of the sorting principle. The sorting of worm populations by means of passive hydrodynamics is supported by integration of constriction filter structures in the filtering layer. The feature size of these filters can be tuned for the selective passage of the larval stage of interest [112]. In fact, we constructed four different versions of the filtering layer with 8, 15, 20 and 26 μm wide filter structures corresponding to a sorting of L1, L2, L3 and L4 larval stages, respectively. We observed that a filter width that is narrower than the targeted worms' diameter by 2-4 μm can accurately sort the population by compensating for minor PDMS inflations. Moreover, the natural elastic behavior of the nematodes facilitates crawling through filter structures that are narrower than their diameter. In parallel, such tight filters block the nematodes at older life stages. Once a worm population is sorted, it is transferred to the output of the device via the transmission layer (Figure 7.1d). The 4 transfer structures are punched in the PDMS part, while the pillars are constructed to prevent collapse during both PDMS-PDMS plasma bonding and operation of the device. The collection layer contains a hole collection structure, which is punched in the PDMS part for extraction of the worm population (Figure 7.1e). The chosen vertical buildup of the chip mimics a classical syringe porous membrane filter that is well known to the user.

7.2.2 Sorting protocol

We optimized a standard protocol for repeatable and rapid sorting of various combinations of worm populations (Figure 7.2). The microfluidic device was initially degassed by injecting 1 mL of filtered S-medium solution loaded in a 1 mL borosilicate syringe while the output of the device was clamped (Figure 7.2a). We left the device in this configuration for a minimum of 6 hours or, in most cases, overnight. Prior to an experiment, the clamp was released and the excessive S-medium was flushed from the output of the microfluidic device. Meanwhile, we designed the target sorting experiment by choosing two consecutive larval stages of interest. Population densities were adjusted to obtain 200-400 worms from each population by counting the worm density in 2 μL droplets from Eppendorf reservoirs, which were obtained by washing NGM agar plates with 1 mL of S-medium solution. After combining the worm populations and adjusting to a total volume of 1 mL, the suspension was loaded in a separate 1 mL borosilicate syringe. The worm syringe was plugged instead of the S-medium syringe and the sorting experiment was initiated by employing a hand-held user-operated method (Figure 7.2b). Our experimental results showed that the worm suspension injection could be done in a range of 30 to 60 seconds, without over-pressurizing the device, which might cause detachment of PDMS layers. The washed-off and sorted population was collected in an Eppendorf tube located at the output of the device. Once the syringe was emptied, it was replaced by another 1 mL borosilicate syringe that was filled with filtered S-medium solution (Figure 7.2c). The main reason of such an approach was to remove any possible worm population remaining in the external tubing. The syringe was, once again, emptied in a time interval of 30 to 60 seconds. In order to collect the worm population residing in the filtering layer, the operation principle of the device was reverted (Figure 7.2d). The input of the device was linked to an Eppendorf reservoir while connecting a 1 mL borosilicate syringe fully filled

with S-medium solution at the output of the device. Another S-medium washing step was performed, in the opposite direction of the initial sorting part within the same sorting time as before, and the unsorted worm population was collected at the input. The bi-directional flow working principle of the microfluidic device empowers rapid sorting and collection of worm populations with this experimental protocol. In a matter of 2 to 3 minutes, the entire sorting operation was performed. We note that we used the same microfluidic devices up to 3 to 5 times without a need of a new device fabrication. We fabricated new devices for additional sorting experiments to ensure reliable measurement results, but these experiments could have been also performed with the priorly fabricated microfluidic chips. We finally highlight the utility and user-friendliness of our device design for multiple sorting experiments and different larval stage synchronization applications.

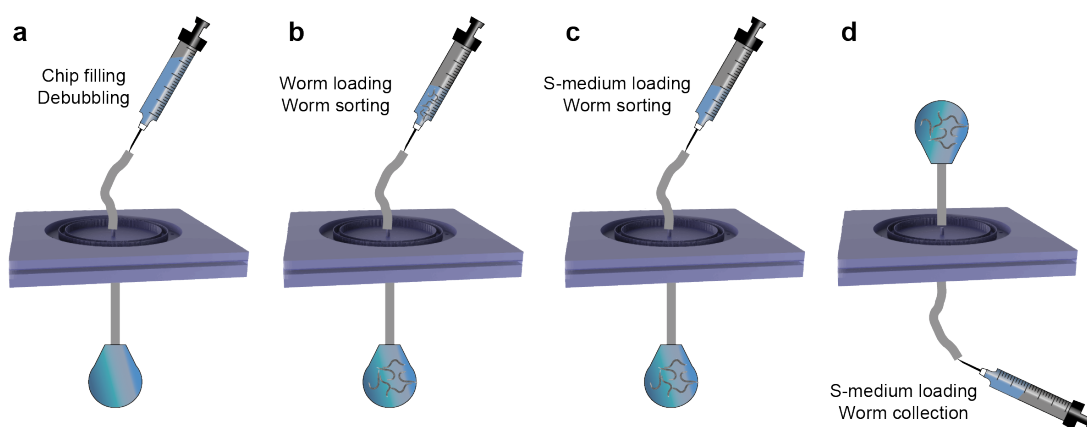


Figure 7.2 – Details of the experimental protocol used during the sorting procedure. (a) In a first step, the PDMS device is degassed using over-pressure by injecting 1 mL of filtered S-medium solution while having the output of the device clamped. After an overnight degassing step, the clamp is released and the device is ready to be used. (b) A mixed worm population loaded in a 1 mL borosilicate syringe is injected in the device. (c) 1 mL of filtered S-medium solution is introduced to remove any remaining worm population in the tubing. The sorted population is collected at the output of the device. (d) 1 mL of filtered S-medium solution is injected from the output of the device to retain the worm population residing in the filtering layer.

7.3 Results of the sorting experiments

We recorded real-time videos to characterize the sorting principle. We analyzed all the experiments from the recorded videos and we illustrated a series of sorting examples by extracting image frames from the video sets in Figure 7.3. We characterized the travelling time of randomly picked target worms across the two filter sets to get the average sorting time per single worm. We initially tested the sorting of L1 populations out of L1 and L2 worm populations (Figure 7.3a). In this particular example, we observed that an L1 worm successfully traveled across the two filter sets that contained filter structures with a width of 8 μm in 2.3 seconds.

At this flow rate, larger worms – L2 worms in this specific experiment – were either blocked in the first or second filter sets. In a similar approach, we analyzed the sorting behavior of L2, L3, L4 and L1 worm populations out of L2 and L3, L3 and L4, L4 and YA, and L1 and YA worm populations, respectively (Figure 7.3b-e). The widths of the filter structures were chosen as 15, 20, 26 and 8 μm with respect to the aforementioned experimental sequences. Our experimental observations revealed that, if the residing population in the filtering layer was not large in body size, sorting can be realized very rapidly. In particular, we noticed that L2 and L3 worm populations can be sorted in a matter of 2-3 seconds per worm (Figure 7.3b, c), mostly due to large number of available filter structures a worm can pass through. On the other hand, when a YA worm was resting in the filtering layer, most of its body was covering filter structures of the first filter set (Figure 7.3d, e). As such, the sorting time was slightly increased to be in the range of 3 to 7 seconds, while the variations in sorting time did not have any correlation with the accuracy of the sorting principle.

We displayed the different diameter values measured after the sorting experiments in Figure 7.4. We observed that for L1-L2 worm sorting experiments, the diameter values before and after sorting experiments lie around the nominal onset diameter values of each larval stage (Figure 7.4a). This means that, while the initial calibration of the worm plates was indeed accurate, after merging the two populations and sorting them with the microfluidic device, the sorted populations were again having the expected diameter and larval stage. However, some outliers were noted, such as worms that exhibit smaller diameter values at the input chamber of the microfluidic chip. In principle, the smaller worms residing in the input chamber could have been removed by an additional S-medium washing step (as shown in Figure 7.2c) but such an additional step would have resulted in an increase in the operation time of the sorting protocol. Similarly, there were a few outlier worms obtained at the output chamber of the microfluidic device. This was probably due to (i) local PDMS inflation during the sorting process or (ii) the crawling behavior of the nematodes. We detected a similar trend for L2-L3 and L3-L4 worm sorting experiments, respectively (Figure 7.4b, c). As the onset diameter values of L2 and L3 worms were rather close to each other (17 and 22.1 μm , respectively), it was challenging to distinguish these two larval stages, while there were quite few outliers measured at the output of the device (Figure 7.4b). This behavior resulted from the presence of worms at the L3-L4 larval stage transition in the filtering layer during L3-L4 worm sorting (Figure 7.4c). Such outliers did not significantly exist in the sorting experiments that included YA worms (Figure 7.4d, e). More specifically, during L4-YA sorting experiments, the majority of the worms collected at the output of the device were around or smaller than the L4 larval stage onset (Figure 7.4d). In a similar fashion, the input of the device mostly consisted of worms around or larger than YA onset, although there were a few outliers. This trend was also noticed for L1-YA worm sorting (Figure 7.4e). The latter also exemplifies our technique as an alternative method to rapidly isolate early L1 progenies from a NGM agar plate that they usually populate along with adult nematodes. While our methodology of using diameter-based statistics summarizes the working principle of the sorting protocol, a quantitative assessment of the sorting experiments requires further data analysis.

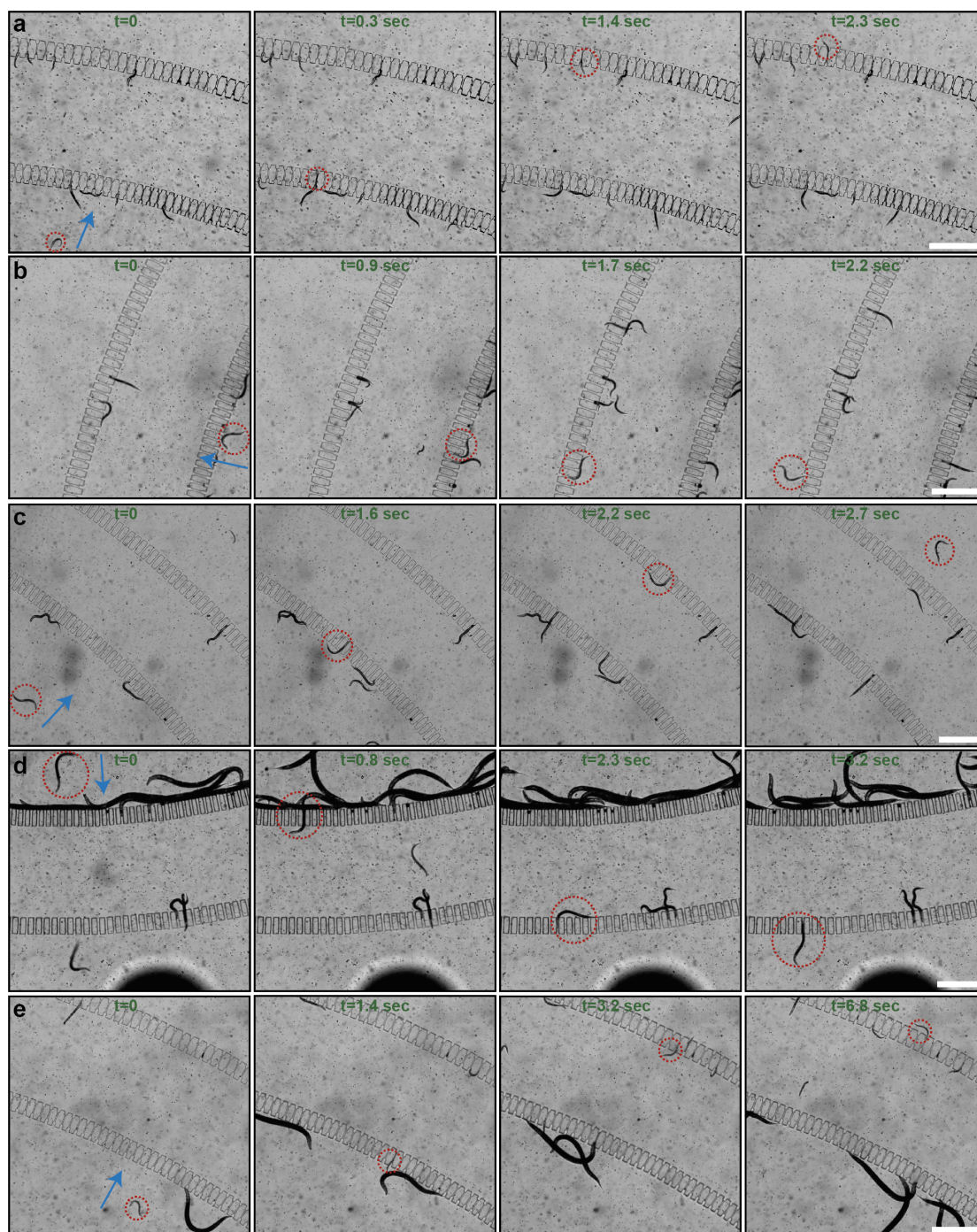


Figure 7.3 – Real-time images illustrating the sorting procedure, the target worms of the sorting are highlighted by red circles. The flow directions during sorting are indicated by blue arrows. The real-time sorting of a (a) L1, (b) L2, (c) L3, (d) L4, (e) L1 worm in a worm population of L1 and L2, L2 and L3, L3 and L4, L4 and YA and L1 and YA worms, respectively. Scale bars: 500 μm .

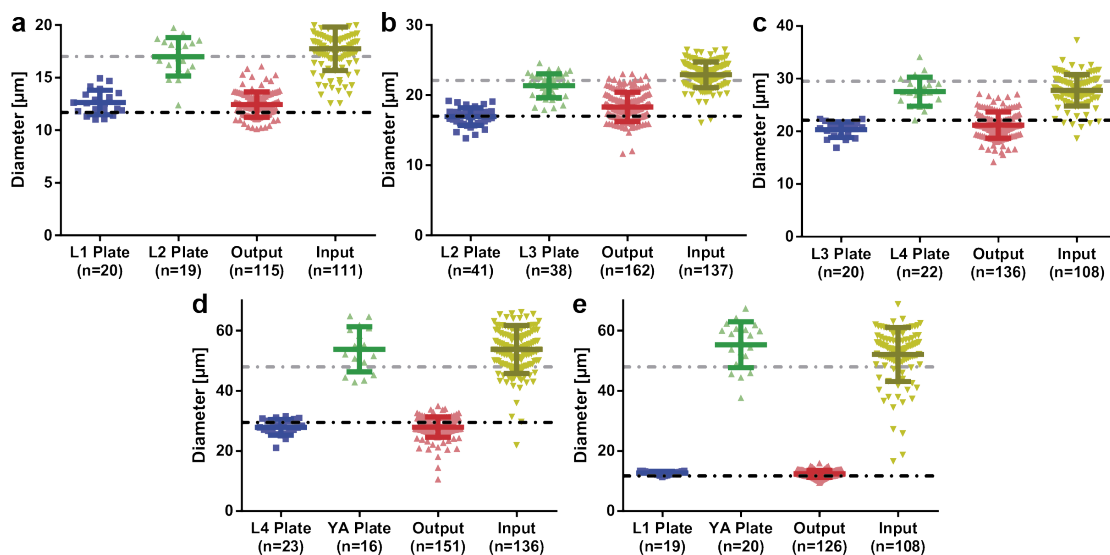


Figure 7.4 – Measured diameter values of worms before and after sorting from different mixed populations. The first two clusters of data in each panel are the diameter values of two selected worm populations obtained from plates (before the sorting experiment). These populations are mixed, sorted on the chip and, after the sorting procedure, the diameters of worms of the two sorted worm populations present in the Input and Output of the filter chip, respectively, are measured. The mixed populations are: (a) L1 and L2, (b) L2 and L3, (c) L3 and L4, (d) L4 and young adult (YA), and (e) L1 and YA, respectively. The black and gray dashed lines in each panel display the onset diameter values of the younger and older larval stages, respectively. Data is expressed as mean \pm SD. All measurements are based on 6 experiments for each sorting experiment. The number “n” is the total number of worms measured for a particular condition.

7.3.1 Population-based statistics of the sorted nematodes

Based on the worm diameter measurements, we can classify the developmental stages of randomly picked worms during their life cycle. To this purpose, we associated each larval stage with a diameter measurement range D_{range} around the average diameter value associated with that larval stage (D_{avg} listed in Table 7.1), as shown in Figure 7.5a. In particular, we checked the diameter D of the worm and we assigned it to a larval stage if it was in the range, $D_{avg} - D_{range} < D < D_{avg} + D_{range}$. We defined D_{range} to be 2.8, 2.5, 2.6, 4.8 and 6 μm for L1, L2, L3, L4 and YA worms, respectively. If a worm was not exactly in one of those intervals, but it was in a developmental stage situated in between the maximum diameter of the earlier stage and the minimum diameter of the later stage, as happened for the later larval stages, it was chosen as being in the ‘transition region’ in between these two larval stages (defining the L4-YA and YA to adult (YA-A) transition stages).

We demonstrated population-based sorting results of all our experiments in Figure 7.5b-f, where we list both the distribution of larval stages within the initial mixed populations and the distribution of the sorted populations collected from both the input and output from our

Chapter 7. PDMS filter structures for size-dependent sorting and on-chip egg extraction of *C. elegans*

Table 7.1 – Average diameter values at the onset of L1, L2, L3, L4 and YA stages of *C. elegans*. For example, the average diameter, D_{avg} , of worms at the onset of L3 larval stage transition is 22.1 μm as adapted from [127].

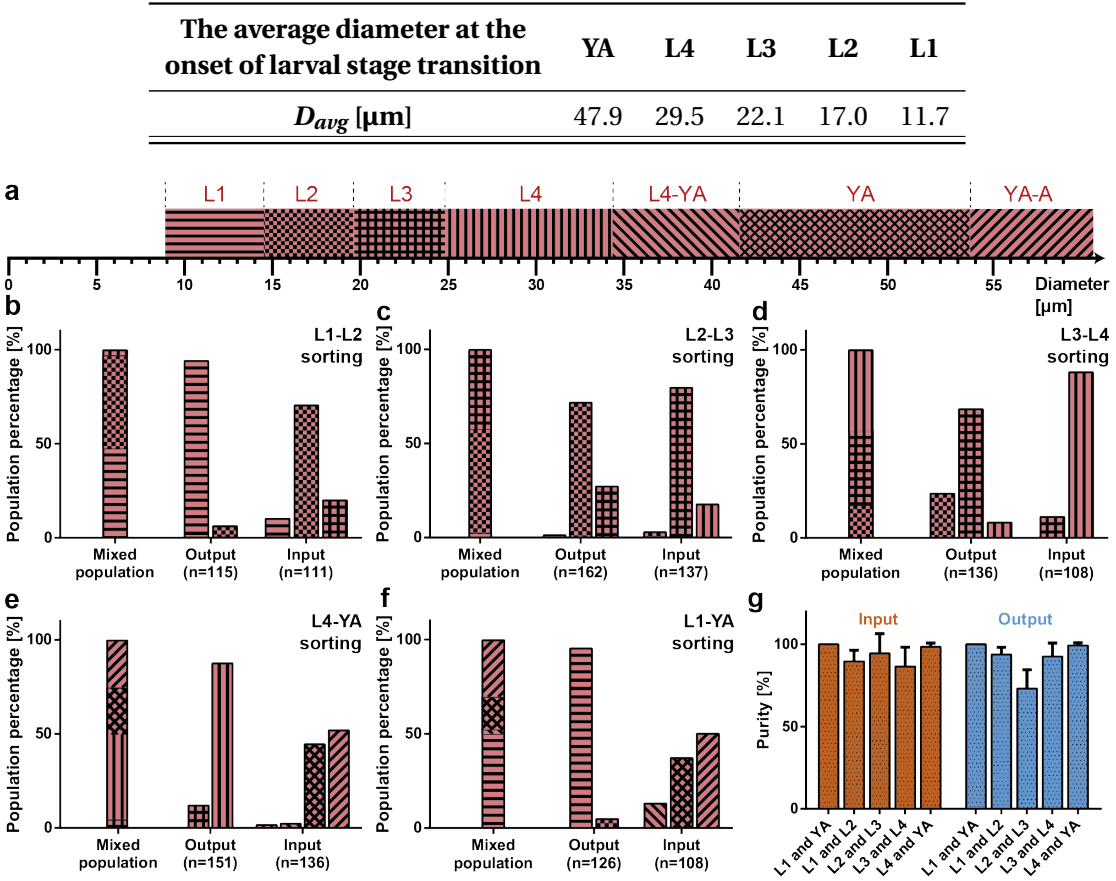


Figure 7.5 – Results from the sorting experiments. (a) Assignment of the larval stage with respect to the diameter. The intermediate stages, L4-YA and YA to adult stage (YA-A), are defined. (b-f) Distribution of worm populations, as determined from the worm diameter, before sorting (“Mixed population” results) and after all sorting experiments (“Output and Input” results) for mixed worm populations of (b) L1 and L2, (c) L2 and L3, (d) L3 and L4, (e) L4 and YA, and (f) L1 and YA, respectively. The total number of worms measured for a particular condition, the number “n”, is noted below the bar plots. (g) Sorting purity of the initially mixed populations (L1 and YA, L1 and L2, L2 and L3, L3 and L4, and L4 and YA) at the input and the output of the microfluidic chip. Ideally, the larger stage larvae are all collected at the input (100% purity), while the smaller stage larvae are all obtained at the output (100% purity). Data is expressed as mean \pm SD. Measurements are based on 6 experiments for each sorting experiment.

filter chip. As already mentioned in the experimental section, we have prepared the different larvae populations by ‘synchronized’ culture on NGM agar plates. We underline the accuracy of the latter cultures, as we obtained 96, 95, 83 and 91% purity of the aimed L1, L2, L3 and L4 larval stages on their NGM plate, respectively (Figure 7.6). The local *E. coli* distribution,

the population density, and the distribution of worms on an NGM plate evidently can cause deviations from the ideal target worm population of 100%, leading to worms with a slightly slower or faster development. Also our method allowed worms in YA and YA-A transition to be collected from an agar plate, with a population of 40 and 58%, respectively. In preparation of a sorting experiment, we combined an approximately identical amount of worms from two consecutive larvae populations, and we loaded the mixed worm suspension in our device, the distribution of which is indicated by the left-hand side bars in Figure 7.5b-f. L1-L2 worm sorting experiments revealed a 94% accuracy in the sorted L1 worms at the output of the device, while the input of the device had only 10% L1 stage larvae and 90% of combined L2 and L3 larvae (Figure 7.5b). While the older stage larvae sorting (L3 larvae and a few L4 larvae) at the input in the L2-L3 sorting experiments demonstrated a sorting accuracy of 97%, the same operation allowed 27% of L3 larvae being transferred to the output (Figure 7.5c). A similar trend was also noted for L3-L4 sorting experiments by permitting only 8% L4 larvae to be collected at the output (Figure 7.5d). In this case, the input side of the filter device had only 10% L3 larvae after finalization of the sorting experiments. The sorting results of the L4-YA worms showed that the output of the device can sort young larvae (L3 and L4) at 100%, whereas the input side displayed a sorting characteristic of a combined 96% for YA and YA-A worms (Figure 7.5e). The same type of behavior was also observed in the L1-YA sorting experiments (Figure 7.5f). We note that, in this case, 5% of L2 larvae were also collected at the output of the sorting device, while they were not spotted initially in the collected samples from the agar culture plates. Summarizing, we demonstrated that the filter device can be conceived for accurate size-dependent sorting of all consecutive larval stages, an exception being the sorting of L2-L3 larvae at the output where 73% of L2 stage larvae could be collected (Figure 7.5c).

7.3.2 Purity of the sorting

A more subtle sorting characteristic was required to prove the efficacy of the microfluidic device. Therefore, we have chosen a ‘purity’ parameter to evaluate the device operation protocol [127, 193, 195]. Purity can be defined as the number of target worms divided by the number of all the worms at a target location (*i.e.* the output or input of the chip). As an example, if there were $a_1\%$ L1, $a_2\%$ L2, and $a_3\%$ L3 worms at the output of the device for an L2-L3 sorting experiment, purity could be calculated as $a_2\%$. For our experiments, we defined purity however as $100\% - a_3\%$ to take into account younger larvae that were eventually present in the mixed population at the output. We looked at the individual experiments, calculated the purity of each one and then combined the data together (Figure 7.5g). We obtained a purity of 100, 90, 95, 87 and 99% at the input and 100, 94, 73, 93 and 99% at the output of the device for L1-YA, L1-L2, L2-L3, L3-L4 and L4-YA sorting experiments, respectively. Interestingly, a set of slightly higher purity values was found at the input compared to the output. This is understandable, as the older worm population can either reside at the input, upstream of the filter structures, or accidentally be transferred to the output. This behavior might lead to a drop in purity for the larval population that is expected to be collected at the output, whereas

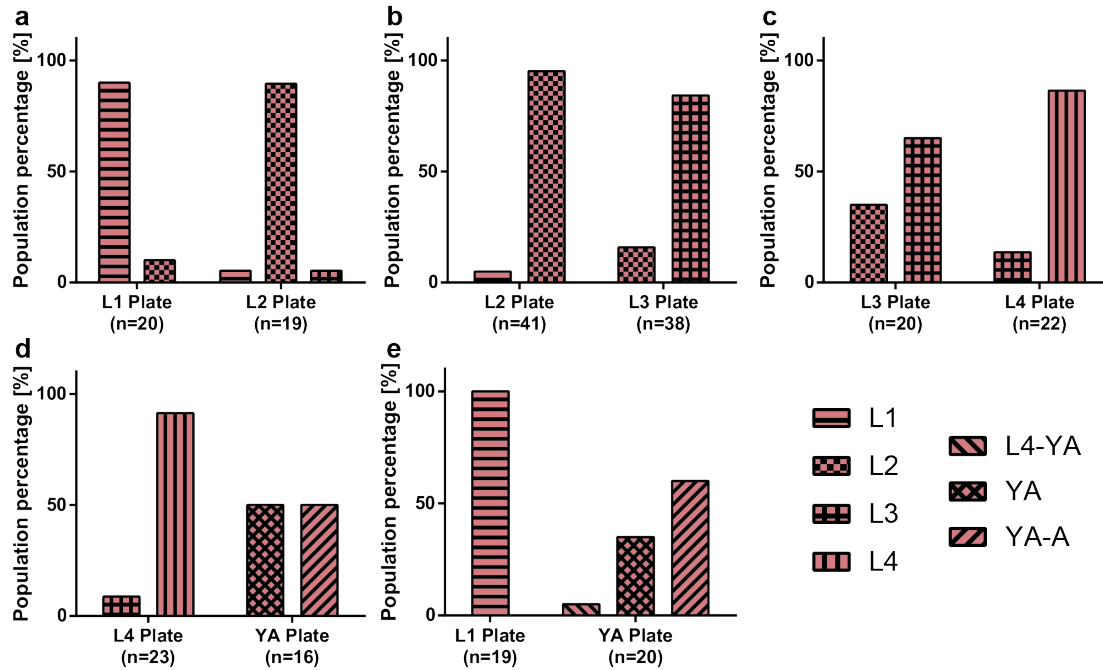


Figure 7.6 – Characterization of worm populations on NGM agar plates prior to sorting experiments. Larvae populations present on ‘synchronized’ NGM agar plates, as determined from the larval diameter, prior to mixing them for subsequent sorting experiments of (a) L1-L2, (b) L2-L3, (c) L3-L4, (d) L4-YA, and (e) L1-YA. The total number of worms measured for characterizing a NGM agar plate, the number “n”, is noted below the bar plots.

the input purity will remain unaffected. The high purity values obtained at the input of the device indicate that the input side of the microfluidic device is the one that can be optimally tuned for sorting applications. We noticed a significant drop of purity at the output of the L2-L3 sorting device, as already noted in the results priorly obtained through population-based statistics. However, the remaining purity values computed here indicate that the sorting purity of the proposed device is competitive compared to the previously proposed sorting results. Moreover, we can perform high purity sorting, while accomplishing such procedures in a significantly shorter period and in a less complicated manner than before.

7.4 On-chip egg extraction

7.4.1 Egg extraction via a standard bleaching procedure

We can also exploit our device to perform additional separation or sorting experiments. In particular, we demonstrated on-chip egg extraction from gravid adults (Figure 7.7) by employing a similar protocol as in the sorting experiments. After having the microfluidic device filled with S-medium solution and degassed, we loaded a synchronized adult worm population in the device (Figure 7.7a). In parallel, a standard bleaching solution was prepared, loaded in a 1

mL borosilicate syringe and plugged in the input of the microfluidic device. The bleaching solution was injected in the device and occasionally, manual pull-push steps by the syringe were required to break adult body fragments utilizing filter structures (Figure 7.7b). Once all the body fragments were dissolved (typically in 10-15 minutes) and only embryos were left in the filtering layer, a 1 mL borosilicate syringe containing filtered S-medium was connected at the input and the device was washed in approximately 30 seconds. The S-medium washing step was repeated at least 3 times to ensure removal of bleaching reagent. In the last S-medium washing step, the output of the device was clamped and it was left in this configuration overnight (Figure 7.7c). The day after – or at least 12 hours later –, the output was gently unclamped to avoid instant S-medium flush in the device due to overpressure. We noticed a population of synchronized L1 larvae, unhatched embryo clusters and debris in the filtering layer (Figure 7.7d). 1 mL of S-medium was injected from the input to collect L1 population at the output. This operation was also performed from the output to retain the remaining debris and embryos from the input. After characterizing the obtained samples under a bright-field microscope (Figure 7.7e), we noticed that the output sample contained 100% L1 larvae, while the sample at the input contained unhatched embryos or aggregates of embryos and debris. The microfluidic filter device served two purposes in this study: (i) allowing the collection of a synchronized L1 worm population, and (ii) removal of any dirt or unhatched embryos created during the bleaching procedure. Additionally, by injecting 1 mL of S-medium from the output as soon as the bleaching process was finalized, the device can be tuned for egg collection from the input. Our method allows rapid egg extraction and L1 larvae synchronization without a need of any external hardware. We believe that this feature is highly valuable for the *C. elegans* research community, as our chip easily replaces all the required hardware needed for a standard bleaching procedure.

7.4.2 Egg extraction via mechanical compression of PDMS

We also tried another methodology in an attempt to exclude even the traditional bleaching step from the protocol (Figure 7.8). This method constituted of a manual and local PDMS deflection to extract eggs from mother nematodes [107]. We noticed that the method works too but is subjected to future optimization opportunities, as it can enable massive egg extraction and L1 larvae synchronization without a need of both external hardware and a bleaching protocol.

7.5 Discussion and conclusion

We report a new microfluidic filter device for size-dependent sorting and rapid egg extraction of *C. elegans*. Worm assays require age-synchronized populations for longitudinal developmental and culture studies, and accurate age synchronization methods traditionally often require tedious manipulation methods. We tackled these issues by providing a hand-held tool that will be easy-to-operate by all *C. elegans* researchers. The proposed device consists

Chapter 7. PDMS filter structures for size-dependent sorting and on-chip egg extraction of *C. elegans*

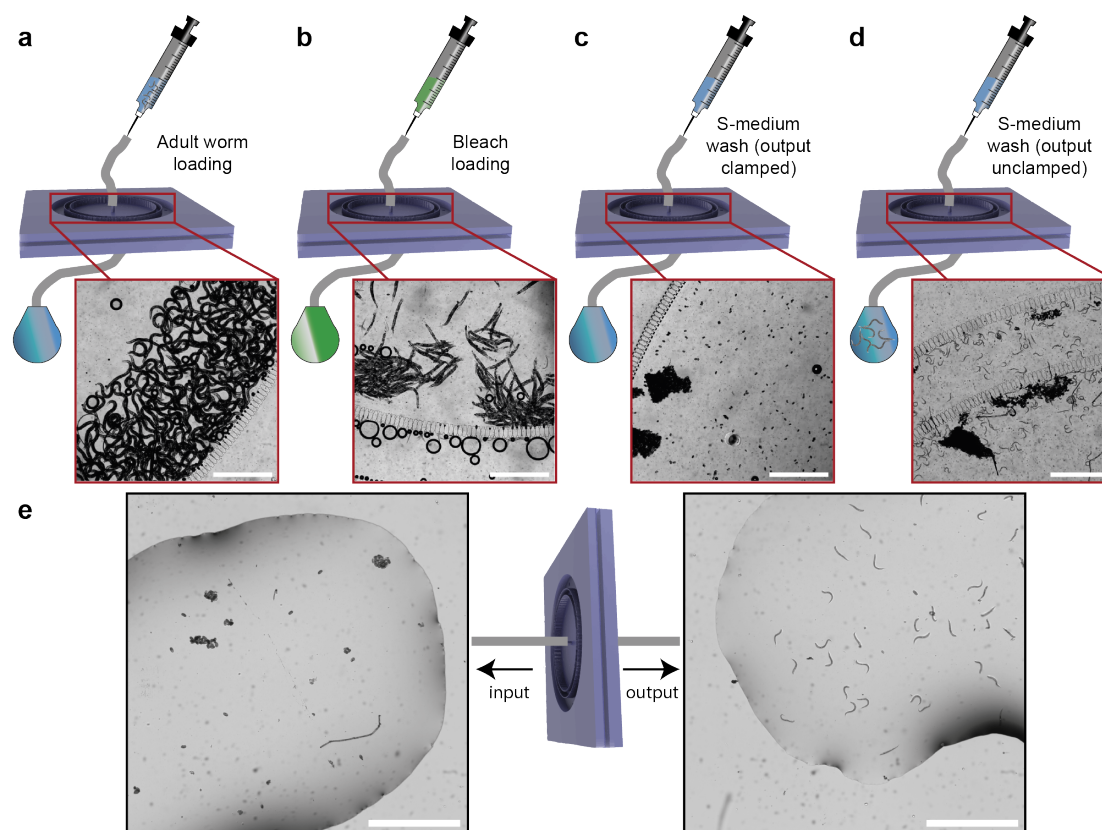


Figure 7.7 – Schematic illustration and real-time images of the experimental protocol for on-chip egg extraction via bleaching. (a) After chip filling and degassing steps, an adult worm population is loaded in the microfluidic device. (b) A standard bleaching solution is exposed to the adult worms present in the filtering layer. (c) Once the adult body fragments disappear, a fresh S-medium solution is injected to terminate the bleaching process. After three cycles of S-medium injection of 1 mL, for degassing of the chip, its output is clamped and S-medium solution is loaded from the input to leave embryos overnight while keeping PDMS chip inflated. (d) After 12 hours, the clamp is released and the L1 population that hatched from the eggs is washed out of the microfluidic device. A similar procedure is also applied to the output of the device to retain unhatched embryo population. (e) Unhatched embryos and embryo aggregates are seen to be retained at the input of the device, while the output of the device produces a synchronized L1 population. Scale bars: 1000 μm .

of three plasma-activated and bonded PDMS parts, in which the adjustable filter structures permit selective sorting of several combinations of adjacent larval stages. We used 8, 15, 20 and 26 μm filter structures for target worm populations of L1, L2, L3 and L4 larvae, respectively. Our device accurately sorts any two consecutive developmental stage with a purity ranging from 73 to 100% at the output and from 87 to 100% at the input of the microfluidic chip. Our device showed possibility of multiple reuse in absence of major clogging issues with the filter structures. As the device was operating with a massive amount of worms, the exact numbers of larvae were not precisely calculated but rather approximated. We characterized the sample

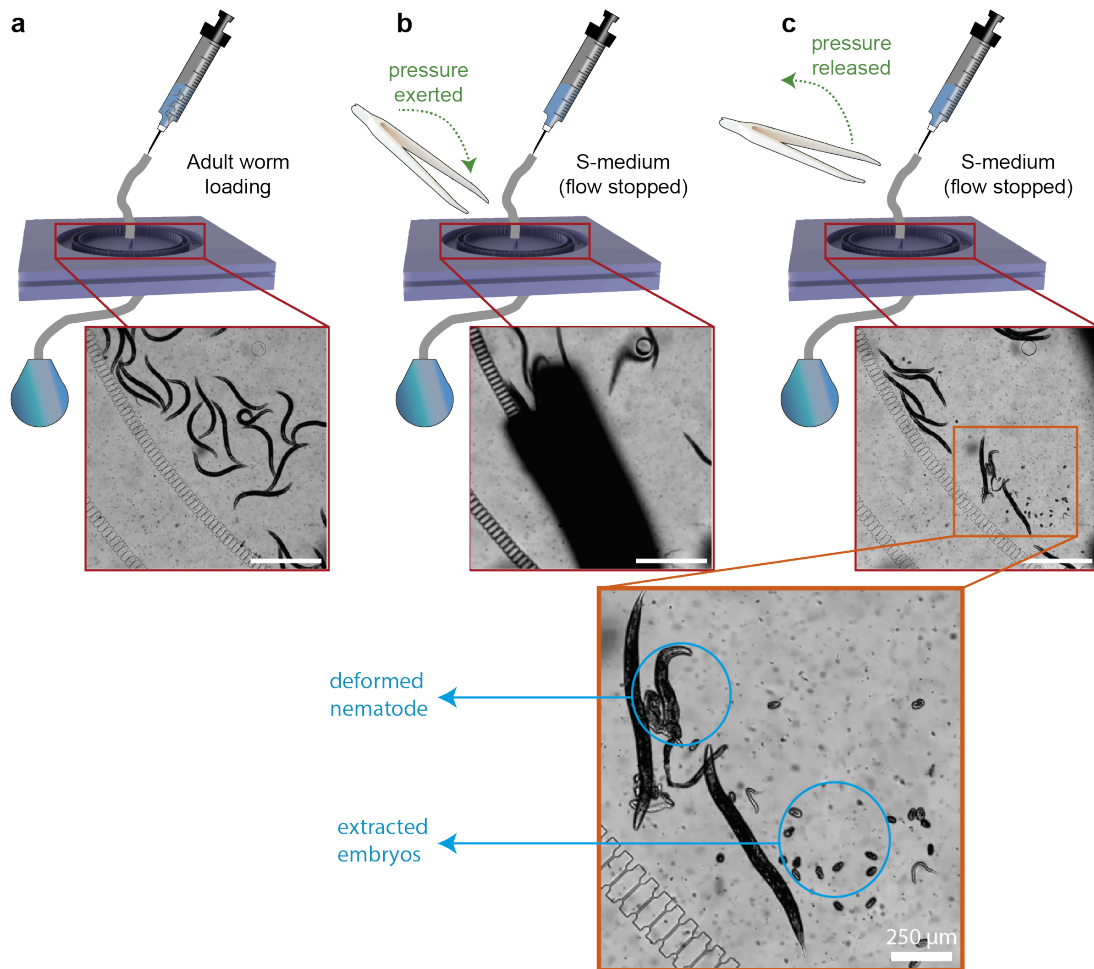


Figure 7.8 – Schematic illustration and real-time images of the experimental protocol for on-chip egg extraction via PDMS deflection. (a) After the chip filling and degassing steps, an adult worm population is loaded in the microfluidic device. (b) A tweezer is used to exert pressure locally on the PDMS chip and hence the adult nematodes are mechanically compressed. (c) After the release of the tweezer, some worms have deformed characteristics and embryos are extracted from these worms. Scale bars: 1000 μm (unless otherwise stated).

sizes by checking a few 2 μL droplets from the population reservoirs and we adjusted the worm populations used in the experiments accordingly. We tried to have almost equal amounts of worms, in the range of 200 to 400 worms, from two adjacent larval stages per experiment. The entire sorting operation took place in 2 to 3 minutes, displaying an average throughput of 160 to 240 worms per minute. We studied the sorting operation with moderate sample sizes to closely observe its functioning. However, the throughput of the device can be enhanced by increasing the sample size without problem. We additionally illustrated an experimental approach to synchronize larvae populations at different stages on NGM agar plates prior to an experiment. In future, this type of microfluidic chip could be used too with different filter combinations to refine the sorting of a target population from a mixed population. For

Chapter 7. PDMS filter structures for size-dependent sorting and on-chip egg extraction of *C. elegans*

example, a L3 population can be obtained by using first a microfluidic chip with 20 μm filter structures and collecting the worm population at the output (containing L3, L2 and L1 worms). In a second step, the thus filtered population can be loaded in a microfluidic chip with 15 μm filter structures (targeting L2 and L1 worms at the output) and one could collect the remaining L3 worm population residing at the input. Eventually, different filter structures could be configured on a single filter chip too.

We exploited some of the microfluidic devices with a filter structure width of 8 μm for egg harvesting applications. Our technique allowed rapid extraction of *C. elegans* eggs without a need of any external hardware. By employing a standard bleaching procedure on-chip, we collected *C. elegans* embryos within 20-30 minutes. Such a method by-passed the requirement of expensive hardware, like centrifugation equipment, and all harvesting protocols could be implemented using a 1 mL borosilicate syringe, microfluidic chip, external tubing, Eppendorf reservoirs and a bleaching solution. 12 hours after embryo collection, we retained a synchronized population of L1 larvae at the output of the microfluidic device.

Overall, we illustrate here our novel platform for rapid larvae sorting and egg extraction of the nematode *C. elegans* at high-throughput. Based on the purity results, highly selective larvae sorting has been performed and an alternative method for egg harvesting has been demonstrated.

We believe that this microfluidic chip can reach out to a broad scientific community to tackle many of labor-intense *C. elegans* handling steps. The hand-held configuration of the device in particular provides massive simplification for applications, as it can be used just like a standard syringe filter. In the near future, with further design optimizations, this device could find wide use in nematode synchronization and egg harvesting applications.

8 Conclusions

The total duration of a drug discovery pipeline is known to be around 15 years to release just one compound to the market. In particular, the drug discovery process consists of 3 to 5 years-long high-throughput screening mostly relying on cell-based assays, which is followed by 1 to 2 years of drug testing with rodents. *C. elegans* provides massive advantages in terms of shortening this process, as motivated by its short life cycle, hermaphroditism, small size and well-annotated genome. Often in combination with microfluidic technologies, reliable and large sets of phenotypic data can be extracted in a short matter of time and ethical limitations can be avoided. Miniaturization of bioanalytical applications with the trending innovations in the LoC field has allowed precise control of reagents to be delivered to the nematodes in an automated manner, while also tackling common issues frequently encountered during manual handling procedures. Despite having a simple body structure that lacks many vital organs, drug testing applications with *C. elegans* is becoming more and more common at the early phases of the drug discovery pipeline. In this thesis, I presented four different microfluidic devices to perform high-throughput, high-resolution, multiplexed and high-content studies based on these nematodes. For almost all the experiments, synchronization of worm populations is demanded to initiate an experiment with an identical population, avoiding heterogeneity in the resultant phenotypic data. A frequent issue during manual handling of the nematodes is the lack of robust and convenient tools to obtain age-synchronized populations. Additionally, I demonstrated an assisting microfluidic tool to solve age-synchronization problems of *C. elegans*.

Longitudinal and high-content phenotyping of the nematodes in a microfluidic device has not been extensively studied. In Chapter 3, I presented a novel microfluidic device that allowed high-throughput, multiplexed, automated and high-content studies of *C. elegans* down to single worm resolution. By regularly confining nematodes in tapered microfluidic channels, we extracted growth-related parameters and observed the fluorescent content of the nematodes. In parallel, the free swimming motion of the nematodes in spacious culture chambers was recorded to obtain swimming gait. We employed a caloric restriction study on a worm model of Huntington's disease by providing various dilutions of *E. coli* concentration as the platform's validation study and obtained 19 phenotyping parameters. We noticed that the

disease significantly regressed under application of caloric restriction and we validated the applicability of this device in neurodegenerative disease studies.

C. elegans is known to exhibit a motility changing behavior under application of toxic compounds. While it is well-established that these nematodes can be exploited to assess toxicity of certain compounds, several days-long culture and the mobile nature of the worms can cause problems. In Chapter 4, we exploited *C. elegans* embryos for potential toxicity-screening, as motivated by their short embryogenesis. We designed a microfluidic platform that can accommodate up to 800 embryos and enabled parallel experimental observation. We extracted the development-related phenotypes in an automated manner utilizing image processing and machine learning algorithms. Our results revealed a severe developmental lag of embryos in ionic solutions such as NaCl and a dose-dependent development with sugar-like molecules and proved the validity of this platform for toxicity assays.

Single-animal resolution culture and imaging of the nematode have always been of high interest. This type of platforms allow the collection of 'personalized' data as well as population-averaged information. While there have been plenty of designs for single-animal culture, these platforms lacked high-content phenotyping and multiplexed experimentation. In Chapter 5, we tackled these common issues by creating microfluidic devices that allow single-animal culture from the onset of embryogenesis to the adulthood of *C. elegans*, and this combined with high-resolution imaging, automated phenotyping and parallel compound screening. We investigated the effect of an anthelmintic drug, tetramisole, on the growth and motility parameters at various time points of the nematodes' life. Our results indicated a dose-dependent response established mainly at the later life stages of *C. elegans*. We also did not notice any severe influence of tetramisole during the embryogenesis.

The epigenetic inheritance in *C. elegans* has been extensively studied by observing generation-wide development, and this mostly on NGM agar plate-based assays. By exploiting the full potential of microfluidics, we illustrated a novel design that allowed us to track the whole dynamics of mother-to-progeny heritable transmission at high-resolution in Chapter 6. We created a platform to culture nematodes from L4 larval stage to the onset of adulthood and thereafter we sealed early embryo progenies in tight embryo traps for 12 hours of imaging. We investigated the early epigenetic stress inheritance by exposing parental generation to the stress-inducer compound doxycycline and we detected the stress induction in embryo progenies. We noticed that short stress inheritance in embryo progenies is possible although such an inheritance did not persist in larval descendants. This platform empowers many more early epigenetic studies to be performed, such as early life stage transition of neurodegenerative diseases.

Manual age-synchronization procedures of worm populations are tedious, low-throughput and complicated. Microfluidic approaches are utilized to facilitate such type of processes by means of easy fluidic control and high-throughput potential. Lastly, in Chapter 7, we illustrated a microfluidic device for rapid age-synchronization of *C. elegans*. Based on an adjustable PDMS filter design and hydrodynamic flow principles, the proposed device sorted two consecutive larval stages accurately. The microfluidic device was also tuned for on-chip egg extraction by exposing a bleaching solution to adult nematodes. The harvested embryos

can be left in the device for 12 hours to obtain a synchronized population of L1 larvae. We believe that this device can be delivered to *C. elegans* laboratories as an assisting tool due to its versatile set of applications.

Taking advantage of modularity and versatility of all the described microfluidic platforms in this thesis, several biological questions can be answered on *C. elegans*. While some of the devices can bring certain benefits such as high-resolution embryogenesis observation, some others can track the full growth dynamics of the nematodes during their life cycle. These devices can be also utilized consecutively. For example, a mixed worm population can be first age-synchronized at L1 larval stage by using the microfluidic device in Chapter 7 and subsequently a test experiment can be initiated with the platform in Chapter 3.

8.1 Future outlook

Currently, many research institutes and pharmaceutical companies are still not aware of the huge potential of using *C. elegans* in drug discovery applications. This is mainly due to existing problems in terms of automation, culture and imaging of the nematodes. By combining the proposed microfluidic platforms in this thesis and genetically modified *C. elegans* strains, rapid assaying of drugs on neurodegenerative disease models can be performed. For instance, we can investigate the polyQ aggregation in a Huntington's disease model, neuron degeneration of a Parkinson's disease model and protein aggregation in amyotrophic lateral sclerosis (ALS) disease model with high-resolution imaging, high-content phenotyping and at high-throughput.

Further improvements can be made on each of the proposed microfluidic platforms. The microfluidic chip described in Chapter 3 might benefit from 3D confinement channels for a more accurate confinement of the nematodes during their life. For the proposed microfluidic chip in Chapter 4, the automated bean stage detection can be ameliorated by including more bean images in the training data. A frequent issue was also the wobbling motion of embryos inside embryo incubators. Therefore, the embryo incubator design can be further optimized to retain embryos in the embryo incubators more tightly. The experimentation could be extended further for visualization of the late life stages of the nematodes for the microfluidic chip described in Chapter 5. This approach would enable possibly the entire lifespan tracking of *C. elegans* at single-animal resolution. As an update for the microfluidic chip explained in Chapter 6, the swimming behavior of the nematodes in culture chambers can also be video-recorded every few hours to obtain phenotypic data associated to motility. We can also improve the microfluidic device in Chapter 7 by a design modification that generates uniform PDMS deflection over the complete microfluidic chamber that hosts the adult nematodes to enable high-throughput egg extraction.

The following step will be to integrate these devices in a more automated setup and increase the throughput even further. We benefited already from the limited automation of a microscopy stage and a syringe pump. Multiple syringe pumps and a custom-made motorized setup must be integrated to host several microfluidic chips together. This implementation

Chapter 8. Conclusions

will offer full-automation and versatility in terms of fluidic control, image acquisition and the range of applications. After establishing an automated motorized setup adaptable to the microfluidic chips presented in this thesis, any of these microfluidic devices can be used and the study-of-interest can be initiated. For example, if a user wants to detect the early epigenetic inheritance on a Huntington's disease, the disease-related worm model will be loaded inside the microfluidic chip explained in Chapter 6. Alternatively, if a user wants to check the toxicity of a compound on human during the drug discovery process, the initial trials can be performed with the nematodes in the microfluidic chip demonstrated in Chapter 5 to collect phenotypic data at single-animal resolution and in populations together.

A challenge in image acquisition was the integration of objectives, such as 63× oil immersion, for extremely high-resolution imaging. The main limitation here was the usage of a standard microscope slide as the PDMS sealing part. The large area of PDMS parts, due to integration of several culture chambers for high-throughput assays, did not allow using a thin cover glass as it can easily break on the platform. The custom-made platform must contain supporting structures to hold the microfluidic chip sealed on a thin cover glass stably and hence the extremely high-resolution imaging will be enabled.

Another issue is that with the current micro-fabrication protocols, it is not possible to extract nematodes back once the experiments are finalized. This is due to the tight constriction filters which are designed to allow only young larvae to pass and makes it not possible to collect the worms off-chip after they pass through a few developmental stages. In many biological assays, worm handling using Eppendorf tubes or micro-titer plates is required to perform gene sequencing, centrifugation or Polymerase chain reaction (PCR). This is currently one of the main reasons why biological research laboratories do not explore the benefits of microfluidic devices. In fact, a micro-fabrication process which could potentially allow unsealing of the device, such as adapting a thermal-bonding process rather than an oxygen plasma-bonding, will be highly useful to retain the worm populations and proceed with additional biological assays. Thus, a microfluidic-based and standard analytical method can be combined together to gather in-depth information.

The uniformity of the bacterial solution inside a microfluidic device is a recurrent question at all times. Prior to an experiment, the bacterial concentration is confirmed using an optical density meter. Later, this solution is dispensed in the microfluidic device, presuming that the concentration is uniform throughout the microfluidic lanes due to frequent media aspiration and excitation from the bacterial reservoirs. However, occasional *E. coli* aggregation in the device might result with locally changing bacterial concentration. To solve this problem, on-chip density measurements must be integrated to ensure the uniformity of the *E. coli* concentration. For example, arrays of light emitting diodes and photodiodes can be utilized to track the on-chip media concentration.

Finally, larva removal must be better optimized. Our fluidic protocol consists of increasing media flow rate at the late stages of the worm development to wash-off larval progenies towards the Eppendorf reservoirs. While this protocol works accurately for our experimental studies, if a user wants to continue to observe the entire lifespan of the nematodes, there might be a massive amount of worm population in the Eppendorf reservoirs and hence significantly

reduced *E. coli* concentration compared to the beginning of the experiment. This problem can be solved by collecting progenies in the waste reservoir or integrating an automated reservoir removal/filling step to ensure bacterial uniformity.

After making the aforementioned improvements, a more compact and robust type of platform can be developed. We anticipate that such a platform will attract several organizations, including pharmaceutical companies, research institutes and biology laboratories. The future of *C. elegans* therefore looks extremely bright with a broad set of possible applications, although there is still a lot to do to build the ultimate platform and to convince stakeholders of the utility of using a *C. elegans* worm model. We hope this thesis has brought this far-away end goal one step closer.

Acronyms

<i>C. elegans</i>	<i>Caenorhabditis elegans</i>
LoC	Lab-on-a-chip
PDMS	Polydimethylsiloxane
DR	Dietary restriction
<i>E. coli</i>	<i>Escherichia coli</i>
UPR ^{mt}	Mitochondrial unfolded protein response reporter
GFP	Green fluorescent protein
NGM	Nematode growth medium
<i>Re</i>	Reynolds number
V_{avg}	The average flow velocity
L	The channel diameter
ρ	The fluid density
μ	The fluid viscosity
u	The fluid velocity
p	The pressure field
γ	The kinematic viscosity
F	The external acceleration field
Cr	Chromium
Si	Silicium
FOTS	<i>1H,1H,2H,2H</i> -Perfluorooctyl-trichlorosilane
TMCS	Trimethylchlorosilane
DI	Deionized
YA	Young adult
CMi	Center of Micro-Nanotechnology
λ	The wavelength
HD	Huntington's disease
YFP	Yellow fluorescent protein
NA	The numerical aperture
GUI	Guided user interface
WT	Wild-type
σ	Standard deviation
I_{SBR}	The corrected fluorescent intensity value

Chapter 8. Acronyms

I_{ROI}	The average worm/embryo fluorescent intensity value
I_{BG}	The average background fluorescent intensity value
B_{final}	The “final” background
$B_{video\ set}$	The “video set” background
$B_{overall}$	The “overall” background
AL	<i>ad libitum</i>
SEM	Standard error of the mean
R^2	The coefficient of determination
CAG	Cytosine-adenine-guanine
polyQ	Polyglutamine
ANOVA	Analysis of variance
ARDE	Aspect ratio dependent etching
3D	Three-dimensional
SEM	Scanning electron microscope
ROS	Reactive oxygen species
FUdR	5-fluorodeoxyuridine
VPL	Liquid velocity profile at the closest point to the media outlet
VPC	Liquid velocity profile at the center point of the microfluidic lane
VPR	Liquid velocity profile at the closest point to the media inlet
CNN	Convolutional neural network
ReLU	Rectified linear unit
MF	Mobility function
A.U.	Arbitrary unit
EPG	Electropharyngeogram
IC ₅₀	The half-maximal effective concentration
EC ₅₀	The half-maximal inhibitory concentration
RNAi	Ribonucleic acid interference
MET	Mothers and embryos both doxycycline-treated
OMT	Only mothers doxycycline-treated for 15 hours
OET	Only embryos doxycycline-treated
CNT	Control – no doxycycline treatment
SD	Standard deviation
D_{range}	The diameter measurement range
D_{avg}	The average diameter at the onset of larval stage transition
D	The diameter of the worm
A	Adult stage
ALS	Amyotrophic lateral sclerosis
PCR	Polymerase chain reaction

Bibliography

- [1] M. Cornaglia, T. Lehnert, and M. A. M. Gijs, "Microfluidic systems for high-throughput and high-content screening using the nematode *Caenorhabditis elegans*," *Lab on a Chip*, vol. 17, no. 22, pp. 3736–3759, 2017.
- [2] M. Artal-Sanz, L. de Jong, and N. Tavernarakis, "Caenorhabditis elegans: A versatile platform for drug discovery," *Biotechnology Journal*, vol. 1, no. 12, pp. 1405–1418, 2006.
- [3] E. Michelini, L. Cevenini, L. Mezzanotte, A. Coppa, and A. Roda, "Cell-based assays: Fuelling drug discovery," *Analytical and Bioanalytical Chemistry*, vol. 398, no. 1, pp. 227–238, 2010.
- [4] T. Denayer, T. Stöhr, and M. Van Roy, "Animal models in translational medicine: Validation and prediction," *New Horizons in Translational Medicine*, vol. 2, no. 1, pp. 5–11, 2014.
- [5] G. D. Coxon, C. B. Cooper, S. H. Gillespie, and T. D. McHugh, "Strategies and challenges involved in the discovery of new chemical entities during early-stage tuberculosis drug discovery," *Journal of Infectious Diseases*, vol. 205, no. SUPPL. 2, pp. S258–S264, 2012.
- [6] T. Kaletta and M. O. Hengartner, "Finding function in novel targets: C. elegans as a model organism," *Nature Reviews Drug Discovery*, vol. 5, no. 5, pp. 387–398, 2006.
- [7] M. S. Boguski, "Comparative genomics: The mouse that roared," *Nature*, vol. 420, no. 6915, pp. 515–516, 2002.
- [8] M. Markaki and N. Tavernarakis, "Modeling human diseases in *Caenorhabditis elegans*," *Biotechnology Journal*, vol. 5, no. 12, pp. 1261–1276, 2010.
- [9] L. P. O'Reilly, C. J. Luke, D. H. Perlmutter, G. A. Silverman, and S. C. Pak, "C. elegans in high-throughput drug discovery," *Advanced Drug Delivery Reviews*, vol. 69-70, pp. 247–253, 2014.
- [10] S. Brenner, "The Genetics of *Caenorhabditis elegans*," *Genetics*, vol. 77, no. 1, pp. 71–94, 1974.

Bibliography

- [11] J. E. Sulston, E. Schierenberg, J. G. White, and J. N. Thomson, "The embryonic cell lineage of the nematode *Caenorhabditis elegans*," *Developmental Biology*, vol. 100, no. 1, pp. 64–119, 1983.
- [12] M. C. Leung, P. L. Williams, A. Benedetto, C. Au, K. J. Helmcke, M. Aschner, and J. N. Meyer, "Caenorhabditis elegans: An emerging model in biomedical and environmental toxicology," *Toxicological Sciences*, vol. 106, no. 1, pp. 5–28, 2008.
- [13] J. Li and W. Le, "Modeling neurodegenerative diseases in *Caenorhabditis elegans*," *Experimental Neurology*, vol. 250, pp. 94–103, 2013.
- [14] S. Ogg, S. Paradis, S. Gottlieb, G. I. Patterson, L. Lee, H. A. Tissenbaum, and G. Ruvkun, "The Fork head transcription factor DAF-16 transduces insulin-like metabolic and longevity signals in *C. elegans*," *Nature*, vol. 389, no. 6654, pp. 994–999, 1997.
- [15] N. Perrimon, "Signalling pathways initiated by receptor protein tyrosine kinases in *Drosophila*," *Current Opinion in Cell Biology*, vol. 6, no. 2, pp. 260–266, 1994.
- [16] V. Ambros, "Control of developmental timing in *Caenorhabditis elegans*," *Current Opinion in Genetics and Development*, vol. 10, no. 4, pp. 428–433, 2000.
- [17] R. Pulak, "Techniques for Analysis, Sorting, and Dispensing of *C. elegans* on the COPAS Flow-Sorting System," *Methods in Molecular Biology*, vol. 351, pp. 275–286, 2006.
- [18] M. Doitsidou, N. Flames, A. C. Lee, A. Boyanov, and O. Hobert, "Automated screening for mutants affecting dopaminergic-neuron specification in *C. elegans*," *Nature Methods*, vol. 5, no. 10, pp. 869–872, 2008.
- [19] T. C. Kwok, N. Ricker, R. Fraser, A. W. Chan, A. Burns, E. F. Stanley, P. McCourt, S. R. Cutler, and P. J. Roy, "A small-molecule screen in *C. elegans* yields a new calcium channel antagonist," *Nature*, vol. 441, no. 7089, pp. 91–95, 2006.
- [20] J. El-Ali, P. K. Sorger, and K. F. Jensen, "Cells on chips," *Nature*, vol. 442, no. 7101, pp. 403–411, 2006.
- [21] H. Andersson and A. Van den Berg, "Microfluidic devices for cellomics: A review," *Sensors and Actuators, B: Chemical*, vol. 92, no. 3, pp. 315–325, 2003.
- [22] S. Le Gac and A. van den Berg, "Single cells as experimentation units in lab-on-a-chip devices," *Trends in Biotechnology*, vol. 28, no. 2, pp. 55–62, 2010.
- [23] D. Di Carlo and L. P. Lee, "Dynamic Single-Cell Analysis for Quantitative Biology," *Anal Chem*, vol. 78, no. 23, pp. 7918–7925, 2006.
- [24] S. Gavrilakis, "Numerical simulation of low-reynolds-number turbulent flow through a straight square duct," *Journal of Fluid Mechanics*, vol. 244, pp. 101–129, 1992.

-
- [25] V. Sivagnanam and M. A. M. Gijs, "Exploring Living Multicellular Organisms, Organs, and Tissues Using Microfluidic Systems," *Chemical Reviews*, vol. 113, no. 5, pp. 3214–3247, 2013.
- [26] B. P. Gupta and P. Rezai, "Microfluidic approaches for manipulating, imaging, and screening *C. elegans*," *Micromachines*, vol. 7, no. 7, 123, 2016.
- [27] M. Muthaiyan Shanmugam and T. Subhra Santra, "Microfluidic Devices in Advanced *Caenorhabditis elegans* Research," *Molecules*, vol. 21, no. 8, E1006, 2016.
- [28] E. Kim, L. Sun, C. V. Gabel, and C. Fang-Yen, "Long-Term Imaging of *Caenorhabditis elegans* Using Nanoparticle-Mediated Immobilization," *PLoS ONE*, vol. 8, no. 1, e53419, 2013.
- [29] N. Chronis, M. Zimmer, and C. I. Bargmann, "Microfluidics for in vivo imaging of neuronal and behavioral activity in *Caenorhabditis elegans*," *Nature Methods*, vol. 4, no. 9, pp. 727–731, 2007.
- [30] C. B. Rohde, F. Zeng, R. Gonzalez-Rubio, M. Angel, and M. F. Yanik, "Microfluidic system for on-chip high-throughput whole-animal sorting and screening at subcellular resolution," *Proceedings of the National Academy of Sciences*, vol. 104, no. 35, pp. 13891–13895, 2007.
- [31] S. Mondal, S. Ahlawat, K. Rau, V. Venkataraman, and S. P. Koushika, "Imaging in vivo Neuronal Transport in Genetic Model Organisms Using Microfluidic Devices," *Traffic*, vol. 12, no. 4, pp. 372–385, 2011.
- [32] W. Keil, L. M. Kutscher, S. Shaham, and E. D. Siggia, "Long-Term High-Resolution Imaging of Developing *C. elegans* Larvae with Microfluidics," *Developmental Cell*, vol. 40, no. 2, pp. 202–214, 2017.
- [33] S. Berger, E. Lattmann, T. Aegerter-Wilmsen, M. Hengartner, A. Hajnal, A. Demello, and X. Casadevall I Solvas, "Long-term *C. elegans* immobilization enables high resolution developmental studies in vivo," *Lab on a Chip*, vol. 18, no. 9, pp. 1359–1368, 2018.
- [34] W. Shi, J. Qin, N. Ye, and B. Lin, "Droplet-based microfluidic system for individual *Caenorhabditis elegans* assay," *Lab on a Chip*, vol. 8, no. 9, pp. 1432–1435, 2008.
- [35] M. Cornaglia, G. Krishnamani, L. Mouchiroud, V. Sorrentino, T. Lehnert, J. Auwerx, and M. A. Gijs, "Automated longitudinal monitoring of in vivo protein aggregation in neurodegenerative disease *C. elegans* models," *Molecular Neurodegeneration*, vol. 11, 17, 2016.
- [36] J. Krajniak and H. Lu, "Long-term high-resolution imaging and culture of *C. elegans* in chip-gel hybrid microfluidic device for developmental studies," *Lab on a Chip*, vol. 10, no. 14, pp. 1862–1868, 2010.

Bibliography

- [37] H. Bringmann, "Agarose hydrogel microcompartments for imaging sleep- and wake-like behavior and nervous system development in *Caenorhabditis elegans* larvae," *Journal of Neuroscience Methods*, vol. 201, no. 1, pp. 78–88, 2011.
- [38] W. E. Pittman, D. B. Sinha, W. B. Zhang, H. E. Kinser, and Z. Pincus, "A simple culture system for long-term imaging of individual *C. elegans*," *Lab on a Chip*, vol. 17, no. 22, pp. 3909–3920, 2017.
- [39] M. A. Churgin, S. K. Jung, C. C. Yu, X. Chen, D. M. Raizen, and C. Fang-Yen, "Longitudinal imaging of *Caenorhabditis elegans* in a microfabricated device reveals variation in behavioral decline during aging," *eLife*, vol. 6, e26652, 2017.
- [40] L. Byerly, R. C. Cassada, and R. Russell, "The life cycle of the nematode *Caenorhabditis elegans*," *Developmental Biology*, vol. 51, no. 1, pp. 23–33, 1976.
- [41] Z. F. Altun and D. H. Hall, "Introduction to *C. elegans* anatomy," 2009.
- [42] F. Yang, Z. Chen, J. Pan, X. Li, J. Feng, and H. Yang, "An integrated microfluidic array system for evaluating toxicity and teratogenicity of drugs on embryonic zebrafish developmental dynamics," *Biomicrofluidics*, vol. 5, no. 2, 24115, 2011.
- [43] D. Choudhury, D. Van Noort, C. Iliescu, B. Zheng, K. L. Poon, S. Korzh, V. Korzh, and H. Yu, "Fish and chips: A microfluidic perfusion platform for monitoring zebrafish development," *Lab on a Chip*, vol. 12, no. 5, pp. 892–900, 2012.
- [44] M. Gershow, M. Berck, D. Mathew, L. Luo, E. A. Kane, J. R. Carlson, and A. D. T. Samuel, "Controlling airborne cues to study small animal navigation," *Nature Methods*, vol. 9, no. 3, pp. 290–296, 2012.
- [45] E. Brouzes, M. Medkova, N. Savenelli, D. Marran, M. Twardowski, J. B. Hutchison, J. M. Rothberg, D. R. Link, N. Perrimon, and M. L. Samuels, "Droplet microfluidic technology for single-cell high-throughput screening," *Proceedings of the National Academy of Sciences*, vol. 106, no. 34, pp. 14195–200, 2009.
- [46] J. Sznitman, P. K. Purohit, P. Krajacic, T. Lamitina, and P. E. Arratia, "Material properties of *Caenorhabditis elegans* swimming at low reynolds number," *Biophysical Journal*, vol. 98, no. 4, pp. 617–626, 2010.
- [47] C. Wählby, L. Kamentsky, Z. H. Liu, T. Riklin-Raviv, A. L. Conery, E. J. O'Rourke, K. L. Sokolnicki, O. Visvikis, V. Ljosa, J. E. Irazoqui, P. Golland, G. Ruvkun, F. M. Ausubel, and A. E. Carpenter, "An image analysis toolbox for high-throughput *C. elegans* assays," *Nature Methods*, vol. 9, no. 7, pp. 714–716, 2012.
- [48] P. Krajacic, X. Shen, P. K. Purohit, P. Arratia, and T. Lamitina, "Biomechanical profiling of *Caenorhabditis elegans* motility," *Genetics*, vol. 191, no. 3, pp. 1015–1021, 2012.

-
- [49] L.-C. Lin and H.-S. Chuang, "Analyzing the locomotory gaitprint of *Caenorhabditis elegans* on the basis of empirical mode decomposition," *PLoS ONE*, vol. 12, no. 7, e0181469, 2017.
- [50] J. Sznitman, X. Shen, P. K. Purohit, and P. E. Arratia, "The effects of fluid viscosity on the kinematics and material properties of *C. elegans* swimming at low reynolds number," *Experimental Mechanics*, vol. 50, pp. 1303–1311, 2010.
- [51] K. Chung, M. Zhan, J. Srinivasan, P. W. Sternberg, E. Gong, F. C. Schroeder, and H. Lu, "Microfluidic chamber arrays for whole-organism behavior-based chemical screening," *Lab on a Chip*, vol. 11, no. 21, pp. 3689–3697, 2011.
- [52] S. Mondal, E. Hegarty, C. Martin, S. K. Gökçe, N. Ghorashian, and A. Ben-Yakar, "Large-scale microfluidics providing high-resolution and high-throughput screening of *Caenorhabditis elegans* poly-glutamine aggregation model," *Nature Communications*, vol. 7, 13023, 2016.
- [53] S. E. Hulme, S. S. Shevkoplyas, A. P. McGuigan, J. Apfeld, W. Fontana, and G. M. Whitesides, "Lifespan-on-a-chip: Microfluidic chambers for performing lifelong observation of *C. elegans*," *Lab on a Chip*, vol. 10, no. 5, pp. 589–597, 2010.
- [54] S. K. Gokce, E. M. Hegarty, S. Mondal, P. Zhao, N. Ghorashian, M. A. Hilliard, and A. Ben-Yakar, "A multi-trap microfluidic chip enabling longitudinal studies of nerve regeneration in *Caenorhabditis elegans*," *Scientific Reports*, vol. 7, 9837, 2017.
- [55] H. Wen, W. Shi, and J. Qin, "Multiparameter evaluation of the longevity in *C. elegans* under stress using an integrated microfluidic device," *Biomedical Microdevices*, vol. 14, no. 4, pp. 721–728, 2012.
- [56] S. Uppaluri and C. P. Brangwynne, "A size threshold governs *Caenorhabditis elegans* developmental progression," *Proceedings of the Royal Society B: Biological Sciences*, vol. 282, no. 1813, 20151283, 2015.
- [57] M. C. Letizia, M. Cornaglia, R. Trouillon, V. Sorrentino, L. Mouchiroud, M. S. Bou Sleiman, J. Auwerx, and M. A. M. Gijs, "Microfluidics-enabled phenotyping of a whole population of *C. elegans* worms over their embryonic and post-embryonic development at single-organism resolution," *Microsystems & Nanoengineering*, vol. 4, 6, 2018.
- [58] S. Li, H. A. Stone, and C. T. Murphy, "A microfluidic device and automatic counting system for the study of *C. elegans* reproductive aging," *Lab on a Chip*, vol. 15, no. 2, pp. 524–531, 2015.
- [59] S. Saberi-Bosari, J. Huayta, and A. San-Miguel, "A microfluidic platform for lifelong high-resolution and high throughput imaging of subtle aging phenotypes in *C. elegans*," *Lab on a Chip*, vol. 18, no. 20, pp. 3090–3100, 2018.

Bibliography

- [60] C. M. McCay, M. F. Crowell, and L. A. Maynard, "The effect of retarded growth upon the length of life span and upon the ultimate body size," *The Journal of Nutrition*, vol. 10, no. 1, pp. 63–79, 1935.
- [61] W. Mair and A. Dillin, "Aging and Survival: The Genetics of Life Span Extension by Dietary Restriction," *Annual Review of Biochemistry*, vol. 77, pp. 727–754, 2008.
- [62] R. J. Colman, T. M. Beasley, J. W. Kemnitz, S. C. Johnson, R. Weindruch, and R. M. Anderson, "Caloric restriction reduces age-related and all-cause mortality in rhesus monkeys," *Nature Communications*, vol. 5, 3557, 2014.
- [63] D. Omodei and L. Fontana, "Calorie restriction and prevention of age-associated chronic disease," *FEBS Letters*, vol. 585, no. 11, pp. 1537–1542, 2011.
- [64] E. L. Greer and A. Brunet, "Different dietary restriction regimens extend lifespan by both independent and overlapping genetic pathways in *C. elegans*," *Aging Cell*, vol. 8, no. 2, pp. 113–127, 2009.
- [65] W. Mair, S. H. Panowski, R. J. Shaw, and A. Dillin, "Optimizing dietary restriction for genetic epistasis analysis and gene discovery in *C. elegans*," *PLoS ONE*, vol. 4, no. 2, e4535, 2009.
- [66] J. F. Morley, H. R. Brignull, J. J. Weyers, and R. I. Morimoto, "The threshold for polyglutamine-expansion protein aggregation and cellular toxicity is dynamic and influenced by aging in *Caenorhabditis elegans*," *Proceedings of the National Academy of Sciences*, vol. 99, no. 16, pp. 10417–10422, 2002.
- [67] T. Yoneda, C. Benedetti, F. Urano, S. G. Clark, H. P. Harding, and D. Ron, "Compartment-specific perturbation of protein handling activates genes encoding mitochondrial chaperones," *Journal of Cell Science*, vol. 117, no. 18, pp. 4055–4066, 2004.
- [68] W. Gilpin, S. Uppaluri, and C. P. Brangwynne, "Worms under pressure: Bulk mechanical properties of *C. elegans* are independent of the cuticle," *Biophysical Journal*, vol. 108, no. 8, pp. 1887–1898, 2015.
- [69] Y. Koren, R. Sznitman, P. E. Arratia, C. Carls, P. Krajacic, A. E. Brown, and J. Sznitman, "Model-independent phenotyping of *C. elegans* locomotion using scale-invariant feature transform," *PLoS ONE*, vol. 10, no. 3, e0122326, 2015.
- [70] J. Sznitman, X. Shen, R. Sznitman, and P. E. Arratia, "Propulsive force measurements and flow behavior of undulatory swimmers at low Reynolds number," *Physics of Fluids*, vol. 22, no. 12, 121901, 2010.
- [71] S.-j. Lin, P.-A. Defossez, and L. Guarente, "Requirement of NAD and SIR2 for Life-Span Extension by Calorie Restriction in *Saccharomyces cerevisiae*," *Science*, vol. 289, no. 5487, pp. 2126–2128, 2000.

-
- [72] A. K. Chippindale, A. M. Leroi, H. Saing, D. J. Borash, and M. R. Rose, "Phenotypic plasticity and selection in *Drosophila* life history evolution. 2. Diet, mates and the cost of reproduction," *Journal of Evolutionary Biology*, vol. 10, no. 3, pp. 269–293, 1997.
- [73] M. R. Klass, "Aging in the nematode *Caenorhabditis elegans*: Major biological and environmental factors influencing life span," *Mechanisms of Ageing and Development*, vol. 6, no. 6, pp. 413–429, 1977.
- [74] R. Weindruch and R. Walford, "Dietary restriction in mice beginning at 1 year of age: effect on life-span and spontaneous cancer incidence," *Science*, vol. 215, no. 4538, pp. 1415–1418, 1982.
- [75] R. H. Houtkooper, E. Pirinen, and J. Auwerx, "Sirtuins as regulators of metabolism and healthspan," *Nature Reviews Molecular Cell Biology*, vol. 13, no. 4, pp. 225–238, 2012.
- [76] E. L. Greer, D. Dowlatshahi, M. R. Banko, J. Villen, K. Hoang, D. Blanchard, S. P. Gygi, and A. Brunet, "An AMPK-FOXO Pathway Mediates Longevity Induced by a Novel Method of Dietary Restriction in *C. elegans*," *Current Biology*, vol. 17, no. 19, pp. 1646–1656, 2007.
- [77] D. Palgunow, M. Klapper, and F. Döring, "Dietary Restriction during Development Enlarges Intestinal and Hypodermal Lipid Droplets in *Caenorhabditis elegans*," *PLoS ONE*, vol. 7, no. 11, e46198, 2012.
- [78] M. Klapper, D. Findeis, H. Koefeler, and F. Döring, "Methyl group donors abrogate adaptive responses to dietary restriction in *C. elegans*," *Genes and Nutrition*, vol. 11, 4, 2016.
- [79] J. Durieux, S. Wolff, and A. Dillin, "The cell-non-autonomous nature of electron transport chain-mediated longevity," *Cell*, vol. 144, no. 1, pp. 79–91, 2011.
- [80] K. Luersen, U. Faust, D.-C. Gottschling, and F. Döring, "Gait-specific adaptation of locomotor activity in response to dietary restriction in *Caenorhabditis elegans*," *Journal of Experimental Biology*, vol. 217, no. 14, pp. 2480–2488, 2014.
- [81] T. A. Prolla and M. P. Mattson, "Molecular mechanisms of brain aging and neurodegenerative disorders: lessons from dietary restriction," *Trends in Neurosciences*, vol. 24, no. 11, pp. S21–S31, 2001.
- [82] L. Bertram and R. E. Tanzi, "The genetic epidemiology of neurodegenerative disease," *Journal of Clinical Investigation*, vol. 115, no. 6, pp. 1449–1457, 2005.
- [83] G. P. Bates, "History of genetic disease: The molecular genetics of Huntington disease - a history," *Nature Reviews Genetics*, vol. 6, no. 10, pp. 766–773, 2005.
- [84] S. Finkbeiner, A. Maria Cuervo, R. I. Morimoto, and P. J. Muchowski, "Disease-Modifying Pathways in Neurodegeneration," *Journal of Neuroscience*, vol. 26, no. 41, pp. 10349–10357, 2006.

Bibliography

- [85] J. Li and W. Le, "Modeling neurodegenerative diseases in *Caenorhabditis elegans*," *Experimental Neurology*, vol. 250, pp. 94–103, 2013.
- [86] S. T. Lamitina and K. Strange, "Transcriptional targets of DAF-16 insulin signaling pathway protect *C. elegans* from extreme hypertonic stress," *American Journal of Physiology-Cell Physiology*, vol. 288, no. 2, pp. C467–C474, 2005.
- [87] J. G. Culotti and R. L. Russell, "Osmotic avoidance defective mutants of the nematode *Caenorhabditis elegans*," *Genetics*, vol. 90, no. 2, pp. 243–256, 1978.
- [88] A. Schlotterer, G. Kukudov, F. Bozorgmehr, H. Hutter, X. Du, D. Oikonomou, Y. Ibrahim, F. Pfisterer, N. Rabbani, P. Thornalley, A. Sayed, T. Fleming, P. Humpert, V. Schwenger, M. Zeier, A. Hamann, D. Stern, M. Brownlee, A. Bierhaus, P. Nawroth, and M. Morcos, "C. elegans as Model for the Study of High Glucose-Mediated Life Span Reduction," *Diabetes*, vol. 58, no. 11, pp. 2450–2456, 2009.
- [89] A. Solomon, S. Bandhakavi, S. Jabbar, R. Shah, G. J. Beitel, and R. I. Morimoto, "Caenorhabditis elegans OSR-1 regulates behavioral and physiological responses to hyperosmotic environments," *Genetics*, vol. 167, no. 1, pp. 161–170, 2004.
- [90] K. Burkewitz, K. Choe, and K. Strange, "Hypertonic stress induces rapid and widespread protein damage in *C. elegans*," *American Journal of Physiology-Cell Physiology*, vol. 301, no. 3, pp. C566–C576, 2011.
- [91] D. J. Selkoe, "Cell biology of protein misfolding: The examples of Alzheimer's and Parkinson's diseases," *Nature Cell Biology*, vol. 6, no. 11, pp. 1054–1061, 2004.
- [92] M. Rodriguez, L. Basten Snoek, M. De Bono, and J. E. Kammenga, "Worms under stress: *C. elegans* stress response and its relevance to complex human disease and aging," *Trends in Genetics*, vol. 29, no. 6, pp. 367–374, 2013.
- [93] T. J. Schulz, K. Zarse, A. Voigt, N. Urban, M. Birringer, and M. Ristow, "Glucose Restriction Extends *Caenorhabditis elegans* Life Span by Inducing Mitochondrial Respiration and Increasing Oxidative Stress," *Cell Metabolism*, vol. 6, no. 4, pp. 280–293, 2007.
- [94] S. J. Lee, C. T. Murphy, and C. Kenyon, "Glucose Shortens the Life Span of *C. elegans* by Downregulating DAF-16/FOXO Activity and Aquaporin Gene Expression," *Cell Metabolism*, vol. 10, no. 5, pp. 379–391, 2009.
- [95] E. N. Anderson, M. E. Corkins, J. C. Li, K. Singh, S. Parsons, T. M. Tucey, A. Sorkaç, H. Huang, M. Dimitriadi, D. A. Sinclair, and A. C. Hart, "C. elegans lifespan extension by osmotic stress requires FUDR, base excision repair, FOXO, and sirtuins," *Mechanisms of Ageing and Development*, vol. 154, pp. 30–42, 2016.
- [96] D. Chandler-Brown, H. Choi, S. Park, B. R. Ocampo, S. Chen, A. Le, G. L. Sutphin, L. S. Shamieh, E. D. Smith, and M. Kaeberlein, "Sorbitol treatment extends lifespan and induces the osmotic stress response in *Caenorhabditis elegans*," *Frontiers in Genetics*, vol. 6, 316, 2015.

- [97] T. Z. Gal, I. Glazer, and H. Koltai, "An LEA group 3 family member is involved in survival of *C. elegans* during exposure to stress," *FEBS Letters*, vol. 577, no. 1-2, pp. 21–26, 2004.
- [98] N. I. Dmitrieva and M. B. Burg, "High NaCl promotes cellular senescence," *Cell Cycle*, vol. 6, no. 24, pp. 3108–3113, 2007.
- [99] S. T. Lamitina, R. Morrison, G. W. Moeckel, and K. Strange, "Adaptation of the nematode *Caenorhabditis elegans* to extreme osmotic stress," *American Journal of Physiology-Cell Physiology*, vol. 286, no. 4, pp. C785–C791, 2004.
- [100] R. Trouillon, M. C. Letizia, K. J. Menzies, L. Mouchiroud, J. Auwerx, K. Schoonjans, and M. A. Gijs, "A multiscale study of the role of dynamin in the regulation of glucose uptake," *Integrative Biology*, vol. 9, no. 10, pp. 810–819, 2017.
- [101] S. P. Curran and G. Ruvkun, "Lifespan regulation by evolutionarily conserved genes essential for viability," *PLoS Genetics*, vol. 3, no. 4, e56, 2007.
- [102] B. Goldstein and S. N. Hird, "Specification of the anteroposterior axis in *Caenorhabditis elegans*," *Development*, vol. 122, no. 5, pp. 1467–1474, 1996.
- [103] J. Hardin, *Imaging Embryonic Morphogenesis in C. elegans*, vol. 106. Elsevier Inc., 2011.
- [104] A. Carvalho, S. K. Olson, E. Gutierrez, K. Zhang, L. B. Noble, E. Zanin, A. Desai, A. Groisman, and K. Oegema, "Acute drug treatment in the early *C. elegans* embryo," *PLoS ONE*, vol. 6, no. 9, e24656, 2011.
- [105] K. Chung, Y. Kim, J. S. Kanodia, E. Gong, S. Y. Shvartsman, and H. Lu, "A microfluidic array for large-scale ordering and orientation of embryos," *Nature Methods*, vol. 8, no. 2, pp. 171–176, 2011.
- [106] M. Cornaglia, L. Mouchiroud, A. Marette, S. Narasimhan, T. Lehnert, V. Jovaisaite, J. Auwerx, and M. A. M. Gijs, "An automated microfluidic platform for *C. elegans* embryo arraying, phenotyping, and long-term live imaging," *Scientific reports*, vol. 5, 10192, 2015.
- [107] L. Dong, R. Jankele, M. Cornaglia, T. Lehnert, P. Gönczy, and M. A. Gijs, "Integrated Microfluidic Device for Drug Studies of Early *C. Elegans* Embryogenesis," *Advanced Science*, vol. 5, no. 5, 1700751, 2018.
- [108] E. B. Espiritu, L. E. Krueger, A. Ye, and L. S. Rose, "CLASPs function redundantly to regulate astral microtubules in the *C. elegans* embryo," *Developmental Biology*, vol. 368, no. 2, pp. 242–254, 2012.
- [109] T. T. K. Vuong-Brender, S. K. Suman, and M. Labouesse, "The apical ECM preserves embryonic integrity and distributes mechanical stress during morphogenesis," *Development*, vol. 144, no. 23, pp. 4336–4349, 2017.

Bibliography

- [110] P. Gönczy, C. Echeverri, K. Oegema, A. Coulson, S. Jones, R. Copley, J. Duperon, J. Oegema, M. Brehm, E. Cassin, E. Hannak, M. Kirkham, S. Pichler, K. Flohrs, A. Goessen, S. Leidel, A. Alleaume, C. Martin, N. Ozlü, P. Bork, and A. Hyman, “Functional genomic analysis of cell division in *C. elegans* using RNAi of genes on chromosome III,” *Nature*, vol. 408, no. 6810, pp. 331–336, 2000.
- [111] K. J. C. Verbrugghe and R. C. Chan, “Imaging *C. elegans* Embryos using an Epifluorescent Microscope and Open Source Software,” *Journal of Visualized Experiments*, no. 49, e2625, 2011.
- [112] H. B. Atakan, M. Cornaglia, L. Mouchiroud, J. Auwerx, and M. A. Gijs, “Automated high-content phenotyping from the first larval stage till the onset of adulthood of the nematode *Caenorhabditis elegans*,” *Lab on a Chip*, vol. 19, no. 1, pp. 120–135, 2019.
- [113] F. Ning, D. Delhomme, Y. LeCun, F. Piano, L. Bottou, and P. E. Barbano, “Toward automatic phenotyping of developing embryos from videos,” in *IEEE Transactions on Image Processing*, vol. 14, pp. 1360–1371, 2005.
- [114] Y. Azuma and S. Onami, “Biologically constrained optimization based cell membrane segmentation in *C. elegans* embryos,” *BMC Bioinformatics*, vol. 18, no. 1, 307, 2017.
- [115] Z. Bao, J. I. Murray, T. Boyle, S. L. Ooi, M. J. Sandel, and R. H. Waterston, “Automated cell lineage tracing in *Caenorhabditis elegans*,” *Proceedings of the National Academy of Sciences*, vol. 103, no. 8, pp. 2707–2712, 2006.
- [116] John Canny, “A Computational Approach To Edge Detection,” in *IEEE Transactions on Pattern Analysis and Machine Intelligence*, vol. 8, pp. 679–698, 1986.
- [117] A. Krizhevsky, I. Sutskever, and G. E. Hinton, “ImageNet Classification with Deep Convolutional Neural Networks,” in *Proceedings of Advances In Neural Information Processing Systems 25*, 2012.
- [118] E. Teshiba, K. Miyahara, and H. Takeya, “Glucose-induced abnormal egg-laying rate in *Caenorhabditis elegans*,” *Bioscience, Biotechnology and Biochemistry*, vol. 80, no. 7, pp. 1436–1439, 2016.
- [119] E. Svensk, R. Devkota, M. Stahlman, P. Ranji, M. Rauthan, F. Magnusson, S. Hammarsten, M. Johansson, J. Borén, and M. Pilon, “*Caenorhabditis elegans* PAQR-2 and IGLR-2 Protect against Glucose Toxicity by Modulating Membrane Lipid Composition,” *PLoS Genetics*, vol. 12, no. 4, e1005982, 2016.
- [120] J. Yu, W. Yang, H. Liu, Y. Hao, and Y. Zhang, “An Aversive Response to Osmotic Upshift in *Caenorhabditis elegans*,” *eNeuro*, vol. 4, no. 2, e0282–16.2017, 2017.
- [121] N. Khanna, C. P. Cressman III, C. P. Tatara, and P. L. Williams, “Tolerance of the Nematode *Caenorhabditis elegans* to pH , Salinity , and Hardness in Aquatic Media,” *Arch. Environ. Contam. Toxicol.*, vol. 32, no. 1, pp. 110–114, 1997.

- [122] H. N. Frazier III and M. B. Roth, "Adaptive Sugar Provisioning Controls Survival of *C. elegans* Embryos in Adverse Environments," *Current Biology*, vol. 19, no. 10, pp. 859–863, 2009.
- [123] L. G. Edgar, *Blastomere Culture and Analysis*, vol. 48. 1995.
- [124] C. M. Haynes and D. Ron, "The mitochondrial UPR - protecting organelle protein homeostasis," *Journal of Cell Science*, vol. 123, no. 22, pp. 3849–3855, 2010.
- [125] A. B. Hwang, D.-E. Jeong, and S.-J. Lee, "Mitochondria and Organismal Longevity," *Current Genomics*, vol. 13, no. 7, pp. 519–532, 2012.
- [126] T. Finkel, "The metabolic regulation of aging," *Nature Medicine*, vol. 21, no. 12, pp. 1416–1423, 2015.
- [127] L. Dong, M. Cornaglia, T. Lehnert, and M. A. Gijs, "Versatile size-dependent sorting of *C. elegans* nematodes and embryos using a tunable microfluidic filter structure," *Lab on a Chip*, vol. 16, no. 3, pp. 574–585, 2016.
- [128] B. Xian, J. Shen, W. Chen, N. Sun, N. Qiao, D. Jiang, T. Yu, Y. Men, Z. Han, Y. Pang, M. Kaeberlein, Y. Huang, and J. D. J. Han, "WormFarm: A quantitative control and measurement device toward automated *Caenorhabditis elegans* aging analysis," *Aging Cell*, vol. 12, no. 3, pp. 398–409, 2013.
- [129] N. Gritti, S. Kienle, O. Filina, and J. S. Van Zon, "Long-term time-lapse microscopy of *C. elegans* post-embryonic development," *Nature Communications*, vol. 7, 12500, 2016.
- [130] H. Wen, Y. Yu, G. Zhu, L. Jiang, and J. Qin, "A droplet microchip with substance exchange capability for the developmental study of *C. elegans*," *Lab on a Chip*, vol. 15, no. 8, pp. 1905–1911, 2015.
- [131] D. Ying, K. Zhang, N. Li, X. Ai, Q. Liang, Y. Wang, and G. Luo, "A droplet-based microfluidic device for long-term culture and longitudinal observation of *Caenorhabditis elegans*," *Biochip Journal*, vol. 6, no. 3, pp. 197–205, 2012.
- [132] J. Aceves, D. Erlij, and R. Martínez-Marañón, "The mechanism of the paralyzing action of tetramisole on *Ascaris* somatic muscle," *British Journal of Pharmacology*, vol. 38, no. 3, pp. 602–607, 1970.
- [133] D. K. Reilly, D. E. Lawler, D. R. Albrecht, and J. Srinivasan, "Using an Adapted Microfluidic Olfactory Chip for the Imaging of Neuronal Activity in Response to Pheromones in Male *C. elegans* Head Neurons," *Journal of Visualized Experiments*, no. 127, e56026, 2017.
- [134] P. R. Hunt, "The *C. elegans* model in toxicity testing," *Journal of Applied Toxicology*, vol. 37, no. 1, pp. 50–59, 2017.
- [135] S. D. Buckingham and D. B. Sattelle, "Fast, automated measurement of nematode swimming (thrashing) without morphometry," *BMC Neuroscience*, vol. 10, 84, 2009.

Bibliography

- [136] S. R. Lockery, S. E. Hulme, W. M. Roberts, K. J. Robinson, A. Laromaine, T. H. Lindsay, G. M. Whitesides, and J. C. Weeks, "A microfluidic device for whole-animal drug screening using electrophysiological measures in the nematode *C. elegans*," *Lab on a Chip*, vol. 12, no. 12, pp. 2211–2220, 2012.
- [137] P. Yadav and R. Singh, "A review on anthelmintic drugs and their future scope," *International Journal of Pharmacy and Pharmaceutical Sciences*, vol. 3, no. 3, pp. 17–21, 2011.
- [138] K. P. Choe, C. K. Leung, and M. M. Miyamoto, "Unique structure and regulation of the nematode detoxification gene regulator SKN-1: implications to understanding and controlling drug resistance," *Drug Metabolism Reviews*, vol. 44, no. 3, pp. 209–223, 2012.
- [139] R. Sangaletti and L. Bianchi, "A Method for Culturing Embryonic *C. elegans* Cells," *Journal of Visualized Experiments*, no. 79, e50649, 2013.
- [140] J. T. Fleming, M. D. Squire, T. M. Barnes, C. Tornoe, K. Matsuda, J. Ahnn, A. Fire, J. E. Sulston, E. A. Barnard, D. B. Sattelle, and J. A. Lewis, "Caenorhabditis elegans Levamisole Resistance Genes lev-1, unc-29, and unc-38 Encode Functional Nicotinic Acetylcholine Receptor Subunits," *The Journal of Neuroscience*, vol. 17, no. 15, pp. 5843–5857, 1997.
- [141] J. A. Lewis, C.-H. Wu, H. Berg, and J. H. Levine, "The genetics of levamisole resistance in the nematode *Caenorhabditis elegans*," *Genetics*, vol. 95, no. 4, pp. 905–928, 1980.
- [142] H. Qian, A. P. Robertson, J. A. Powell-Coffman, and R. J. Martin, "Levamisole resistance resolved at the single-channel level in *Caenorhabditis elegans*," *The FASEB Journal*, vol. 22, no. 9, pp. 3247–3254, 2008.
- [143] T. Boulin, M. Gielen, J. E. Richmond, D. C. Williams, P. Paoletti, and J.-L. Bessereau, "Eight genes are required for functional reconstitution of the *Caenorhabditis elegans* levamisole-sensitive acetylcholine receptor," *Proceedings of the National Academy of Sciences*, vol. 105, no. 47, pp. 18590–18595, 2008.
- [144] M. J. Smout, A. C. Kotze, J. S. McCarthy, and A. Loukas, "A novel high throughput assay for anthelmintic drug screening and resistance diagnosis by real-time monitoring of parasite motility," *PLoS Neglected Tropical Diseases*, vol. 4, no. 11, e885, 2010.
- [145] J. A. Carr, A. Parashar, R. Gibson, A. P. Robertson, R. J. Martin, and S. Pandey, "A microfluidic platform for high-sensitivity, real-time drug screening on *C. elegans* and parasitic nematodes," *Lab on a Chip*, vol. 11, no. 14, pp. 2385–2396, 2011.
- [146] B. Chen, A. Deutmeyer, J. Carr, A. P. Robertson, R. J. Martin, and S. Pandey, "Microfluidic bioassay to characterize parasitic nematode phenotype and anthelmintic resistance," *Parasitology*, vol. 138, no. 1, pp. 80–88, 2011.
- [147] T. Walston and J. Hardin, "An Agar Mount for Observation of *Caenorhabditis elegans* Embryos," *Cold Spring Harbor Protocols*, no. 12, pdb.prot5540, 2010.

-
- [148] D. M. Raizen, J. E. Zimmerman, M. H. Maycock, U. D. Ta, Y. J. You, M. V. Sundaram, and A. I. Pack, "Lethargus is a *Caenorhabditis elegans* sleep-like state," *Nature*, vol. 451, no. 7178, pp. 569–572, 2008.
- [149] A. J. Wolstenholme, I. Fairweather, R. Prichard, G. Von Samson-Himmelstjerna, and N. C. Sangster, "Drug resistance in veterinary helminths," *Trends in Parasitology*, vol. 20, no. 10, pp. 469–476, 2004.
- [150] K. Bull, A. Cook, N. A. Hopper, A. Harder, L. Holden-Dye, and R. J. Walker, "Effects of the novel anthelmintic emodepside on the locomotion, egg-laying behaviour and development of *Caenorhabditis elegans*," *International Journal for Parasitology*, vol. 37, no. 6, pp. 627–636, 2007.
- [151] J. Marré, E. C. Traver, and A. M. Jose, "Extracellular RNA is transported from one generation to the next in *Caenorhabditis elegans*," *Proceedings of the National Academy of Sciences*, vol. 113, no. 44, pp. 12496–12501, 2016.
- [152] J. Bernardo, "Maternal Effects in Animal Ecology," *American Zoologist*, vol. 36, no. 2, pp. 83–105, 1996.
- [153] M. Slatkin, "Epigenetic inheritance and the missing heritability problem," *Genetics*, vol. 182, no. 3, pp. 845–850, 2009.
- [154] B. T. Heijmans, E. W. Tobi, A. D. Stein, H. Putter, G. J. Blauw, E. S. Susser, P. E. Slagboom, and L. H. Lumey, "Persistent epigenetic differences associated with prenatal exposure to famine in humans," *Proceedings of the National Academy of Sciences*, vol. 105, no. 44, pp. 17046–17049, 2008.
- [155] L. Daxinger and E. Whitelaw, "Transgenerational epigenetic inheritance: More questions than answers," *Genome Research*, vol. 20, no. 12, pp. 1623–1628, 2010.
- [156] N. M. Bonini and S. L. Berger, "The sustained impact of model organisms—in genetics and epigenetics," *Genetics*, vol. 205, no. 1, pp. 1–4, 2017.
- [157] U. Grossniklaus, W. G. Kelly, A. C. Ferguson-Smith, M. Pembrey, and S. Lindquist, "Transgenerational epigenetic inheritance: how important is it?," *Nature Reviews Genetics*, vol. 14, no. 3, pp. 228–235, 2013.
- [158] B. Horsthemke, "A critical view on transgenerational epigenetic inheritance in humans," *Nature Communications*, vol. 9, 2973, 2018.
- [159] C. H. Rankin, "A review of transgenerational epigenetics for RNAi, longevity, germline maintenance and olfactory imprinting in *Caenorhabditis elegans*," *Journal of Experimental Biology*, vol. 218, no. 1, pp. 41–49, 2015.
- [160] O. Rechavi, L. Hourí-Ze'evi, S. Anava, W. S. S. Goh, S. Y. Kerk, G. J. Hannon, and O. Hobert, "Starvation-induced transgenerational inheritance of small RNAs in *C. elegans*," *Cell*, vol. 158, no. 2, pp. 277–287, 2014.

Bibliography

- [161] S. C. Harvey and H. E. Orbidans, “All eggs are not equal: The maternal environment affects progeny reproduction and developmental fate in *Caenorhabditis elegans*,” *PLoS ONE*, vol. 6, no. 10, e25840, 2011.
- [162] M. F. Perez, M. Francesconi, C. Hidalgo-Carcedo, and B. Lehner, “Maternal age generates phenotypic variation in *Caenorhabditis elegans*,” *Nature*, vol. 552, pp. 106–109, 2017.
- [163] A. Tauffenberger and J. A. Parker, “Heritable Transmission of Stress Resistance by High Dietary Glucose in *Caenorhabditis elegans*,” *PLoS Genetics*, vol. 10, no. 5, e1004346, 2014.
- [164] A. Klosin, E. Casas, C. Hidalgo-Carcedo, T. Vavouri, and B. Lehner, “Transgenerational transmission of environmental information in *C. elegans*,” *Science*, vol. 356, no. 6335, pp. 320–323, 2017.
- [165] E. L. Greer, T. J. Maures, D. Ucar, A. G. Hauswirth, E. Mancini, J. P. Lim, B. A. Benayoun, Y. Shi, and A. Brunet, “Transgenerational epigenetic inheritance of longevity in *Caenorhabditis elegans*,” *Nature*, vol. 479, pp. 365–371, 2011.
- [166] N. Chronis, “Worm chips: Microtools for *C. elegans* biology,” *Lab on a Chip*, vol. 10, no. 4, pp. 432–437, 2010.
- [167] H. B. Atakan, R. Xiang, M. Cornaglia, L. Mouchiroud, J. Auwerx, and M. A. M. Gijs, “Automated high-content phenotyping of the nematode *C. elegans* at single animal resolution with a microfluidic platform,” in *20th International Conference on Solid-State Sensors, Actuators and Microsystems (TRANSDUCERS)*, pp. 2209–2212, 2019.
- [168] D. T. Shaughnessy, K. McAllister, L. Worth, A. C. Haugen, J. N. Meyer, F. E. Domann, B. Van Houten, R. Mostoslavsky, S. J. Bultman, A. A. Baccarelli, T. J. Begley, R. W. Sobol, M. D. Hirschey, T. Ideker, J. H. Santos, W. C. Copeland, R. R. Tice, D. M. Balshaw, and F. L. Tyson, “Mitochondria, energetics, epigenetics, and cellular responses to stress,” *Environmental health perspectives*, vol. 122, no. 12, pp. 1271–1278, 2014.
- [169] M. M. Crane, K. Chung, J. Stirman, and H. Lu, “Microfluidics-enabled phenotyping, imaging, and screening of multicellular organisms,” *Lab on a Chip*, vol. 10, no. 12, pp. 1509–1517, 2010.
- [170] H. E. Kinser and Z. Pincus, “High-throughput screening in the *C. elegans* nervous system,” *Molecular and Cellular Neuroscience*, vol. 80, pp. 192–197, 2017.
- [171] Y. Tian, G. Garcia, Q. Bian, K. K. Steffen, L. Joe, S. Wolff, B. J. Meyer, and A. Dillin, “Mitochondrial Stress Induces Chromatin Reorganization to Promote Longevity and UPRmt,” *Cell*, vol. 165, no. 5, pp. 1197–1208, 2016.
- [172] O. Matilainen, P. M. Quirós, and J. Auwerx, “Mitochondria and Epigenetics – Crosstalk in Homeostasis and Stress,” *Trends in Cell Biology*, vol. 27, no. 6, pp. 453–463, 2017.

- [173] E. A. Schroeder, N. Raimundo, and G. S. Shadel, "Epigenetic silencing mediates mitochondria stress-induced longevity," *Cell Metabolism*, vol. 17, no. 6, pp. 954–964, 2013.
- [174] N. Moullan, L. Mouchiroud, X. Wang, D. Ryu, E. G. Williams, A. Mottis, V. Jovaisaite, M. V. Frochaux, P. M. Quiros, B. Deplancke, R. H. Houtkooper, and J. Auwerx, "Tetracyclines disturb mitochondrial function across eukaryotic models: A call for caution in biomedical research," *Cell Reports*, vol. 10, no. 10, pp. 1681–1691, 2015.
- [175] S. Maglioni, N. Arsalan, L. Franchi, A. Hurd, A. W. Pipari, G. D. Glick, and N. Ventura, "An automated phenotype-based microscopy screen to identify pro-longevity interventions acting through mitochondria in *C. elegans*," *Biochimica et Biophysica Acta - Bioenergetics*, vol. 1847, no. 11, pp. 1469–1478, 2015.
- [176] M. A. Sanz, W. Y. Tsang, E. M. Willems, L. A. Grivell, B. D. Lemire, H. Van der Spek, and L. G. Nijtmans, "The mitochondrial prohibitin complex is essential for embryonic viability and germline function in *Caenorhabditis elegans*," *Journal of Biological Chemistry*, vol. 278, no. 34, pp. 32091–32099, 2003.
- [177] M. Samson, M. M. Jow, C. C. Wong, C. Fitzpatrick, A. Aslanian, I. Saucedo, R. Estrada, T. Ito, S. k. R. Park, J. R. Yates III, and D. S. Chu, "The Specification and Global Reprogramming of Histone Epigenetic Marks during Gamete Formation and Early Embryo Development in *C. elegans*," *PLoS Genetics*, vol. 10, no. 10, e1004588, 2014.
- [178] J. D. Hibshman, A. Hung, and L. R. Baugh, "Maternal Diet and Insulin-Like Signaling Control Intergenerational Plasticity of Progeny Size and Starvation Resistance," *PLoS Genetics*, vol. 12, no. 10, e1006396, 2016.
- [179] W. Reik and J. Walter, "Genomic imprinting: parental influence on the genome," *Nature Reviews Genetics*, vol. 2, no. 1, pp. 21–32, 2001.
- [180] E. M. Jorgensen and S. E. Mango, "The art and design of genetic screens: *Caenorhabditis elegans*," *Nature Reviews Genetics*, vol. 3, no. 5, pp. 356–369, 2002.
- [181] A. Ben-Yakar, N. Chronis, and H. Lu, "Microfluidics for the analysis of behavior, nerve regeneration, and neural cell biology in *C. elegans*," *Current Opinion in Neurobiology*, vol. 19, no. 5, pp. 561–567, 2009.
- [182] A. San-Miguel and H. Lu, "Microfluidics as a tool for *C. elegans* research," 2013.
- [183] N. A. Bakhtina and J. G. Korvink, "Microfluidic laboratories for *C. elegans* enhance fundamental studies in biology," *RSC Advances*, vol. 4, no. 9, pp. 4691–4709, 2014.
- [184] K. Chung, M. M. Crane, and H. Lu, "Automated on-chip rapid microscopy, phenotyping and sorting of *C. elegans*," *Nature Methods*, vol. 5, no. 7, pp. 637–643, 2008.
- [185] P. Rezai, S. Salam, P. R. Selvaganapathy, and B. P. Gupta, "Electrical sorting of *Caenorhabditis elegans*," *Lab on a Chip*, vol. 12, no. 10, pp. 1831–1840, 2012.

Bibliography

- [186] X. Manière, F. Lebois, I. Matic, B. Ladoux, J. M. Di Meglio, and P. Hersen, “Running worms: *C. elegans* self-sorting by electrotaxis,” *PLoS ONE*, vol. 6, no. 2, e16637, 2011.
- [187] X. Wang, R. Hu, A. Ge, L. Hu, S. Wang, X. Feng, W. Du, and B. F. Liu, “Highly efficient microfluidic sorting device for synchronizing developmental stages of *C. elegans* based on deflecting electrotaxis,” *Lab on a Chip*, vol. 15, no. 11, pp. 2513–2521, 2015.
- [188] B. Han, D. Kim, U. H. Ko, and J. H. Shin, “A sorting strategy for *C. elegans* based on size-dependent motility and electrotaxis in a micro-structured channel,” *Lab on a Chip*, vol. 12, no. 20, pp. 4128–4134, 2012.
- [189] Y. Yan, L. F. Ng, L. T. Ng, K. B. Choi, J. Gruber, A. A. Bettiol, and N. V. Thakor, “A continuous-flow *C. elegans* sorting system with integrated optical fiber detection and laminar flow switching,” *Lab on a Chip*, vol. 14, no. 20, pp. 4000–4006, 2014.
- [190] J. Yuan, J. Zhou, D. M. Raizen, and H. H. Bau, “High-throughput, motility-based sorter for microswimmers such as *C. elegans*,” *Lab on a Chip*, vol. 15, no. 13, pp. 2790–2798, 2015.
- [191] L. Yang, T. Hong, Y. Zhang, J. G. S. Arriola, B. L. Nelms, R. Mu, and D. Li, “A microfluidic diode for sorting and immobilization of *Caenorhabditis elegans*,” *Biomedical Microdevices*, vol. 19, no. 2, 38, 2017.
- [192] G. Aubry, M. Zhan, and H. Lu, “Hydrogel-droplet microfluidic platform for high-resolution imaging and sorting of early larval *Caenorhabditis elegans*,” *Lab on a Chip*, vol. 15, no. 6, pp. 1424–1431, 2015.
- [193] X. Ai, W. Zhuo, Q. Liang, P. T. McGrath, and H. Lu, “A high-throughput device for size based separation of *C. elegans* developmental stages,” *Lab on a Chip*, vol. 14, no. 10, pp. 1746–1752, 2014.
- [194] X. C. I. Solvas, F. M. Geier, A. M. Leroi, J. G. Bundy, J. B. Edel, and A. J. DeMello, “High-throughput age synchronisation of *Caenorhabditis elegans*,” *Chemical Communications*, vol. 47, no. 35, pp. 9801–9803, 2011.
- [195] S. Sofela, S. Sahloul, M. Rafeie, T. Kwon, J. Han, M. E. Warkiani, and Y. A. Song, “High-throughput sorting of eggs for synchronization of: *C. elegans* in a microfluidic spiral chip,” *Lab on a Chip*, vol. 18, no. 4, pp. 679–687, 2018.

Curriculum Vitae

Hüseyin Barış Atakan

Address: Rue du Maupas 63, CH-1004 Lausanne Switzerland
Phone: +41 78 770 63 35
E-mail: huseyinbarisatakan@gmail.com, baris.atakan@epfl.ch



Education

Ecole Polytechnique Fédérale de Lausanne , Switzerland Ph.D. candidate, LMIS2, Doctoral program of Microsystems and Microelectronics	2015 - 2019
Eidgenössische Technische Hochschule Zürich , Switzerland M.Sc. in Micro and Nanosystems, Mechanical and Process Engineering	2013 - 2015 5.61 / 6.00
Middle East Technical University , Ankara, Turkey B.Sc. in Electrical and Electronics Engineering	2009 - 2013 3.98 / 4.00

Work and Research Experience

Ecole Polytechnique Fédérale de Lausanne , Switzerland Research and teaching assistant, supervised by Prof. Martin Gijs Research Area: Microfluidic devices for automated manipulation and high-content phenotyping of <i>C. elegans</i> Supervision: 1 B.Sc. Project, 3 M.Sc. Projects and 1 M.Sc. thesis project Teaching: Cleanroom theoretical and practical courses for B.Sc. students MICRO-331 Technologie des microstructures I MICRO-332 TP en salle blanche	November 2015 - November 2019
Riken Quantitative Biology Center , Kobe, Japan Frey Initiative Research Unit Research Area: On-chip integration and characterization of CNT sensor arrays	September 2014 - February 2015

Ecole Polytechnique Fédérale de Lausanne, Switzerland July 2012
 Microelectronic Systems Laboratory (LSM) - September 2012
Research Area: Implementation of depth map estimation algorithms in Matlab
 from the captured images of several horizontally aligned cameras

ASELSAN Inc., Ankara, Turkey June 2011
 Defense System and Technologies Unit - July 2011
Work Area: The test applications of a servo motor analog card, the design and
 implementation of a regenerative energy dumping circuit on a board

Technical Skills

Cleanroom Technologies

Photolithography, Dry and wet etching, Sputtering, Mask design and fabrication, Surface treatment, SEM, AFM, Profilometer devices, PDMS applications

Programing Languages and Software Skills

Matlab, Fiji, ImageJ, CleWin, KLayout, COMSOL, Adobe Illustrator - Photoshop, SolidWorks, MS tools, C, Python, AutoCAD

Biotechnology

C. elegans maintenance and handling, *E. coli* culture, BSL-2 tools and devices

Awards & Honors

High Honor Student - Ranked 2nd in Middle East Technical University	2013
Recipient of Excellence Scholarship & Opportunity Award from ETH Zurich	2013
Recipient of Fulbright Scholarship (not attended)	2012
Received Bülent Kerim Altay High Success Award six times from Middle East Technical University, Electrical and Electronics Engineering Department	2009 - 2012
Listed in High Honor Roll in Middle East Technical University, Electrical and Electronics Engineering Department	2009 - 2012

Language Skills

Turkish	Native
English	Fluent (C2)
French	Intermediate (B1)
German	Beginner (A2)

List of Publications

Journal Contributions

H. B. Atakan, K. S. Hof, M. Cornaglia, J. Auwerx and M. A. M. Gijs, “The detection of early epigenetic inheritance of mitochondrial stress in *C. elegans* with a microfluidic phenotyping platform”, *Scientific Reports*, under review, 2019.

V. Viri, M. Cornaglia, **H. B. Atakan**, T. Lehnert and M. A. M. Gijs, “An *in vivo* microfluidic study of bacterial digestion in *C. elegans* nematodes”, *Lab Chip*, under review, 2019.

H. B. Atakan, F. Ayhan and M. A. M. Gijs, “PDMS filter structures for size-dependent larval sorting and on-chip egg extraction of *C. elegans*”, *Lab Chip*, under review, 2019.

H. B. Atakan, T. Alkanat, M. Cornaglia, R. Trouillon and M. A. M. Gijs, “Automated phenotyping of *C. elegans* embryos with a high-throughput-screening microfluidic platform”, *Microsystems & Nanoengineering*, under review, 2019.

H. B. Atakan, R. Xiang, M. Cornaglia, L. Mouchiroud, E. Katsyuba, J. Auwerx and M. A. M. Gijs, “Automated platform for long-term culture and high-content phenotyping of single *C. elegans* worms”, *Scientific Reports*, vol. 9, 14340, 2019.

H. B. Atakan, M. Cornaglia, L. Mouchiroud, J. Auwerx and M. A. M. Gijs, “Automated high-content phenotyping from the first larval stage till the onset of adulthood of the nematode *Caenorhabditis elegans*”, *Lab Chip*, vol. 19, no. 1, pp. 120-135, 2019.

N. Shamsudhin, N. Laeubli, **H. B. Atakan**, H. Vogler, C. Hu, W. Haeberle, A. Sebastian, U. Grossniklaus and B. J. Nelson, “Massively parallelized pollen tube guidance and mechanical measurements on a lab-on-a-chip platform”, *PLoS One*, vol. 11, no. 12, e0168138, 2016.

Conference Contributions

H. B. Atakan, R. Xiang, M. Cornaglia, L. Mouchiroud, J. Auwerx and M. A. M. Gijs, “Automated high-content phenotyping of the nematode *C. elegans* at single animal resolution with a microfluidic platform”, in *20th International Conference on Solid-State Sensors, Actuators and Microsystems (TRANSDUCERS)*, pp. 2209-2212, 2019.

H. B. Atakan, M. Cornaglia, L. Mouchiroud, J. Auwerx and M. A. M. Gijs, “Slow-down of Huntington’s disease progression in a *Caenorhabditis elegans* worm model by decreasing bacterial food supply on-chip”, in *22nd International Conference on Miniaturized Systems for Chemistry and Life Sciences*, pp. 1543-1545, 2018.

H. B. Atakan, R. Xiang and M. A. M. Gijs, “Variable-height microfluidic channels for accurate immobilization of *C. elegans* worms by using a single dry etching step”, in *22nd International Conference on Miniaturized Systems for Chemistry and Life Sciences*, pp. 630-631, 2018.

H. B. Atakan, M. Cornaglia, T. Alkanat, R. Trouillon and M. A. M. Gijs, “Automated on-chip phenotyping of *Caenorhabditis elegans* embryos: a developmental study as function of exposure to various compounds”, in *22nd International Conference on Miniaturized Systems for Chemistry and Life Sciences*, pp. 119-121, 2018.

H. B. Atakan, M. Cornaglia, L. Mouchiroud, J. Auwerx and M. A. M. Gijs, “A microfluidic platform for automated phenotyping during full lifespan of *Caenorhabditis elegans* at high-throughput”, in *21st International Conference on Miniaturized Systems for Chemistry and Life Sciences*, pp. 50-51, 2017.

N. Shamsudhin, **H. B. Atakan**, N. Läubli, H. Vogler, C. Hu, A. Sebastian, U. Grossniklaus and B. J. Nelson, “Probing the micromechanics of the fastest growing plant cell – the pollen tube”, in *38th Annual International Conference of the IEEE Engineering in Medicine and Biology Society (EMBC)*, pp. 461-464, 2016.

A. Akin, I. Baz, **B. Atakan**, I. Boybat, A. Schmid and Y. Leblebici, “A hardware-oriented dynamically adaptive disparity estimation algorithm and its real-time hardware”, in *Proceedings of the 23rd ACM international conference on Great lakes symposium on VLSI*, pp. 155-160, 2013.

Patents

A. Akin, Y. Leblebici, A. Schmid, I. Baz, I. Boybat, **H. B. Atakan**, "Hardware-oriented dynamically adaptive disparity estimation algorithm and its real-time hardware", US 2015/0319419 A1, Nov. 5, 2015.

